Strategies to Reduce Seismic Losses and Improve Seismic Loss Assessments

Strategies to Reduce Seismic Losses and Improve Seismic Loss Assessments

by:
MirAmir Banihashemi, MASc

A Thesis Submitted to the School of Graduate Studies
in Partial Fulfillment of the Requirements for the Degree Doctor of Philosophy

McMaster University

Thesis Information

Degree: Doctor of Philosophy (2023)

Department: Civil Engineering

Institution: McMaster University

City: Hamilton, ON

Title: Strategies to Reduce Seismic Losses and Improve Seismic Loss Assessments

Author: MirAmir Banihashemi, MASc (Sharif University of Technology, 2017)

Supervisor: Dr. Lydell Wiebe, P.Eng.

Number of pages: xxiii, 187

LAY ABSTRACT

Observations from past earthquakes have shown that while modern buildings could typically withstand earthquakes without collapsing, they often required extensive repairs due to structural and nonstructural damage. To address these concerns, controlled rocking braced frames (CRBFs) have been suggested as a novel building technology to prevent damage to steel buildings during earthquakes and to minimize residual deformations. However, a pertinent question arises: does the reduction in structural damage achieved by CRBFs come at the cost of heightened acceleration demands and associated damage to nonstructural components? Such trade-offs can be assessed by estimating earthquake-induced losses, with FEMA P-58 defining a methodology that stands as the current benchmark in this field. The growing emphasis on enhancing structural performance and community resilience has led to the widespread adoption of this methodology and its comprehensive library of component models.

In the first half of the thesis, seismic loss assessments are conducted to examine the trade-offs between structural damage and damage to nonstructural components. This involves a comparison between buildings that rely on ductile steel seismic force-resisting systems (SFRSs) and those with CRBFs. Additionally, the influence of CRBF design parameters on seismic loss assessments is also studied in order to determine if constraints are needed on these parameters to control the total earthquake-induced losses of CRBFs.

In the second half of the thesis, the focus shifts to enhancing the FEMA P-58 seismic loss assessment methodology itself. Suitable engineering demand parameters for assessing damage to acceleration-sensitive nonstructural components are identified, and the modeling of economies of scale in the calculation of repair costs is investigated.

ABSTRACT

While seismic design provisions have improved building safety and reduced collapse incidents, the socio-economic impact of earthquakes persists as a significant concern. Excessive residual drifts and damage to structural and non-structural components may lead to building demolition or costly repairs, resulting in business interruptions, economic losses, and protracted disaster recovery for cities. This thesis commences by exploring approaches to mitigate seismic losses by comparing controlled rocking braced frames (CRBFs) to more conventional ductile steel seismic force-resisting systems (SFRSs). Three widely used ductile SFRS types in the seismic design of buildings are special moment resisting frames (SMRFs), special concentrically braced frames (SCBFs), and buckling-restrained braced frames (BRBFs). However, these ductile SFRSs have been associated with prominent structural damage and substantial residual deformations in past observed earthquakes. CRBFs offer an alternative SFRS with less structural damage, but concerns exist about potential trade-offs, such as increased acceleration and displacement demands, and associated nonstructural damage. This thesis explores these trade-offs in buildings of varying heights with both ductile SFRSs and CRBFs, assessing the structural response under varying earthquakes and focusing on expected annual losses (EALs). The results show that CRBF-equipped buildings still have lower total EALs even when considering these factors.

CRBFs offer designers a high degree of control during the design process, with previous research demonstrating low collapse risk across a broad spectrum of design options. However, some studies have also highlighted the increased demands on nonstructural components in CRBF buildings. Therefore, while CRBFs have shown satisfactory collapse performance for various design options, assessing these options in terms of nonstructural component performance is essential. This thesis examines how two design parameters, namely the response modification factor (R) for rocking joint design and the amplification factor for considering higher-mode

forces in steel member capacity design, influence earthquake-induced losses in CRBFs. The results indicate that although total EALs do not differ significantly across various design options, the distribution of losses between repairable and irreparable losses varies.

In the above-mentioned portions of the thesis, the seismic loss assessments follow the FEMA P-58 methodology, which involves two essential steps: first, evaluating damage using damage fragility curves, and then assessing the effects of this damage through consequence models. Both of these steps are critically evaluated in the second half of this thesis.

Fragility curves, including those in the FEMA P58 library, typically use peak floor accelerations (PFAs) to estimate losses in acceleration-sensitive nonstructural components. However, PFAs, like peak ground accelerations (PGAs) for buildings, have limitations as engineering demand parameters (EDPs) because they do not reflect the period of these components. In search of suitable options for creating seismic damage fragility curves, this thesis evaluates fifteen other EDPs proposed in the literature.

This thesis also addresses an ambiguity in FEMA P-58's consequence modeling. The modeling of economies of scale is an integral part of consequence modeling. However, the lack of a clear definition for aggregate damage, which is a factor that significantly influences component modeling of economies of scale, can substantially impact simulated repair costs, repair times, and performance assessment.

Overall, this thesis provides insights into reducing seismic losses by designing CRBFs as an alternative to commonly used SFRSs, and into improving seismic loss assessments by enhancing the damage fragility curves and consequence models within the widely-used FEMA P58 methodology.

ACKNOWLEDGEMENTS

I wish to express my heartfelt appreciation to my supervisor, Dr. Lydell Wiebe, for his unwavering support, generous allocation of his time, extensive knowledge, and invaluable insights during my doctoral studies. I am genuinely grateful for the opportunity provided by Dr. Lydell Wiebe, which has allowed me to both develop as an individual through his companionship and receive his expert guidance throughout my doctoral journey. I would also like to extend my sincere gratitude to Dr. Andre Filiatrault, whose invaluable contributions greatly enriched my doctoral studies. His guidance, patience, and support were instrumental in facilitating numerous research breakthroughs throughout my doctoral journey.

I would like to acknowledge the valuable contributions of Dr. Adám Zsarnóczay, whose feedback and fresh insights significantly contributed to the development of some aspects of this thesis. I would also like to express my gratitude to Alessandra Miliziano for her valuable collaborations and contributions to some parts of my thesis.

Sincere thanks are due to Dr. Georgios Balomenos, Dr. Cancan Yang, and Dr. Dimitrios Konstantinidis, who served as outstanding members of my Ph.D. supervisory committee. I am grateful for their generous encouragement, engagement, and valuable insights throughout my doctoral journey.

I would also like to express my gratitude to Dr. Abbie Liel for dedicating time to serving as the external examiner for this thesis. I am deeply thankful for her considerate and insightful evaluation of my thesis.

I would like to express my heartfelt gratitude to my dear friends, especially Nastaran, Maryam, Saeed, Sahar, and Kazem, who have become my second family in Hamilton.

All my success is owed to my parents, Lida and Mansoor, and I am forever grateful to them. Their sacrifices, dedication, unwavering support, and unconditional love have enabled me to pursue my passions and ultimately present this work.

DEDICATION

To

my Mother & Father

PREFACE

This thesis adheres to the sandwich thesis format requirements specified by the School of Graduate Studies at McMaster University. In compliance with the criteria for the manuscript-based sandwich thesis format, Chapters 2 through 5 have been submitted for publication consideration to peer-reviewed journals. The numerical analysis and methodology development presented in this thesis were conducted by the author, with primary supervision, guidance, and review provided by Dr. Lydell Wiebe, and with assistance from Dr. Andre Filiatrault, as indicated in the authorship of each manuscript. Additionally, the section titled “Drivers of economies of scale in FEMA P-58” received contributions from Dr. Ádám Zsarnóczay and Alessandra Miliziano. Dr. Ádám Zsarnóczay also offered assistance in writing Chapter 5, particularly in the recommendations and conclusion section. The manuscripts comprising the chapters of this thesis are co-authored, and their current status as of November 2023 is as follows:

Chapter 2: “Seismic loss comparison for buildings designed with ductile steel seismic force-resisting systems and with controlled rocking braced frames”

Authors: MirAmir Banihashemi and Lydell Wiebe

Under review by *Earthquake Spectra* (Reference number: EQS-23-0245)

Chapter 3: “Effect of design parameters on earthquake-induced losses of controlled rocking braced frames”

Authors: MirAmir Banihashemi and Lydell Wiebe

Under review by *Journal of Earthquake Engineering* (Reference number: 236756428)

Chapter 4: “Suitable Engineering Demand Parameters for Acceleration-Sensitive Nonstructural Components”

Authors: MirAmir Banihashemi, Lydell Wiebe, and Andre Filiatrault

Under review by *Earthquake Engineering & Structural Dynamics* (Reference number: EQE-23-0501)

Chapter 5: “Consequences of consequence models: the impact of economies of scale on seismic loss estimates”

Authors: MirAmir Banihashemi, Alessandra Miliziano, Ádám Zsarnóczay, Lydell Wiebe, and Andre Filiatrault

Earthquake Spectra (DOI: 10.1177/87552930231220001/ ID: EQS-23-0084.R1)

TABLE OF CONTENTS

LIST OF TABLES

LIST OF FIGURES

Chapter 1

1. INTRODUCTION

1.1 MOTIVATION

The risk associated with earthquakes rises as human society becomes more urbanized. The primary goal of conventional seismic design and retrofitting of buildings is to maintain the collapse risk below a predefined threshold by ensuring the building possesses adequate strength and ductility (ACI 318-19, 2019; ANSI/AISC 341-16, 2016; EN 1998-1:2008, 2008). Real-world events over the past decade validated that such designs effectively prevent collapses and achieve life safety objectives. However, these events also underscored the considerable economic consequence of structural damage in buildings that remained standing but were impaired (McKevitt et al., 1995; Tremblay et al., 1996). As a result, concerns regarding the earthquake resilience of buildings have emerged, prompting occupants and building owners to consider whether seismic safety objectives should encompass more than just ensuring life safety.

In this context, numerous research initiatives and industry strategies have actively pursued enhanced seismic resilience, giving rise to the development of seismic force-resisting systems (SFRSs) that surpass the basic code requirements. Within this category of systems, often referred to as "low-damage" and "high-performance," self-centering systems have emerged as one of the prominent solutions. Self-centering systems replace the force-limiting mechanism of material yielding that is used in conventional SFRSs with an alternative mechanism, often by employing geometric nonlinearity, thereby ensuring that no structural damage is experienced in the frame. However, while some self-centering systems have emerged as promising low-damage alternative SFRSs, concerns have also been raised about whether the reduction in structural damage with self-centering systems may come at the cost of increased acceleration or drift demands and associated nonstructural damage.

Extensive nonstructural damage was observed across various building types during previous seismic events, such as the 1994 Northridge earthquake in the USA and the 2010 Maule earthquake in Chile (Reitherman et al., 1995; Miranda et al., 2012). The design of nonstructural components holds a critical role in ensuring structural resilience for several reasons, including (i) nonstructural components tend to sustain damage at much lower seismic intensities compared to structural elements (Miranda and Taghavi, 2003); (ii) even minor nonstructural damage, like a crack in a pressure pipe, can severely impact the functionality of vital facilities, such as hospitals, even if the building structure remains undamaged (Filiatrault and Sullivan, 2014); and (iii) losses stemming from nonstructural damage surpass those associated with structural components and framing (Filiatrault and Sullivan, 2014; Miranda and Taghavi, 2003). To illustrate, following the 2010 offshore Maule earthquake in Chile with a magnitude of 8.8, the primary economic losses were attributed to nonstructural damage and the disruption of critical facilities, while only a few buildings experienced structural damage (Miranda et al., 2012). It is also worth noting that a significant portion of the overall investment in buildings comprises contents and nonstructural components. Specifically, these average investments have been estimated as 82%, 87%, and 92% of the total investment in office, hotel, and hospital buildings (Miranda and Taghavi, 2003), respectively.

Hence, considering the aftermath and the socioeconomic impact of past earthquakes, the field of performance-based earthquake engineering has evolved, giving rise to a comprehensive framework for seismic loss assessments (Cornell and Krawinkler, 2000; FEMA P-58-1, 2018).

The ATC-58 project developed the FEMA P-58 methodology (FEMA P-58-1, 2018), which provides a numerical approach to this framework. Additionally, as part of the ATC-58 project, a library of damage fragility curves and consequence functions was prepared for a diverse array of over 700 prevalent structural and nonstructural components typically found in building structures (FEMA P-58-3, 2018). These resources encompass the essential parameters required to construct models of damage and evaluate the resulting consequences for structural and nonstructural components during earthquakes. Empowered by this framework, engineers and a wide spectrum of stakeholders have the means to conduct a nuanced evaluation of potential ramifications of earthquakes. This capability ultimately equips them with the insights required to make decisions concerning design and retrofitting.

This thesis builds on the work described above by seeking to provide strategies for: (1) reducing seismic losses; and (2) enhancing seismic loss assessments. An overview of the structure of this thesis is shown in Figure 1-1. Firstly, it involves a comparative analysis of the effectiveness of controlled rocking braced frames (CRBFs) as self-centering systems relative to conventional ductile SFRSs, with a focus on earthquake-induced losses. Additionally, it explores the impact of design parameters on the seismic performance of CRBFs with regard to expected seismic losses. Secondly, the study delves into the improvement of damage fragility curves and consequence functions within the FEMA P58 methodology. As background for this work, Section 1.2 provides an explanation of recent findings and conclusions from previous studies on CRBFs. Then, the FEMA P-58 methodology, which is widely used for seismic loss assessment, is discussed in detail in Section 1.3 before a more detailed discussion of the thesis objectives in Section 1.4.

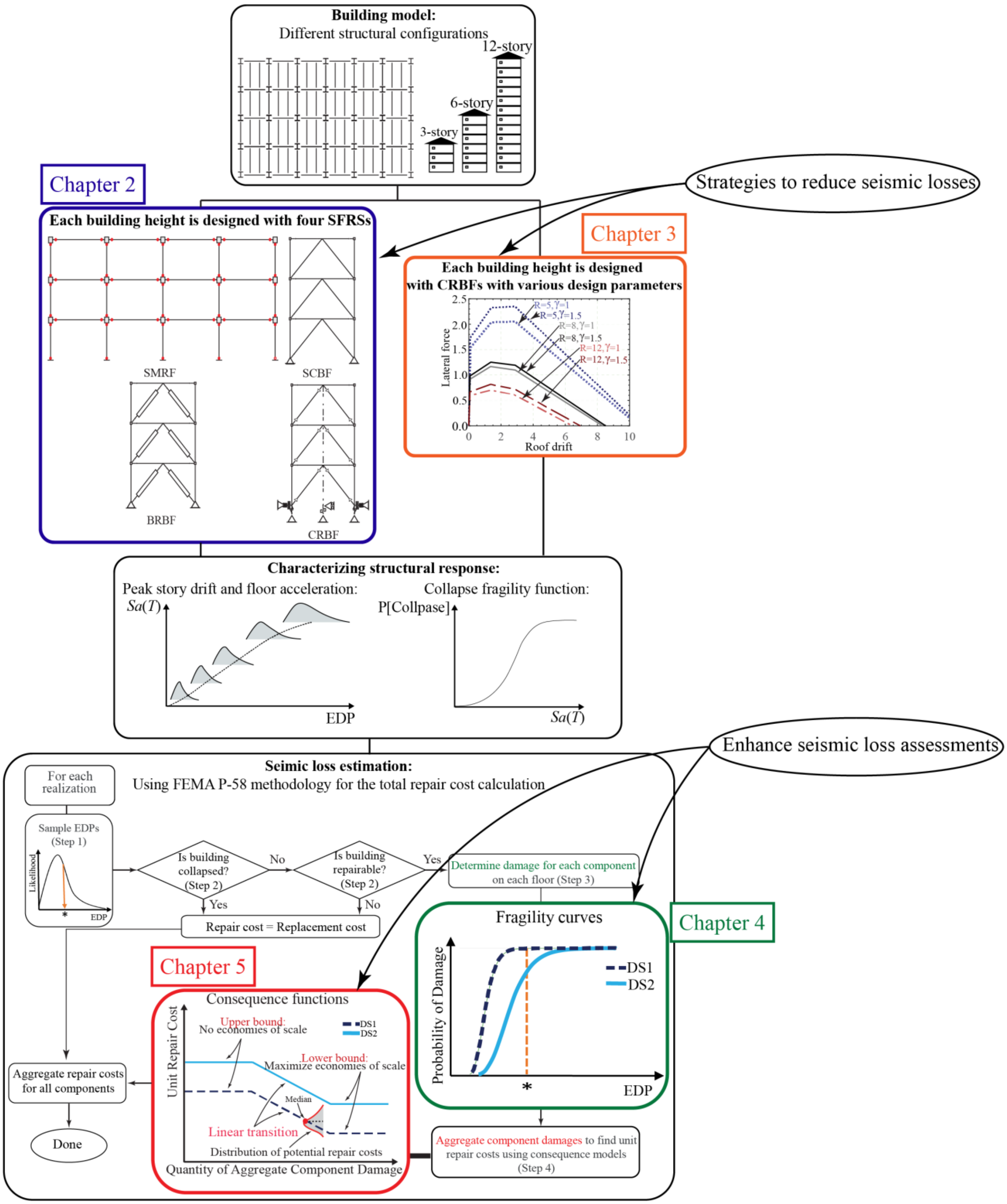

Figure 1-1. Overview of the structure of this thesis.

1.2 CONTROLLED ROCKING BRACED FRAMES

CRBFs differentiate themselves from conventional ductile SFRSs by utilizing a nonlinear mechanism involving the uplifting of the frame. Vertical post-tensioning is incorporated to inherently self-center the system and introduce positive stiffness during rocking motion. Furthermore, energy dissipation mechanisms can be integrated to alleviate displacement demands. Figure 1-2 illustrates the conceptual behavior of a CRBF.

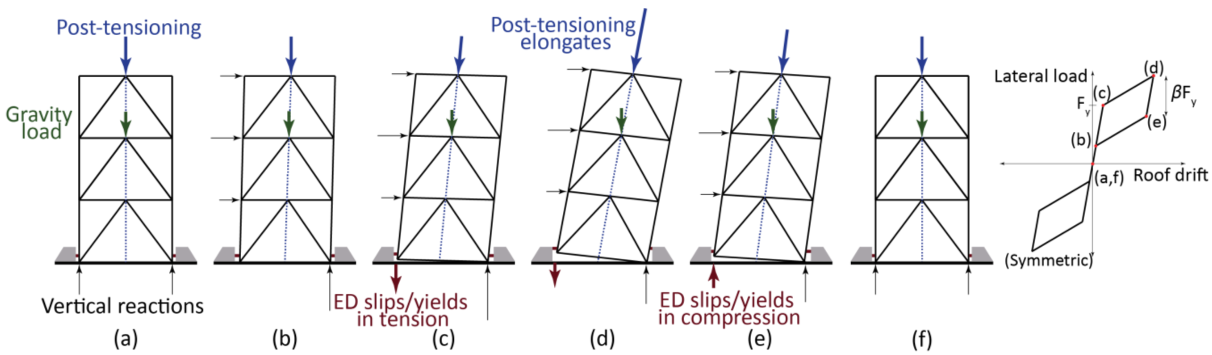

Figure 1-2. CRBF hysteretic response (Used also in Chapter 3).

Figure 1-3 delineates two primary strategies proposed for CRBF design and integration within building systems (Steel Construction New Zealand, 2015; Steele and Wiebe, 2020). The first configuration, represented in Figure 1-3 (a), entails designing a CRBF that integrates with the gravity framing, thereby introducing uplifting displacements on the floor system tributary to the columns of the braced bay (Eatherton et al., 2014). Concerns have emerged regarding dynamic effects resulting from the impact of uplifting columns on the foundation and localized damage to floor slabs caused by rotational demands during uplift. Responding to these concerns, Figure 1-3 (b) presents an alternative positioning of the CRBF between gravity columns (Roke et al., 2010; Wiebe and Christopoulos, 2015). This arrangement incorporates special connection details, enabling the frame to rock without imposing uplift on adjacent gravity framing, effectively decoupling them. Consequently, the CRBF in this configuration avoids bearing tributary gravity loads, potentially mitigating localized damage and dynamic effects of column impact on the floor system. Moreover, when designed to be decoupled from the gravity system, the CRBF is not expected to transmit vertical accelerations resulting from CRBF uplifting and rocking to the floor diaphragms (Buccella, 2019). This study investigates CRBFs that are decoupled from gravity system.

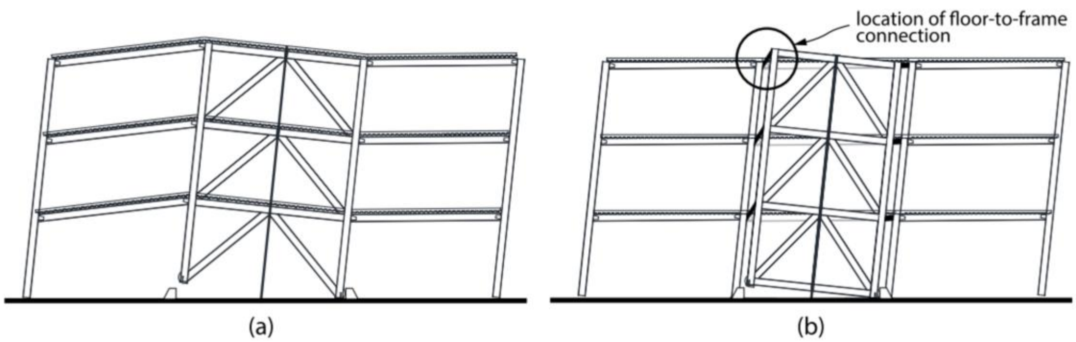

Figure 1-3. Design suggestions for CRBFs within buildings: (a) coupled with gravity framing and (b) decoupled from gravity (Steele and Wiebe, 2020).

Studies assessing the potential for collapse in CRBFs consistently indicate minimal damage to their steel components and a low probability of collapse (Rahgozar et al., 2016; Steele and Wiebe, 2017). Moreover, research conducted by Wiebe and Christopoulos (2015) underscores that structures designed with CRBFs exhibit minimal residual drifts, even when subjected to severe ground motions at the maximum considered earthquake (MCE) level. Recognizing the significant advantages of CRBFs, Steele and Wiebe (2021) quantified key design parameters for CRBFs, including response modification factors (R) employed in the design of base rocking joints, as well as a parameter related to the intensity level considered for higher modes in the capacity design of steel members within CRBFs. Their findings affirm that CRBFs maintain an acceptably low risk of collapse, even when employing larger values of R (indicating less resistance to rocking) and considering the use of the design earthquake (DE) intensity level to account for higher mode effects in the capacity design of steel members. However, Buccella et al. (2021) demonstrated increased acceleration demands in CRBFs, particularly resulting in spikes in the floor spectra that align with the modal periods of the building (Figure 1-4), since the base rocking mechanism does not fully control higher-mode vibration, and the frame members are capacity designed to remain linear elastic.

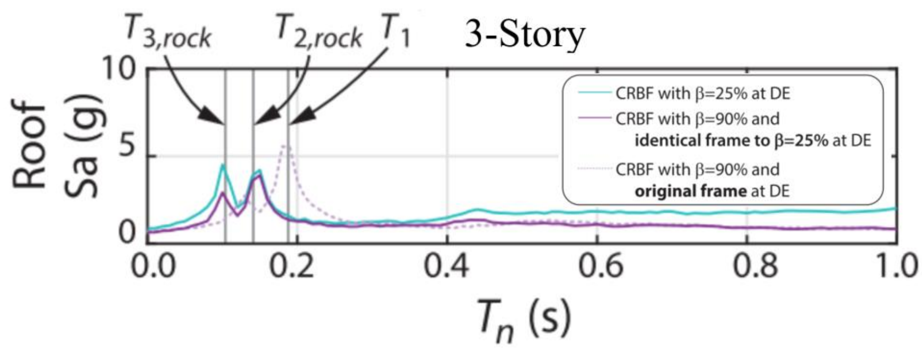

Figure 1-4. Median pseudo-acceleration floor spectra for 3-story CRBFs (Buccella et al., 2021).

Over the past decade, a few studies have employed seismic loss assessment to compare self-centering lateral force-resisting systems with ductile systems. Due to the potentially higher construction costs associated with CRBFs, researchers have conducted cost-benefit analyses comparing CRBFs to special concentrically braced frames (SCBFs) (Dyanati et al., 2017; Huang et al., 2018). These investigations found that, for six- and eight-story buildings, CRBFs result in lower total annual losses compared to SCBFs (Figure 1-5). However, in the case of ten-story buildings, SCBFs exhibited lower total annual losses than CRBFs. Notably, the primary source of loss in the examined CRBF buildings was identified as damage to acceleration-sensitive nonstructural components. Even though these studies were fairly comprehensive, the most recent version of FEMA P-58-3 (2018) now includes updated damage fragility curves for nonstructural components. Furthermore, Martin et al. (2019) demonstrated that alternative methods for capacity design of CRBF members, such as those proposed by Steele and Wiebe

(2016), have yielded more reliable and accurate capacity design results than the methods used by Dyanati et al. (2017) and Huang et al. (2018).

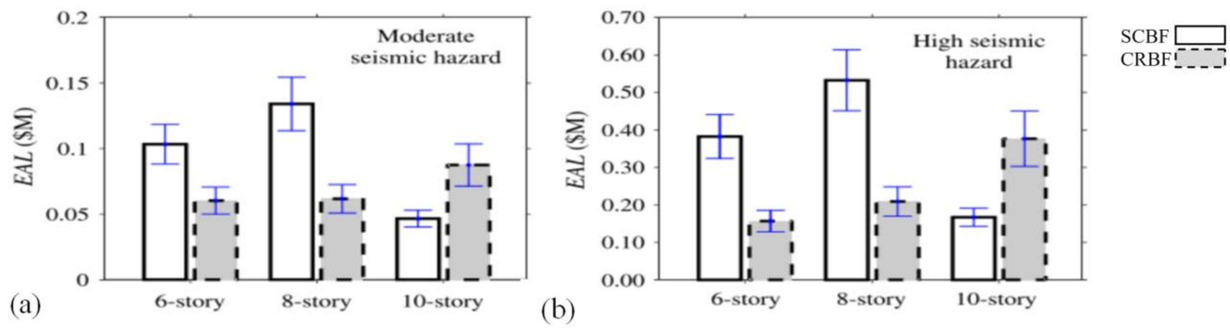

Figure 1-5. Expected annual loss (EAL) of prototype buildings for different seismic hazards: (a) Moderate seismic hazard; and (b) High Seismic hazard (Huang et al., 2018).

1.3 SEISMIC LOSS ASSESSMENT WITH FEMA P-58

In recent decades, significant research efforts have been devoted to creating a framework for simulating seismic damage and losses in buildings. This framework aims to assist engineers and other stakeholders in effectively communicating these outcomes and making informed design and retrofit decisions. The Pacific Earthquake Engineering Research (PEER) center pioneered a performance-based earthquake engineering framework designed to simulate the seismic performance of both structural and non-structural elements within buildings. This framework includes calculating various decision variables, such as repair costs, downtime, and casualties (Cornell and Krawinkler, 2000; Miranda and Aslani, 2003; Moehle and Deierlein, 2004). The PEER framework systematically quantifies and accounts for uncertainties associated with seismic hazards and structural behavior. It breaks down the modeling process into distinct components, namely the seismic event's intensity (IM - intensity measure), structural response (EDP - Engineering Demand Parameter), expected damage (DM - Damage Measure), and the consequences of that damage (DV - Decision Variable). These models are integrated using the total probability theorem three times, resulting in the following triple integral, which has become a standard tool in structural performance assessment (Attary et al., 2017; Barbato et al., 2013; Ciampoli et al., 2011):

$$G(DV) = \iiint G(DV|DM) \cdot |dG(DM|EDP)| \cdot |dG(EDP|IM)| \cdot |d\lambda(IM)| \quad (1\text{-}1)$$

where $G()$ represents the complementary cumulative distribution function or exceedance function, and $\lambda()$ denotes the hazard intensity exceedance function, commonly referred to as the hazard curve.

Obtaining a closed-form solution for this triple integral is a challenge due to the inherent complexity and nonlinearity of the underlying models. To address this, the PEER framework served as the basis for the development of the FEMA P-58 methodology within the ATC-58 project (FEMA P-58-1, 2018). This methodology offers a numerical approach that employs Monte Carlo simulation to estimate the triple integral. The FEMA P-58 methodology consists of five primary steps for determining repair consequences in each iteration of a Monte Carlo simulation (see Figure 1-1): (1) the building's response is characterized by randomly selecting engineering demand parameters (EDPs) based on the expected behavior at intensity measures that represent the local seismic hazard; (2) the building is then assessed for irreparable damage, whether due to collapse or excessive residual drift; (3) for reparable buildings, the damage state (DS) of each building component is computed using the EDP realizations obtained in step 1, along with component-specific fragility functions; (4) the unit repair cost for each damaged component is determined by considering the cumulative damaged quantities and the consequence model corresponding to each DS; and (5) the product of unit repair costs and damaged quantities is aggregated for all components within the building.

1.3.1 DAMAGE ASSESSMENT IN NONSTRUCTURAL COMPONENTS

Nonstructural components are generally categorized into two groups: displacement-sensitive and acceleration-sensitive. The assessment of damage in displacement-sensitive nonstructural components is directly based on the story drift of buildings. Conversely, the damage of acceleration-sensitive nonstructural components is indirectly evaluated, as their potential to overturn or experience excessive displacements is influenced by inertia forces. Therefore, their damage assessment is conducted using a parameter associated with floor accelerations.

Historically, early earthquake design codes used peak ground accelerations (PGAs) as intensity measures (IMs) to measure the impact of ground motions on structures. However, these codes have since transitioned to using spectral accelerations as IMs, recognizing their superior representation of seismic demands. A similar approach has been adopted in designing acceleration-sensitive nonstructural components. Modern codes are founded on an estimate of the spectral acceleration corresponding to the period of these nonstructural components. Nonetheless, most fragility curves used for assessing losses in acceleration-sensitive nonstructural components, including those found in the FEMA P58 library, continue to rely on peak floor accelerations (PFAs) as their basis. Similar to PGAs for buildings, PFA has a limitation in that it ignores the period of nonstructural components when employed as an EDP.

1.3.2 EVALUATION OF DAMAGE CONSEQUENCES FOR DAMAGED COMPONENTS

Consequence models are responsible for quantifying the effects of damage (FEMA P-58-1, 2018) by employing distributions that describe potential consequences, including repair costs and repair times. The typical median consequence function for a particular damage state is represented within the red box in Figure 1-1. To compute the median unit repair cost for each damaged component, the aggregate component damage is used as an input for the consequence functions. The unit repair cost is determined by random sampling from a distribution of potential repair costs, assuming either a normal or lognormal distribution with a predefined variance and using the median unit repair cost derived from the consequence function. Upper and lower bound quantities introduce economies of scale or operational efficiencies in the model to consider the cost savings when similar repairs are performed multiple times, or the same preparations affect multiple repairs in the building. Such economies of scale may involve tasks like content removal or protection in proximity to damaged areas, procurement and delivery of new materials, and cleanup and replacement of contents. When the number of damaged components falls below the lower bound quantity, no economies of scale are considered; conversely, if more components are damaged than the upper bound quantity, all economies of scale and operational efficiencies are taken into account, resulting in the lowest attainable median unit repair cost. Median consequences for quantities falling in between are calculated through linear interpolation. Notably, the FEMA P-58 manual lacks explicit instructions on computing aggregate damage, which leads to varying interpretations and corresponding estimates of repair costs.

1.4 OBJECTIVES AND ORGANIZATION

This thesis follows a sandwich format, wherein the research objectives outlined below are addressed within four journal articles incorporated as chapters of this thesis. The scope of the thesis has been set to achieve the following objectives:

1. Evaluate whether CRBFs can be an alternative to conventional ductile SFRSs, taking into account their potential cost savings from less structural damage and residual drift, but also the possibility of higher construction costs and greater acceleration demands (the blue box in Figure 1-1);

2. Evaluate whether design parameters of CRBFs, particularly the response modification factor and amplification factor used to account for higher-mode forces in the design process, can be used to control total seismic loss, especially losses attributed to nonstructural components (the orange box in Figure 1-1);

3. Evaluate whether PFAs are suitable engineering demand parameters (EDP) for seismic damage fragility curves of acceleration-sensitive nonstructural components and investigate a more suitable EDP than PFAs, considering the component characteristics such as its period and yield strength (the green box in Figure 1-1); and

4. Investigate the impact of different approaches for computing the aggregate damage to use as an input to consequence models on seismic loss estimates, and develop guidelines to identify the components that cause large discrepancies in seismic loss assessment when different approaches are employed (the red box in Figure 1-1).

Chapter 2 of this thesis addresses the first research objective. Three widely employed ductile steel SFRSs for resisting earthquake loads are special moment resisting frames (SMRFs), special concentrically braced frames (SCBFs), and buckling-restrained braced frames (BRBFs). In this chapter, the three mentioned ductile SFRSs, as well as CRBFs, are designed in accordance with the 2016 standards. Subsequently, loss assessments are conducted on all example structures using current damage fragility functions. The considered SFRSs are compared in two stages: first, by considering their expected losses at a given seismic intensity, and second, by examining the expected annual losses. Additionally, the chapter identifies nonstructural components that have a major impact on seismic losses, highlighting areas for future research aimed at minimizing such losses. Finally, the net present value of the total cost over an assumed 50-year building lifespan is calculated to evaluate the cost-effectiveness of investing in seismic performance upgrades, considering a range of return rates and construction costs.

Chapter 3 of this thesis addresses the second research objective. This chapter involves the design and loss assessment of three-story, six-story, and 12-story buildings using CRBFs as the SFRS. Each building height is designed with various options of CRBF, considering different values of R ranging from 5 to 12 and using the amplification factor considered for including higher-mode forces in the design at two seismic intensity levels: the design earthquake and the maximum considered earthquake. To quantify the influence of the design parameters, the study initially explores various options based on expected losses at a given seismic intensity level and subsequently evaluates the expected annual losses. Additionally, the study investigates whether CRBF design parameters can alleviate the contribution of specific types of nonstructural components to total seismic losses.

Chapter 4 of this thesis addresses the third research objective. This chapter assesses fifteen potential EDPs, alongside PFA, to determine which ones are most suitable for developing damage fragility curves for acceleration-sensitive nonstructural components. To accomplish this, nonstructural components are modeled using elastic perfectly plastic single-degree-of-freedom (SDOF) models, each with a variety of fundamental periods and strength levels. These components are subjected to floor motions derived from nonlinear response history analyses of buildings designed in accordance with relevant codes. The analyses are carried out on two different building heights (six- and 12-story buildings) each designed with the four different SFRSs that were introduced in the second chapter. The assessment relies on statistical criteria, particularly efficiency and sufficiency, to identify the most appropriate EDP by comparing pairs of candidate EDPs in terms of correlation with ductility demand. Finally, the chapter evaluates the impact of EDP selection by comparing the expected annual losses from seismic loss assessments performed on SDOF nonstructural components employing different candidate EDPs.

Chapter 5 of this thesis addresses the fourth research objective. This chapter explores the issue of ambiguity within FEMA P-58's consequence modeling, which can have a notable influence on the estimation of repair costs and times, subsequently affecting performance assessments. The primary goal of this chapter is to examine how different methods of calculating aggregate damage affect seismic loss estimation through economies of scale and to underscore scenarios where the results are significantly influenced by the adopted interpretation. The specific focus of this chapter is on the consequence models used in the fourth step of the FEMA P-58 methodology. Four distinct approaches are examined as edge cases to encompass the full spectrum of potential interpretations regarding aggregate damage within FEMA P-58's scope. The study also explores which component types are particularly sensitive to the interpretation of economies of scale and other seismic performance assessment parameters that can substantially affect this aspect of repair cost calculation. These findings are demonstrated through a comprehensive seismic loss assessment of a nine-story building equipped with various nonstructural and structural components.

Chapter 6 serves as the conclusion of the thesis, providing a summary of the research findings and synthesizing the results while also outlining recommendations and potential avenues for future research.

1.5 REFERENCES

ACI 318-19, 2019. *Building code requirements for structural concrete*. Farmington Hills, MI, United States: American Concrete Institute.

ANSI/AISC 341-16, 2016. *Seismic provisions for structural steel buildings*. Chicago, IL, United States: American Institute of Steel Construction.

ASCE/SEI 41-17, 2017. *Seismic evaluation and retrofit of existing buildings*. Reston, VA, United States: American Society of Civil Engineers.

ASCE/SEI 7-16, 2016. *Minimum design loads and associated criteria for buildings and other structures*. Reston, VA, United States: American Society of Civil Engineers.

ATC 138-3, 2021. Seismic performance assessment of buildings volume 8 – methodology for assessment of functional recovery time – preliminary report. *Applied Technology Council*. Redwood City, CA, United States.

Attary, N., Unnikrishnan, V. U., van de Lindt, J. W., Cox, D. T., and Barbosa, A. R., 2017. Performance-based tsunami engineering methodology for risk assessment of structures. *Engineering Structures*, **141**, 676–686. Elsevier Ltd. DOI: https://doi.org/10.1016/j.engstruct.2017.03.071

Barbato, M., Petrini, F., Unnikrishnan, V. U., and Ciampoli, M., 2013. Performance-based hurricane engineering (PBHE) framework. *Structural Safety*, **45**, 24–35. DOI: https://doi.org/10.1016/j.strusafe.2013.07.002

Buccella, N., 2019. Nonstructural component demands in buildings with controlled rocking steel braced frames. M.A.Sc. Thesis, McMaster University, Hamilton, Ontario, Canada

Buccella, N., Wiebe, L., Konstantinidis, D., and Steele, T., 2021. Demands on nonstructural components in buildings with controlled rocking braced frames. *Earthquake Engineering and Structural Dynamics*, **50**(4), 1063–1082. John Wiley and Sons Ltd. DOI: https://doi.org/10.1002/eqe.3385

Ciampoli, M., Petrini, F., and Augusti, G., 2011. Performance-based wind engineering: towards a general procedure. *Structural Safety*, **33**(6), 367–378. DOI: https://doi.org/10.1016/j.strusafe.2011.07.001

Cornell, C. A., and Krawinkler, H., 2000. Progress and challenges in seismic performance assessment. *PEER Center News*, **3**(2), 1–3.

Deierlein, G. G., McKenna, F., Zsarnóczay, A., Kijewski-Correa, T., Kareem, A., Elhaddad, W., Lowes, L., et al., 2020. A cloud-enabled application framework for simulating regional-scale impacts of natural hazards on the built environment. *Frontiers in Built Environment*, **6**, 558706. DOI: http://doi.org/10.3389/fbuil.2020.558706

Dyanati, M., Huang, Q., and Roke, D., 2017. Cost-benefit evaluation of self-centring concentrically braced frames considering uncertainties. *Structure and Infrastructure Engineering*, **13**(5), 537–553. DOI: https://doi.org/10.1080/15732479.2016.1173070

Eatherton, M. R., Ma, X., Krawinkler, H., Mar, D., Billington, S., Hajjar, J. F., and Deierlein, G.

G., 2014. Design concepts for controlled rocking of self-centering steel-braced frames. Journal of Structural Engineering, 140(11), 04014082. American Society of Civil Engineers. DOI: https://doi.org/10.1061/(ASCE)ST.1943-541X.0001047

EERI, 2019. Functional Recovery: A Conceptual Framework with Policy Options. *Earthquake Engineering Research Institute*. Oakland, CA,United States.

EN 1998-1:2008, 2008. *Eurocode 8: Design of structures for earthquake resistance – Part 1: Genreal rules, seismic actions and rules for buildings*. European Committee for Standardization (CEN).

FEMA P-2090 / NIST SP-1254, 2021. Recommended options for improving the built environment for post-earthquake reoccupancy and functional recovery time. *Federal Emergency Management Agency and National Institute of Standards and Technology*. DOI: https://doi.org/10.6028/NIST.SP.1254

FEMA P-58-1, 2018. *Seismic performance assessment of buildings volume 1-methodology*. Washington, DC, United States: prepared by the Applied Technology Council for the Federal Emergency Management Agency.

FEMA P-58-2, 2018. *Seismic Performance Assessment of Buildings Volume 2 – Implementation Guide* (2nd Edit.). Washington, D.C.: prepared by the Applied Technology Council for the Federal Emergency Management Agency.

FEMA P-58-3, 2018. *Seismic Performance Assessment of Buildings, Volume 3–Supporting Electronic Materials and Background Documentation: 3.1 Performance Assessment Calculation Tool (PACT)*. Version 3.1.2. Washington, DC, United States: prepared by the Applied Technology Council for the Federal Emergency Management Agency.

FEMA P695, 2009. *Quantification of Building Seismic Performance Factors*. Washington, DC, United States: prepared by the Applied Technology Council for the Federal Emergency Management Agency.

Filiatrault, A., and Sullivan, T., 2014. Performance-based seismic design of nonstructural building components: The next frontier of earthquake engineering. *Earthquake Engineering and Engineering Vibration*, **13**(1), 17–46. DOI: 10.1007/s11803-014-0238-9

Haselton Baker Risk Group, 2020. Seismic Performance Prediction Program (SP3). *Retrieved from www.hbrisk.com*.

Huang, Q., Dyanati, M., Roke, D. A., Chandra, A., and Sett, K., 2018. Economic feasibility study of self-centering concentrically braced frame systems. *Journal of Structural Engineering*, **144**(8), 04018101. DOI: https://doi.org/10.1061/(ASCE)ST.1943-541X.0002093

Martin, A., Deierlein, G. G., and Ma, X., 2019. Capacity design procedure for rocking braced frames using modified modal superposition method. *Journal of Structural Engineering*, **145**(6), 04019041. DOI: https://doi.org/10.1061/(ASCE)ST.1943-541X.0002329

McKevitt, W. E., Timler, P. A. M., and Lo, K. K., 1995. Nonstructural damage from the Northridge earthquake. *Canadian Journal of Civil Engineering*, **22**(2), 428–437. DOI: https://doi.org/10.1139/l95-051

Miranda, E., and Aslani, H., 2003. *Probabilistic response assessment for building-specific loss estimation*. Pacific Earthquake Engineering Research Center.

Miranda, E., Mosqueda, G., Retamales, R., and Pekcan, G., 2012. Performance of nonstructural components during the 27 February 2010 Chile earthquake. *Earthquake Spectra*, **28**(S1), S453–S471. DOI: https://doi.org/10.1193/1.4000032

Miranda, E., and Taghavi., S., 2003. Estimation of seismic demands on acceleration-sensitive nonstructural components in critical facilities. *Proceedings of the Seminar on Seismic Design, Performance, and Retrofit of Nonstructural Components in Critical Facilities.*, 29–2.

Moehle, J., and Deierlein, G. G., 2004. A framework methodology for performance-based earthquake engineering. *13th world conference on earthquake engineering*, (679).

Molina Hutt, C., Vahanvaty, T., and Kourehpaz, P., 2022. An analytical framework to assess earthquake-induced downtime and model recovery of buildings. *Earthquake Spectra*, **38**(2), 1283–1320. DOI: https://doi.org/10.1177/87552930211060856

Rahgozar, N., Moghadam, A. S., and Aziminejad, A., 2016. Quantification of seismic performance factors for self-centering controlled rocking special concentrically braced frame. *The Structural Design of Tall and Special Buildings*, **25**(14), 700–723. DOI: https://doi.org/10.1002/tal.1279

Reitherman, B., Sabol, T., Bachman, R., Bellet, D., Bogen, R., Cheu, D., Coleman, P., et al., 1995. Nonstructural damage. *Earthquake Spectra*, **11**(2), 453–514.

Roke, D., Sause, R., Ricles, J. M., and Chancellor, N. B., 2010. Damage-free seismic-resistant self-centering concentrically-braced frames. Report 10-09. Bethlehem,PA, United States: Advanced Technology for Large Structural Systems Engineering Research Center.

RSMeans, 2020. *Building construction cost data*. RSMeans Construction Publishers and Consultants.

Shrestha, S. R., Orchiston, C. H. R., Elwood, K. J., Johnston, D. M., and Becker, J. S., 2021. To cordon or not to cordon: The inherent complexities of post-earthquake cordoning learned from Christchurch and Wellington experiences. *Bulletin of the New Zealand Society for Earthquake Engineering*, **54**(1), 40–48. DOI: https://doi.org/10.5459/bnzsee.54.1.40-48

Steel Construction New Zealand, 2015. Design guide for controlled rocking steel braced frames. *Report No. SCNZ - 110:2015*, Christchur.

Steele, T. C., and Wiebe, L. D. A., 2020. Large-scale experimental testing and numerical modeling of floor-to-frame connections for controlled rocking steel braced frames. Journal of Structural Engineering, 146(8). American Society of Civil Engineers (ASCE). DOI: https://doi.org/10.1061/(asce)st.1943-541x.0002722

Steele, T., and Wiebe, L., 2016. Dynamic and equivalent static procedures for capacity design of controlled rocking steel braced frames. *Earthquake Engineering and Structural Dynamics*, **45**(14), 2349–2369. DOI: https://doi.org/10.1002/eqe.2765

Steele, T., and Wiebe, L., 2017. Collapse risk of controlled rocking steel braced frames with different post-tensioning and energy dissipation designs. *Earthquake Engineering and Structural Dynamics*, **46**(13), 2063–2082. John Wiley and Sons Ltd. DOI: c10.1002/eqe.2892

Steele, T., and Wiebe, L., 2021. Collapse risk of controlled rocking steel braced frames considering buckling and yielding of capacity-protected frame members. *Engineering Structures*, **237**, 111999. Elsevier BV. DOI: https://doi.org/10.1016/j.engstruct.2021.111999

Stevenson, J. R., Kachali, H., Whitman, Z., Seville, E., Vargo, J., and Wilson, T., 2011. Preliminary observations of the impacts the 22 February Christchurch earthquake had on organisations and the economy: A report from the field (22 February - 22 March 2011). *Bulletin of the New Zealand Society for Earthquake Engineering*, **44**(2), 65–76. DOI: http://doi.org/10.5459/bnzsee.44.2.65-76

TBI, 2017. *Guidelines for Performance-Based Seismic Design of Tall Buildings*. *Tall Buildings Initiative*. PEER Report 2017/06.

Terzic, V., Villanueva, P. K., Saldana, D., and Yoo., D. Y., 2021. F-Rec Framework: Novel framework for probabilistic evaluation of functional recovery of building systems. *Pacific Earthquake Engineering Research Center*, PEER Report 2021/06. Berkeley, CA, United States.

Tremblay, R., Fliatrault, A., Bruneau, M., Nakashima, M., Prion, H. G., and DeVall, R., 1996. Seismic design of steel buildings: lessons from the 1995 Hyogo-ken Nanbu earthquake. *Canadian Journal of Civil Engineering*, **23**(3), 727–756. NRC Research Press Ottawa, Canada. DOI: https://doi.org/10.1139/l96-885

Trifunac, M., and Novikova, E., 1994. *State of the art review on strong motion duration*. Vienna, Austria: Proceedings of the Tenth European conference on earthquake engineering.

Vecchio, C. Del, Ludovico, D. M., and Prota, A., 2020. Repair costs of reinforced concrete building components: From actual data analysis to calibrated consequence functions. *Earthquake Spectra*, **36**(1), 353–377. SAGE Publications Inc. DOI: http://doi.org/10.1177/8755293019878194

Wiebe, L., and Christopoulos, C., 2015. Performance-based seismic design of controlled rocking steel braced frames. I: methodological framework and design of base rocking joint. *Journal of Structural Engineering*, **141**(9), 04014226. DOI: https://doi.org/10.1061/(ASCE)ST.1943-541X.0001202

Zsarnóczay, A., and Deierlein, G. G., 2020. PELICUN - A Computational Framework for Estimating Damage , Loss and Community Resilience. *17th World Conference on Earthquake Engineering*. Japan.

Zsarnóczay, A., and Kourehpaz, P., 2021. NHERI-SimCenter/pelicun: v2.6, Zenodo. DOI: http://doi.org/10.5281/zenodo.5167371

Chapter 2

2. Seismic loss comparison for buildings designed with ductile steel seismic force-resisting systems and with controlled rocking braced frames

2.1 Abstract

Observations from past earthquakes have highlighted the structural damage and significant residual deformations experienced by ductile steel seismic force-resisting systems (SFRSs), such as special moment resisting frames (SMRFs), special concentrically braced frames (SCBFs), and buckling-restrained braced frames (BRBFs). To mitigate these challenges, controlled rocking braced frames (CRBFs) have emerged as a promising low-damage alternative SFRS. However, concerns have been raised about whether the reduction in structural damage with CRBFs may come at the cost of increased acceleration demands and associated nonstructural damage. This study offers a comprehensive investigation of such trade-offs by analyzing three buildings of different heights, each designed with the three ductile SFRSs identified above and with CRBFs. After examining the structural response at different earthquake intensities, the focus of the chapter is on earthquake-induced economic losses. Among the considered SFRSs, greater total expected annual losses (EAL) are observed in the SMRF and SCBF buildings, primarily due to demolition losses and repairable losses, including repairs of structural and nonstructural components. The total EAL is lower for the BRBFs and lowest for the CRBFs, with the losses in the BRBF buildings primarily attributed to demolition loss, considered as irreparable loss, while the losses in the CRBF buildings are mainly due to acceleration-sensitive nonstructural components, considered as reparable loss. To provide a more detailed comparison, cost-effectiveness analyses are also performed, indicating that a modest cost premium for CRBFs is justified to reduce earthquake economic costs over the building lifetime.

KEYWORDS: seismic loss assessment; special moment resisting frames; special concentrically braced frames; buckling-restrained braced frames; controlled rocking braced frames; nonstructural components

2.2 INTRODUCTION

Although significant progress has been made in seismic design provisions for building safety, as evidenced by the reduced number of new and retrofitted building collapses after extreme earthquakes (Okazaki et al., 2013; Westenenk et al., 2012), the socioeconomic impact of earthquakes is still a major concern. Observations of the aftermath of past earthquakes have revealed that excessive residual drifts (Rosenblueth and Meli, 1986) and damage to structural and non-structural components (Dhakal, 2010; Miranda et al., 2012; Perrone et al., 2019) can lead to buildings being demolished or requiring extensive repairs, both of which are expensive and cause downtime and business interruptions that compound the direct economic losses (Hwang and Lignos, 2017a) and impede the ability of cities to recover from a disaster. Therefore, a performance-based earthquake engineering framework has been developed to evaluate earthquake-induced losses (Cornell and Krawinkler, 2000; FEMA P-58-1, 2018), allowing engineers and other stakeholders to assess potential consequences and therefore make more efficient design and retrofit decisions.

Three common ductile steel seismic force-resisting systems (SFRSs) used worldwide to resist earthquake loads are special moment resisting frames (SMRFs), special concentrically braced frames (SCBFs) and buckling-restrained braced frames (BRBFs). SMRFs and SCBFs are historically common and thus have been the subjects of numerous research studies focusing on their seismic performance, behavior, and seismic loss assessment. Over the past 20 years, BRBFs have gained popularity due to their ability to provide high energy dissipation by effectively restraining buckling in the braces. Ramirez and Miranda (2012) noted that building demolition may become a controlling seismic loss parameter for buildings with typical SFRSs due to large residual drifts. The residual story drifts in SMRFs can be attributed to the plastic hinging in SMRFs resulting in irrecoverable inelastic deformations in the beams (Erochko et al., 2011), particularly for mid- to high-rise SMRFs that are susceptible to P-Delta effects (Elkady and Lignos, 2014; Hwang and Lignos, 2017a). SCBFs can experience concentrated plastic deformations due to the asymmetric hysteretic behavior of their braces that may lead to the development of local story collapse mechanisms (Hwang and Lignos, 2017b), resulting in significant residual story deformations or even structural collapse (Tremblay et al., 1995, 1996). BRBFs can experience an average peak residual drift ratio ranging from 0.8% to 2.0% following a design earthquake (DE) (Erochko et al., 2011) due to their full hysteresis (Asgarkhani et al., 2020). In addition, it was found that for this system, while the maximum drift demands were almost unaffected by the strain hardening ratio, even a slight variation in this ratio could greatly increase the residual drift of BRBFs (Mahdavipour and Deylami, 2014).

Controlled rocking braced frames (CRBFs) have been developed as a lateral force-resisting system to mitigate structural damage during earthquakes at and beyond design levels (Eatherton et al., 2014; Roke et al., 2010; Steele and Wiebe, 2021; Wiebe et al., 2013). Unlike more traditional ductile SFRSs, CRBFs benefit from uplift mechanisms, while post-tensioned tendons and the frame weight provide a restoring force that allows the system to self-center after an earthquake. Additionally, energy-dissipating devices are typically employed to reduce displacement demands. Collapse assessment studies conducted on CRBFs demonstrate that these structures have a low probability of collapse and minimal damage to their steel components (Rahgozar et al., 2016; Steele and Wiebe, 2017, 2021). Additionally, Wiebe and Christopoulos (Wiebe and Christopoulos, 2015) indicated that buildings designed with CRBFs exhibit minimal residual drifts, even under the most severe ground motions at the maximum considered earthquake (MCE) level. However, the research conducted by Buccella et al. (2021) revealed that higher mode effects can result in higher acceleration demands in CRBFs compared to BRBFs, particularly in the form of peaks in the floor spectra near the modal periods of the buildings.

Over the past decade, several studies have used seismic loss assessment to evaluate the performance of various ductile SFRSs (Ghasemof et al., 2022; Molina Hutt et al., 2019; Ramirez et al., 2012). Hwang and Lignos investigated the impact of modeling and design assumptions on the earthquake-induced losses of buildings with SMRFs (Hwang and Lignos, 2017a) and SCBFs (Hwang and Lignos, 2017b). They discussed that neglecting the contribution of the composite floor and gravity framing system in the analytical building model may lead to an overestimation of the loss due to demolition and collapse in buildings. Also, although they considered only three acceleration-sensitive nonstructural components (suspended ceiling, elevator, and sprinklers) for seismic loss assessments, they found that the repair costs of these components account for more than half of the total expected annual losses. Others have compared the cost-benefit evaluation of SCBFs and CRBFs (Dyanati et al., 2017; Huang et al., 2018), including potentially higher construction costs for CRBFs. These studies found that for the archetype six- and eight-story buildings that were considered, CRBFs had less total annual loss than SCBFs, whereas the ten-story buildings with SCBFs had less total annual loss than those with CRBFs. Also, damage to acceleration-sensitive nonstructural components was identified as the major source of loss for the considered CRBF buildings. Hu and Zhu (2023) introduced hybrid self-centering braced frames with shape memory alloy-based braces and viscous dampers that not only can achieve better performance in reducing seismic annual loss than BRBFs and SCBFs but also demonstrate comparable performance in controlling peak floor accelerations (PFAs) to that of BRBFs and less than SCBFs.

Although there are studies that assess the structural performance of each of these individual steel systems and a few papers that include seismic loss assessment, there is a lack of research that systematically compares all four steel SFRSs described above. In addition, the emergence of self-centering systems, such as CRBFs, raises questions for building owners and stakeholders about whether such systems will indeed reduce overall seismic costs, particularly in light of potentially higher acceleration-related losses. To address this research gap, the four SFRSs discussed above are designed according to the 2016 standards and codes, and loss assessments are performed on all example structures using current damage fragility functions. The SFRSs are compared, first by considering their expected losses given a seismic intensity, and then by considering the expected annual losses. Moreover, nonstructural components with a major impact on seismic losses are identified to highlight areas for future research in minimizing such losses. Finally, the net present value of the total cost over an assumed 50-year building life span is computed to evaluate the cost-effectiveness of investing in seismic performance upgrades, for a range of return rates and construction costs.

2.3 Design of prototype buildings

Three different heights of steel-framed office buildings were each designed using four different SFRSs, namely SMRFs, SCBFs, BRBFs, and CRBFs. The design site for the buildings was assumed to be site class D (stiff soil) and in a seismically active area with mapped short-period and 1-second spectral accelerations of S_s=1.5 g and S_1=0.5 g, respectively (ASCE/SEI 7-16, 2016). The typical floor plan for the buildings is shown in Figure 2-1. Each story of the buildings is 4.57 m high, with a total seismic weight of 10,200 kN and 6,430 kN for each floor and roof, respectively. Four-bay moment frames were positioned along the exterior of the buildings in a symmetric plan configuration for the SMRF designs (Figure 2-1 (a)), while for the braced frames, two frames were used in each direction for the three-story buildings and four for the six-story and 12-story buildings (Figure 2-1 (b)). None of the frame members in the SFRSs were designed or modelled to carry any tributary gravity loads, and the CRBFs were designed to be 90% of the bay width to fit between two gravity columns. In all cases, members were selected to avoid overdesign by maximizing the utilization ratio.

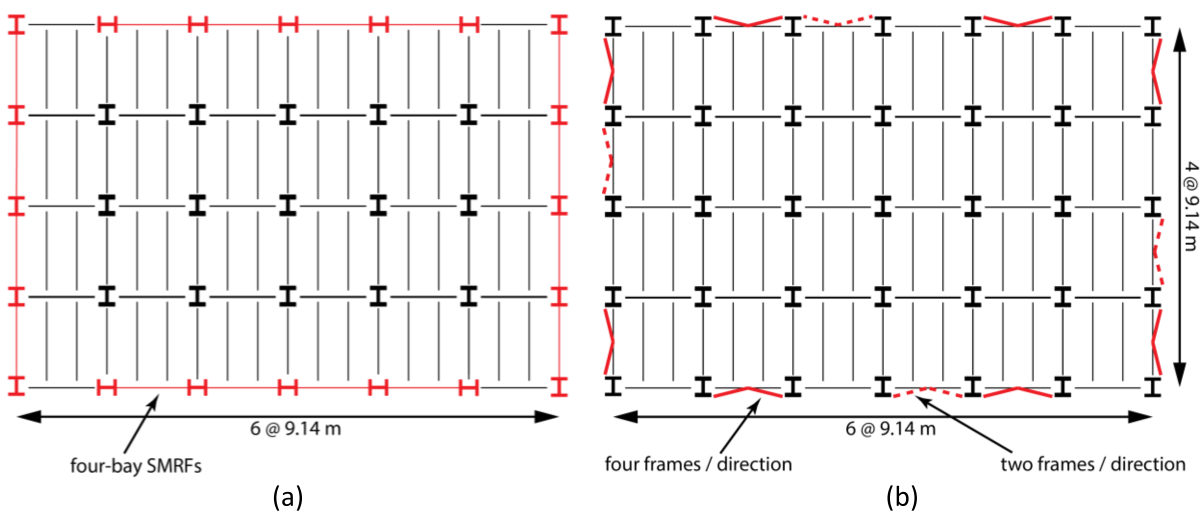

Figure 2-1. Floor plan of the building with location of SFRSs: (a) SMRFs and (b) braced frames.

The SMRFs were designed with reduced beam sections (RBS) per ANSI/AISC 358-16 (2016). The equivalent lateral force method of ASCE/SEI 7-16 (2016) was used with a response modification factor (*R*) of 8 to find the demands on the SMRF members. Also, steel beam and column sections were designed using ANSI/AISC 360-16 (2016) with a yield strength of 345 MPa and were proportioned to satisfy the requirements specified in ANSI/AISC 341-16 (2016). Welded doubler plates were designed using AISC 360-16 to fulfill the panel zone strength criteria. Table 2-1 provides a summary of the fundamental period, T, and all designed members for the SMRFs.

The equivalent lateral force method of ASCE/SEI 7-16 (2016) and the capacity design procedure provided in ANSI/AISC 341-16 (2016) were used to design the steel members of SCBFs and BRBFs, with *R* of 6 and 8, respectively. All members of the SCBFs, and the beams and columns of the BRBFs, were designed based on AISC 360-16 with a yield strength of 345 MPa, while a yield strength of 290 MPa was assumed for the core area of buckling-restrained braces (BRBs). For the SCBFs and BRBFs, braces were assumed to be pinned to the beam-column connections, and the effective length of the braces was assumed to be 70% of the work-point-to-work-point length of braces. The regression equations suggested by Saxey and Daniels (2014) were used to estimate the strain hardening and compressive strength adjustment factors for the BRBs, assuming that braces reached their probable tensile or compressive force at a strain experienced by the brace cores at the target design drift of 1.5%. All designed members for the SCBFs and BRBFs and their initial periods are summarized in Table 2-1.

The design of CRBFs followed a two-step procedure by Wiebe and Christopoulos (2015), which involved designing the base rocking joints with post-tensioning (PT) and energy dissipation (ED) to control over-rotation and limit displacements, and capacity designing all steel members to withstand the forces induced by rocking, including higher-mode forces. To determine the required base overturning moment resistance, the equivalent lateral force approach (ASCE/SEI 7-16, 2016) was used with *R*=8, as suggested by several studies (Eatherton et al., 2014; Ma et al., 2010; Roke et al., 2010). Frictional energy dissipation elements were specified at the base of either side of the CRBFs' columns. To ensure a self-centering behavior, the hysteretic ED ratio (β), which is defined as the ratio of the height of the CRBFs' flag-shaped hysteresis to the linear limit, should be less than one (Steele and Wiebe, 2021), so β of 0.9 was targeted in this study. The PT prestress was selected as 50% of the ultimate stress of PT to ensure the PT would remain elastic up to at least 2.5% base rotation. One set of PT in the center of the frame and two sets of PT aligned with each column were respectively anchored at the roof of the three-story and six-story CRBFs. For the 12-story CRBF, two sets of PT were anchored to the frame's side columns on the sixth floor. The dynamic capacity design procedure developed by Steele and Wiebe (2016) was used to design the steel frame members of the CRBFs. This procedure combines the forces from frame rocking to the ultimate base rotation with higher-mode vibration forces that are computed using modal analysis using a truncated spectrum at the MCE level. A yield strength of 345 MPa was assumed for all steel members of the CRBFs. Additionally, the gusset plates between the braces and the beam-column connections were capacity designed based on the capacity of the braces. The initial period, T, initial post-tensioning force, PT_0, energy dissipation activation force, ED_{act}, and all designed steel members for the CRBFs are summarized in Table 2-1.

Table 2-1. Section sizes and design parameters.

	SMRF			SCBF			BRBF			CRBF		
Story	Exterior Columns	Inner Columns	Beam	Column	Beam	Brace	Column	Beam	Brace	Column	Beam	Brace
3	W21X13	W24X22	W18X10	W14X82	W30X29	HSS7X7X1/4	W12X58	W12X87	3.5	W14X28	W14X15	W14X17
2	W21X13	W24X22	W18X10	W14X82	W30X29	HSS8X8X3/8	W12X58	W12X87	6.5	W14X28	W14X15	W14X12
1	W21X13	W24X22	W18X10	W14X82	W30X29	HSS8X8X1/2	W12X58	W12X87	8	W14X28	W14X15	W14x15
		T_1 (s)			T_1 (s)			T_1 (s)		T_1 (s)	PT_0 (kN)	ED_{act} (kN)
		1.20			0.67			0.87		0.44	2031	914
6	W24X13	W24X22	W21X12	W14X61	W30X23	HSS5X5X1/4	W12X87	W12X87	2 (in^2)	W14X14	W12X72	W10X77
5	W24X13	W24X22	W21X12	W14X61	W30X23	HSS6X6X5/1	W12X87	W12X87	3	W14X14	W12X72	W12X72
4	W24X13	W24X22	W21X12	W14X61	W30X23	HSS6X6X1/2	W12X87	W12X87	4	W14X14	W12X72	W12X72
3	W24X13	W24X22	W21X18	W14X12	W30X21	HSS7X7X3/8	W12X10	W12X10	4.5	W14X28	W12X10	W12X79
2	W24X13	W24X22	W21X18	W14X12	W30X21	HSS8X8X5/1	W12X10	W12X10	5	W14X28	W12X10	W12X96
1	W24X13	W24X22	W21X18	W14X12	W30X21	HSS8X8X5/1	W12X10	W12X10	5.5	W14X28	W12X10	W14X90
		T_1			T_1			T_1		T_1	PT_0	ED_{act}
		2.12			1.17			1.5		0.97	1282	1153
12	W30X10	W30X19	W21X13	W12X72	W27X25	HSS8X8X3/1	W12X96	W12X10	3 (in^2)	W14X10	W21X12	W12X58
11	W30X10	W30X19	W21X13	W12X72	W27X25	HSS8X8X1/4	W12X96	W12X10	3	W14X10	W21X12	W12X87
10	W30X10	W30X19	W21X13	W12X72	W27X25	HSS8X8X3/8	W12X96	W12X10	5	W14X10	W21X12	W12X12
9	W30X19	W33X24	W27X19	W14X25	W27X30	HSS8X8X3/8	W14X14	W14X10	6.5	W14X34	W21X13	W12X12
8	W30X19	W33X24	W27X19	W14X25	W27X30	HSS8X8X3/8	W14X14	W14X10	6.5	W14X34	W21X13	W14X10
7	W30X19	W33X24	W27X19	W14X25	W27X30	HSS8X8X3/8	W14X14	W14X10	7	W14X34	W21X13	W12X12
6	W30X21	W33X26	W30X21	W14X25	W30X32	HSS8X8X3/8	W14X23	W14X10	7	W14X45	W21X13	W12X96
5	W30X21	W33X26	W30X21	W14X25	W30X32	HSS8X8X3/8	W14X23	W14X10	7	W14X45	W21X13	W12X10
4	W30X21	W33X26	W30X21	W14X25	W30X32	HSS8X8X1/2	W14X23	W14X10	7	W14X45	W21X13	W14X10
3	W30X21	W33X26	W30X23	W14X37	W30X32	HSS8X8X1/2	W14X34	W14X10	7	W14X50	W21X18	W14X13
2	W30X21	W33X26	W30X23	W14X37	W30X32	HSS8X8X1/2	W14X34	W14X10	7	W14X50	W21X18	W14X14
1	W30X21	W33X26	W30X23	W14X37	W30X32	HSS8X8X1/2	W14X34	W14X10	7	W14X50	W21X18	W14X14
		T_1			T_1			T_1		T_1	PT_0	ED_{act}
		3.16			2.32			2.80		1.94	2832	2549

2.4 SEISMIC HAZARD AND GROUND MOTION SELECTION

The Los Angeles Bulk Mail Center (33.996°N, 118.162°W) was selected as representative of the site conditions used to design the SFRSs. The seismic hazard curves for the chosen site were retrieved from the USGS website (https://earthquake.usgs.gov/hazards/interactive/, last accessed 17 October 2022). The suite of far-field ground motion records suggested by FEMA P695 (2009) was employed for the time-history analyses. The selected ground motions were scaled to minimize the geometric mean differences between the MCE spectrum and the median acceleration spectrum of the records over a range based on the periods of the buildings. This range extended from 0.2 times the first fundamental period of the fixed-base CRBF building to 2.0 times the first fundamental period of the BRBF building for each set of buildings of the same height designed with different SFRSs. This was implemented so that the four separate SFRSs for each height would all use a consistent scaled ground motion suite. The upper limit of the scaling range was set using the period of the BRBFs instead of the SMRFs to minimize any unnecessary overshooting over the low period range, considering the large range in periods for the different SFRSs. Figure 2-2 shows the scaled records for the set of three-story buildings along with the median of the suite and the MCE spectrum. The performance of each building was evaluated by multiple-stripe analyses (MSA) (Baker, 2015) with six different intensity stripes: $^{1}/_{4}$, $^{1}/_{2}$, and 1 times the DE, and 1, 1.5, and 2 times the MCE.

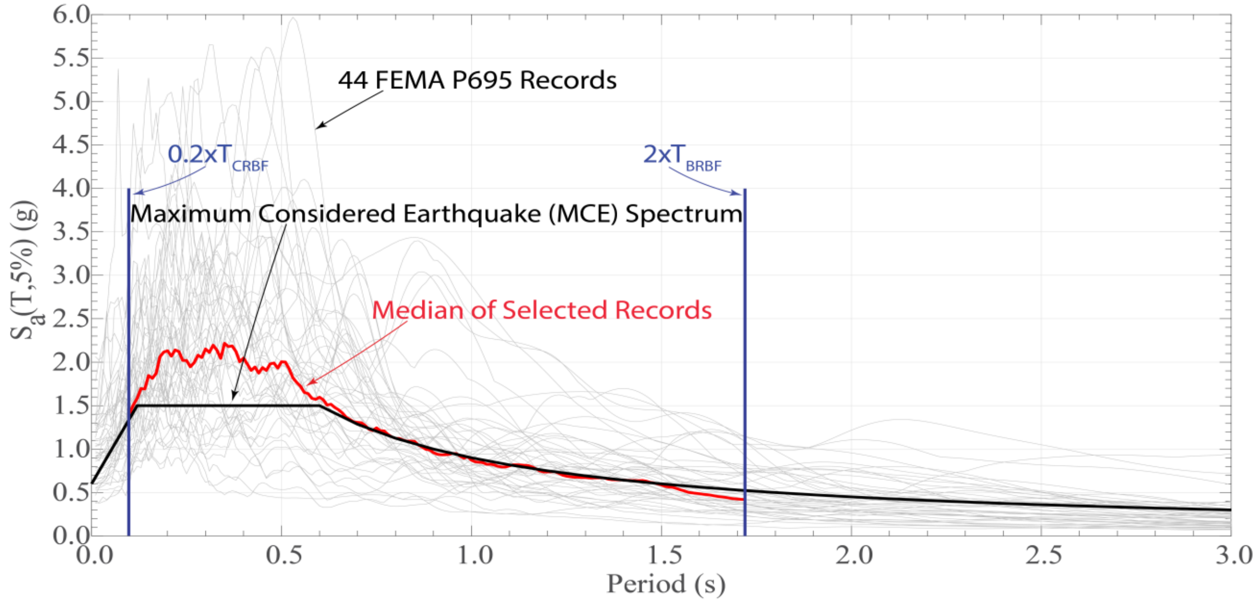

Figure 2-2. Scaling of the selected suite of ground motions for the three-story buildings.

2.5 MODELLING OF THE EXAMPLE STRUCTURES

OpenSees (Pacific Earthquake Engineering Research Centre (PEER), 2021) was used to perform the MSA on the designed buildings. Figure 2-3 depicts schematics of the numerical models developed for the three-story SFRSs; similar models were developed for the six- and twelve-story designs. The SMRFs, SCBFs, and BRBFs were simulated in a 2D plane, whereas the CRBFs were simulated in 3D to capture buckling out-of-plane about the braces' weak axes.

The SMRF (Figure 2-3(a)) members were idealized using elastic beam-column elements with stiffness modifiers (ModElasticBeam2d), which were developed to prevent unrealistic damping forces caused by stiffness-proportional damping (Zareian and Medina, 2010), and concentrated plasticity flexural hinges at their ends. The modified Ibarra-Medina-Krawinkler deterioration model (Ibarra et al., 2005) was adopted to model cyclic deterioration in flexural strength and stiffness of the beams and columns. In addition, the beam hinges were modeled following Lignos and Krawinkler (2011) and column hinges were modeled following Lignos et al. (2019). The panel zones were modeled as recommended elsewhere (Skiadopoulos et al., 2021).

For the SCBFs (Figure 2-3(b)), nonlinear fiber beam-column elements with ten integration points were employed to capture the distributed inelastic plasticity behavior along the beams and columns. The buckling response of braces was modeled using six fiber nonlinear beam-column elements, following Uriz and Mahin (2008), with initial geometric imperfection equal to 0.001 of effective length (L/1000). In addition, each fiber was assigned a uniaxial Giuffre-Menegotto-Pinto steel material (Steel02) with brace yield strength and kinematic and isotropic strain hardening properties. Fracture due to low cycle fatigue was modelled for all members using the recommendations of Uriz and Mahin (2004, 2008). Also, the model considered the effect of rigid offsets on frame stiffness and assumed pin-ended connections for the brace members.

The braces of the BRBFs were modeled using nonlinear truss elements with a Steel4 uniaxial material developed by Zsarnóczay (2013). Using this material also allowed this study to leverage recommended parameters based on large-scale experimental data calibrated for the behavior of BRBs (Zsarnóczay, 2013). All other aspects of the BRBF models (Figure 2-3(c)) were modeled as explained for the SCBFs.

The CRBFs (Figure 2-3(d)) were modeled as recommended by Steele and Wiebe (2017). Gap elements in the vertical direction were considered to allow CRBFs to uplift due to rocking, and gap elements in the horizontal direction transferred the base shear to the rigid foundation. These gap elements were modeled using a much larger stiffness than the first-story column axial stiffness and in parallel with an elastic spring of negligible stiffness, which improves the models' numerical stability. All frame members were modeled with six fiber nonlinear beam-column sub-elements using ten integration points each and initial geometric imperfection of L/1000 considering the Steel02 material and a low cycle fatigue model (Uriz and Mahin, 2004, 2008) for each fiber. Additionally, the effect of gusset plates at the ends of the braces was modeled using fiber nonlinear beam-column elements, as described by Uriz and Mahin (2008). The frictional energy dissipation elements were modeled using truss elements with an elastic-perfectly plastic material model whose yield force equals the specified ED_{act}. The PT was included as co-rotational truss elements using a multi-linear material model, with properties recommended by Ma et al. (2010), prestressed using an initial stress material with a force equal to the defined PT_0. Also, hook elements were added in series with the PT elements to prevent compression from developing in the PT.

All four types of SFRSs incorporated a leaning column in their models to account for P-Delta effects from the building's gravity frames. The tributary seismic mass of each floor was concentrated at the nodes of the leaning columns, which were laterally constrained to the frames' first joints on each floor. The inherent damping of all SFRSs was modeled using 5% Rayleigh damping based on the first and third fixed-base periods. For the braced frames, to avoid artificial damping when the structure yields, the stiffness proportional damping was considered with 20% of the initial-stiffness matrix and 80% of the committed tangent-stiffness matrix (Charney, 2008; Steele and Wiebe, 2017), while constant stiffness proportional damping was based on the initial-stiffness matrix for the SMRFs.

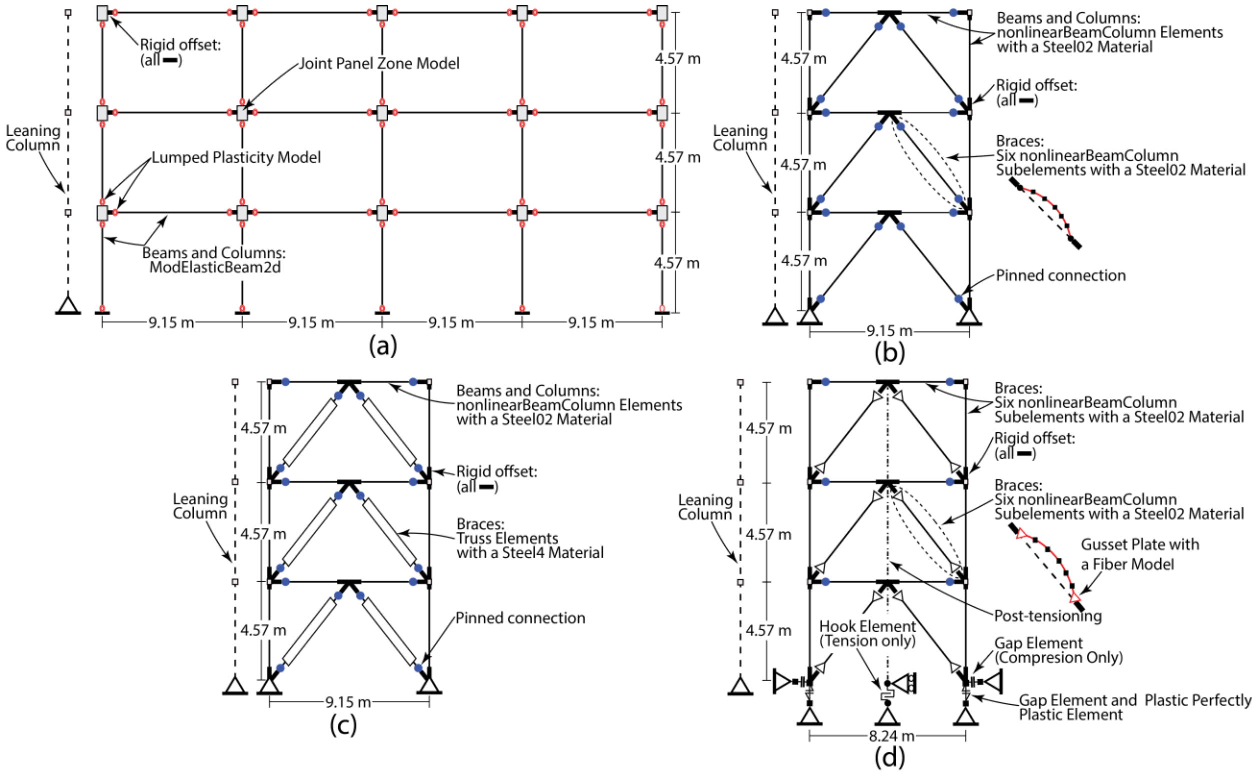

Figure 2-3. Schematics of the numerical models for the SFRSs: (a) SMRF, (b) SCBF, (c) BRBF, and (d) CRBF.

2.6 Construction cost and loss assessment

The construction cost and replacement cost of buildings with SMRFs and SCBFs were assumed to be \$2691 per m^2 (\$250 per ft^2) (Hwang and Lignos, 2017a) and \$1884 per m^2 (\$175 per ft^2) (Hwang and Lignos, 2017b) based on 2013 U.S. dollars, respectively. The replacement cost of BRBF buildings was estimated to be the same as for the SCBF buildings. The CRBF buildings' replacement cost was assumed to be 2% more than SCBF buildings (i.e., \$1922 per m^2), justified by the post-construction cost evaluation of past real-world projects such as the Casa Adelante nine-story housing project, which had only a 0.25% additional construction cost compared to conventionally designed buildings (Aher et al., 2020).These replacement costs were taken as the loss associated with both building collapse and the demolition of irreparable buildings. Building demolition loss was assessed conditioned on the maximum residual story drift ratio from all of the stories using a lognormal distribution, defined by a median of 0.015 radians and a logarithmic standard deviation of 0.3 as used by Ramirez and Miranda (Ramirez and Miranda, 2012).

To calculate the earthquake-induced losses for the buildings in line with the FEMA P58-1 probabilistic loss estimating methodology (FEMA P-58-1, 2018), damage fragility functions and repair cost consequence functions for both structural and nonstructural components are required. For the seismic losses associated with structural components, the FEMA P58-3 (2018) library was the main reference for damage fragility functions and repair cost consequence functions. There are two categories of structural component costing: per connection and per bay basis. For three-story buildings with various SFRSs, Table 2-2 shows an example of the considered structural components and their quantities; the appended letter or number at the end of the mentioned group components' IDs denotes the specific component in each group depending on the size of the structural elements. The repair cost on a per connection basis includes the steel column base plates and welded column splices, for which group components with IDs of B1031.011 and B1031.021 were used, respectively. The components with repair cost on a per bay basis were selected as follows: (i) SMRFs: Post-Northridge RBS connection with beam one side (B1035.00) and both sides (B1035.01) of column; (ii) SCBFs: Special chevron braced frame with hollow structural section (HSS) braces designed with the American Institute of Steel Construction (AISC) minimum standard (B1033.021); (iii) BRBFs: Chevron steel buckling restrained brace (B1033.101); (iv) CRBFs: Special chevron braced frame with wide flange braces designed with balanced design criteria (B1033.001). B1033.001 was used because it is a component group with higher repair costs at lower story drift ratios relative to other special chevron braced frames with wide flange bracing components. Story drift for the CRBFs involves both a rigid body deformation brought on by the rocking behavior of the body and an additional deformation of the frame itself. Accordingly, to assess the damage to bracing in the CRBF, the maximum compression deformation of the braces was employed instead of story drift as the engineering demand parameter (EDP) in the damage fragility functions of the B1033.001 component group (Banihashemi and Wiebe, 2022). If the PT strain was greater than the yield strain of 0.83% (Ma et al., 2010), it was assumed that replacement of the PT strands and the accompanying connected equipment in the CRBFs would be required. The cost of such a replacement was estimated to be $8 per kilogram (kg) of steel strands according to DYWIDAG Systems International (2020) in 2020 U.S. dollars. The frictional energy dissipation elements in the CRBFs were assumed to be designed with large displacement capacity that would not fail before buildings' collapse.

Table 2-2. Summary of considered structural components and their quantities for the 3-story building.

SFRSs	Component description	Component ID[a]	Quantity[b]	Location
SMRF	Column base plates (column weight < 223 kg/m)	B1031.011a	4	Base Floor
	Column base plates (223 < column weight < 446 kg/m)	B1031.011b	6	Base Floor
	RBS connections (one-side, < W27)	B1035.001	4	Story 1-3
	RBS connections (two-side, < W27)	B1035.011	6	Story 1-3
SCBF	Column base plates (column weight < 223 kg/m)	B1031.011a	4	Base Floor
	HSS brace (61 < brace weight < 147 kg/m)	B1033.021b	2	Story 1
	HSS brace (brace weight < 60 kg/m)	B1033.021a	2	Story 2-3
BRBF	Column base plates (column weight < 223 kg/m)	B1031.011a	4	Base Floor
	BRB (brace weight < 60 kg/m)	B1033.101a	2	Story 1-3
CRBF	Column base plates (223 < column weight < 446 kg/m)	B1031.011b	4	Base Floor
	Wide flange brace (brace weight > 148 kg/m)	B1033.001c	2	Story 1-3
	Post-tensioning strands	-	479 (kg)	-

[a] In accordance with FEMA P58-3 library.
b Unless the unit stated, all quantities are expressed as "each."

Table 2-3 lists the 21 nonstructural components, including acceleration-sensitive and drift-sensitive components, that were included in the seismic loss assessment, along with their quantities assigned to each floor of the three-story building. Nonstructural component quantities were allocated to each floor using the FEMA P-58 normative quantity estimation tool (FEMA P-

58-3, 2018), and estimated quantities were rounded up to the next whole number. The same nonstructural components and quantities were also considered for the six- and 12-story buildings, but the quantities of the components denoted by an asterisk vary depending on the number of floors. The damage fragility functions were primarily adopted from FEMA P58-3 (2018) and other identified nonstructural research findings, as indicated in Table 2-3. Also, repair cost consequence functions provided by FEMA P58-3 were employed to evaluate loss due to nonstructural components. All anchorages and bracing for types of equipment that require them were assumed to be designed such that they would not be damaged before the equipment failure; thus, they were not considered for the loss assessment.

Since 2011 serves as the reference year for costs in the FEMA P58-3 consequence functions, all anticipated costs that were not in 2011 were scaled to a 2011-equivalent value using data from the RSMeans historical cost index (RSMeans, 2020). The Pelicun software (Zsarnóczay, 2019), which was developed based on the FEMA P58 methodology by the Computational Modelling and Simulation Center (SimCenter), was used to conduct the seismic loss analyses.

Table 2-3. Summary of considered nonstructural components and their quantities for the 3-story building.

Component description	Component iD[a]	EDP	Source of damage fragility function	Quantity	Unit	Location
Curtain wall	B2022.002	SDR	Behr (2001)	217	3 m^2	Each story
Wall partition (Gypsum with metal studs)	C1011.001c	SDR	Retamales et al. (2013)	22	30 m	Each story
Wall partition (Gypsum + wallpaper)	C3011.001c	SDR	FEMA P58-3 (2018)	2	30 m	Each story
Stair	C2011.021a	SDR	Bull (2011)	3	EA	Each story
Raised access floor	C3027.002	PFA	FEMA P58-3	163	9 m^2	Each floor
Suspended ceiling	C3032.004b	PFA	FEMA P58-3	33	56 m^2	Each floor
Pendant lighting	C3034.002	PFA	FEMA P58-3	325	EA	Each floor
Cold or hot potable piping (small diam.)	D2021.014b	PFA	FEMA P58-3	1	305 m	Each floor
Cold or hot potable piping (large diam.)	D2021.024b	PFA	FEMA P58-3	2	305 m	Each floor
Sanitary piping	D2031.023b	PFA	FEMA P58-3	2	305 m	Each floor
Small HVAC duct	D3041.011c	PFA	FEMA P58-3	2	305 m	Each floor
Fire sprinkler water piping	D4011.023a	PFA	Soroushian et al. (2015)	5	305 m	Each floor
Large HVAC duct	D3041.012d	PFA	FEMA P58-3	1	305 m	Each floor
HVAC diffuser	D3041.032d	PFA	FEMA P58-3	20	10 EA	Each floor
Variable air volume box	D3041.041b	PFA	FEMA P58-3	5	10 EA	Each floor
Low voltage switchgear (400 Amp)	D5012.023e	PFA	FEMA P58-3	1	EA	Each floor
Chiller (500 ton)*	D3031.013h	PFA	FEMA P58-3	1	EA	Roof
Cooling tower (500 ton)*	D3031.023h	PFA	FEMA P58-3	1	EA	Roof
Air handling unit (30000 CFM)*	D3052.013k	PFA	FEMA P58-3	2	EA	Roof
Motor control center*	D5012.013c	PFA	FEMA P58-3	3	EA	Roof
Elevator*	D1014.011	PGA	FEMA P58-3	2	EA	Ground

Note: Amp= Ampere; CFM=Cubic feet per minute; EA=Each; HVAC=Heating, ventilation, and air conditioning; PFA = Peak floor acceleration (g); PGA = Peak ground acceleration (g); SDR= Story drift ratio.

[a] In accordance with FEMA P58-3 library.

* The number of floors affects the number of components.

2.7 STRUCTURAL PERFORMANCE

As a representative example, Figure 2-4 depicts the time history of the roof drift and roof acceleration responses for the three-story SFRSs, as well as the column uplift of the CRBF, during the first component of the Northridge (Canyon Country) ground at the DE level. For this scaled ground motion, all SFRSs experience a roof drift larger than 1% between 4 s and 10 s, and yielding or buckling in the braces of the BRBF and SCBF leads to a residual drift larger than 0.6%. In contrast, the SMRF exhibits a smaller residual drift, and the CRBF shows no residual drift. During this period, the roof acceleration response reveals that while the SMRF exhibits slightly higher demand levels compared to SCBF and BRBF, the instants of column impact and uplift in the CRBF result in local peak responses, which is distinct from findings in other studies (Buccella et al., 2021; Wiebe et al., 2013). These peaks also appear to be influenced by higher mode effects, similar to those identified by Buccella et al. (2021).

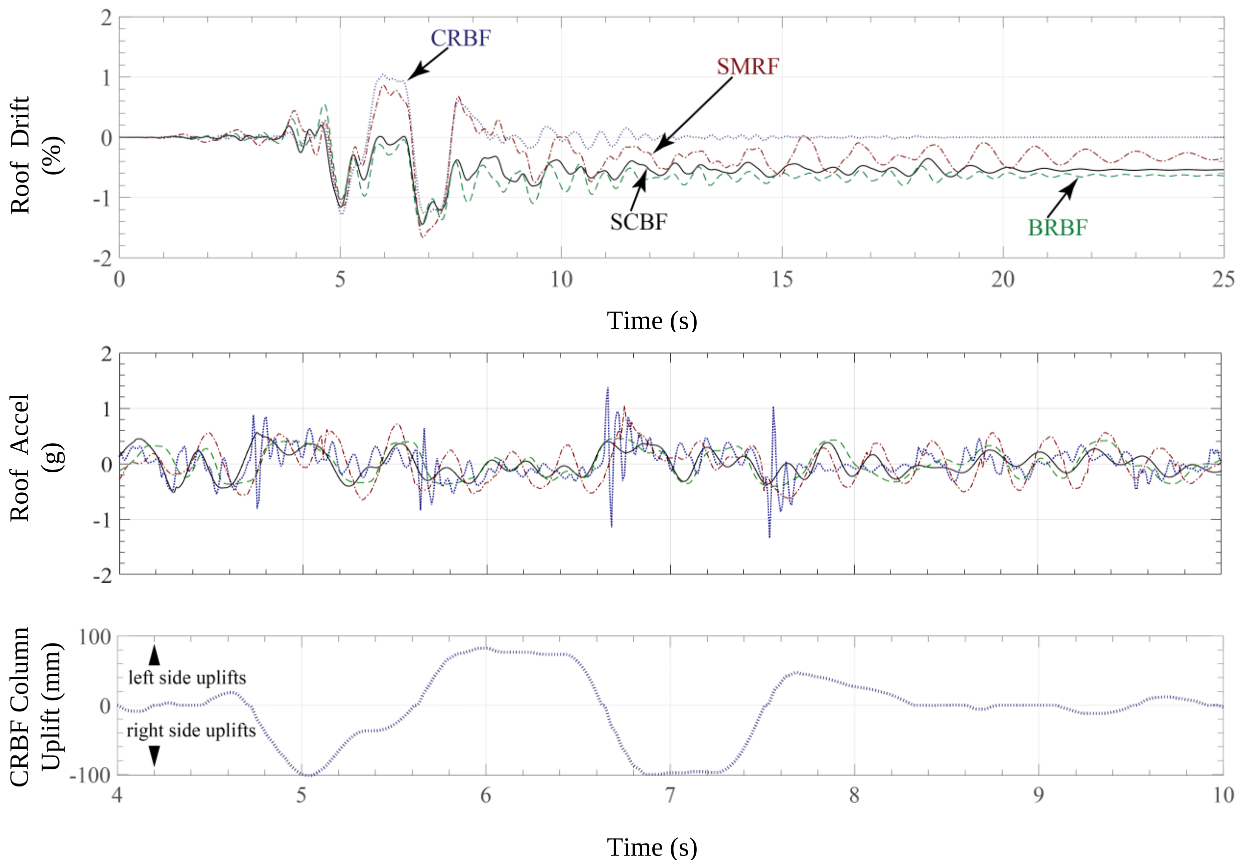

Figure 2-4.Three-story buildings: roof drift, roof acceleration, and CRBF column uplift during the first component of the Northridge (Canyon Country) ground motion at the DE level.

Figure 2-5 illustrates the hysteretic response of the beam and column in the first story of the SMRF, as well as the hysteretic response of the brace in the first story of the other SFRSs, for the three-story buildings under the same scaled ground motion. For the SMRF, most nonlinearity effects are attributed to the beam due to the design principle of having strong columns and weak beams. Additionally, while the braces of the SCBF and BRBF experience buckling and yielding, respectively, the braces of the CRBF remain linear due to the implementation of capacity design principles.

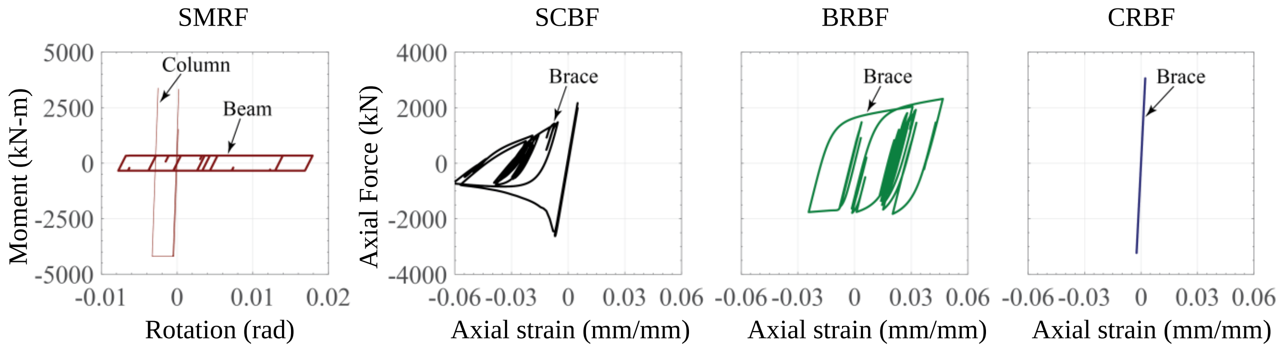

Figure 2-5. Three-story buildings during the first component of the Northridge (Canyon Country) ground motion scaled to DE level: hysteretic response of the first story beam and interior column base of the SMRF, and the hysteretic response of the first-story left brace of other SFRSs.

Figure 2-6 shows the median peak story drift ratios (SDRs), peak floor accelerations (PFAs), and residual story drift ratios (RSDRs) at the DE level for all considered SFRSs. The SMRF and SCBF have the largest and smallest drifts, respectively, among the three-story SFRSs. Additionally, the drifts of the CRBF are nearly constant over the height of the building, indicating that the rocking mode dominates the displacements of the CRBFs (Buccella et al., 2021). Similar outcomes can be seen for taller structures, although the differences in drifts for the various SFRSs become less evident and the higher mode effects are more pronounced. Comparing the PFAs shows that SMRFs have higher demands than other SFRSs, and CRBFs experience large demands on the roof. Also, the buckling and yielding of the lower story braces in the SCBFs and BRBFs prevents large PFAs for higher floors. Comparing residual drifts among the three-story SFRSs highlights the distinctive behavior of the CRBF, which exhibits no residual drifts due to its self-centering mechanism, contrasting with the other three SFRSs that demonstrate residual drifts, particularly at lower stories. This trend holds in the taller buildings, where CRBFs exhibit minimal residual drifts while the SCBFs, BRBFs, and six-story SMRFs have higher residual drifts on lower stories. However, the 12-story SMRF experiences increasing residual drifts at higher stories.

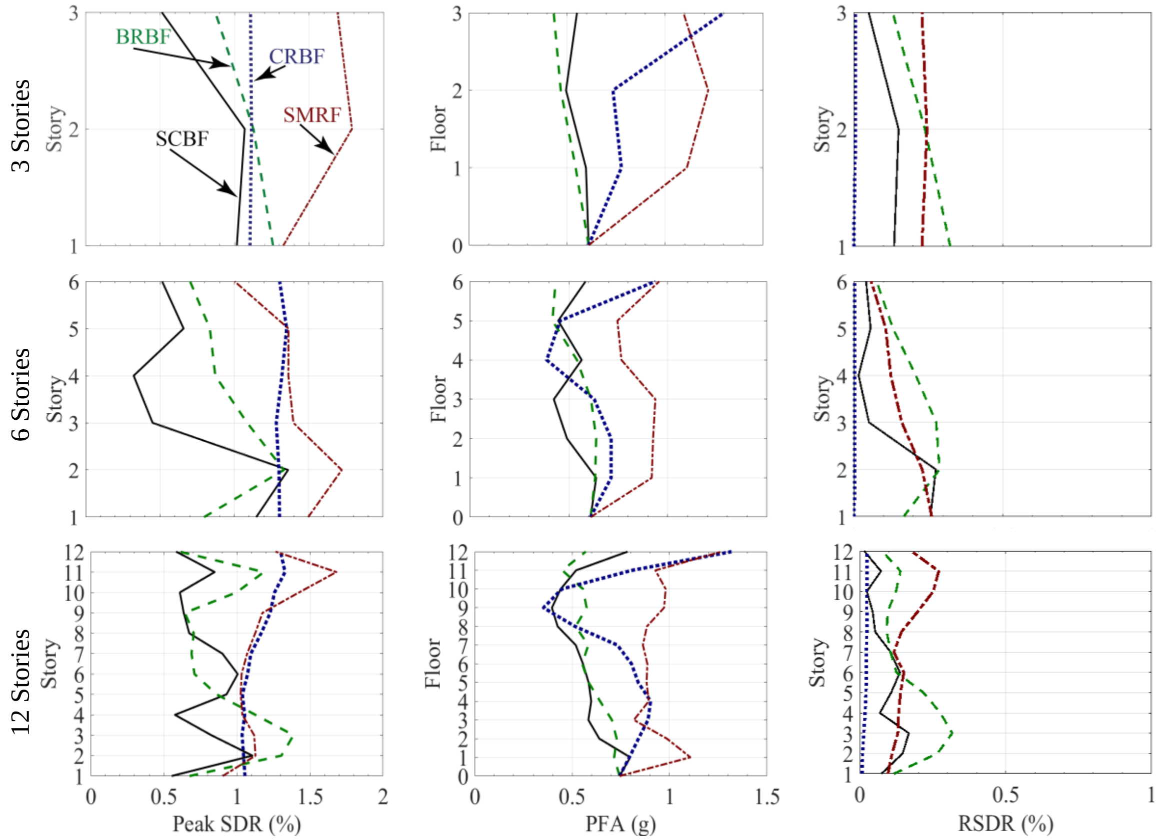

Figure 2-6. Median values of peak story drift ratio (SDR), peak floor acceleration (PFA), and residual story drift ratio (RSDR) at the DE level.

The collapse probability of each building was assessed for each intensity level of the MSA, based on a collapse definition of any SDR exceeding 10%. The collapse fragility curves of the SFRSs, which were developed employing the software tools provided by Baker (2015), are compared in Figure 2-7 with the x-axis showing the ratio of the demand intensity to the MCE spectral acceleration at the elastic period of that building (i.e. $S_a(T_1,5\%)/S_{MT}$). All three- and six-story SFRSs have a collapse probability of less than 5% at the MCE level. For the 12-story SFRSs, the SMRF has a collapse probability of 11%, while that of the other structures is less than 10%. Comparing collapse margin ratios (CMRs), defined as the median collapse spectral acceleration divided by S_{MT}, reveals that all three-story SFRSs have almost identical CMRs, while the CMR of taller buildings is lowest for the SMRFs and highest for the BRBFs, with the other SFRSs in between. These results are generally consistent with the performance requirements of FEMA P695, considering that the ground motion scaling differs from the recommendation of FEMA P695 in order to directly compare the different SFRSs, and that neither a spectral shape factor nor a total system collapse uncertainty has been applied.

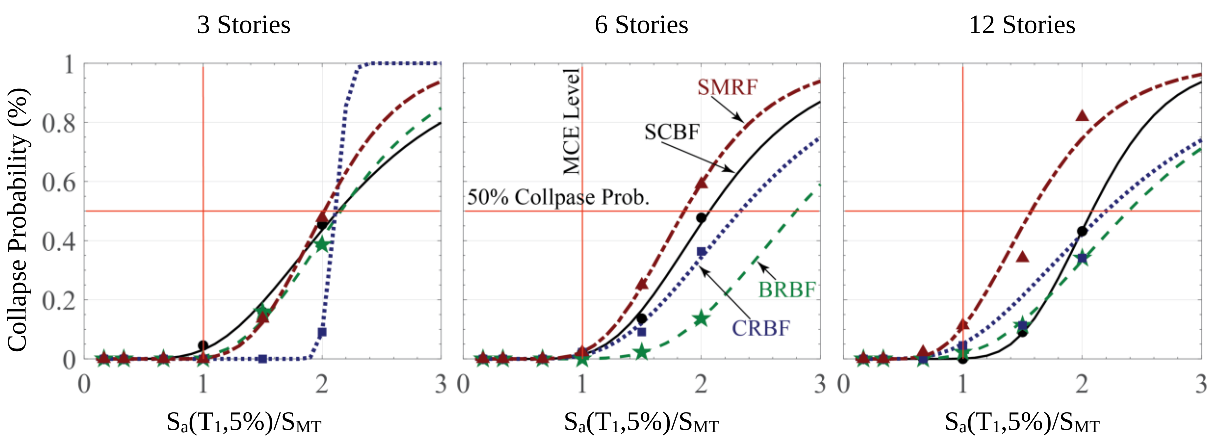

Figure 2-7. Collapse fragility curves.

2.8 SEISMIC INTENSITY-BASED EXPECTED LOSSES

Figure 2-8 compares total expected losses of the four SFRSs at seismic intensity levels of 0.5 DE, DE, and MCE. The losses from the SFRSs at each building height were normalized by the SMRFs' replacement cost. Also, the total expected losses are subdivided into losses owing to drift-sensitive and acceleration-sensitive nonstructural components, structural repairs, demolition, and building collapse.

At the 0.5 DE level, the expected loss for all buildings is less than 8% of the SMRF replacement cost. Among the SFRSs, the SCBFs exhibit the largest expected loss, followed by the SMRFs. The expected loss for the BRBFs and CRBFs is relatively small, less than 2%, across all building heights. Acceleration-sensitive nonstructural components are the primary source of the loss for all systems except the SCBFs. For the SCBFs, the yielding and buckling of braces at the bottom floors even at low-intensity levels reduces PFAs at higher floors (Ray-Chaudhuri and Hutchinson, 2011), but at the cost of greater losses owing to structural components. Some small percentage of the loss due to demolition can be seen in Figure 2-8 (a), even though all story residual drifts at the 0.5DE level were much less than 1.5%. This is because the FEMA P58 Monte Carlo-based methodology (FEMA P-58-1, 2018) uses the Yang et al. algorithm (Yang et al., 2006, 2009) to generate a set of demands in each realization and incorporate the effects of uncertainties, and this algorithm produces a distribution with a longer tail than that of the original data set.

Similarly, at the DE level (Figure 2-8 (b)), the expected loss for the SCBFs, BRBFs, and CRBFs is less than 10%, and generally lowest for the BRBFs and CRBFs. However, the SMRFs exhibit a greater expected loss, exceeding 20% for the three-story SMRF. Also, at this intensity level, the loss resulting from demolition is the greatest source of loss for almost all SFRSs at different heights, except for the CRBFs, where the lack of demolition-related losses is of a similar value to the increase in calculated losses related to non-structural components.

At the MCE level (Figure 2-8 (c)), the SMRFs exhibit expected losses surpassing 35% of the building replacement cost. Even just the irreparable losses of the SMRFs, namely losses due to collapse and demolition, are greater than the total expected losses for all other SFRSs. Figure 2-8 (c) shows that the buildings with CRBFs greatly benefit from having little to no losses due to demolition at the MCE level, which leads to these buildings having the lowest expected losses at each height compared to buildings with other SFRSs. According to Figure 2-7, the collapse probabilities were low or zero for most SRFSs at the MCE level, resulting in the expected losses due to collapse remaining below 4% for most SFRSs at all heights However, in the 12-story

SMRF where the collapse probability was 11%, the associated expected loss due to collapse is 11%.

2.9 Expected annual losses

2.9.1 Total expected annual loss

This section examines earthquake-induced losses in the designed SFRSs in terms of expected annual loss (EAL), representing an average amount that is expected to be spent on earthquake damage repairs annually. This quantity is the area under the distribution curve of mean annual total repair cost (FEMA P-58-1, 2018). Such a curve was constructed for each building using time-based assessments following the guidelines of FEMA P58-1. The process involved multiplying the cumulative probability distribution of total loss at each intensity, which was obtained using Pelicun software (Zsarnóczay, 2019), by the annual frequency of occurrence within the corresponding intensity interval. The annual frequencies for a given loss level were then summed across all intensity-based loss curves. In this way, all seismic hazard levels were considered as well as all uncertainties provided in the FEMA P58-3 library for damage fragility functions and repair cost consequence functions.

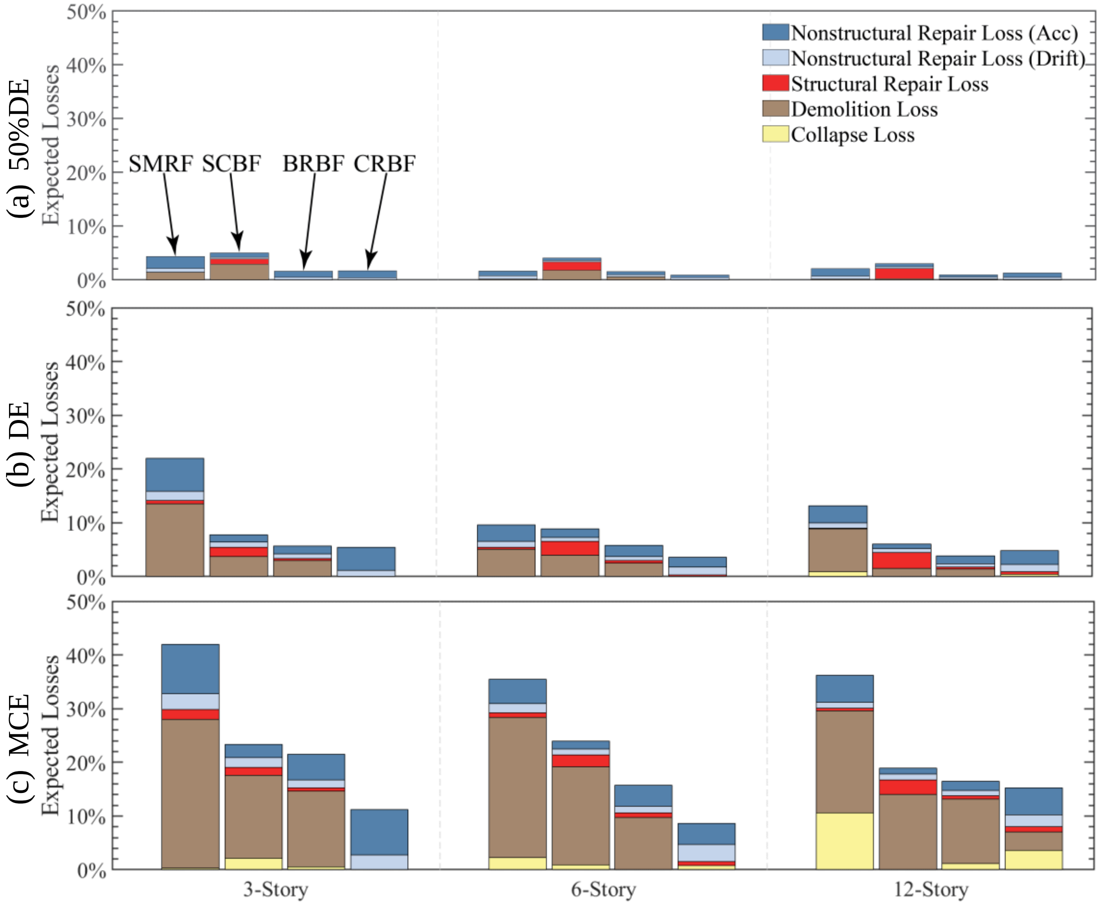

Figure 2-8. Expected losses (normalized by the replacement cost of the SMRFs for each building height) at three seismic intensities.

Figure 2-9 illustrates the computed EALs of the SFRSs for each building height, normalized by the SMRF replacement cost. Figure 2-9 shows that the normalized EALs range from 0.05% to 0.3%, with the CRBF always having the lowest normalized EAL. Among the three-story buildings, the SMRF and CRBF exhibit the greatest and smallest normalized EAL, respectively. The normalized EAL of the three-story BRBF is only slightly greater than that of the CRBF. Comparing the irreparable losses, the three-story CRBF exhibits a minimal contribution from collapse losses, almost zero, consistent with the collapse fragility curve in Figure 2-6, which remains zero even until the 1.5 MCE level. The demolition losses from the three-story SMRF, SCBF, and BRBF account for over 45% of the total normalized EAL, making this the primary contributor to their total EAL. In contrast, the three-story CRBF benefits from self-centering behavior, resulting in zero demolition losses. In terms of repairable losses, the three-story SCBF exhibits the largest normalized EAL due to structural repairs, as SCBFs require repairs for braces and connections even at small drift ratios. In contrast, the three-story SMRF and BRBF experience smaller structural repair losses compared to the SCBF, and the CRBF has negligible structural repair losses due to capacity design and its rigid body rocking deformation. The normalized EAL caused by drift-sensitive nonstructural components is similar among the three-story SFRSs, while the SMRF and CRBF have relatively significant EALs due to acceleration-sensitive components. Indeed, the three-story CRBF's major loss source is damage to acceleration-sensitive components, accounting for 75% of the total normalized EAL. Owing primarily to improved damage fragility curves in the most recent version of FEMA P58-3 (2018) compared to the earlier one (FEMA P-58-3, 2012), Figure 2-9 demonstrates that losses due to acceleration-sensitive nonstructural components do not dominate the normalized EALs for SMRFs and SCBFs in the way that was found by Hwang and Lignos (2017a, 2017b).

The six-story buildings show similar trends as three-story buildings, but the SCBF has the greatest normalized EAL because it has both the greatest contribution from demolition losses among all SFRSs and the greatest contribution from structural losses. The EALs are generally lower than for the three-story buildings because the taller buildings benefit from economies of scale in repairs, and because the probability of excessive residual drifts leading to demolition is lower for the SMRF building. Considering the 12-story buildings, similar trends can also be observed. The normalized EAL from structural repair loss is more evident for the higher-rise SCBFs because larger-sized braces and more seismic frames were used, although such loss is still small independent of building height for the other SFRSs. Figure 2-9 demonstrates that while the irreparable losses in the CRBFs contribute a small amount to the total annualized loss, the irreparable losses in other SFRSs contribute to more than half of the total EAL.

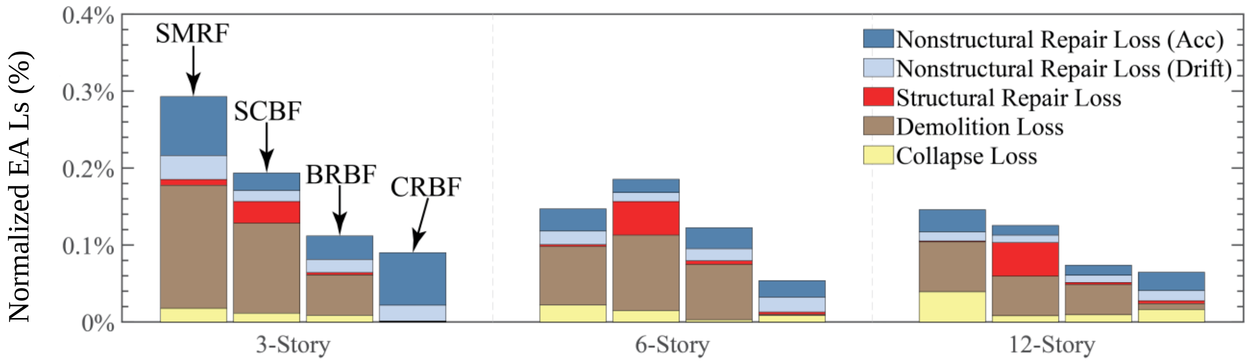

Figure 2-9. Expected annual losses (EALs) normalized by the replacement cost of the building with SMRFs for each building height.

2.9.2 Contribution of individual nonstructural components

Figure 2-10 shows the contributions to expected annual losses from the five most significant nonstructural components, which collectively account for more than 70% of the total nonstructural component losses presented in Figure 2-9 for all cases. To evaluate the impact of these nonstructural components, their damage fragility function parameters and repair costs are given in Table 2-4, to be considered along with their quantities as listed in Table 2-3.

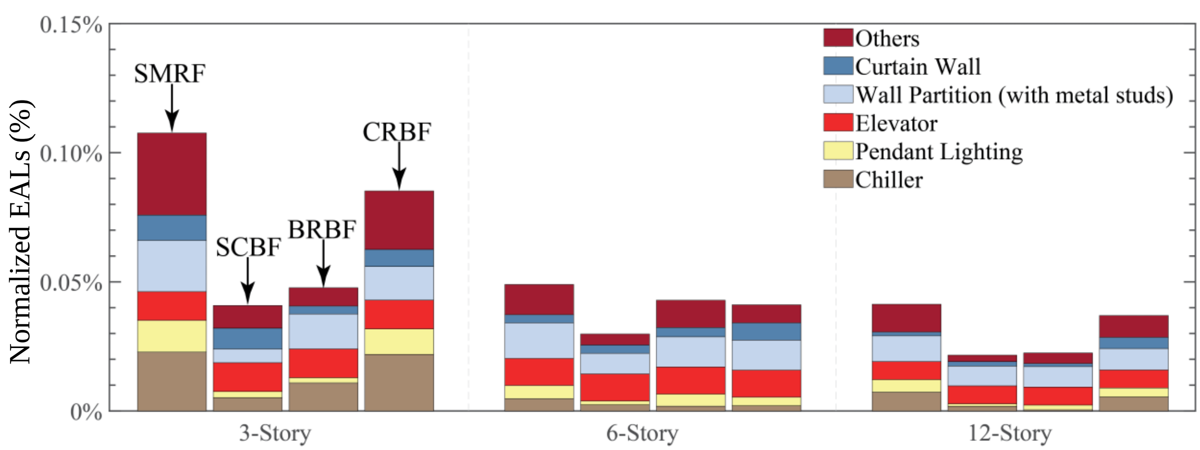

Figure 2-10. Nonstructural components with the greatest contributions to the total expected annual losses (EALs).

Although there is only a single chiller installed on the roof of each three-story building, it makes a notable contribution to the total losses due to its modest 0.72 g median acceleration capacity and high repair costs exceeding $280,000. This contribution is relatively smaller for the three-story SCBF and BRBF because brace buckling and yielding at low earthquake intensities result in reduced acceleration demands on the roof. Pendant lighting contributes significantly to the total losses in the three-story SMRF and CRBF, despite having a median acceleration capacity of 1.5 g and an inexpensive unit repair cost, because of their high quantities, with more than 300 installed on each ceiling of each story. The elevator has a meaningful contribution to the losses because it has a high unit repair cost and a single damage state with a median acceleration capacity of only 0.39 g, which is less than the median peak ground acceleration (PGA) at the DE level (Figure 2-6). Damage to wall partitions often contributes significantly to the total losses due to their low capacity compared to the buildings' story drifts. For example, moderate cracking can occur at a story drift ratio of 0.7%, which is smaller than the median demands of almost all floors of all three-story buildings at the DE level (Figure 2-6), although the associated loss is noteably lower in the three-story SCBF building.

The trends that were described for the three-storey buildings are also generally applicable to the six- and 12-story buildings, although with lower total EALs as noted previously. One additional difference is that the contribution of the chiller reduces for the six- and 12-storey buildings. This difference is primarily because of the discretization of the number of chillers, where one is assumed for both the three- and the six-story buildings and two chillers are assumed for the 12-story buildings, while the replacement value of the building is proportional to the number of stories. In addition, while Figure 2-6 often shows similar peak roof accelerations for all three building heights at the DE level of ground shaking, this is not true at all ground motion intensities.

Table 2-4. Damage fragility and repair cost for the seven nonstructural components with the most contributions to the total expected annual losses (EALs).

Component description	Damage state	Damage fragility function			Repair cost [a]
		Median	β	Fraction	
Chiller	Equipment failed	0.72 g [b]	0.20	-	280700
Pendant Lighting	Disassembly of rod system	1.50 g [b]	0.40	-	1000
Elevator	Machine anchorages failed	0.39 g	0.45	26 % [c]	8800
	Rail distortion			79 % [c]	37400
	Cab walls/door damaged			68 % [c]	32000
	Cab ceiling damaged			17 % [c]	5000
Wall Partition (with metal studs)	Slight cracking	0.43 % [b]	0.43	-	1400
	Moderate cracking	0.70 % [b]	0.45	-	3600
	Walls displaced	1.47 % [b]	0.51	-	7000
Curtain Wall	Glass cracking	2.1 % [b]	0.45	-	3000
	Glass falls from frame	2.4 % [b]	0.45	-	3000

Note: β = lognormal standard deviation.
[a] Unit repair cost based on 2011 (FEMA P-58-3, 2018) with no reduction for economies of scale.
Damage Logic: [b] Damage states occur in sequential order; [c] Damage states independently can occur simultaneously based on the fraction (FEMA P-58-3, 2018).

2.10 Cost-effectiveness

This section investigates the cost-effectiveness of the BRBFs and CRBFs in comparison to the SCBFs, taking into consideration the influence of the return rate, *r*, as well as potential differences in construction and replacement costs. SMRFs are omitted because of their higher construction costs and the findings from the previous section that the considered SMRFs generally have higher EALs compared to braced frames. To make this comparison, the total of the initial building construction cost and the present value of earthquake-induced losses over the assumed 50 years of building life expectancy (Hwang and Lignos, 2017a) are determined as follows:

$$C_{SFRS,r,n} = IC_{SCBF}(1+n) + EAL_{SFRS}\frac{1-\left(\frac{1}{(1+r)^{50}}\right)}{r} \tag{2-1}$$

where IC_{SCBF} is the construction cost of the considered building when using an SCBF as the seismic force resisting system, and n is the relative premium in the building's construction cost and replacement cost when using a different SFRS relative to the same height of SCBF. The cost-effectiveness of the BRBFs or CRBFs in comparison to the SCBFs is evaluated using the cost-effectiveness index $CE_{\mathrm{SFRS},r,n}$, which is defined to be normalized by the construction cost of the SCBF and is calculated for a range of for different values of r and n:

$$CE_{\mathrm{SFRS},r,n} = \frac{C_{\mathrm{SFRS},r,n} - C_{\mathrm{SCBF},r,0}}{IC_{\mathrm{SCBF}}} \times 100\% \tag{2-2}$$

Figure 2-11 illustrates the cost-effectiveness of the BRBFs and CRBFs using the above equation for ranges of 0 to 4% for r and 0 to 5% for n. This figure shows that the BRBF and CRBF are generally cost-effective, relative to the SCBF, for the three-story building because they have a positive index for most of the considered combinations of r and n. The three-story CRBF is slightly more cost-effective than the BRBF because it has a wider range of combinations of r and n that produce a positive cost-effectiveness index. For example, considering r of 3% and n of 4%, the BRBF is not more cost-effective than the SCBF but the CRBF is. The six-story CRBF also has a positive index for almost all considered combinations of r and n, making it generally more cost-effective than the BRBF. According to the result for the 12-story buildings, the BRBF and CRBF have a positive index for fewer combinations of r and n. Nonetheless, the 12-story CRBF is marginally more economical than the BRBF.

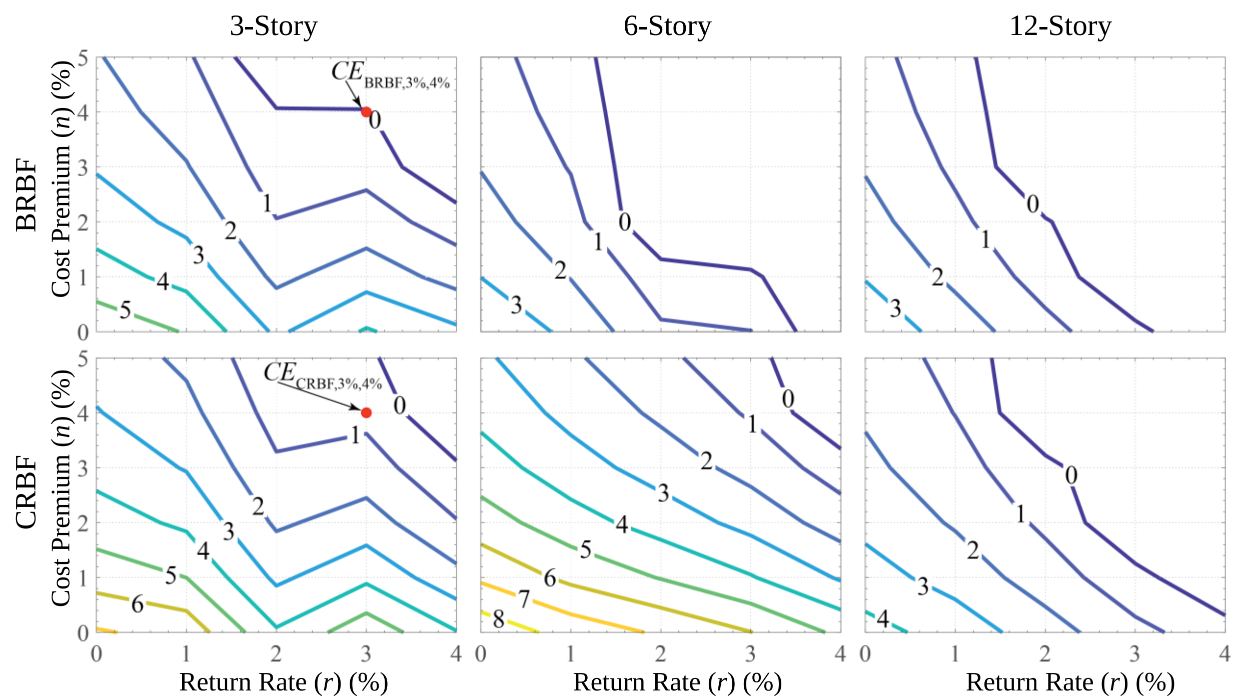

Figure 2-11. Cost-effectiveness comparison of the BRBFs and CRBFs to SCBFs.

2.11 Conclusions

The present study provided a comprehensive assessment and comparison of four distinct steel seismic force-resisting systems (SFRSs) as potential choices for designing buildings at three different heights (three-, six-, and 12-story). These SFRSs included three common ductile SFRSs: special moment resisting frames (SMRFs), special concentrically braced frames (SCBFs), and buckling-restrained braced frames (BRBFs), as well as one low-damage self-centering SFRS: controlled rocking braced frames (CRBFs). The FEMA P58 methodology (FEMA P-58-1, 2018) was used to translate the unique structural performance attributes of each system into economic costs using the metric of expected annual loss (EAL).This also made it possible to compare irreparable losses, such as collapse and demolition due to excessive residual drifts, with reparable losses, involving repairs to structural and nonstructural components, for each distinct SFRS.

While all buildings designed with the four SFRSs demonstrated acceptable collapse capacities, their behavior at the design earthquake (DE) level revealed distinct characteristics. The SCBF and SMRF buildings showed the smallest and largest peak story drifts, respectively. The CRBF buildings maintained nearly constant story drifts throughout the building height due to the dominance of the rocking mode. Brace yielding and buckling in the lower stories of the SCBF and BRBF buildings led to decreased acceleration demands on the roof. Conversely, both the CRBF and SMRF buildings experienced higher roof accelerations, with the SMRF buildings generally exhibiting the greatest accelerations across all floors among the four systems. Moreover, the CRBF buildings exhibited minimal residual drift and member yielding, in contrast to the moderate residual drifts and larger contribution of yielding observed in the buildings with other SFRSs.

The CRBF buildings exhibited the lowest total EAL, with the saving in irreparable losses relative to other SFRSs more than compensating for the increased expected losses from acceleration-sensitive nonstructural components. The BRBF buildings showed only slightly higher EAL compared to the CRBF buildings, but the CRBFs offered a more favorable cost-effectiveness in terms of earthquake-induced losses over the assumed 50-year building life, for a wider range of combinations of cost premiums and return rates. In contrast, in the buildings designed with more common ductile SFRSs, more than half of the total EAL was attributed to irreparable losses, primarily driven by demolition losses. Notably, the contribution of only irreparable losses to the EAL of the SMRF and SCBF buildings was typically greater than the total EAL for the buildings with CRBFs.

Although the total EAL for the buildings with CRBFs was only slightly less than for buildings with BRBFs, the trade-off between irreparable and repairable losses would introduce complex factors when comparing expected recovery time. While further study is needed on this point, using CRBFs may be more advantageous because repairable losses are likely associated with less downtime than irreparable losses that require building demolition and rebuilding. Another limitation of this study lies in FEMA P58's damage fragility curves, which only consider peak accelerations as the engineering demand parameter for acceleration-sensitive components, while prior research indicates that buildings designed with different SFRSs exhibit diverse shapes of floor acceleration spectra.

2.12 Acknowledgements

Financial support for this work was provided by the Ontario Ministry of Colleges and Universities through an Early Researcher Award, and the Natural Sciences and Engineering Research Council of Canada (NSERC) through the Discovery Grant program.

2.13 References

Aher, S., Mar, D., and Rodgers, G., 2020. Casa Adelante: behavior, design, modeling choices, and performance insights of a rocking mat foundation system. *SEAOC Convention Proceedings* (pp. 1–13).

ANSI/AISC 341-16, 2016. *Seismic provisions for structural steel buildings*. Chicago, IL, United States: American Institute of Steel Construction.

ANSI/AISC 358-16, 2016. *Prequalified connections for special and intermediate steel moment frames for seismic applications*. Chicago, IL, United States: American Institute of Steel Construction. Retrieved from https://www.aisc.org/globalassets/aisc/publications/standards/a358-20w.pdf

ANSI/AISC 360-16, 2016. *Specification for structural steel buildings*. *ANSI/AISC 360-16*. Chicago, IL, United States: American Institute of Steel Construction.

ASCE/SEI 7-16, 2016. *Minimum design loads and associated criteria for buildings and other structures*. Reston, VA, United States: American Society of Civil Engineers.

Asgarkhani, N., Yakhchalian, M., and Mohebi, B., 2020. Evaluation of approximate methods for estimating residual drift demands in BRBFs. *Engineering Structures*, **224**, 110849. Elsevier Ltd. DOI: https://doi.org/10.1016/j.engstruct.2020.110849

Baker, J. W., 2015. Efficient analytical fragility function fitting using dynamic structural analysis. *Earthquake Spectra*, **31**(1), 579–599. DOI:

https://doi.org/10.1193/021113EQS025M

Banihashemi, A., and Wiebe, L., 2022. Design of low-rise controlled rocking braced frames for life cycle costs. *Proceedings of the 10th International Conference on Behaviour of Steel Structures in Seismic Areas: STESSA*, **262**, 746–754. DOI: https://doi.org/10.1007/978-3-031-03811-2_81

Behr, R., 2001. Architectural glass for earthquake-resistant buildings. *Proceedings of the 7th International Glass in Tampere (Glass Processing Days 2001)*. Tampere, Finland. Retrieved from www.glassfiles.com

Buccella, N., Wiebe, L., Konstantinidis, D., and Steele, T., 2021. Demands on nonstructural components in buildings with controlled rocking braced frames. *Earthquake Engineering and Structural Dynamics*, **50**(4), 1063–1082. John Wiley and Sons Ltd. DOI: https://doi.org/10.1002/eqe.3385

Bull, D., 2011. Stairs and access ramps between floors in multi-story buildings. *Report to the Canterbury Earthquakes Royal Commission.* (pp. 1–8). Christchurch, New Zealand: Holmes Consulting Group.

Charney, F. A., 2008. Unintended consequences of modeling damping in structures. *Journal of Structural Engineering*, **134**(4), 581–592. DOI: https://doi.org/10.1061/(ASCE)0733-9445(2008)134:4(581)

Cornell, C. A., and Krawinkler, H., 2000. Progress and challenges in seismic performance assessment. *PEER Center News*, **3**(2), 1–3.

Dhakal, R. P., 2010. Damage to non-structural components and contents in 2010 Darfield earthquake. *Bulletin of the New Zealand Society for Earthquake Engineering*, **43**(4), 404–411. DOI: https://doi.org/10.5459/bnzsee.43.4.404-411

Dyanati, M., Huang, Q., and Roke, D., 2017. Cost-benefit evaluation of self-centring concentrically braced frames considering uncertainties. *Structure and Infrastructure Engineering*, **13**(5), 537–553. DOI: https://doi.org/10.1080/15732479.2016.1173070

DYWIDAG Systems International, 2020. DYWIDAG post-tensioning systems.

Eatherton, M. R., Ma, X., Krawinkler, H., Mar, D., Billington, S., Hajjar, J. F., and Deierlein, G. G., 2014. Design concepts for controlled rocking of self-centering steel-braced frames. *Journal of Structural Engineering*, **140**(11), 04014082. American Society of Civil Engineers. DOI: https://doi.org/10.1061/(ASCE)ST.1943-541X.0001047

Elkady, A., and Lignos, D. G., 2014. Modeling of the composite action in fully restrained beam-to-column connections: implications in the seismic design and collapse capacity of steel special moment frames. *Earthquake Engineering and Structural Dynamics*, **43**(13), 1935–1954. John Wiley and Sons Ltd. DOI: https://doi.org/10.1002/eqe.2430

Erochko, J., Christopoulos, C., Tremblay, R., and Choi, H., 2011. Residual drift response of SMRFs and BRB frames in steel buildings designed according to ASCE 7-05. *Journal of Structural Engineering*, **137**(5), 589–599. American Society of Civil Engineers (ASCE). DOI: https://doi.org/10.1061/(ASCE)ST.1943-541X.0000296

FEMA P-58-1, 2018. *Seismic performance assessment of buildings volume 1-methodology*. Washington, DC, United States: prepared by the Applied Technology Council for the Federal Emergency Management Agency.

FEMA P-58-3, 2012. *Seismic Performance Assessment of Buildings, Volume 3–Supporting Electronic Materials and Background Documentation: 3.1 Performance Assessment Calculation Tool (PACT)*. Washington, DC, United States: prepared by the Applied Technology Council for the Federal Emergency Management Agency.

FEMA P-58-3, 2018. *Seismic Performance Assessment of Buildings, Volume 3–Supporting Electronic Materials and Background Documentation: 3.1 Performance Assessment Calculation Tool (PACT)*. Version 3.1.2. Washington, DC, United States: prepared by the Applied Technology Council for the Federal Emergency Management Agency.

FEMA P695, 2009. *Quantification of Building Seismic Performance Factors*. Washington, DC, United States: prepared by the Applied Technology Council for the Federal Emergency Management Agency.

Ghasemof, A., Mirtaheri, M., and Karami Mohammadi, R., 2022. Multi-objective optimization for probabilistic performance-based design of buildings using FEMA P-58 methodology. *Engineering Structures*, **254**, 113856. Elsevier Ltd. DOI: https://doi.org/10.1016/j.engstruct.2022.113856

Hu, S., and Zhu, S., 2023. Life-cycle benefits estimation for hybrid seismic-resistant self-centering braced frames. *Earthquake Engineering and Structural Dynamics*, **52**(10). John Wiley and Sons Ltd. DOI: https://doi.org/10.1002/eqe.3914

Huang, Q., Dyanati, M., Roke, D. A., Chandra, A., and Sett, K., 2018. Economic feasibility study of self-centering concentrically braced frame systems. *Journal of Structural Engineering*, **144**(8), 04018101. DOI: https://doi.org/10.1061/(ASCE)ST.1943-541X.0002093

Hwang, S. H., and Lignos, D. G., 2017a. Earthquake-induced loss assessment of steel frame buildings with special moment frames designed in highly seismic regions. *Earthquake Engineering and Structural Dynamics*, **46**(13), 2141–2162. John Wiley and Sons Ltd. DOI: https://doi.org/10.1002/eqe.2898

Hwang, S. H., and Lignos, D. G., 2017b. Effect of modeling assumptions on the earthquake-induced losses and collapse risk of steel-frame buildings with special concentrically braced frames. *Journal of Structural Engineering*, **143**(9), 04017116. American Society of Civil Engineers (ASCE). DOI: https://doi.org/10.1061/(ASCE)ST.1943-541X.0001851

Ibarra, L. F., Medina, R. A., and Krawinkler, H., 2005. Hysteretic models that incorporate strength and stiffness deterioration. *Earthquake Engineering and Structural Dynamics*, **34**(12), 1489–1511. DOI: https://doi.org/10.1002/eqe.495

Lignos, D. G., Hartloper, A. R., Elkady, A., Deierlein, G. G., and Hamburger, R., 2019. Proposed updates to the ASCE 41 nonlinear modeling parameters for wide-flange steel columns in support of performance-based seismic engineering. *Journal of Structural Engineering*, **145**(9), 04019083. American Society of Civil Engineers (ASCE). DOI: https://doi.org/10.1061/(ASCE)ST.1943-541X.0002353

Lignos, D. G., and Krawinkler, H., 2011. Deterioration modeling of steel components in support of collapse prediction of steel moment frames under earthquake loading. *Journal of Structural Engineering*, **137**(11), 1291–1302. American Society of Civil Engineers (ASCE). DOI: https://doi.org/10.1061/(ASCE)ST.1943-541X.0000376

Ma, X., Krawinkler, H., and Deierlein, G. G., 2010. Seismic design and behavior of self-centering braced frame with controlled rocking and energy dissipating fuses. *Report 174* (p. 438). Stanford, CA, United States: Blume Earthquake Engineering Center. Retrieved from http://blume.stanford.edu

Mahdavipour, M. A., and Deylami, A., 2014. Probabilistic assessment of strain hardening ratio effect on residual deformation demands of Buckling-Restrained Braced Frames. *Engineering Structures*, **81**, 302–308. Elsevier Ltd. DOI: https://doi.org/10.1016/j.engstruct.2014.10.004

Miranda, E., Mosqueda, G., Retamales, R., and Pekcan, G., 2012. Performance of nonstructural components during the 27 February 2010 Chile earthquake. *Earthquake Spectra*, **28**(S1), S453–S471. DOI: https://doi.org/10.1193/1.4000032

Molina Hutt, C., Rossetto, T., and Deierlein, G. G., 2019. Comparative risk-based seismic assessment of 1970s vs modern tall steel moment frames. *Journal of Constructional Steel Research*, **159**, 598–610. Elsevier Ltd. DOI: https://doi.org/10.1016/j.jcsr.2019.05.012

Okazaki, T., Lignos, D. G., Midorikawa, M., Ricles, J. M., and Love, J., 2013. Damage to steel buildings observed after the 2011 Tohoku-oki earthquake. *Earthquake Spectra*, **29**(S1), S219–S243. Earthquake Engineering Research Institute. DOI: https://doi.org/10.1193/1.4000124

Pacific Earthquake Engineering Research Centre (PEER), 2021. Open System for Earthquake Engineering Simulation v3.3.0 [Computer Software].

Perrone, D., Calvi, P. M., Nascimbene, R., Fischer, E. C., and Magliulo, G., 2019. Seismic performance of non-structural elements during the 2016 Central Italy earthquake. *Bulletin of Earthquake Engineering*, **17**, 5655–5677. Springer Netherlands. DOI: https://doi.org/10.1007/s10518-018-0361-5

Rahgozar, N., Moghadam, A. S., and Aziminejad, A., 2016. Quantification of seismic performance factors for self-centering controlled rocking special concentrically braced frame. *The Structural Design of Tall and Special Buildings*, **25**(14), 700–723. DOI: https://doi.org/10.1002/tal.1279

Ramirez, C. M., Liel, A. B., Mitrani-Reiser, J., Haselton, C. B., Spear, A. D., Steiner, J., Deierlein, G. G., et al., 2012. Expected earthquake damage and repair costs in reinforced concrete frame buildings. *Earthquake Engineering and Structural Dynamics*, **41**(11), 1455–1475. DOI: https://doi.org/10.1002/eqe.2216

Ramirez, C. M., and Miranda, E., 2012. Significance of residual drifts in building earthquake loss estimation. *Earthquake Engineering and Structural Dynamics*, **41**(11), 1477–1493. DOI: https://doi.org/10.1002/eqe.2217

Ray-Chaudhuri, S., and Hutchinson, T. C., 2011. Effect of nonlinearity of frame buildings on peak horizontal floor acceleration. *Journal of Earthquake Engineering*, **15**(1), 124–142. DOI: https://doi.org/10.1080/13632461003668046

Retamales, R., Davies, R., Mosqueda, G., and Filiatrault, A., 2013. Experimental seismic fragility of cold-formed steel framed gypsum partition walls. *Journal of Structural Engineering*, **139**(8), 1285–1293. DOI: https://doi.org/10.1061/(ASCE)ST.1943-541X.0000657

Roke, D., Sause, R., Ricles, J. M., and Chancellor, N. B., 2010. Damage-free seismic-resistant self-centering concentrically-braced frames. *Report 10-09*. Bethlehem,PA, United States: Advanced Technology for Large Structural Systems Engineering Research Center.

Rosenblueth, E., and Meli, R., 1986. The 1985 Earthquake causes and effects in Mexico City. *Concrete International*, **8**(5), 12.

RSMeans, 2020. *Building construction cost data*. RSMeans Construction Publishers and Consultants.

Saxey, B., and Daniels, M., 2014. *Characterization of overstrength factors for buckling restrained braces*. *Proc of the 2014 Australasian Structural Engineering Conference (ASEC), Auckland, New Zealand*. Auckland, New Zealand: Proc of the 2014 Australasian Structural Engineering Conference.

Skiadopoulos, A., Elkady, A., and Lignos, D. G., 2021. Proposed panel zone model for seismic design of steel moment-resisting frames. *Journal of Structural Engineering*, **147**(4), 04021006. American Society of Civil Engineers (ASCE). DOI: https://doi.org/10.1061/(ASCE)ST.1943-541X.0002935

Soroushian, S., Zaghi, A. E., Maragakis, M., Echevarria, A., Tian, Y., and Filiatrault, A., 2015. Analytical seismic fragility analyses of fire sprinkler piping systems with threaded joints. *Earthquake Spectra*, **31**(2), 1125–1155. Earthquake Engineering Research Institute. DOI: https://doi.org/10.1193/083112EQS277M

Steele, T. ., and Wiebe, L. ., 2017. Collapse risk of controlled rocking steel braced frames with different post-tensioning and energy dissipation designs. *Earthquake Engineering and Structural Dynamics*, **46**(13), 2063–2082. John Wiley and Sons Ltd. DOI: https://doi.org/10.1002/eqe.2892

Steele, T., and Wiebe, L., 2016. Dynamic and equivalent static procedures for capacity design of controlled rocking steel braced frames. *Earthquake Engineering and Structural Dynamics*, **45**(14), 2349–2369. DOI: https://doi.org/10.1002/eqe.2765

Steele, T., and Wiebe, L. ., 2021. Collapse risk of controlled rocking steel braced frames considering buckling and yielding of capacity-protected frame members. *Engineering Structures*, **237**, 111999. Elsevier BV. DOI: https://doi.org/10.1016/j.engstruct.2021.111999

Tremblay, R., Fliatrault, A., Bruneau, M., Nakashima, M., Prion, H. G., and DeVall, R., 1996. Seismic design of steel buildings: lessons from the 1995 Hyogo-ken Nanbu earthquake. *Canadian Journal of Civil Engineering*, **23**(3), 727–756. NRC Research Press Ottawa, Canada. DOI: https://doi.org/10.1139/l96-885

Tremblay, R., Timler, P., Bruneau, M., and Filiatrault, A., 1995. Performance of steel structures during the 1994 Northridge earthquake. *Canadian Journal of Civil Engineering*, **22**(2), 338–360. DOI: https://doi.org/10.1139/l95-046

Uriz, P., and Mahin, S. A., 2004. Seismic vulnerability assessment of concentrically braced steel frames. *International Journal of Steel Structures*, **4**(4), 239–248.

Uriz, P., and Mahin, S. A., 2008. Toward Earthquake-Resistant Design of Concentrically Braced Steel-Frame Structures. *PEER Report 2008/08*. Berkeley,CA, United States: Pacific Earthquake Engineering Research Center.

Westenenk, B., De La Llera, J. C., Besa, J. J., Jünemann, R., Moehle, J., Lüders, C., Inaudi, J. A., et al., 2012. Response of reinforced concrete buildings in concepción during the maule earthquake. *Earthquake Spectra*, **28**(S1), S257–S280. Earthquake Engineering Research Institute. DOI: https://doi.org/10.1193/1.4000037

Wiebe, L., and Christopoulos, C., 2015. Performance-based seismic design of controlled rocking steel braced frames. I: methodological framework and design of base rocking joint. *Journal of Structural Engineering*, **141**(9), 04014226. DOI: https://doi.org/10.1061/(ASCE)ST.1943-541X.0001202

Wiebe, L., Christopoulos, C., Tremblay, R., and Leclerc, M., 2013. Mechanisms to limit higher mode effects in a controlled rocking steel frame. 2: large-amplitude shake table testing. *Earthquake Engineering and Structural Dynamics*, **42**(7), 1069–1086. DOI: https://doi.org/10.1002/eqe.2258

Yang, T. Y., Moehle, J., Stojadinovic, B., and Kiureghian, D., 2006. An application of PEER performance-based earthquake engineering methodology. *8th U.S. National Conference on Earthquake Engineering*.

Yang, T. Y., Moehle, J., Stojadinovic, B., and Kiureghian, D., 2009. Seismic performance evaluation of facilities: methodology and implementation. *Journal of Structural Engineering*, **135**(10), 1146–1154. DOI: https://doi.org/10.1061/(ASCE)0733-9445(2009)135:10(1146)

Zareian, F., and Medina, R. A., 2010. A practical method for proper modeling of structural damping in inelastic plane structural systems. *Computers and Structures*, **88**(1–2), 45–53. DOI: https://doi.org/10.1016/j.compstruc.2009.08.001

Zsarnóczay, A., 2013. Experimental and numerical investigation of buckling restrained braced frames for eurocode conform design procedure development. *Ph.D. Thesis*. Budapest, Hungary: Budapest University of Technology and Economics.

Zsarnóczay, A., 2019. NHERI-SimCenter/pelicun: v2.0.0, Zenodo. DOI: http://doi.org/10.5281/zenodo.3491100

Chapter 3

3. DEFINING DESIGN PARAMETERS FOR CONTROLLED ROCKING BRACED FRAMES TO CONTROL SEISMIC LOSSES

3.1 ABSTRACT

Controlled rocking braced frames (CRBFs) are a self-centering lateral force-resisting system aimed at reducing structural damage potential. Previous research has shown that relatively low design forces for rocking and for structural elements in CRBFs would be acceptable based on collapse fragility analysis. However, past studies have also highlighted the potential for significant story drifts and for increased demands on acceleration-sensitive nonstructural components installed in buildings with CRBFs. Therefore, while CRBFs have demonstrated acceptable performance in terms of collapse across a wide range of design options, these design options must be evaluated considering the performance of nonstructural components if the intended low-damage potential of CRBFs is to be fully realized. To address this need, this chapter investigates the influence of two key design parameters on seismic losses of buildings with CRBFs, namely the response modification factor (R) for the rocking joint design and the amplification factor (γ) used to incorporate higher-mode forces into the capacity design of frame members. Three different heights of CRBF buildings are designed using different design options, with values of R ranging from 5 to 12 and with higher-mode forces considered based on two seismic intensity levels: the design earthquake (DE) and the maximum considered earthquake (MCE). Then, following an assessment of structural responses, the chapter's primary emphasis is on earthquake-induced economic losses. While the computed total expected annual losses (EALs) using various design options are remarkably similar, the distribution of losses attributed

to collapse or to nonstructural components varies. The CRBFs with lower resistance to rocking exhibit greater losses attributed to collapse and to drift-sensitive nonstructural components, but this is counterbalanced by a simultaneous reduction in losses related to acceleration-sensitive nonstructural components. Furthermore, in taller CRBF buildings, using amplified higher-mode forces based on the MCE level slightly decreases total EALs compared to those using the DE level, primarily due to a reduction in collapse losses.

KEYWORDS: Seismic loss assessment; controlled rocking braced frames; self-centering systems; higher mode effects; capacity design; nonstructural components

3.2 INTRODUCTION

Despite notable advancements in seismic design codes that have contributed to a decline in the number of building collapses during and after severe earthquakes (Okazaki et al. 2013; Westenenk et al. 2012), the socioeconomic repercussions of earthquakes remain a pressing concern. Insights from the aftermath of previous earthquakes have revealed that buildings can require demolition or extensive repair due to excessive residual drifts (Rosenblueth and Meli 1986) and damage to both structural and non-structural components (Dhakal 2010; Miranda et al. 2012; Perrone et al. 2019). These expenditures not only cause property losses but also disrupt businesses, leading to further financial losses (Hwang and Lignos 2017b). Consequently, cities' abilities to recover from such catastrophes face substantial hindrances. To address these challenges, innovative self-centering lateral force-resisting systems have been developed not only to curb demolition losses caused by excessive residual drifts, but also to mitigate structural damage during earthquakes exceeding design levels (Eatherton et al. 2014; Roke et al. 2010; Steele and Wiebe 2021; Wiebe et al. 2013). One such pioneering system is the controlled rocking braced frame (CRBF). The CRBF distinguishes itself from ductile lateral force-resisting systems by employing a non-linear mechanism involving the uplifting of the frame. Vertical post-tensioning can be designed to help self-center the system and introduce positive stiffness during rocking motion, and energy dissipation mechanisms can be integrated to mitigate displacement demands. Figure 1 illustrates the conceptual behavior of a CRBF.

Studies assessing the collapse potential of CRBFs have consistently shown a low collapse probability and minimal damage to their steel components (Rahgozar, Moghadam, and Aziminejad 2016; Steele and Wiebe 2017). Recognizing the advantages of CRBFs, Steele and Wiebe (2021) quantified key design parameters for CRBFs, including response modification factors (R) used in the design of base rocking joints, as well as a parameter related to the intensity level considered for higher modes (γ) in the capacity design of steel members within CRBFs. Their findings indicated that CRBFs demonstrate an acceptably low risk of collapse, even when employing larger values of R (i.e., less resistance to rocking) and considering the use of the design earthquake (DE) intensity level to account for higher mode effects in the capacity design of steel members (γ=1.0). Nevertheless, findings from Buccella et al. (2021) indicated that the presence of higher mode effects can lead to increased acceleration demands in CRBFs, particularly manifesting as spikes in the floor acceleration spectra near the modal periods of the buildings, while others have found that displacements in self-centering systems may be larger than in a conventional yielding system with similar strength (Seo and Sause 2005; Zhang, Steele, and Wiebe 2018).

To enable engineers and other stakeholders to assess potential consequences and, consequently, make more informed design and retrofit decisions, a performance-based earthquake engineering framework has been developed for evaluating earthquake-induced losses (Cornell and Krawinkler 2000; FEMA P-58-1 2018). Over the past decade, several studies have used seismic loss assessment to compare self-centering lateral force-resisting systems with ductile systems. Due to the potentially higher construction costs associated with CRBFs, researchers have conducted cost-benefit analyses comparing CRBFs to special concentrically braced frames (SCBFs) (Banihashemi and Wiebe 2023; Dyanati, Huang, and Roke 2017; Huang et al. 2018). While their results indicated lower total repair losses for CRBFs compared to SCBFs, they also identified a higher loss attributed to acceleration-sensitive nonstructural components in CRBFs compared to SCBFs.

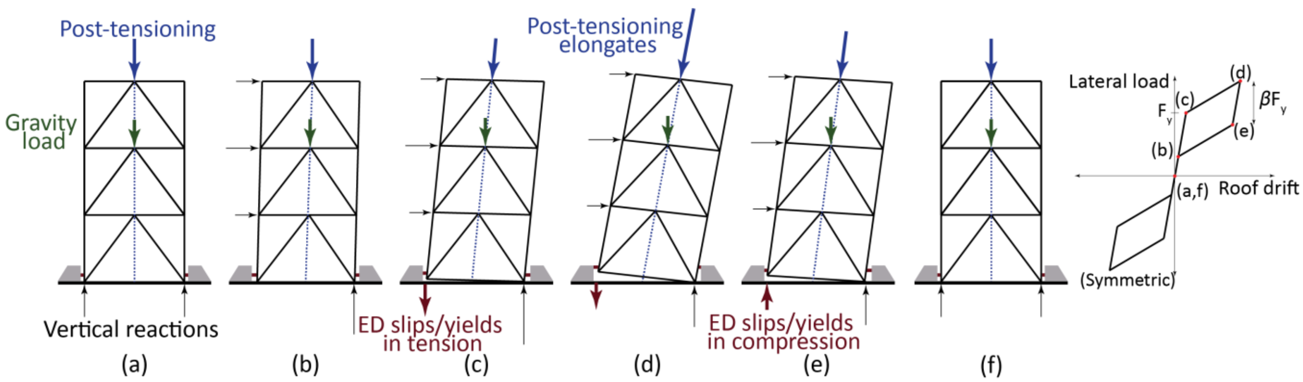

Figure 3-1. CRBF hysteretic response.

Other studies have defined design parameters for CRBFs and quantified their impact on collapse probability. However, additional investigation into these parameters is needed to consider their potential impact on seismic losses, including damage to drift- and acceleration-sensitive nonstructural components. To address this research gap, three-story, six-story, and 12-story buildings are designed using CRBFs. Each building height is designed with various design options, considering different values of *R* ranging from 5 to 12 and using the forces associated with the higher-mode response at two intensity levels, DE and maximum considered earthquake (MCE). To assess the influence of these design parameters, after examining the response in terms of engineering demand parameters (EDPs), the study compares various options based on expected losses at given seismic intensity levels and subsequently evaluates the expected annual losses. Additionally, critical nonstructural components that contribute greatly to seismic losses are identified, highlighting areas for future research aimed at mitigating such losses and better characterizing their behavior.

3.3 Design of prototype buildings

Three different heights of steel-framed office buildings were each designed using CRBFs. The buildings were located in a seismically active area with mapped short-period and 1-second spectral accelerations of S_s=1.5 g and S_1=0.5 g, respectively, assuming a site class D (stiff soil) condition (ASCE/SEI 7-16 2016). Figure 3-2 (a) illustrates the typical floor plan for these buildings, each having a story height of 4.57 m. The total seismic weight for each floor and roof was 10,200 kN and 6,430 kN, respectively. For the three-story buildings, two frames were used in each direction, while four frames were used for the six-story and 12-story buildings. The CRBFs were designed to have a width of 90% of the bay width to fit between two gravity columns and were not intended to carry any tributary gravity loads. During the design process, members were selected to maximize the utilization ratio and avoid overdesign.

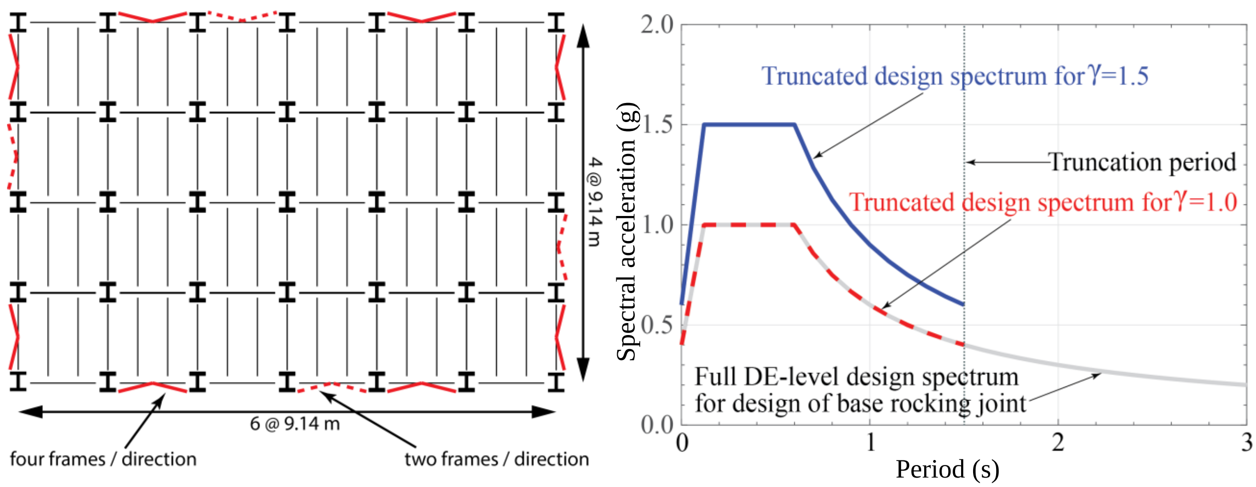

(a) (b)

Figure 3-2. (a) Floor plan of the CRBF buildings and (b) Elastic design spectra.

The design of CRBFs followed a two-step procedure by Wiebe and Christopoulos (2015). In the first step, the base rocking joints were designed with post-tensioning (PT) and energy dissipation (ED) to control over-rotation and limit displacements. The required base overturning moment resistance was determined using the equivalent lateral force approach (ASCE/SEI 7-16 2016) with different response modification factors (R) ranging from 5 to 12. Frictional energy dissipation elements were installed at the base of the CRBF columns to ensure self-centering behavior with a hysteretic ED ratio (β as described in Figure 3-1) of 0.9. The PT prestress was set at 50% of the ultimate stress of PT to ensure elastic behavior up to at least 2.5% base rotation.

The second step involved capacity designing all steel members to withstand the forces induced by rocking, including higher-mode forces. The steel frame members were designed using the dynamic capacity design procedure developed by Steele and Wiebe (Steele and Wiebe 2016). In this procedure, the design force of members is a combination of the resultant force from the code-prescribed lateral forces, multiplied by the system overstrength, and the higher-mode forces. These higher-mode forces are calculated using a spectrum that is truncated between the first- and second-mode periods and is amplified by a ratio γ (Figure 3-2 (b)). The design option for higher-mode forces was assessed by calculating them based on both the design earthquake (DE) intensity level (γ=1) and the maximum considered earthquake (MCE) intensity level (γ=1.5). A yield strength of 345 MPa was assumed for all CRBF steel members. Additionally, the design of the gusset plates between the braces and beam-column connections was performed based on the capacity of the braces. For each design option, Table 3-1 displays the design base shear (V), design base overturning moment ($M_{b,rock}$), initial post-tensioning force (PT_0), energy dissipation activation force (ED_{act}), the first fixed-base fundamental period (T), which is used to calculate the spectral demand, the tangent stiffness-based period of the structure while rocking (T_{rock}), and the second and third fixed-base periods (T_2, T_3). Also, Table 3-2 shows the section sizes of the CRBFs designed with γ=1.5. A12-story CRBF building with R=12 and γ=1 was not included in the study due to the estimation of a significant number of collapses at the MCE level intensity; further discussion regarding this will be presented in the subsequent sections.

Table 3-1. Design parameters for base rocking joints and model periods.

Stories	Design	V (kN)	$M_{b,rock}$ (kN-m)	PT_0 (kN)	ED_{act} (kN)	T (s)	T_{rock} (s)	T_2 (s)	T_3 (s)
3	R=5,γ=1.0	2683	26753	3249	1462	0.45	3.40	0.11	0.07
3	R=5,γ=1.5	2683	26753	3249	1462	0.42	3.38	0.10	0.06
3	R=8,γ=1.0	1678	16744	2033	915	0.50	4.04	0.14	0.09
3	R=8,γ=1.5	1677	16721	2031	914	0.44	4.02	0.12	0.08
3	R=12,γ=1.0	1118	11155	1355	610	0.52	4.76	0.15	0.10
3	R=12,γ=1.5	1118	11146	1354	609	0.46	4.74	0.13	0.09
6	R=5,γ=1.0	1706	33466	2032	1829	1.01	5.59	0.22	0.13
6	R=5,γ=1.5	1915	37268	2263	2037	0.91	5.41	0.20	0.11
6	R=8,γ=1.0	1012	19916	1209	1088	1.07	6.59	0.27	0.15
6	R=8,γ=1.5	1077	21108	1282	1153	0.97	6.46	0.24	0.14
6	R=12,γ=1.0	647	12769	775	698	1.11	7.78	0.30	0.17
6	R=12,γ=1.5	734	14368	872	785	0.98	7.41	0.26	0.14
12	R=5,γ=1.0	1926	77932	4732	4258	1.84	8.31	0.42	0.23
12	R=5,γ=1.5	2093	84029	5102	4592	1.70	8.04	0.36	0.19
12	R=8,γ=1.0	1015	41747	2535	2281	2.19	10.81	0.51	0.27
12	R=8,γ=1.5	1148	46641	2832	2549	1.94	10.26	0.42	0.23
12	R=12,γ=1.5	744	30331	1842	1658	1.99	12.40	0.44	0.23

Table 3-2. Section sizes of the CRBFs designed with γ=1.5.

	R=5			*R*=8			*R*=12		
Story	Column	Beam	Brace	Column	Beam	Brace	Column	Beam	Brace
3	W14X398	W14X176	W14X283	W14X283	W14X159	W14X176	W14X233	W14X120	W14X120
2	W14X398	W14X176	W14X145	W14X283	W14X159	W14X120	W14X233	W14X120	W14X99
1	W14X398	W14X176	W14X193	W14X283	W14X159	W14X159	W14X233	W14X120	W12X152
6	W14X233	W12X106	W10X100	W14X145	W12X72	W10X77	W14X120	W10X77	W10X60
5	W14X233	W12X106	W12X96	W14X145	W12X72	W12X72	W14X120	W10X77	W14X74
4	W14X233	W12X106	W12X106	W14X145	W12X72	W12X72	W14X120	W10X77	W10X68
3	W14X426	W12X152	W12X120	W14X283	W12X106	W12X79	W14X233	W12X87	W10X77
2	W14X426	W12X152	W14X120	W14X283	W12X106	W12X96	W14X233	W12X87	W12X79
1	W14X426	W12X152	W14X132	W14X283	W12X106	W14X90	W14X233	W12X87	W12X87
12	W14X120	W21X147	W12X65	W14X109	W21X122	W12X58	W14X109	W21X122	W12X58
11	W14X120	W21X147	W12X106	W14X109	W21X122	W12X87	W14X109	W21X122	W12X87
10	W14X120	W21X147	W12X136	W14X109	W21X122	W12X120	W14X109	W21X122	W12X106
9	W14X426	W27X146	W12X152	W14X342	W21X132	W12X120	W14X342	W21X122	W12X120
8	W14X426	W27X146	W14X145	W14X342	W21X132	W14X109	W14X342	W21X122	W14X99
7	W14X426	W27X146	W12X152	W14X342	W21X132	W12X120	W14X342	W21X122	W12X106
6	W14X605	W21X201	W14X132	W14X455	W21X132	W12X96	W14X426	W21X122	W12X87
5	W14X605	W21X201	W14X145	W14X455	W21X132	W12X106	W14X426	W21X122	W12X96
4	W14X605	W21X201	W14X159	W14X455	W21X132	W14X109	W14X426	W21X122	W14X99
3	W14X730	W24X229	W14X176	W14X500	W21X182	W14X132	W14X455	W21X182	W14X120
2	W14X730	W24X229	W14X193	W14X500	W21X182	W14X145	W14X455	W21X182	W14X145
1	W14X730	W24X229	W14X193	W14X500	W21X182	W14X145	W14X455	W21X182	W14X145

3.4 SEISMIC HAZARD AND GROUND MOTION SELECTION

The Los Angeles Bulk Mail Center, situated at 33.996°N and 118.162°W, was chosen to represent the site conditions of the archetype buildings. Seismic hazard curves for this site were obtained from the USGS website (https://earthquake.usgs.gov/hazards/interactive/, last accessed on 17 October 2022). For the time-history analyses, the suite of far-field ground motion records recommended by FEMA P695 (FEMA P695 2009) was used. The selected ground motions were scaled to minimize geometric mean differences between the MCE spectrum and the median acceleration spectrum of the records, considering a range spanning from 0.2 times to 2.0 times the first fundamental period of each CRBF building design option. Figure 3-3 displays the scaled records for the six-story CRBF building with R = 5 and γ=1, alongside the suite's median and the MCE spectrum. The performance of each building was assessed using multiple-stripe analysis (MSA) (Baker 2015), incorporating six different intensity stripes: 1/4, 1/2, and 1 times the DE, and 1, 1.5, and 2 times the MCE.

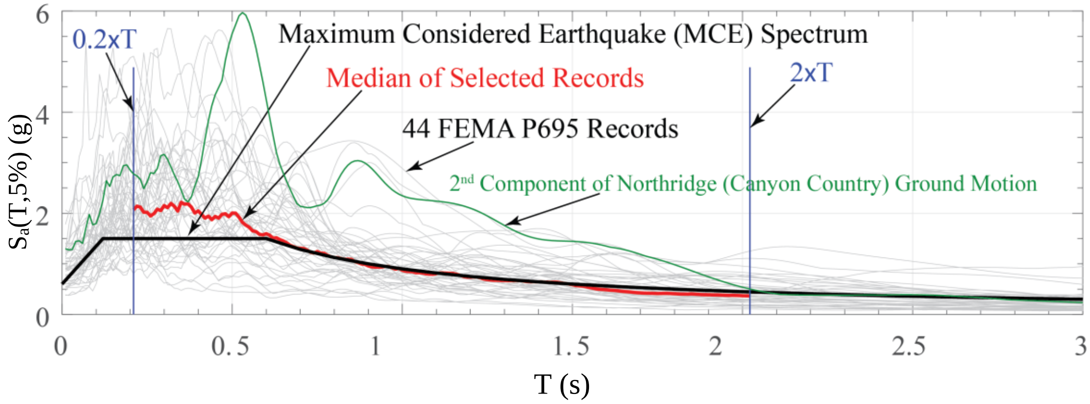

Figure 3-3. Scaling of the selected suite of ground motions for the six-story CRBF with R = 5 and γ=1.

3.5 Structural modelling

OpenSees (McKenna, Fenves, and Scott 2000) was used to model the CRBF buildings, using three dimensions to capture out-of-plane buckling about the braces' weak axes. Figure 3-4 shows a schematic of the numerical model developed for the three-story CRBFs, which followed the recommendations by Steele and Wiebe (2021). Gap elements were introduced in both the vertical direction, to allow the CRBFs to uplift due to rocking, and the horizontal direction, to transfer the base shear to the rigid foundation. The gap elements were modeled with much larger larger stiffness than the first-story column's axial stiffness. In addition, they were modeled in parallel with an elastic spring of negligible stiffness, to enhance the numerical stability of the models.

Each frame member was represented using six fiber nonlinear beam-column sub-elements, with ten integration points each and an initial geometric imperfection of L/1000. The material properties were defined according to the Steel02 model, and a low cycle fatigue model was used for each fiber (Uriz and Mahin 2004; Uriz and Mahin 2008). Furthermore, the influence of gusset plates at the brace ends was taken into account using fiber nonlinear beam-column elements (Uriz and Mahin 2008). To model the frictional energy dissipation, truss elements with an elastic-perfectly plastic material model were employed, with the yield force set to equal the specified ED_{act}. PT was included as co-rotational truss elements using a multi-linear material model and an initial stress material with a force equal to the defined PT_0, following a model similar to that proposed by Ma et al. (2010), where a maximum strain of 1.3% was allowed before the first wire fractures, and a gradual decrease in the PT force until complete fracture at a strain of 4.8%. To prevent the PT from developing compression, hook elements were introduced in series with the PT elements.

A leaning column was added to account for P-Delta effects from the building's gravity frames, and inherent damping was modeled using 2.5% Rayleigh damping. To avoid artificial damping during structural yielding, stiffness proportional damping was considered with 20% of the initial-stiffness matrix and 80% of the committed tangent-stiffness matrix (Charney 2008; Steele and Wiebe 2017).

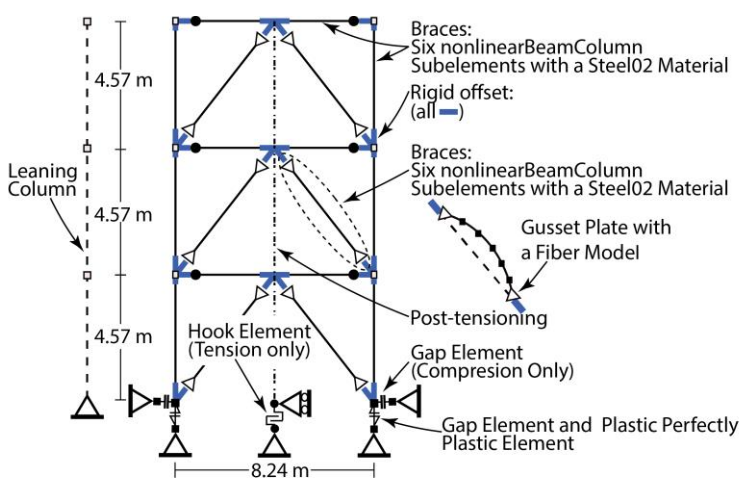

Figure 3-4. Schematic of the numerical model for the three-story CRBF

3.6 CONSTRUCTION COST AND LOSS ASSESSMENT

Past real-world projects, such as the Casa Adelante nine-story housing project that incorporated a rocking slab and self-centering cable anchorage, have incurred only a marginal additional construction cost of 0.24% compared to conventionally designed buildings (Aher, Mar, and Rodgers 2020). Hence, in this chapter, the replacement cost for CRBF buildings was estimated based on a small cost premium of 2% over special concentrically braced frame buildings, for which the replacement cost was estimated at \$1884 per m^2 (Hwang and Lignos 2017a) based on 2013 U.S. dollars. These replacement costs were considered both for building collapse and for demolition due to excessive residual drifts. As the additional cost of CRBFs in terms of construction expenses is expected to be marginal compared to conventional seismic force resisting frames, this study did not consider the additional differences in costs between different design options associated with factors such as the amount of CRBF steel, size of frictional energy dissipation devices, or amount of post-tensioning. The demolition loss assessment was based on the maximum residual story drift ratio from all stories, using a lognormal distribution defined by a median of 0.015 radians and a logarithmic standard deviation of 0.3, similar to the approach used by Ramirez and Miranda (Ramirez and Miranda 2012).

To calculate earthquake-induced losses for the designed CRBF buildings following the FEMA P58-1 probabilistic loss estimating methodology (FEMA P-58-1 2018), damage fragility functions and repair cost consequence functions for both structural and nonstructural components were required. To assess seismic losses related to structural components, damage fragility functions and repair cost consequence functions were taken from the FEMA P-58-3 (2018) library. These structural components were categorized into two groups based on cost: per-connection and per-bay basis. The considered structural components and their quantities for three-story CRBF buildings are presented in Table 3-3. The appended letter or number at the end of the group components' IDs signifies the specific component size within each group, depending on the size of the structural elements.

For the repair cost on a per-connection basis, group components with IDs B1031.011 and B1031.021 were used to represent the steel column base plates and welded column splices, respectively. To represent the steel braces of CRBFs, special chevron braced frames with wide flange braces designed with balanced design criteria (B1033.001) were employed. Since the inter-story drift of CRBF buildings comprises both a rigid body deformation arising from the rocking behavior and an additional deformation of the frame itself, the engineering demand parameter (EDP) for the B1033.001 component group was modified to use the maximum compression deformation of the braces instead of the inter-story drift (Banihashemi and Wiebe 2022). Furthermore, if the PT strain surpassed the yield strain of 0.83% (Ma, Krawinkler, and Deierlein 2010), it was assumed that replacing the PT strands would be necessary. The estimated cost for this replacement is $8 per kilogram (kg) of steel strands (DYWIDAG Systems International 2020), in 2020 U.S. dollars. Additionally, it was assumed that the frictional energy dissipation elements in the CRBFs were designed with a substantial displacement capacity, ensuring they would not fail or be damaged before the buildings' collapse. Table 3-3 provides a comprehensive list of 21 nonstructural components, including both acceleration-sensitive and drift-sensitive ones, that were considered for the seismic loss assessment. These components were allocated to each floor of the three-story building, and the same set of nonstructural components and quantities were applied to the six- and 12-story buildings, with slight variations in quantities for some components based on the building's height. The damage fragility functions utilized in the study were primarily adopted from FEMA P58-3 (FEMA P-58-3 2018), supplemented by other relevant nonstructural research findings as indicated in Table 3-3. To assess losses attributed to nonstructural components, repair cost consequence functions provided by FEMA P58-3 were employed.

For cost comparisons, the year 2011 was chosen as the reference year in the FEMA P58-3 consequence functions. Therefore, any projected costs beyond 2011 were adjusted to their 2011-equivalent values using data from the RSMeans historical cost index (RSMeans 2020). The seismic loss analyses were conducted using the Pelicun software (Zsarnóczay 2019), which is based on the FEMA P58 methodology, developed by the Computational Modelling and Simulation Center (SimCenter).

3.7 STRUCTURAL PERFORMANCE

3.7.1 PUSHOVER RESPONSE

Figure 3-5 displays the pushover curves for all designed CRBFs. The pushover analyses were conducted using the same code-prescribed lateral force distributions that were employed in designing the base rocking joints. For each height, the lateral strengths of different design options are normalized by the linear limit of the design option with R=8 and γ=1, and plotted against the roof drift (i.e., roof displacement divided by building height). For the three-story CRBFs, the structures with lower resistance to rocking (i.e., using larger R) not only initiate rocking under lower uplift loads but also exhibit reduced secondary stiffness and energy dissipated per cycle (the latter is not shown in Figure 3-5). The final branch of the pushover curves corresponds to PT yield and first-wire fracture. As the roof displacement increases, the resistance of the frames with lower design base overturning moment reduces at a similar rate starting from a smaller initial value, ultimately leading to a complete loss of lateral resistance at a smaller roof drift. These results are in agreement with the findings presented by Steele and

Wiebe (2017). For the three-story CRBFs designed with the same R but different γ values, the differences in pushover curves are negligible when using higher-mode forces at the DE or MCE levels. Similar overall results are observed for taller CRBFs as for three-story CRBFs, except that the lateral resistance in all branches of the pushover curves for the CRBFs designed with a given R are reduced when higher-mode forces are computed at the DE level because this makes the frame more flexible, leading to a lower design base shear.

Table 3-3. Summary of considered structural and nonstructural components for the 3-story CRBF buildings.

Component description	Component iD+	EDP	Source of damage fragility function	Quantity	Unit	Location
Column base plates (223 < column weight < 446 kg/m)	B1031.011b	SDR	FEMA P-58-3 (2018)	4	EA	Base Floor
Wide flange brace (brace weight > 148 kg/m)	B1033.001c	SDR	FEMA P58-3	2	EA	Story 1-3
Post-tensioning strands	-	Yield strain	-	479 (kg)	-	-
Curtain wall	B2022.002	SDR	Behr (2001)	217	3 m^2	Each story
Wall partition (Gypsum with metal studs)	C1011.001c	SDR	Retamales et al. (2013)	22	30 m	Each story
Wall partition (Gypsum + wallpaper)	C3011.001c	SDR	FEMA P58-3	2	30 m	Each story
Stair	C2011.021a	SDR	Bull (2011)	3	EA	Each story
Raised access floor	C3027.002	PFA	FEMA P58-3	163	9 m^2	Each floor
Suspended ceiling	C3032.004b	PFA	FEMA P58-3	33	56 m^2	Each floor
Pendant lighting	C3034.002	PFA	FEMA P58-3	325	EA	Each floor
Cold or hot potable piping (small diam.)	D2021.014b	PFA	FEMA P58-3	1	305 m	Each floor
Cold or hot potable piping (large diam.)	D2021.024b	PFA	FEMA P58-3	2	305 m	Each floor
Sanitary piping	D2031.023b	PFA	FEMA P58-3	2	305 m	Each floor
Small HVAC duct	D3041.011c	PFA	FEMA P58-3	2	305 m	Each floor
Fire sprinkler water piping	D4011.023a	PFA	Soroushian et al. (2015)	5	305 m	Each floor
Large HVAC duct	D3041.012d	PFA	FEMA P58-3	1	305 m	Each floor
HVAC diffuser	D3041.032d	PFA	FEMA P58-3	20	10 EA	Each floor
Variable air volume box	D3041.041b	PFA	FEMA P58-3	5	10 EA	Each floor
Low voltage switchgear (400 Amp)	D5012.023e	PFA	FEMA P58-3	1	EA	Each floor
Chiller (500 ton)	D3031.013h	PFA	FEMA P58-3	1*	EA	Roof
Cooling tower (500 ton)	D3031.023h	PFA	FEMA P58-3	1*	EA	Roof
Air handling unit (30000 CFM)	D3052.013k	PFA	FEMA P58-3	2*	EA	Roof
Motor control center	D5012.013c	PFA	FEMA P58-3	3*	EA	Roof
Elevator	D1014.011	PGA	FEMA P58-3	2*	EA	Ground

Note: Amp= Ampere; CFM=Cubic feet per minute; EA=Each; HVAC=Heating, ventilation, and air conditioning; PFA = Peak floor acceleration (g); PGA = Peak ground acceleration (g); SDR= Story drift ratio.
+ In accordance with FEMA P58-3 library.
* The number of floors affects the number of components.

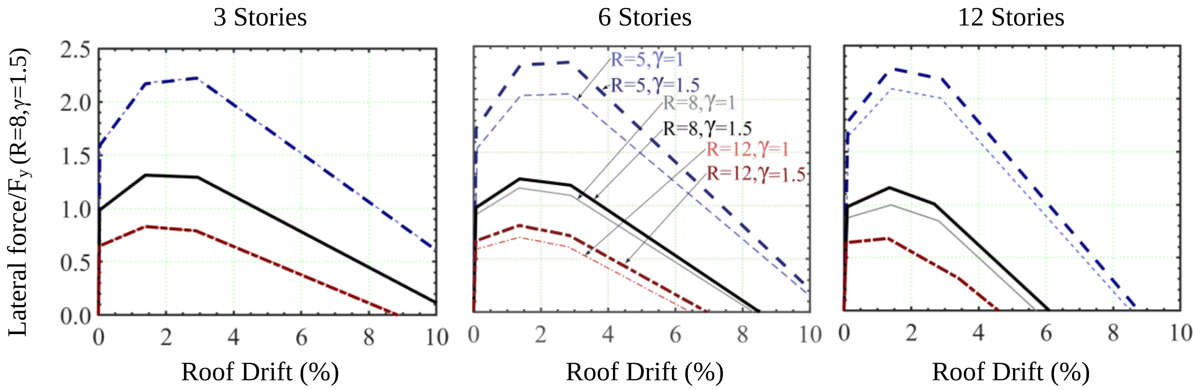

Figure 3-5. Monotonic pushover curves for different design options.

3.7.2 Response to a single ground motion

Figure 3-6 displays the response history of roof drift, roof acceleration, and column uplift for the three-story CRBFs with three design options, including the strongest design (R=5 and γ=1.5), weakest design (R=12 and γ=1), and an intermediate option with R=8 and γ=1.5. The input acceleration used in the analysis is the second component of the Northridge (Canyon Country) ground motion at the DE level, where its acceleration spectrum is shown in Figure 3-3. For this scaled ground motion, all three design options experience a roof drift larger than 1% between 7 s and 14 s with no residual drift. The strongest design option produces the lowest uplift, and the weakest design option produces the largest uplift, resulting in the smallest and largest roof drifts, respectively. However, the roof acceleration is highest for the strongest design and lowest for the weakest design. Additionally, the three examined CRBFs exhibit high frequency acceleration spikes upon column impact and uplift, which is unlike the findings of prior investigations (Buccella et al. 2021; Wiebe et al. 2013). Higher mode effects also appear to have an impact on these peaks, similar to those described by Buccella et al. (2021).

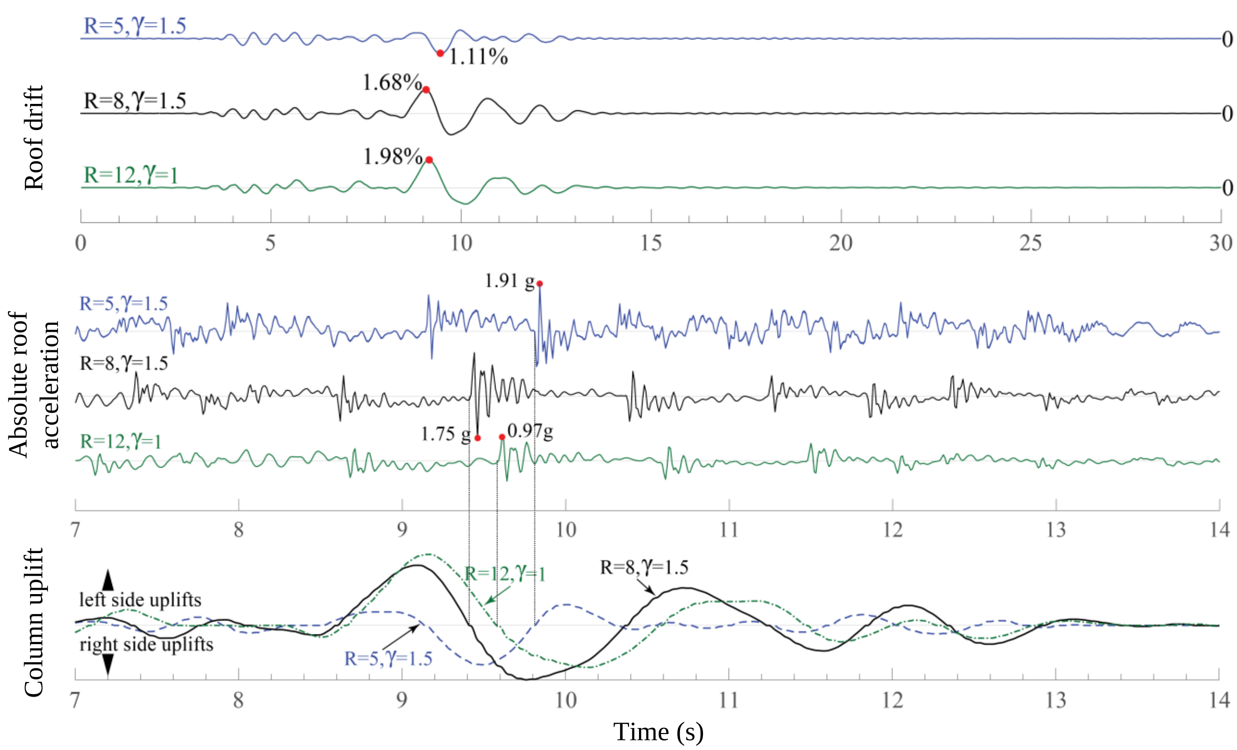

Figure 3-6. Three-story CRBF buildings: roof drift, roof acceleration, and column uplift during the second component of the Northridge (Canyon Country) ground motion at the DE level.

3.7.3 RESPONSE TO SUITE OF GROUND MOTIONS

Figure 3-7 shows the median of peak story drift ratios (SDRs) and peak floor accelerations (PFAs) at the DE level for all the designed CRBFs. For the three-story CRBF buildings, similar to what was seen for the single ground motion, increasing the resistance to rocking (i.e., using lower *R*) causes the SDRs to decrease. However, using lower *R* (i.e., more resistance to rocking) in the design also leads to larger PFAs. Furthermore, among the three-story buildings designed with the same *R*, those designed with larger steel framing to resist the higher-mode forces at the MCE intensity (i.e., using γ=1.5) exhibit lower SDRs than those designed for the DE intensity. However, buildings designed with the same *R* but different γ also exhibit slightly different PFAs, with larger PFAs in the buildings that used the higher-mode forces at the MCE intensity for design.

Similar results are observed for taller structures. However, the differences in PFAs for the various design options become less pronounced in taller CRBF buildings. Also, while the story drift ratios remain nearly uniform throughout the height of the buildings, indicating the dominance of the rocking mode in the displacements of the CRBFs (Buccella et al. 2021), they become less uniform for taller buildings.

The residual story drift ratios are not shown because they are always less than 0.2% for all designed CRBF buildings, with most being less than 0.1%.

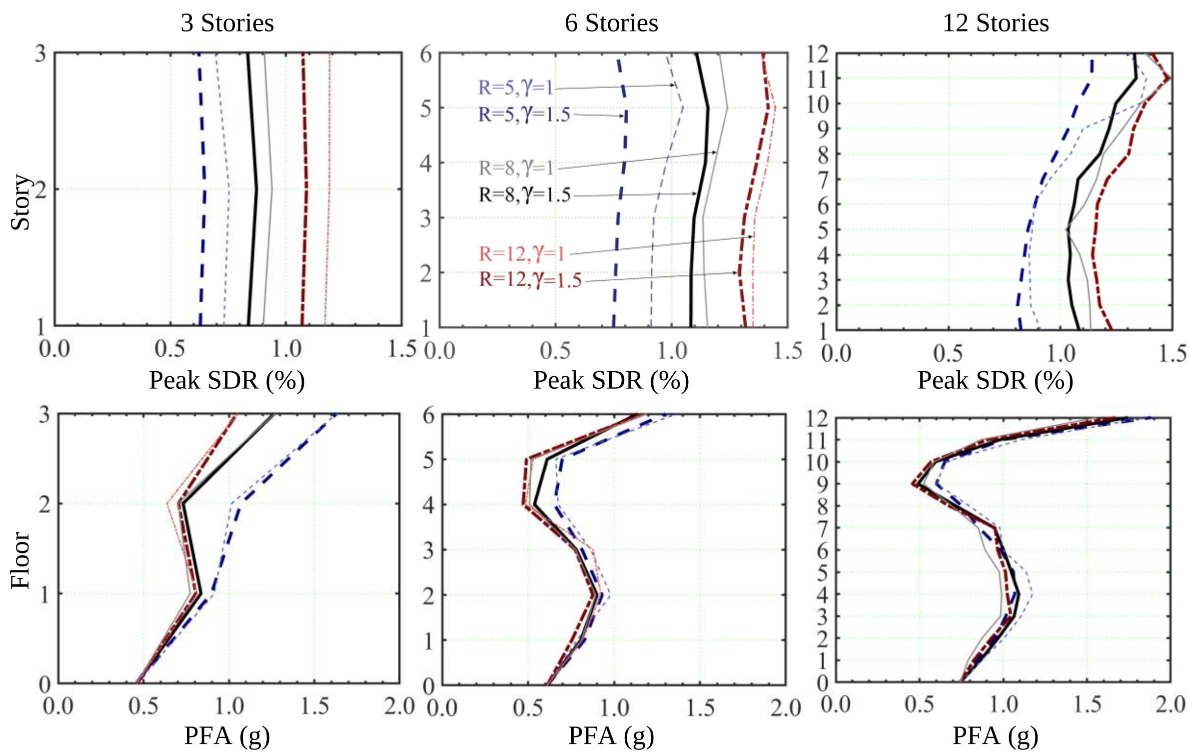

Figure 3-7. Median values of peak story drift ratio (SDR) and peak floor acceleration (PFA) at the DE level.

Table 3-4 shows the number of collapses out of 44 FEMA P695 ground motions for each design option at the intensity levels of MCE, 1.5 MCE, and 2 MCE. In this chapter, collapse is assumed if any SDR exceeds 10%. None of the designed three-story CRBF buildings collapse at the MCE intensity. The three-story buildings designed with *R*=5 demonstrate a very high collapse capacity as they withstand even the ground motions scaled to 2MCE intensity level without any instances of collapse. While the probability of collapse is generally low, the results for all three building heights consistently demonstrate that the number of collapses increases as the CRBFs are made less resistant to rocking (i.e., using larger *R*). Moreover, when comparing buildings designed with the same *R* but different γ, those designed with the higher-mode forces at the DE intensity (i.e. γ=1) exhibit a greater number of collapses than those designed with the higher-mode forces at the MCE intensity (i.e. γ=1.5). The higher mode effects in six- and twelve-story buildings result in certain design options having a collapse probability of more than 10% at the MCE level. For instance, in the case of the twelve-story building designed with *R*=12, even when the building is designed considering the higher mode effects at the MCE level (i.e., γ=1.5), the number of collapses exceeds a 10% collapse probability. This finding differs from the conclusions drawn by Steele and Wiebe (2021), primarily due to a more conservative approach to modeling damping and scaling ground motions in this study.

Table 3-4. Number of collapses out of 44 FEMA P695 ground motions.

Stories	*R*	γ=1			γ=1.5		
		MCE	1.5MCE	2MCE	MCE	1.5MCE	2MCE
3	5	0	0	0	0	0	0
	8	0	0	7	0	0	3
	12	0	6	9	0	5	8
6	5	0	0	4	0	0	2
	8	0	5	17	0	3	10
	12	5	13	26	3	8	19
12	5	1	6	9	0	2	7
	8	3	10	18	1	7	15
	12	-	-	-	6	11	19

3.7.4 Floor acceleration spectra

Figure 3-8 compares the median floor acceleration spectra for all designs at the DE intensity level. For the three-story CRBFs, the spectral peaks are observed at the natural periods of each structure. The peaks mostly occur near the second and third periods and are less apparent at the first period of the structures. These peaks can reach up to 4 g, which is two or three times the

PFAs. The acceleration spectra of structures with higher resistance to rocking (i.e., using lower *R*) are generally slightly greater than the spectra of those with lower resistance to rocking. Also, no significant differences can be observed for buildings designed with the same *R* but different *γ*, except that the peaks occur at slightly different periods due to the varying natural periods with different design options. The same conclusions are observed for taller CRBFs. These differences in the acceleration spectra underscore the importance of taking into account the acceleration spectrum when assessing the potential for damage to acceleration-sensitive nonstructural components, as PFAs cannot reflect the differences in acceleration spectra. However, this issue is not addressed further in this chapter because the damage fragility curves for acceleration-sensitive nonstructural components are currently defined based on PFA in FEMA P-58-3 (2018).

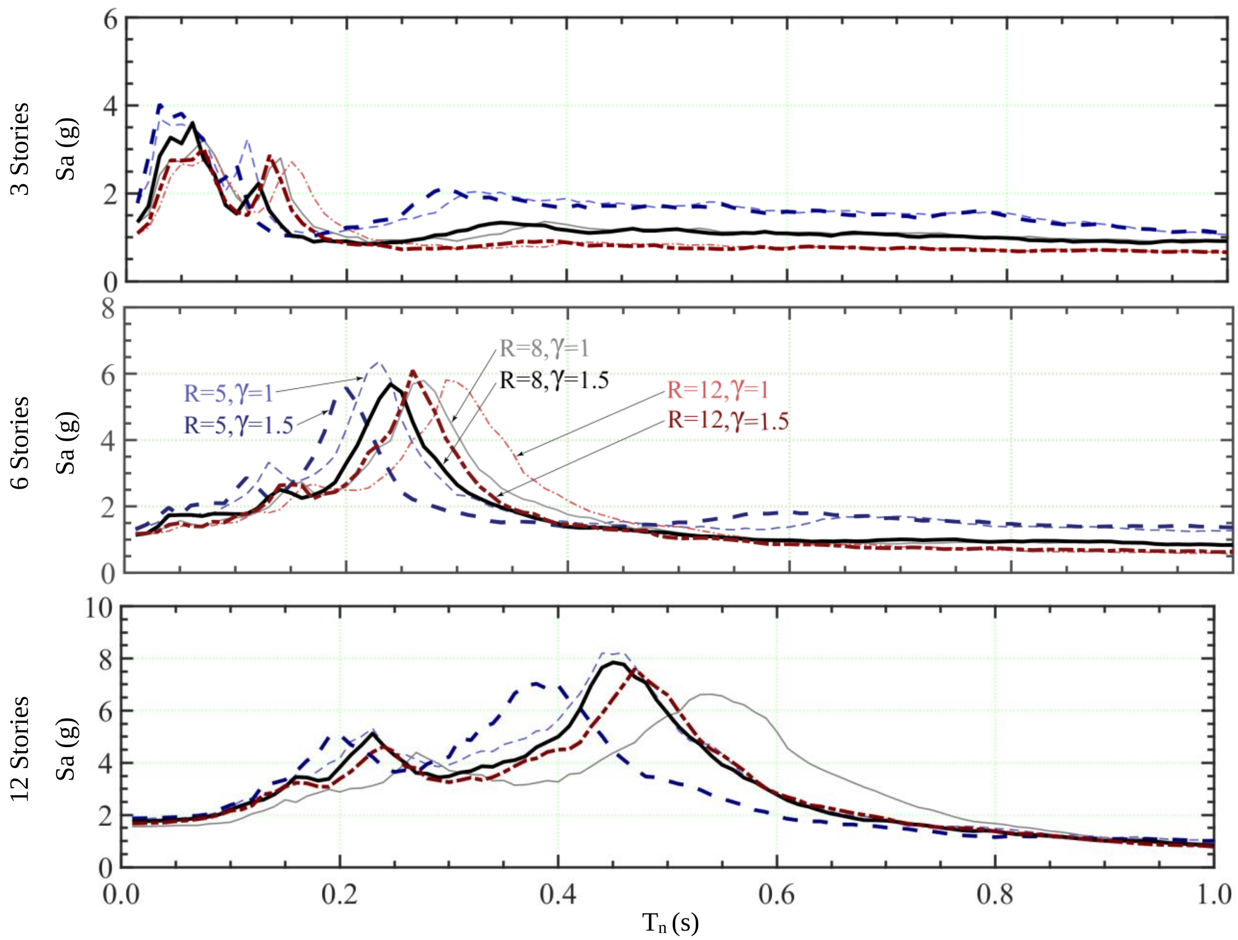

Figure 3-8. Median floor acceleration spectra with 5% damping at DE intensity level.

3.8 Seismic Intensity-based Expected Losses

This section evaluates the design options for the CRBF buildings in terms of earthquake-induced losses. Figure 3-9 compares the total expected losses of various design options for all building heights at the seismic intensity levels of DE and MCE. The losses for each building height are normalized with respect to the construction cost of the building. Additionally, the total expected losses are subdivided into losses attributed to drift-sensitive and acceleration-sensitive nonstructural components, structural repair and demolition losses, as well as losses due to building collapse.

For the three-story CRBF buildings, the results of losses resulting from different sources at the DE and MCE intensity levels are only slightly different across different options. The total normalized expected losses are less than 10% at the DE intensity level, with losses due to acceleration-sensitive nonstructural components being the main contributor, while losses due to structural repair or to irreparable loss, including collapse and demolition loss, have a negligible contribution. At the DE intensity level, losses due to acceleration-sensitive components increase as the CRBF is made more resistant to rocking (i.e., using lower R). This is because the acceleration demand increases in design options with lower R (see Figure 3-7), especially the acceleration on the roof. Conversely, losses due to drift-sensitive nonstructural components increase slightly for design options with less resistance to rocking. However, due to the dominance of acceleration-sensitive loss, the total normalized expected loss decreases slightly by increasing R at the DE intensity level. Regarding design options with the same R but different γ, the expected losses are similar when the CRBFs are designed with higher-mode forces at the DE or MCE intensity levels. Similar trends are also observed for normalized expected losses at the MCE level, but the total losses are higher at about 12% of the building replacement cost.

Moreover, at the MCE intensity level, the contribution of losses due to drift-sensitive components becomes more pronounced when the CRBF has lower resistance to rocking (i.e., using larger *R*), leading to very similar total normalized expected losses regardless of the value of *R*.

For the six-story CRBF buildings, the total normalized expected losses are less than 10% at the DE intensity level and less than 25% at the MCE intensity level, with variations in losses from different sources becoming prominent when comparing different options at the MCE level. Similar trends observed in the three-story CRBF buildings can also be observed with regard to losses due to acceleration-sensitive and drift-sensitive components in different design options of the six-story CRBF building. However, as the CRBF is made less resistant to rocking (i.e., using larger *R*), the contribution of irreparable loss becomes more pronounced, leading to an increase in the total loss. Also, at the MCE intensity level, the design options with the same *R* but including the higher-mode forces at the DE intensity for design (i.e. using $\gamma = 1$) exhibit larger total normalized expected losses, primarily due to the larger contribution of irreparable losses. Although the median RSDR is small at the MCE level intensity, with a maximum of 0.2% for the design option of R=12 and γ=1, a 5% expected loss due to demolition is still observed for this specific design option. This is due to the application of the FEMA P58 Monte Carlo-based methodology (FEMA P-58-1 2018), which employs the Yang et al. algorithm (Yang et al. 2006; Yang et al. 2009) to generate demand sets in each realization and account for uncertainties. As a result, the algorithm produces a distribution with a longer tail than the original data set.

For the 12-story CRBF buildings, while similar trends are observed as for the six-story buildings, the effect of irreparable loss is more accentuated. Overall, the losses attributed to various sources of repairable damage are similar across different options, but differences in the losses due to collapse or demolition drive the variations in total seismic losses. Most notably, the design options with the same *R* but γ=1 exhibit larger total normalized expected losses compared to those with γ=1.5, primarily due to the larger contribution of irreparable losses.

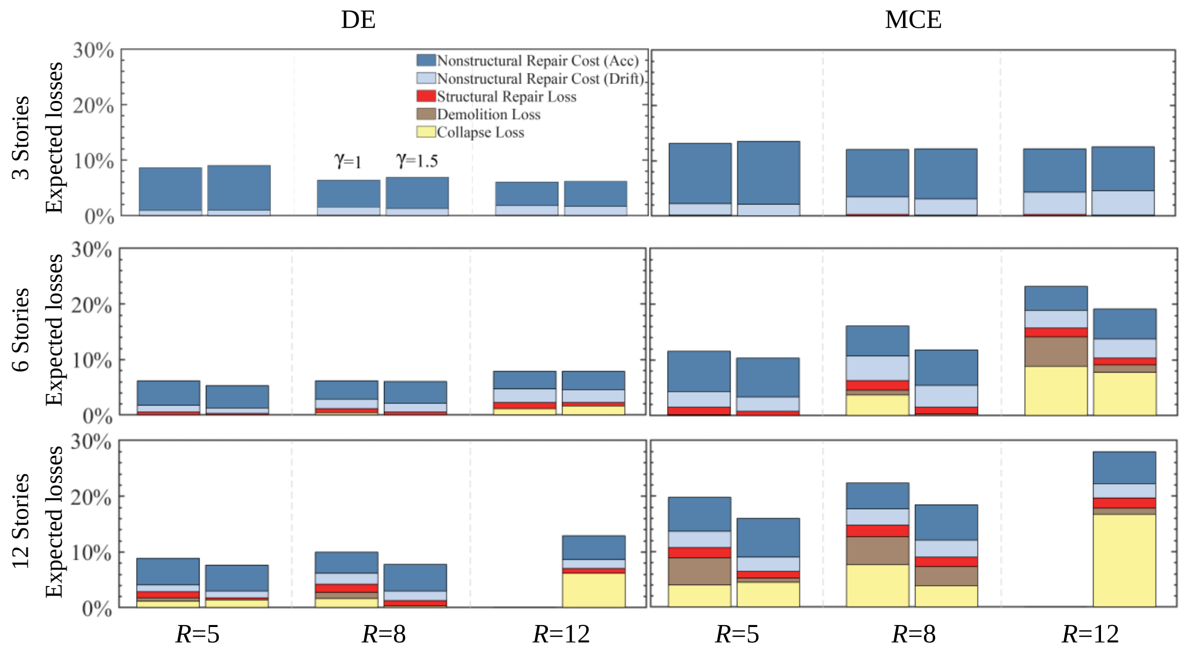

Figure 3-9. Expected losses (normalized to the construction cost for each building height) at two seismic intensities.

3.9 EXPECTED ANNUAL LOSSES

The expected annual loss (EAL), which is an estimate of the expected average annual cost of repairing earthquake damage, is used in this section to compare the CRBFs with different design options. The EAL is calculated by evaluating the area under the distribution curve of mean annual total repair cost (FEMA P-58-1 2018). To construct this curve for each designed building, time-based assessments were conducted in accordance with FEMA P58-1 guidelines. The procedure involved multiplying the cumulative probability distribution of total loss at each intensity, obtained using Pelicun software (Zsarnóczay 2019), by the annual frequency of occurrence within the corresponding intensity interval. The annual frequencies for a given loss level were then aggregated across all intensity-based loss curves. This comprehensive approach accounts for all seismic hazard levels and considered uncertainties provided in the FEMA P58-3 library, including damage fragility functions and repair cost consequence functions. Figure 3-10 depicts the computed expected annual losses (EALs) of the designed CRBFs for each building height, normalized by their construction cost.

Among the three-story CRBF buildings, although the contributions of irreparable loss and structural repair loss increase for the CRBFs with lower resistance to rocking (i.e. using larger R), their impact on the total expected loss remains negligible. The results show the three-story CRBFs with lower resistance to rocking (i.e., using larger R) experience increased losses related to drift-sensitive nonstructural components, while also resulting in a decrease in losses associated with acceleration-sensitive nonstructural components. In the three-story CRBF buildings, the loss due to acceleration-sensitive nonstructural components dominates the overall losses, resulting in CRBFs designed with larger R having lower total normalized expected annual loss. A comparison of three-story CRBF buildings designed with the same R but different γ values reveals that those including the higher-mode forces at the DE intensity for design (i.e. using $\gamma = 1$) exhibit slightly lower total normalized expected loss, primarily due to lower losses related to acceleration-sensitive nonstructural components.

For the six-story CRBF buildings, the contribution of collapse-related losses becomes more pronounced when the six-story CRBF buildings are less resistant to rocking. The losses due to demolition and structural damage also show a slight increase compared to those for three-story CRBFs. In addition, similar trends to those observed in three-story buildings are also apparent in six-story CRBFs, where the buildings with more resistance to rocking experience reduced losses due to drift-sensitive nonstructural components, while losses due to acceleration-sensitive nonstructural components increase. However, the contribution of acceleration-sensitive nonstructural components is less significant in the total annualized expected loss for six-story buildings relative to the three-story CRBFs. As such, the total expected annual loss reduces as *R* reduces for six-story CRBFs. Comparing six-story CRBF buildings designed with the same *R* but different γ reveals that those designed with the higher-mode forces at the DE intensity (i.e. using γ = 1) have larger total normalized expected losses due to a larger contribution of irreparable losses. Similar trends as explained for the six-story CRBFs can also be observed in the case of the 12-story CRBF buildings, but with a greater contribution from demolition and collapse losses.

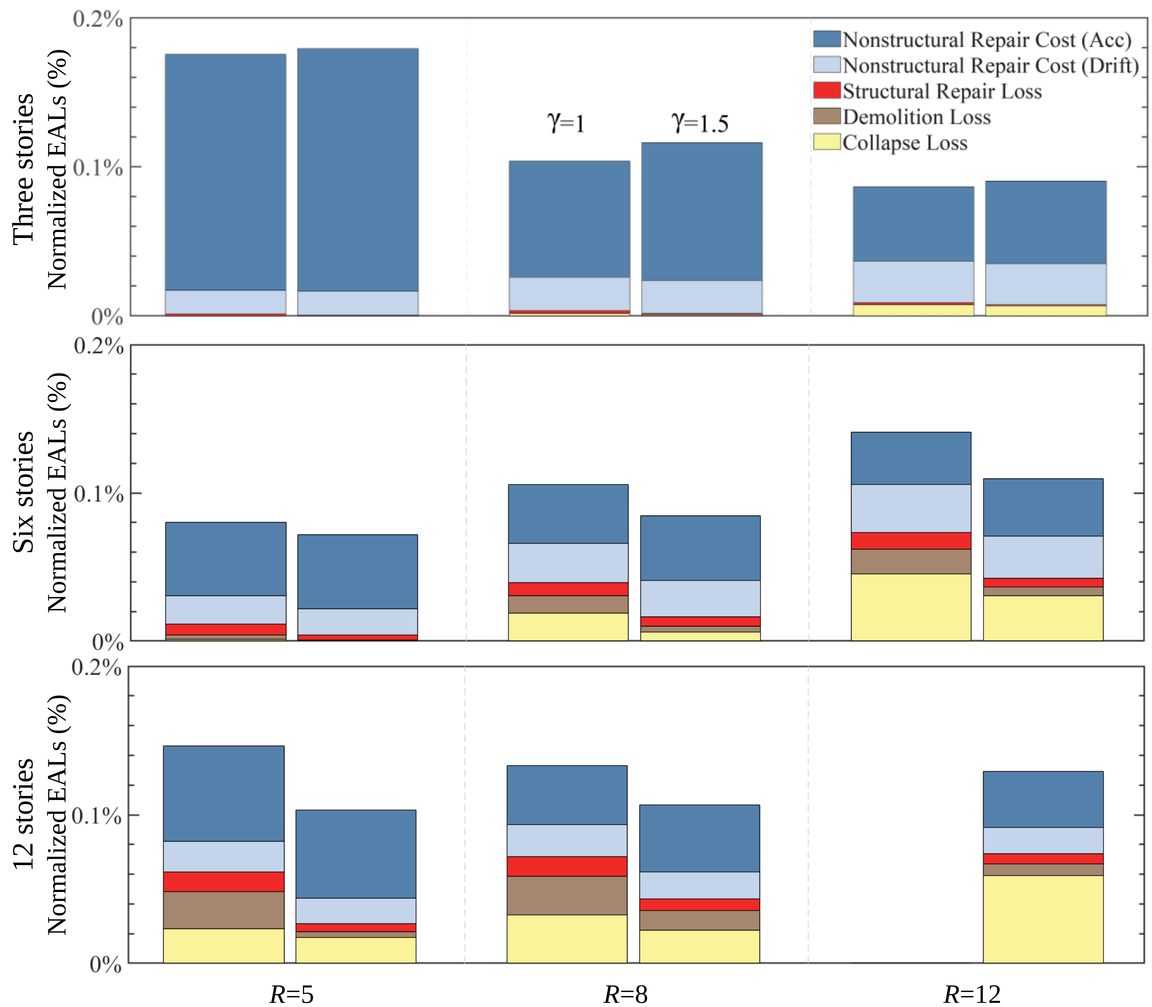

Figure 3-10. Expected annual losses (EALs) of the CRBF buildings normalized by thier construction cost.

3.9.1 Contribution of individual nonstructural components

Figure 3-11 illustrates the contributions to expected annual losses from the five most significant nonstructural components, which collectively constitute over 70% of the total nonstructural component losses that were presented in Figure 3-10 for all options.

Depending on the value of *R* used to design the three-story CRBF buildings, the first five nonstructural components with more than 70% contribution can vary. As depicted in Figure 3-11, the first five nonstructural components in three-story CRBF buildings designed with *R*=5 (i.e. more resistance to rocking) are exclusively acceleration-sensitive components, which aligns with the dominant loss contribution observed for such buildings in Figure 3-7. However, chiller, pendant lighting, and elevator are consistently identified as primary loss contributors regardless of the design options. The single chiller on the roof of each three-story building significantly contributes to the total losses due to its modest 0.72 g median acceleration capacity and high repair costs exceeding $280,000. Pendant lighting, with over 300 installations on each ceiling of every story, contributes significantly to the total losses despite its relatively high median acceleration capacity of 1.5 g and inexpensive unit repair cost. Despite the use of peak ground acceleration (PGA) in the damage fragility curve of the elevator and its response not being affected by the CRBF design, the elevator still makes a significant contribution to the losses due to its high unit repair cost and having a single damage state with a median acceleration capacity of only 0.39 g. When three-story CRBF buildings are designed with *R* greater than 5, the contribution from drift-sensitive nonstructural components, such as curtain walls and partition walls with metal studs, increases. The damage to wall partitions constitutes a large contribution to the overall losses due to their limited capacity compared to the buildings' story drifts. For instance, moderate cracking is expected at median inter-story drift ratios of 0.7%, which is smaller than the median demands of almost all floors in most of three-story CRBF buildings designed with various options at the DE level (Figure 3-7).

In the six-story and 12-story buildings, the contribution of loss due to the chiller is less pronounced than in the three-story buildings. Additionally, the larger story drifts in the six-story and 12-story CRBF buildings compared to the three-story CRBF buildings, as evident in Figure 3-7, result in a larger contribution of wall partitions to the total losses. Otherwise, the trends observed in the three-story CRBF buildings designed with *R* greater than 5 are also evident for the nonstructural components installed in the taller CRBF buildings.

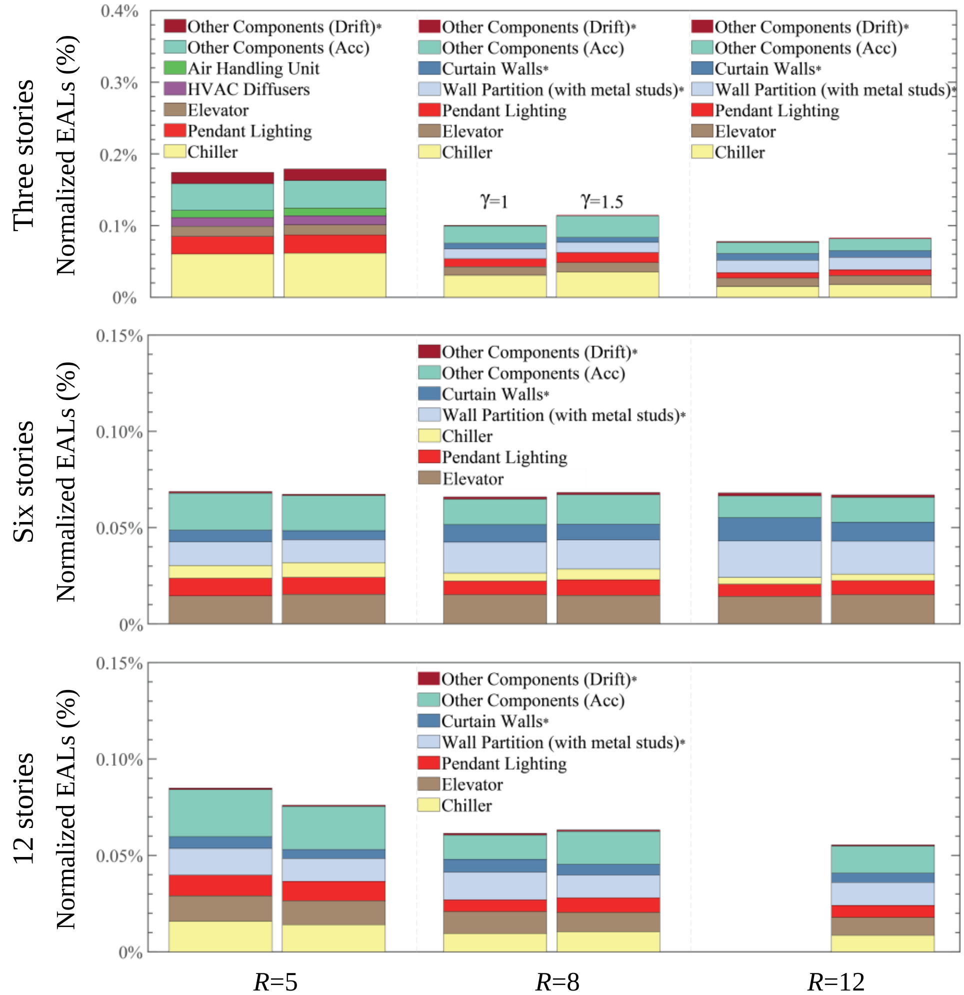

Figure 3-11. Nonstructural components with the greatest contributions to the total expected annual losses (EALs); Drift-sensitive nonstructural components are distinguished with an asterisk, while all others are acceleration-sensitive nonstructural components.

3.10 CONCLUSIONS

The present study assessed the impact of design parameters on CRBF buildings of three different heights (three, six, and 12 stories), with a particular emphasis on their expected seismic loss. It specifically investigated the following two design parameters: (i) the response modification factor (R) used in the equivalent lateral force approach for designing the base rocking joints, and (ii) the amplification factor (γ) that is applied to calculate higher-mode forces that are then integrated with equivalent lateral forces for the design of steel frame members. In this study, each CRBF building height was designed using several design options, considering different values of R ranging from 5 to 12, as well as higher-mode forces that were amplified based on two target intensity levels: the design earthquake (DE) and the maximum considered earthquake (MCE). The structural performance of the various design options for CRBFs was compared through pushover analysis, response history nonlinear analysis, and floor acceleration spectra. Then, using the FEMA P58 methodology (FEMA P-58-1 2018), the structural performance characteristics of each design option were translated into economic costs, employing the expected annual loss (EAL) metric. This approach allowed for a comparison between irreparable losses, such as building collapse and demolition due to excessive residual drifts, and reparable losses, including the repair of both structural and nonstructural elements, across different design options.

This study reaffirmed the generally low collapse probability of buildings designed with CRBFs, particularly when designing for higher mode effects at the MCE level and avoiding very low rocking design moments (i.e., avoiding R=12). Moreover, it demonstrated that for more flexible CRBFs, the reduction in seismic losses due to acceleration-sensitive nonstructural components approximately offsets the increase in seismic losses resulting from drift-sensitive components and irreparable losses. In this way, while there were significant differences in the sources of seismic loss with different design options, the total expected annual loss for a given height of building with CRBFs was quite consistent, regardless of the parameters selected for design. This indicates that, in the design of controlled rocking braced frames and as they progress towards codification, it is reasonable to define their design parameters based on considerations of collapse fragility, without excessive concern about the influence of these decisions on expected seismic losses.

While this study compared expected economic losses with different design options, repair time estimates were not compared. Considering the different breakdowns of loss sources between repairable and irreparable losses with different design options, it is possible that comparing repair time may lead to more significant differences among design options. An additional limitation of this study lies in the damage fragility curves provided in FEMA P58, which consider peak accelerations as the engineering demand parameter (EDP) for acceleration-sensitive components. This research identified that the CRBFs displayed peaks in the floor acceleration spectra near the building's higher-mode periods, which varied depending on the design option. This suggests the need for further research on period-dependent EDPs to assess damage in nonstructural components.

3.11 ACKNOWLEDGEMENTS

This research received funding from the Ontario Ministry of Colleges and Universities in the form of an Early Researcher Award, as well as support from the Natural Sciences and Engineering Research Council of Canada (NSERC) through their Discovery Grant program.

3.12 REFERENCES

Aher, Sandesh, David Mar, and Geoffrey Rodgers. 2020. Casa Adelante: Behavior, Design, Modeling Choices, and Performance Insights of a Rocking Mat Foundation System. In

SEAOC Convention Proceedings, 1–13.

ASCE/SEI 7-16. 2016. *Minimum Design Loads and Associated Criteria for Buildings and Other Structures*. Reston, VA, United States: American Society of Civil Engineers.

Baker, Jack W. 2015. Efficient Analytical Fragility Function Fitting Using Dynamic Structural Analysis. *Earthquake Spectra* 31 (1):579–599. doi:https://doi.org/10.1193/021113EQS025M.

Banihashemi, Amir, and Lydell Wiebe. 2022. Design of Low-Rise Controlled Rocking Braced Frames for Life Cycle Costs. *Proceedings of the 10th International Conference on Behaviour of Steel Structures in Seismic Areas: STESSA* 262:746–754. doi:https://doi.org/10.1007/978-3-031-03811-2_81.

Banihashemi, Miramir, and Lydell Wiebe. 2023. Seismic Loss Comparison for Buildings Designed with Ductile Steel Seismic Force-Resisting Systems and with Controlled Rocking Braced Frames. *Submitted to Earthquake Spectra*.

Behr, Richard. 2001. Architectural Glass for Earthquake-Resistant Buildings. In *Proceedings of the 7th International Glass in Tampere (Glass Processing Days 2001)*. Tampere, Finland. www.glassfiles.com.

Buccella, Nathan, Lydell Wiebe, Dimitrios Konstantinidis, and Taylor Steele. 2021. Demands on Nonstructural Components in Buildings with Controlled Rocking Braced Frames. *Earthquake Engineering and Structural Dynamics* 50 (4). John Wiley and Sons Ltd:1063–1082. doi:https://doi.org/10.1002/eqe.3385.

Bull, Des. 2011. Stairs and Access Ramps between Floors in Multi-Story Buildings. In *Report to the Canterbury Earthquakes Royal Commission.*, 1–8. Christchurch, New Zealand: Holmes Consulting Group.

Charney, Finley A. 2008. Unintended Consequences of Modeling Damping in Structures. *Journal of Structural Engineering* 134 (4):581–592. doi:https://doi.org/10.1061/(ASCE)0733-9445(2008)134:4(581).

Cornell, C. Allin, and Helmut Krawinkler. 2000. Progress and Challenges in Seismic Performance Assessment. *PEER Center News* 3 (2):1–3.

Dhakal, Rajesh P. 2010. Damage to Non-Structural Components and Contents in 2010 Darfield Earthquake. *Bulletin of the New Zealand Society for Earthquake Engineering* 43 (4):404–411. doi:https://doi.org/10.5459/bnzsee.43.4.404-411.

Dyanati, Mojtaba, Qindan Huang, and David Roke. 2017. Cost-Benefit Evaluation of Self-Centring Concentrically Braced Frames Considering Uncertainties. *Structure and Infrastructure Engineering* 13 (5):537–553. doi:https://doi.org/10.1080/15732479.2016.1173070.

DYWIDAG Systems International. 2020. DYWIDAG Post-Tensioning Systems.

Eatherton, Matthew R., Xiang Ma, Helmut Krawinkler, David Mar, Sarah Billington, Jerome F. Hajjar, and Gregory G. Deierlein. 2014. Design Concepts for Controlled Rocking of Self-Centering Steel-Braced Frames. *Journal of Structural Engineering* 140 (11). American

Society of Civil Engineers:04014082. doi:https://doi.org/10.1061/(ASCE)ST.1943-541X.0001047.

FEMA P-58-1. 2018. *Seismic Performance Assessment of Buildings Volume 1-Methodology*. Washington, DC, United States: prepared by the Applied Technology Council for the Federal Emergency Management Agency.

FEMA P-58-3. 2018. *Seismic Performance Assessment of Buildings, Volume 3–Supporting Electronic Materials and Background Documentation: 3.1 Performance Assessment Calculation Tool (PACT)*. Version 3.1.2. Washington, DC, United States: prepared by the Applied Technology Council for the Federal Emergency Management Agency.

FEMA P695. 2009. *Quantification of Building Seismic Performance Factors*. Washington, DC, United States: prepared by the Applied Technology Council for the Federal Emergency Management Agency.

Huang, Qindan, Mojtaba Dyanati, David A Roke, Akhilesh Chandra, and Kallol Sett. 2018. Economic Feasibility Study of Self-Centering Concentrically Braced Frame Systems. *Journal of Structural Engineering* 144 (8):04018101. doi:https://doi.org/10.1061/(ASCE)ST.1943-541X.0002093.

Hwang, Seong Hoon, and Dimitrios G. Lignos. 2017a. Effect of Modeling Assumptions on the Earthquake-Induced Losses and Collapse Risk of Steel-Frame Buildings with Special Concentrically Braced Frames. *Journal of Structural Engineering* 143 (9). American Society of Civil Engineers (ASCE):04017116. doi:https://doi.org/10.1061/(ASCE)ST.1943-541X.0001851.

Hwang, Seong Hoon, and Dimitrios G. Lignos. 2017b. Earthquake-Induced Loss Assessment of Steel Frame Buildings with Special Moment Frames Designed in Highly Seismic Regions. *Earthquake Engineering and Structural Dynamics* 46 (13). John Wiley and Sons Ltd:2141–2162. doi:https://doi.org/10.1002/eqe.2898.

Ma, Xiang, Helmut Krawinkler, and Gregory G Deierlein. 2010. Seismic Design and Behavior of Self-Centering Braced Frame with Controlled Rocking and Energy Dissipating Fuses. In *Report 174*, 438. Stanford, CA, United States: Blume Earthquake Engineering Center. http://blume.stanford.edu.

McKenna, Frank, Gregory Fenves, and Michael Scott. 2000. Open System for Earthquake Engineering Simulation v3.3.0. University of California Berkeley, CA, United States.

Miranda, Eduardo, Gilberto Mosqueda, Rodrigo Retamales, and Gokhan Pekcan. 2012. Performance of Nonstructural Components during the 27 February 2010 Chile Earthquake. *Earthquake Spectra* 28 (S1):S453–S471. doi:https://doi.org/10.1193/1.4000032.

Okazaki, Taichiro, Dimitrios G. Lignos, Mitsumasa Midorikawa, James M. Ricles, and Jay Love. 2013. Damage to Steel Buildings Observed after the 2011 Tohoku-Oki Earthquake. *Earthquake Spectra* 29 (S1). Earthquake Engineering Research Institute:S219–S243. doi:https://doi.org/10.1193/1.4000124.

Perrone, Daniele, Paolo Calvi, Roberto Nascimbene, Erica C. Fischer, and Gennaro Magliulo. 2019. Seismic Performance of Non-Structural Elements during the 2016 Central Italy

Earthquake. *Bulletin of Earthquake Engineering* 17 (October). Springer Netherlands:5655–5677. doi:https://doi.org/10.1007/s10518-018-0361-5.

Rahgozar, Navid, Abdolreza S Moghadam, and Armin Aziminejad. 2016. Quantification of Seismic Performance Factors for Self-centering Controlled Rocking Special Concentrically Braced Frame. *The Structural Design of Tall and Special Buildings* 25 (14):700–723. doi:https://doi.org/10.1002/tal.1279.

Ramirez, C. Marcelo, and Eduardo Miranda. 2012. Significance of Residual Drifts in Building Earthquake Loss Estimation. *Earthquake Engineering and Structural Dynamics* 41 (11):1477–1493. doi:https://doi.org/10.1002/eqe.2217.

Retamales, Rodrigo, Ryan Davies, Gilberto Mosqueda, and Andre Filiatrault. 2013. Experimental Seismic Fragility of Cold-Formed Steel Framed Gypsum Partition Walls. *Journal of Structural Engineering* 139 (8):1285–1293. doi:https://doi.org/10.1061/(ASCE)ST.1943-541X.0000657.

Roke, David, Richard Sause, James M. Ricles, and Nathan Brent Chancellor. 2010. Damage-Free Seismic-Resistant Self-Centering Concentrically-Braced Frames. In *Report 10-09*. Bethlehem,PA, United States: Advanced Technology for Large Structural Systems Engineering Research Center.

Rosenblueth, Emilio, and Roberto Meli. 1986. The 1985 Earthquake Causes and Effects in Mexico City. *Concrete International* 8 (5):12.

RSMeans. 2020. *Building Construction Cost Data*. RSMeans Construction Publishers and Consultants.

Seo, Choung-Yeol, and Richard Sause. 2005. Ductility Demands on Self-Centering Systems under Earthquake Loading. *ACI Structural Journal* 102 (2):275–285.

Soroushian, Siavash, Arash E. Zaghi, Manos Maragakis, Alicia Echevarria, Yuan Tian, and Andre Filiatrault. 2015. Analytical Seismic Fragility Analyses of Fire Sprinkler Piping Systems with Threaded Joints. *Earthquake Spectra* 31 (2). Earthquake Engineering Research Institute:1125–1155. doi:https://doi.org/10.1193/083112EQS277M.

Steele, Taylor, and Lydell Wiebe. 2016. Dynamic and Equivalent Static Procedures for Capacity Design of Controlled Rocking Steel Braced Frames. *Earthquake Engineering and Structural Dynamics* 45 (14):2349–2369. doi:https://doi.org/10.1002/eqe.2765.

Steele, Taylor, and Lydell Wiebe. 2017. Collapse Risk of Controlled Rocking Steel Braced Frames with Different Post-Tensioning and Energy Dissipation Designs. *Earthquake Engineering and Structural Dynamics* 46 (13). John Wiley and Sons Ltd:2063–2082. doi:https://doi.org/10.1002/eqe.2892.

Steele, Taylor, and Lydell Wiebe. 2021. Collapse Risk of Controlled Rocking Steel Braced Frames Considering Buckling and Yielding of Capacity-Protected Frame Members. *Engineering Structures* 237 (June). Elsevier BV:111999. doi:https://doi.org/10.1016/j.engstruct.2021.111999.

Uriz, Patxi, and Stephan A Mahin. 2004. Seismic Vulnerability Assessment of Concentrically Braced Steel Frames. *International Journal of Steel Structures* 4 (4):239–248.

Uriz, Patxi, and Stephen A Mahin. 2008. Toward Earthquake-Resistant Design of Concentrically Braced Steel-Frame Structures. In *PEER Report 2008/08*. Berkeley,CA, United States: Pacific Earthquake Engineering Research Center.

Westenenk, Benjamín, Juan Carlos De La Llera, Juan José Besa, Rosita Jünemann, Jack Moehle, Carl Lüders, José Antonio Inaudi, Kenneth J. Elwood, and Shyh Jiann Hwang. 2012. Response of Reinforced Concrete Buildings in Concepción during the Maule Earthquake. *Earthquake Spectra* 28 (S1). Earthquake Engineering Research Institute:S257–S280. doi:https://doi.org/10.1193/1.4000037.

Wiebe, Lydell, and Constantin Christopoulos. 2015. Performance-Based Seismic Design of Controlled Rocking Steel Braced Frames. I: Methodological Framework and Design of Base Rocking Joint. *Journal of Structural Engineering* 141 (9):04014226. doi:https://doi.org/10.1061/(ASCE)ST.1943-541X.0001202.

Wiebe, Lydell, Constantin Christopoulos, Robert Tremblay, and Martin Leclerc. 2013. Mechanisms to Limit Higher Mode Effects in a Controlled Rocking Steel Frame. 2: Large-Amplitude Shake Table Testing. *Earthquake Engineering and Structural Dynamics* 42 (7):1069–1086. doi:https://doi.org/10.1002/eqe.2258.

Yang, Tony, Jack Moehle, Bozidar Stojadinovic, and A. Der Kiureghian. 2006. An Application of PEER Performance-Based Earthquake Engineering Methodology. *8th U.S. National Conference on Earthquake Engineering*.

Yang, Tony, Jack Moehle, Bozidar Stojadinovic, and A. Der Kiureghian. 2009. Seismic Performance Evaluation of Facilities: Methodology and Implementation. *Journal of Structural Engineering* 135 (10):1146–1154. doi:https://doi.org/10.1061/(ASCE)0733-9445(2009)135:10(1146).

Zhang, Changxuan, Taylor Steele, and Lydell Wiebe. 2018. Design-Level Estimation of Seismic Displacements for Self-Centering SDOF Systems on Stiff Soil. *Engineering Structures* 177:431–443. doi:https://doi.org/10.1016/j.engstruct.2018.09.067.

Zsarnóczay, Adám. 2019. NHERI-SimCenter/Pelicun: V2.0.0, Zenodo. doi:http://doi.org/10.5281/zenodo.3491100.

Chapter 4

4. SUITABLE ENGINEERING DEMAND PARAMETERS FOR ACCELERATION-SENSITIVE NONSTRUCTURAL COMPONENTS

4.1 ABSTRACT

Early earthquake design codes used peak ground accelerations (PGAs) as intensity measures (IMs) to characterize the demands of ground motions on structures, but have since shifted towards using spectral accelerations because they provide a better indication of demand. The design of acceleration-sensitive nonstructural components has followed a similar approach, with modern codes being based on an estimate of the spectral acceleration at the period of the nonstructural component. However, most fragility curves for loss assessment of acceleration-sensitive nonstructural components, including the existing FEMA P58 library, continue to be based on peak floor accelerations (PFAs). Similar to PGAs as an IM for buildings, a limitation of PFA as an engineering demand parameter (EDP) for nonstructural components is its lack of dependence on the period of those components. In this study, fifteen alternative EDPs suggested in the literature are evaluated as potential candidates for developing seismic damage fragility curves. Acceleration-sensitive nonstructural components are simulated by single-degree-of-freedom (SDOF) components with elastic perfectly plastic behavior, with a period range of 0.01 to 1 s, and varying strength levels. Nonlinear response history analyses are conducted for the SDOFs, using floor motions obtained from both the first floor and the roof of buildings designed with four distinct seismic force-resisting systems. Ductility demands for each SDOF are taken as an indicator of damage and are predicted using a linear regression model developed for each specific EDP. The suitability of candidate EDPs is evaluated based on their efficiency and relative sufficiency. Furthermore, a comparison is made between the expected annual loss

calculated using fragility curves derived from the selected EDPs to quantify how the EDP used for a fragility curve can affect the seismic loss assessment. The results reveal that the PFA is a suitable EDP only for nonstructural components with very short periods (i.e., less than 0.1 s). Moreover, although the spectral acceleration at the period of the SDOF nonstructural component is a suitable EDP for components that are nearly elastic and are located on the roof of the buildings, an average of the spectral accelerations near the period of the SDOF nonstructural component is more appropriate when the component encounters higher levels of nonlinear behavior or is installed on a lower floor.

KEYWORDS: damage fragility curves; acceleration-sensitive nonstructural components; engineering demand parameters (EDPs); single-degree-of-freedom (SDOF) components; numerical analysis; seismic loss assessment.

4.2 INTRODUCTION

The aftermath of recent earthquakes has revealed that nonstructural components play a crucial role in causing downtime and business interruptions (Dhakal, 2010; Miranda et al., 2012; Perrone et al., 2019), leading to significant economic losses (Hwang and Lignos, 2017). These losses can pose challenges to the recovery efforts of earthquake-resilient cities. Nonstructural components are typically categorized as either displacement-sensitive or acceleration-sensitive. Displacement-sensitive components are evaluated directly based on the inter-story drift of buildings, while acceleration-sensitive components are assessed indirectly due to the potential for overturning or excessive displacements caused by inertia forces. In order to evaluate the damage to acceleration-sensitive components, a parameter related to floor accelerations is used. The current FEMA P-58-3 (2018) library uses peak floor accelerations (PFAs) to define damage fragility curves for such components. However, the effectiveness of PFA in correlating with damage is likely to be limited because it does not consider parameters such as the component's natural periods or the floor motion’s spectral shape.

There is already an established set of engineering demand parameters (EDPs), such as the maximum displacement at the roof, the PFA, and the floor response spectrum, that are widely used to quantify the response of a structure to an earthquake. These EDPs are defined to capture the effects of ground motion intensity measures (IMs), such as the peak ground accelerations (PGAs) and the ground response spectrum, on the structure's behavior. Historically, among the early introduced IMs, PGAs were predominantly employed. However, other IMs such as Arias intensity (Arias, 1970), root mean of the acceleration (Housner, 1975), and specific energy density (Sarma, 1971) were also proposed for characterizing ground motions. As response spectrum theory advanced (Housner and Jennings, 1982; Newmark and Hall, 1982), the earthquake engineering community shifted its focus to the spectral acceleration at the fundamental period of a structure (Sa), which emerged as the predominant IM in earthquake engineering. In the past decade, various IMs have emerged that take into account the spectral shape and the influence of nonlinearity in buildings, to enhance the estimation of buildings’ seismic behavior (Bojórquez and Iervolino, 2011; Cordova et al., 2000; Eads et al., 2015). Several studies have demonstrated the greater suitability of IMs that are based on the average spectral acceleration around the building’s fundamental period (Adam et al., 2017; Bianchini et al., 2009; De Biasio et al., 2014; Bojórquez and Iervolino, 2011; Eads et al., 2015; Kazantzi and Vamvatsikos, 2015). However, Sa and PGA remain the most widely used IMs in the seismic performance assessment of buildings.

Both IMs and EDPs are random variables exhibiting high dispersion, with IMs influenced by the complexity of ground motions and EDPs affected by seismic input, material properties, structural geometry, and other factors (Vargas-Alzate et al., 2022). Several statistical properties have been proposed to extract information from IM-EDP pairs to select the most suitable IM (Cornell et al., 2002; Jalayer et al., 2015; Jalayer and Cornell, 2009; Di Sarno and Pugliese, 2021; Vargas-Alzate et al., 2019, 2022). Among them, efficiency and sufficiency are the most widely used statistical properties. Efficiency can be quantified by measuring the dispersion of IM-EDP data points, with lower scatter indicating higher efficiency (Vargas-Alzate et al., 2022). An IM is said to be sufficient if the structural response conditioned on that IM is independent of other ground motion characteristics, such as magnitude and source-to-site-distance (Jalayer et al., 2012). In addition to using statistical properties as measures of suitable IMs, some researchers directly compare IMs based on the collapse risk estimates they generate (Bradley et al., 2010; Eads et al., 2015; Tothong and Luco, 2007).

Similar to previous research efforts aimed at identifying ground motion IMs that can predict structural response in terms of EDPs, there is a need to understand the EDPs that can accurately predict nonstructural damage. However, unlike the numerous studies focused on selecting suitable IMs for predicting EDPs in buildings, there is a lack of research comparing the performance of EDPs in predicting damage for acceleration-sensitive nonstructural components. This is despite the significant differences in frequency content between ground motions and floor motions, which are characterized by spectral peaks that reflect the characteristics of the structure in ways that may vary depending on the seismic force-resisting system (SFRS) of a building and the location within that building (Filiatrault and Sullivan, 2014).

To address this research gap, this study evaluates fifteen candidate EDPs, along with PFA, to identify suitable EDPs for the damage fragility curves of acceleration-sensitive nonstructural components. For this purpose, nonstructural components are represented as elastic perfectly plastic single-degree-of-freedom (SDOF) models with different fundamental periods and designed with different strength levels. These components undergo floor motions derived from nonlinear response history analyses of buildings designed in compliance with relevant codes. The analyses are conducted for two building heights (six- and 12-story buildings), with each height designed with four different SFRSs. For brevity, this chapter presents results only from the analyses of the nonstructural components mounted on the 12-story buildings, as similar conclusions are applicable to all cases (Appendix A). The statistical criteria of efficiency and sufficiency are used to determine the most appropriate EDP by comparing ductility-candidate EDP pairs. Finally, the impact of EDP selection is assessed by comparing the expected annual losses from seismic loss assessments conducted for the SDOF nonstructural components using different candidate EDPs.

4.3 CONSIDERED ENGINEERING DEMAND PARAMETERS

This section explains the EDPs that are evaluated in this study and categorizes them following previous studies to compare intensity measures of ground (Ebrahimian et al., 2015; Mollaioli et al., 2013). The investigated EDPs are categorized into two groups: (i) Component period-independent EDPs, and (ii) Component period-dependent EDPs. Table 4-1 provides a summary and definition for all the EDPs investigated in this study.

The component period-independent EDPs are further classified into three sub-categories (Mollaioli et al., 2013): (a) acceleration-related, (b) velocity-related, and (c) displacement-related EDPs. PFA (peak floor acceleration), PFV (peak floor velocity), and PFD (peak floor displacement) are time domain parameters of floor motions. I_F (Fajfar intensity) is an EDP that relates to PFV and also considers the duration of motions. I_A (Arias intensity), CAV (cumulative absolute velocity), a_{rms} (root mean square of the acceleration), I_C (characteristic intensity), v_{rms}

(root mean square of the velocity), SED (specific energy density), and d_{rms} (root mean square of the displacement) are all integral-based EDPs that take into account the duration and amplitude, but not the frequency content of floor motions (Mollaioli et al., 2013).

The component period-dependent EDPs are further classified into three sub-categories, which are explained below.

a) Spectral acceleration at certain periods: This category includes Sa (spectral acceleration) at the period of the nonstructural component and I_{CO} (Cordova intensity). The I_{CO} is a two-parameter EDP that accounts for both Sa and period elongation due to softening of the inelastic behavior of nonstructural components (Cordova et al., 2000).

b) Average of spectral accelerations over a period range: The EDPs in this category reflect inelastic response of nonstructural components (Bianchini et al., 2009). The Sa_{ave} (Eads intensity) is an EDP that calculates the geometric mean of spectral acceleration values between 0.2 and 3 times the period of nonstructural components (Eads et al., 2015). The I_{NP} (Bojórquez intensity) is the normalized average spectral acceleration combined with Sa (Bojórquez and Iervolino, 2011).

c) Frequency content filtered-based EDP: Dávalos and Miranda (2019) proposed FIV3 (filtered incremental velocity) as a method to extract the effective acceleration pulse segments that produce large lateral displacement demands. In this method, low-pass filtered accelerations are accumulated according to the period of nonstructural components. In this study, all the spectral values are calculated at 5% damping.

Table 4-1. EDPs evaluated in this study

Notation	Name	Definition	Reference
(i) Component period-independent EDPs			
(a) Acceleration-related			
PFA	Peak floor acceleration	$PGA = \max(\lvert\ddot{u}(t)\rvert)$ $\ddot{u}(t)$ =acceleration time history	
I_A	Arias intensity	$I_A = \frac{\pi}{2\times 9.81}\int_{t_{5\%}}^{t_{95\%}} \ddot{u}(t)^2 dt$	Arias (1970)
CAV	Cumulative absolute velocity	$CAV = \int_{t_{5\%}}^{t_{95\%}} \lvert\ddot{u}(t)\rvert dt$	Reed and Kassawara (1990)
a_{rms}	Root mean square of the acceleration	$a_{rms} = \sqrt{\frac{1}{\Delta}\int_{t_{5\%}}^{t_{95\%}} \ddot{u}(t)^2 dt}$	Housner (1975)
I_C	Characteristic intensity	$I_c = a_{rms}^{1.5}\sqrt{\Delta}$	Park et al. (1985)
(b) Velocity-related			
PFV	Peak floor velocity	$PFV = \max(\lvert\dot{u}(t)\rvert)$ $\dot{u}(t)$ =velocity on time history	
v_{rms}	Root mean square of the velocity	$v_{rms} = \sqrt{\frac{1}{\Delta}\int_{t_{5\%}}^{t_{95\%}} \dot{u}(t)^2 dt}$	Vargas-Alzate et al. (2022)
SED	Specific energy density	$SED = \int_{t_{5\%}}^{t_{95\%}} \dot{u}(t)^2 dt$	Sarma (1971)
I_F	Fajfar intensity	$I_F = PGV \times \Delta^{0.25}$	Fajfar et al. (1990)
(c) Displacement-related			
PFD	Peak floor displacement	$PFD = \max(\lvert u(t)\rvert)$ $u(t)$ =displacement on time history	
d_{rms}	Root mean square of the displacement	$d_{rms} = \sqrt{\frac{1}{\Delta}\int_{t_{5\%}}^{t_{95\%}} u(t)^2 dt}$	
(ii) Component period-dependent EDPs			
(a) Spectral acceleration at certain periods			
Sa	Spectral acceleration	$S_a(T)$ T = period of SDOF nonstructural component	
I_{CO}	Cordova intensity	$I_{CO} = S_a(T)\left[\frac{S_a(2T)}{S_a(T)}\right]^{0.5}$	Cordova et al. (2000)
(b) Average of spectral accelerations over a period range			
Sa_{ave}	Eads intensity	$Sa_{ave} = [\prod_i^N S_a(t_i)]^{(\frac{1}{N})}$ $t_i = 0.2T;\ t_N = 3T$	Eads et al. (2015)
I_{NP}	Bojórquez intensity	$I_{NP} = S_a(T)\left(\frac{[\prod_i^N S_a(t_i)]^{(\frac{1}{N})}}{S_a(T)}\right)^{0.4}$ $t_i = T;\ t_N = \max(2, 2.5T)$	Bojórquez and Iervolino (2011)
(c) Frequency content filtered-based EDP			
FIV3	Filtered incremental velocity	$FIV3 = \max\{V_{s,max1} + V_{s,max2} + V_{s,max3};\ \lvert V_{s,min1} + V_{s,min2} + V_{s,min3}\rvert\}$ $V_s = \{\int_t^{t+0.7T} \ddot{u}_f(\tau)d\tau;\ \forall t < t_{end} - 0.7T\}$ $V_{s,max1}/V_{s,min1}$ is first local largest/minimum of V_s $\ddot{u}_f(t)$ = filtered acceleration time history using a second-order Butterworth low-pass filter with a cut-off frequency of $0.85\frac{1}{T}$	Dávalos and Miranda (2019)

$t_{5\%}$ and $t_{95\%}$ are the times related to the 5% and 95% of the Husid diagram (Trifunac and Novikova, 1994); Δ is the significant duration (i.e. $t_{95\%}$- $t_{5\%}$); N is the number of periods in a period range between t_i and t_N with a uniform period spacing of 0.001 s.

Among these EDPs, PFA is currently used as the EDP for acceleration-sensitive nonstructural components in FEMA P-58-3 (2018). Additionally, Sa is deemed the preferable alternative to PFA within the engineering community due to its wide usage in estimating demands in buildings subjected to ground motions, as well as the analogous relationship between floor motions and demands in acceleration-sensitive nonstructural components, and between ground motions and demands in the building.

4.4 PROTOTYPE BUILDINGS AND SEISMIC FORCE RESISTING SYSTEMS

This study examines SDOF nonstructural components mounted on the first floor and roof of six- and 12-story office buildings. Each building height was designed using four different SFRSs: special moment-resisting frames (SMRFs), special concentrically braced frames (SCBFs), buckling-restrained braced frames (BRBFs), and controlled rocking braced frames (CRBFs). The buildings were located in a seismically active area with stiff soil (site class D). The mapped short-period (0.2-second) and 1-second spectral accelerations were S_S=1.5 g and S_1=0.5 g, respectively (ASCE/SEI 7-16, 2016). The buildings had a typical floor plan shown in Figure 4-1, each story height was 4.57 m, and the total seismic weights for the floors and roofs were 10,200 kN and 6,430 kN, respectively. The SFRS configurations for buildings with the SMRFs and all other SFRSs (i.e., the braced frames), are shown in Figure 4-1 (a) and Figure 4-1 (b), respectively.

All four considered SFRSs were designed using the equivalent lateral force method of ASCE/SEI 7-16 (2016). The SMRFs were designed using reduced beam sections, in accordance with ANSI/AISC 358-16 (2016), with a response modification factor (*R*) of 8 (ASCE/SEI 7-16, 2016). The capacity design method of ANSI/AISC 341-16 (2016) was used to design the members of the SCBF and BRBF buildings, with *R* values of 6 and 8, respectively. The braces of the BRBF buildings were designed with a yield strength of 290 MPa, considering the strain hardening and compressive strength adjustment factors obtained from Saxey and Daniels (2014). Wiebe and Christopoulos' two-step procedure (Wiebe and Christopoulos, 2015) was used to design the CRBFs: (I) base rocking joint design, which included post-tensioning and energy dissipation design for equivalent lateral forces using R of 8; and (II) capacity design of all steel members for the forces expected to develop during rocking (Steele and Wiebe, 2016), which include the higher-mode forces at the maximum considered earthquake (MCE) level. All steel members of all SFRSs, except for the braces of BRBFs, were designed using a yield strength of 345 MPa and considering the ANSI/AISC 360-16 (2016) requirements.

4.5 Ground motion selection and scaling

The Los Angeles Bulk Mail Center with coordinates of 33.996°N and 118.162°W was chosen as representative of the site conditions used in designing the SFRSs. The seismic hazard curves for this site were obtained from the USGS website (https://earthquake.usgs.gov/hazards/interactive/, last accessed 17 October 2022). To estimate the hazard curve for the building's fundamental period, interpolation was applied between the periods for which data were provided. The suite of far-field ground motion records recommended by FEMA P695 (2009) was used for the nonlinear response history analyses of the SFRSs. The chosen ground motions were scaled to minimize the geometric mean differences between the MCE spectrum derived from ASCE/SEI 7-16 (2016) and the median acceleration spectrum of the records over a single period range for all SFRSs of the same building height. This range extended from 0.2 times the fundamental period of the fixed-base CRBF (T_{CRBF}) building to 2.0 times the fundamental period of the BRBF (T_{BRBF}) building, to ensure consistency in ground motions for different SFRSs. Figure 2 displays the scaled records for the set of 12-story buildings, along with the median of the selected ground motion suite and the MCE spectrum. Nonlinear response history analyses were performed on each SFRS using the ground motion suite scaled to six different intensity stripes: 0.25, 0.50, and 1.0 times the design earthquake (DE, considered as 2/3 times the MCE), and 1.0, 1.5, and 2.0 times the MCE. OpenSees was used to develop advanced numerical models for nonlinear response history analyses of the designed SFRSs. Detailed information regarding the numerical modeling of the SFRSs in OpenSees is provided in Chapter 2.

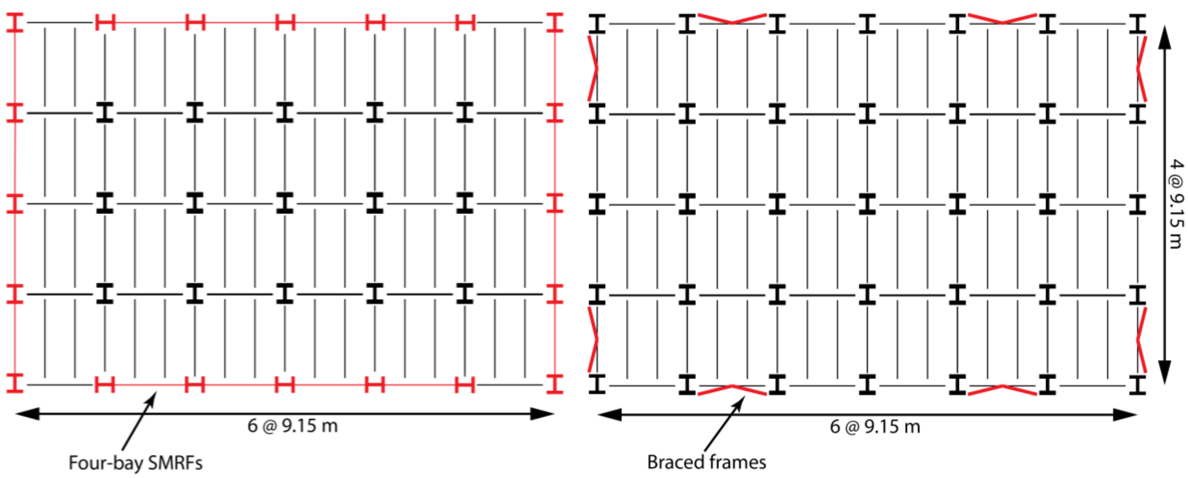

(a) (b)

Figure 4-1. Floor plan of buildings: (a) with SMRFs and (b) with braced frames.

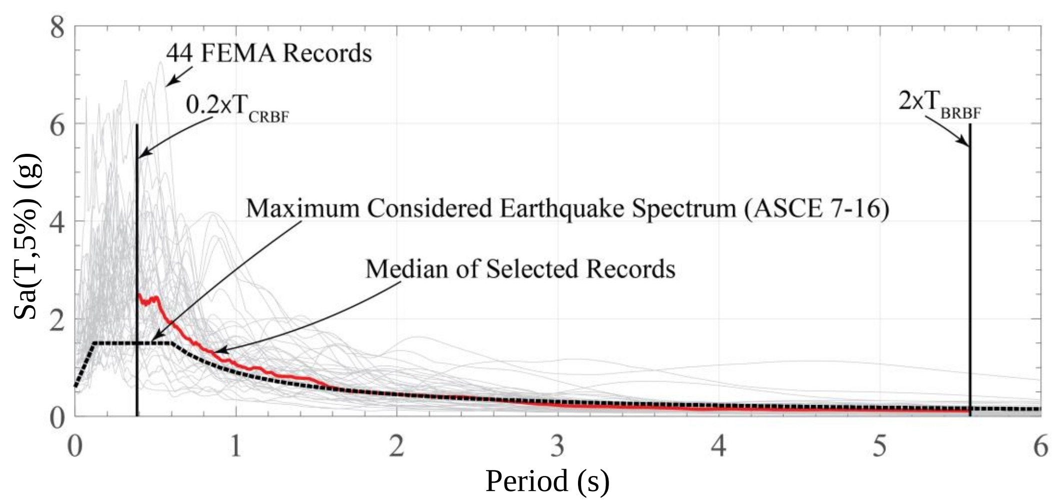

Figure 4-2.Scaling of the selected suite of ground motions for the 12-story SFRSs.

4.6 Floor motions and modeling of acceleration-sensitive nonstructural components

This study is based on the simplifying assumption that acceleration-sensitive nonstructural components can be modelled as damped SDOF systems that are rigidly attached to their supporting buildings. To evaluate the demand on these SDOF nonstructural components, floor motions at the first floor and roof of the buildings resulting from the nonlinear response history analyses of the SFRSs are used. Any floor motions corresponding to a scaled ground motion that caused building collapse, which was assumed if any interstory drift exceeded 10% or any residual interstory drift exceeded 3% in the nonlinear response history analyses, were excluded. Also, baseline corrections were performed on the floor acceleration time history by fitting a polynomial trend to ensure that the final displacement and velocity from the integrals of acceleration are zero. The baseline corrections resulted in less than a 1% difference between the PFA of the modified floor motions and the PFA of the original floor motions.

Figure 4-3 shows the individual and median 5% damped elastic acceleration FRS for the first floor and roof of the 12-story buildings at the DE level. The first fixed-base elastic natural period of every structure is greater than 1 s, and the next five periods are indicated in Figure 4-3. The floor response spectra in Figure 4-3 illustrate the various behaviors that the same building exhibits when equipped with different SFRSs. The distinctive modal periods of the SFRSs result in the occurrence of peak values at different periods in the FRS. Another factor is different levels of nonlinearity occurring in different SFRSs at the same earthquake intensity level. As discussed by Sullivan et al. (2013), increasing levels of nonlinearity lead to a broadening of peaks over a wider range of periods in the floor response spectra. For example, the buckling of braces in SCBFs and yielding of BRBFs at even low-intensity levels cause capping of forces in each story, resulting in a flattening effect in the FRS for these systems in Figure 4-3. Because the level of nonlinearity in a given system is different for each individual ground motion, this spreading effect is not consistent across ground motions, meaning that even the flattened peaks are not well defined in the median FRS. Conversely, the SMRF experienced less nonlinearity at the ends of its beams and columns at the DE level, making the spectral peaks sharper around higher modes. Unlike these other systems, the FRS of the CRBF exhibits a sharp and well-defined peak near the second-mode period because the base rocking mechanism does not fully control higher-mode vibration, and the frame members are capacity-designed to remain linear elastic during the scaled motions at the DE intensity level. Moreover, comparing motions at different floors reveals that the characteristics of SFRSs affect the roof motions more than the motions at the lower floors. This is because the dynamic response of the SFRSs filters distinct excitation frequencies, amplifies demands within specific period ranges (Sullivan et al., 2013), and leads to greater effects from higher modes for the upper floors.

The initial elastic periods of the considered SDOF nonstructural components range from 0.01 to 1 second, with 0.01-second increments. To model the nonlinear behavior of SDOF nonstructural components, a bilinear elastic-perfectly-plastic hysteresis model with a damping ratio of 5% and no strain hardening was used. The yield strength (f_y) of the hysteresis model was determined by dividing the DE level median acceleration floor response spectrum (FRS) at the period of the SDOF nonstructural component by a coefficient factor of R_{NS}, for which three distinct values of 1.5, 2.0, and 3.0 were chosen. In this chapter, the results are presented for the SDOF nonstructural components designed with R_{NS} values of 1.5 and 3 and mounted on 12-story buildings. Similar conclusions arise from considering all cases (shown in Appendix A), but other results are omitted for brevity.

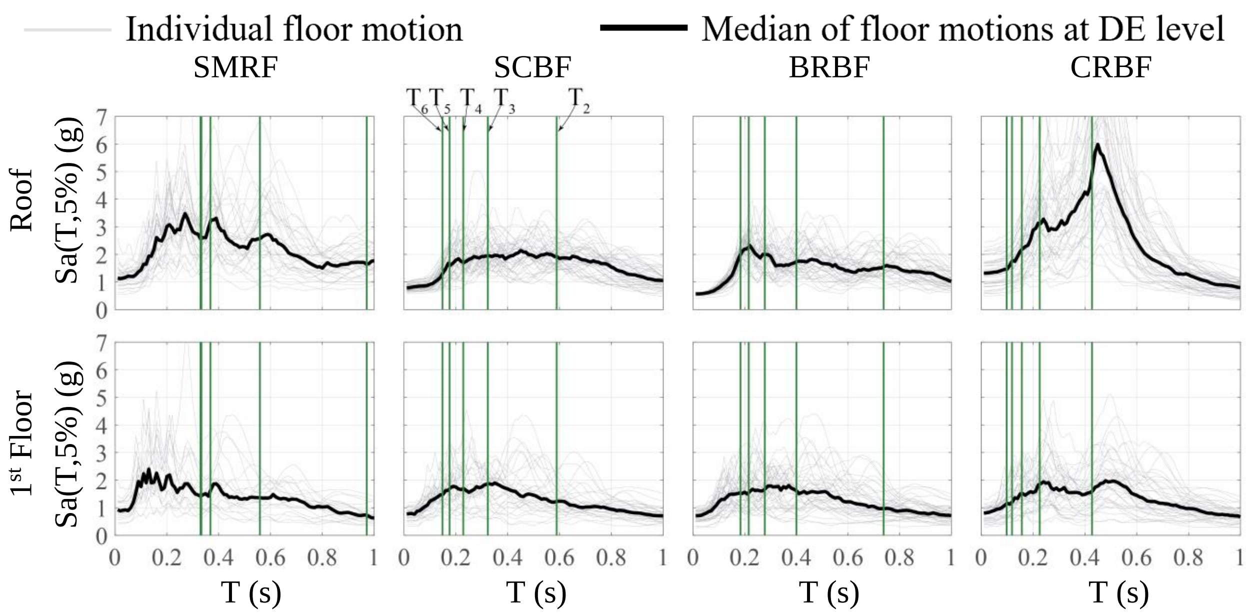

Figure 4-3. Median acceleration floor response spectra for 12-story buildings at the design earthquake (DE) level.

Nonlinear response history analyses were conducted on each SDOF nonstructural component using the absolute floor accelerations obtained from the building's nonlinear response history analyses at the six intensity levels defined above. The level of damage that a nonstructural component that is not brittle would be expected to incur was taken to be represented by its ductility demand, μ. This ductility demand can manifest in various elements, including the component itself, the attachment of the component to the anchor, the anchor structure, or a combination of these items (NIST, 2018). These potential sources of ductility are simplified by representing them together with an SDOF model (NIST, 2018).

The ductility demands for these components were plotted against the various EDPs listed in Table 4-1, and a least squares regression analysis was conducted in log-log space. As an example, Figure 4-4 shows dots indicating the ductility demands for the SDOF nonstructural component with a nonstructural period of 0.5 s and R_{NS} of 3, installed on the first floor of the 12-story SCBF, plotted against the PFA, Sa, and Sa_{ave}. At lower intensity levels, such as 0.25 and

0.5 times the DE, the component exhibits mostly linear response with ductility values below 1. The results confirm a linear relationship between Sa and ductility within this range. The ductility demand of this component reaches a maximum value of nearly 25 when subjected to scaled floor motions at 1.5 to 2.0 times the MCE levels. The results also show that using Sa_{ave} reduces the heteroscedasticity associated with the response of SDOF nonstructural components at different intensity levels, which is consistent with the findings presented in by Bojórquez and Iervolino (2011).

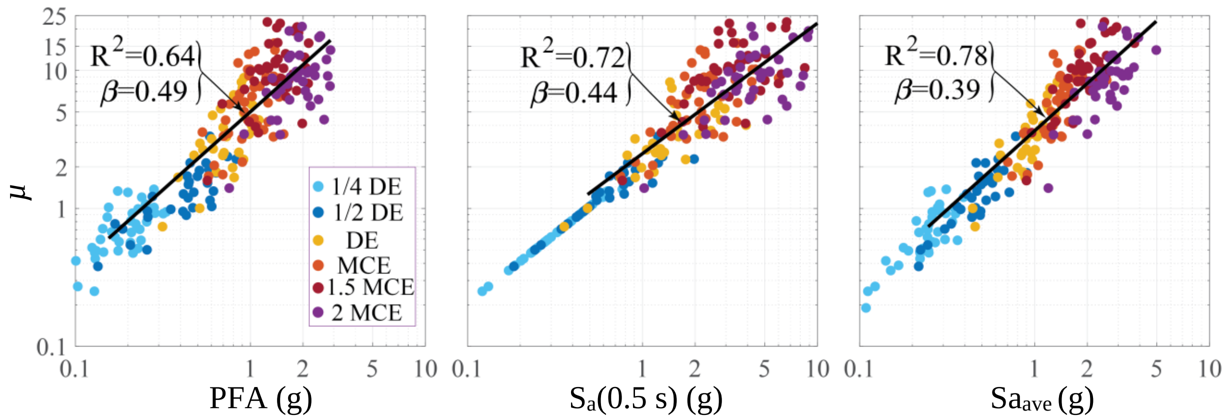

Figure 4-4. Ductility demands of the SDOF nonstructural component with a period of 0.5 s and RNS of 3, installed on the first floor of the 12-story SCBF, in terms of PFA, Sa(0.5 s), and Saave.

4.7 SEISMIC DAMAGE FRAGILITY EVALUATION

A damage fragility curve indicates the probability of the seismic demand on a nonstructural component, represented in this study by the ductility demand (μ), surpassing a certain capacity or damage state level. The fragility curve is defined based on a selected EDP and is normally assumed to follow the standard normal cumulative distribution function, as outlined in the equation below (Cornell et al., 2002; Nielson and DesRoches, 2007):

$$P(\mu \geq C|EDP) = \Phi\left(\frac{\ln(M_{\mathrm{d}}) - \ln(M_{\mathrm{C}})}{\sqrt{\beta_{\mathrm{d|EDP}}^2 + \beta_{\mathrm{C}}^2}}\right) \tag{4-1}$$

where $P(\mu \geq C|EDP)$ is the conditional probability that μ exceeds the limit state capacity C, given the selection of a particular EDP, which is known as damage fragility, M_{d} represents the median estimate of μ as a function of EDP, M_{c} denotes the median estimate of the capacity, which is taken as deterministic in this chapter, $\beta_{\mathrm{d|EDP}}$ corresponds to the logarithmic standard deviation of the demand conditioned on the EDP, β_{c} represents the logarithmic standard deviation of the capacity, and Φ represents the standard normal cumulative distribution.

In this study, the linear least squares method is used to calculate the median and the logarithmic standard deviation of μ conditioned on a particular EDP. The power law model (Housner, 1975) is employed, assuming that the standard deviation remains constant with respect to the EDP (Kazantzi and Vamvatsikos, 2015):

$$M_d = aEDP^b \tag{4-2}$$

where the parameters a and b represent the regression coefficients. The associated value of $\beta_{\mathrm{d|EDP}}$ is determined using equation:

$$\beta_{\mathrm{d|EDP}} = \sqrt{\frac{\sum_{i=1}^{N} [\ln(\mu_{\mathrm{i}}) - \ln{(aedp_{\mathrm{i}}^b)}]^2}{N-2}} \tag{4-3}$$

where N is the total number of floor acceleration response history records, while μ_{i} and edp_{i} represent the μ and EDP values, respectively, associated with the i$^{\mathrm{th}}$ floor acceleration response history. For each SDOF nonstructural component, a linear regression model was constructed using logarithmically transformed variables of the considered μ -EDP pair. To focus the regression on data related to component damage, only data with ductility demands greater than unity were included in the regression model. The regression models for the examples depicted in Figure 4-4 are represented by a solid black line for the μ-PFA, μ-Sa, and μ-Sa_{ave} pairs. For this example, the regression analysis shows that the least scatter is obtained by using Sa_{ave} (β = 0.39), followed by Sa (β = 0.44)and then PFA (β = 0.49). A similar process, as shown in Figure 4-4, is repeated for further analyses in subsequent sections.

4.8 Criteria for the selection of suitable EDPs

To assess the suitability of candidate EDPs, it is necessary to establish quantitative criteria. This study uses efficiency and sufficiency/relative sufficiency, which are two widely used criteria found in the literature, as described below.

4.8.1 Efficiency

Efficiency in selecting EDPs for acceleration-sensitive nonstructural components is associated with the variability in the μ for a given EDP value (Padgett et al., 2008). One quantitative measure used to assess efficiency is the logarithmic standard deviation ($\beta_{d|EDP}$), denoted as β hereafter, which indicates the degree of variability in the estimated μ values. A lower β value indicates less variability, and an ideal EDP would have β=0 indicating that the EDP directly predicts the ductility demand. Another measure used is the R-squared (R^2) value, which assesses how well the regression model (Equation (4-2)) fits the data:

$$R^2 = 1 - \frac{\sum_{i=1}^{N} [\ln(\mu_{\mathrm{i}}) - \ln{(aedp_{\mathrm{i}}^{b})}]^2}{\sum_{i=1}^{N} [\ln(\mu_{\mathrm{i}}) - \ln(\bar{\mu})]^2} \tag{4-4}$$

where $\bar{\mu}$ represents the mean of all the μ values. R^2 ranges from 0 to 1, with values closer to 1 indicating a better fit of the model. Figure 4-4 displays these two measures for the regression models applied to the example case. Specifically, in this example, the regression model using Sa_{ave} as the EDP better predicts ductility demand (i.e., lower β) and exhibits a better fit to the data (i.e., higher R^2) compared to using Sa. On the other hand, PFA proves to be the least suitable EDP.

To narrow the choice of candidate EDPs presented in Table 4-1, the regression analyses were performed individually for each SDOF nonstructural component, with periods ranging from 0.1 to 1s (incremented by 0.1) and designed for three levels of R_{NS}. The components were mounted on the first floor and roof of the six- and 12-story buildings designed with the four different SFRSs. Figure 4-5 indicates which EDPs are most commonly the most efficient among the 480 cases of regression model analysis conducted on the SDOF nonstructural components. PFA and Sa were pre-selected for consideration in the subsequent analysis and therefore not included in this screening process. The frequency of EDPs indicates the number of cases where each EDP has the greatest efficiency, determined by the highest R^2 values obtained from the regression model analysis. Among the selected EDPs, the I_{NP} and Sa_{ave}, both representing the average of spectral accelerations over a period range, were by far the most frequent to exhibit the highest efficiency. Specifically, Sa_{ave} demonstrated the highest efficiency in 214 out of the 480 total cases. Based on these results, subsequent investigations and comparisons focus on PFA, Sa, and Sa_{ave} as the candidate EDPs, while recognizing that many of the obsevations related to Sa_{ave} would also apply to I_{NP}.

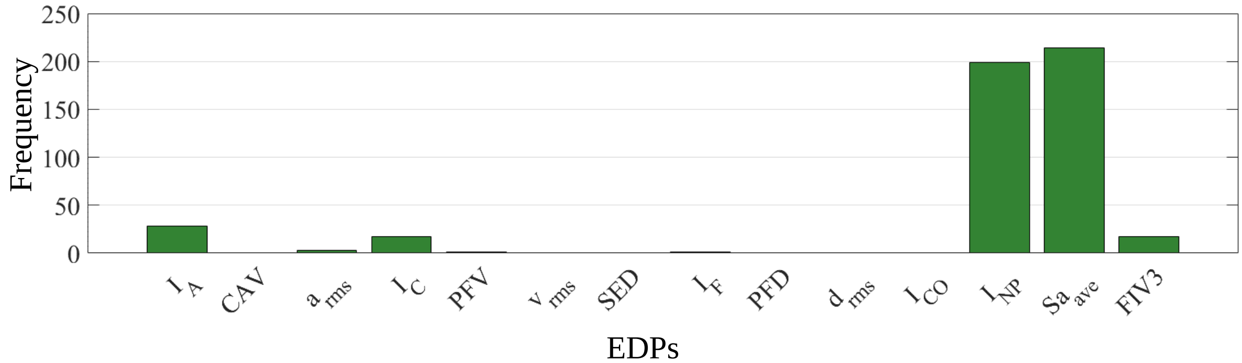

Figure 4-5. The frequency of EDPs with the highest efficiency was determined among 480 regression model analyses conducted on SDOF nonstructural components.

Figure 4-6 compares the R^2 values derived from regression models applied to the SDOF nonstructural components, designed with R_{NS} values of 1.5 and 3 and mounted on the first floor and roof of the 12-story buildings. For almost all examined SDOF nonstructural components with periods exceeding 0.5 s, the regression models employing PFA exhibited the lowest R^2 values compared to that of the EDPs of Sa and Sa_{ave}. For SDOF nonstructural components with periods between 0.2 and 0.5 s, the relative ranking of PFA, Sa, and Sa_{ave} depend on the specific type of SFRS, location in the building, and R_{NS}.Within this period range, using PFA sometimes resulted in higher R^2 values compared to either Sa or Sa_{ave}, but never the highest overall. Using PFA as an EDP for the SDOF nonstructural components with periods less than 0.2 s occasionally led to highest R^2 values, although the differences in R^2 values among the three presented EDPs were generally small.

For SDOF nonstructural components mounted on the first floor (Figure 4-6 (b)), with periods longer than 0.2 s and designed with an R_{NS} of 3, using Sa_{ave} as the EDP yields the highest R^2 values, although the difference compared to using Sa is slight. Conversely, for stronger SDOF nonstructural components (R_{NS}=1.5), Sa is slightly more efficient to Sa_{ave}. When SDOF nonstructural components are designed with a lower strength level (larger R_{NS}), they experience higher nonlinear demands, leading to an elongation of the component's effective period. In such cases, using Sa_{ave} as the EDP becomes advantageous because it accounts for the effect of this period elongation by considering a range of periods. Furthermore, it is observed that increasing R_{NS} results in higher R^2 values for all regression models using the three alternative EDPs.

For SDOF nonstructural components mounted on the roof (Figure 4-6 (a)) with periods longer than 0.2 s and designed with an R_{NS} of 1.5, using Sa as the EDP was generally the most efficient. This is because the natural periods of the buildings act as frequency content filters, which reduces the effectiveness of Sa_{ave}. Additionally, the nonstructural components designed with an R_{NS} of 1.5 exhibit relatively little nonlinearity. As a result, Sa yielded higher R^2 values compared to the regression models developed using other alternative EDPs. However, as nonlinearity increases, the efficiency of regression models based on Sa diminishes. Conversely, similar trends to those observed in Figure 4-6 (b) emerge, indicating that regression models dependent on PFA and Sa_{ave} exhibit higher R^2 as R_{NS} increases.

When comparing using Sa_{ave} for different floors where SDOF nonstructural components are mounted, it was observed that Sa_{ave} is particularly more effective for components mounted on the first floor of buildings. By averaging the spectral values over a range of periods, Sa_{ave} effectively takes into account the effects of underlying pulses in floor motions on lower floors (Eads et al., 2015). In these lower floors, frequency content filtering caused by natural periods of buildings has a lesser effect than at higher floors, while the ground motions have more influence.

Figure 4-7 replicates similar analyses as those presented in Figure 4-6, but replacing the floor motion input with the scaled ground motions as described in the previous section. This case is equivalent to the SDOF nonstructural components being mounted directly at ground level. Using PGA in regression models resulted in the highest R^2 values only for the SDOF nonstructural components with periods less than 0.2 s. For almost all SDOF nonstructural components with a period longer than 0.2 s, including all considered levels of R_{NS}, using Sa_{ave} led to the highest R^2 values in the regression models compared to using other EDPs. Also, Figure 4-7 shows that by increasing R_{NS}, the R^2 values for regression models with Sa_{ave} increase. These findings align closely with the results obtained from the regression models applied to the SDOF nonstructural components mounted on the first floor of the 12-story buildings (Figure 4-6 (b)), indicating the greater influence of the dynamic response of the SFRSs on upper floors, as has also been discussed by Sullivan et al. (2013).

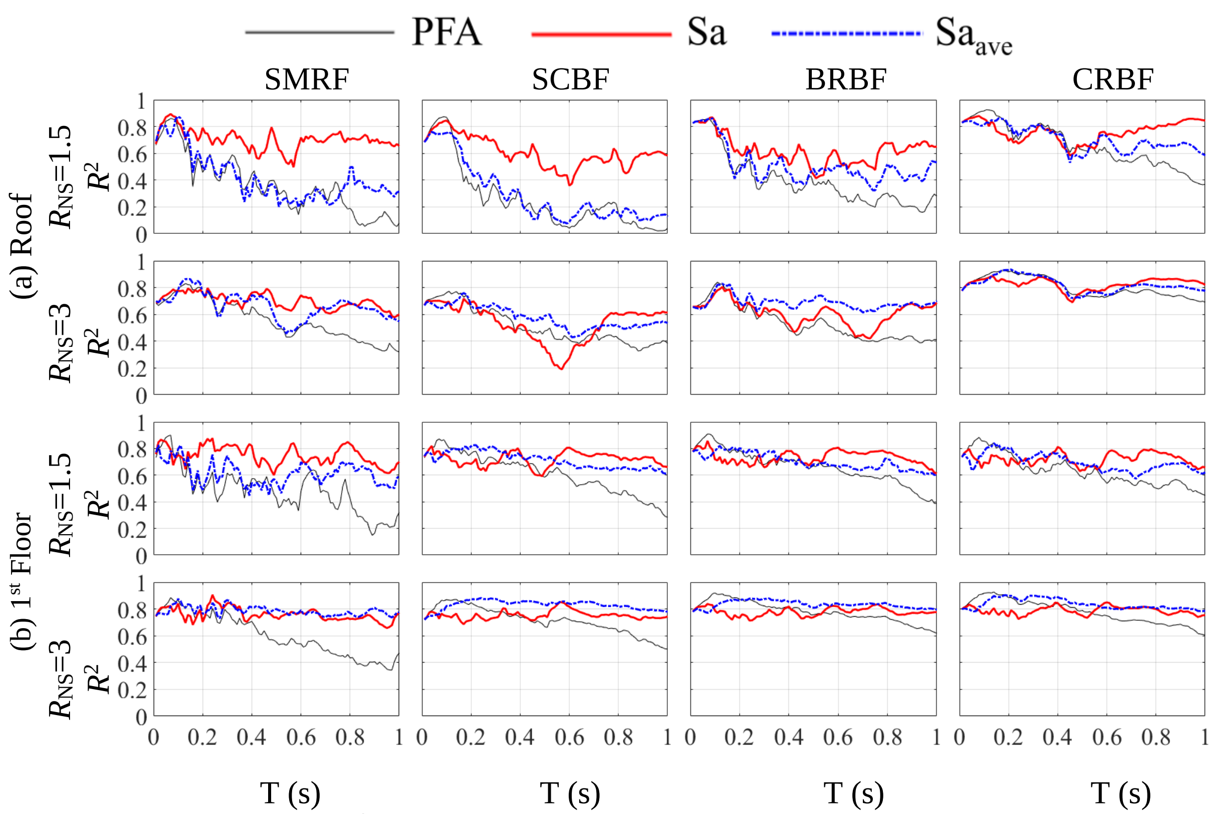

Figure 4-6. Comparing R^2 of the regression models for the SDOF nonstructural components mounted on 12-story buildings.

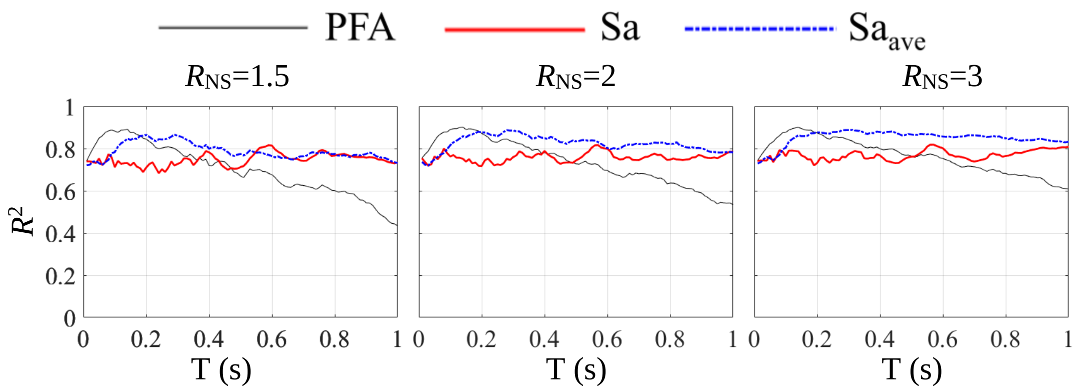

Figure 4-7. Comparing R^2 of the regression models for the SDOF nonstructural components on the ground.

Figure 4-8 presents a comparison of β values calculated from regression models applied to the same nonstructural components examined in Figure 4-6, where these components were designed with two different R_{NS} values (1.5 and 3) and were located on the first floor and roof of the 12-story buildings. Similar conclusions to those observed for the R^2 values can be drawn for the β values. In contrast to the R^2 indicator, which generally indicates that increasing R_{NS} (reducing strength) enhances the efficiency of most regression models with the three alternative EDPs, the β values slightly increase with an increase in R_{NS}, indicating a decrease in efficiency for all regression models. While higher R_{NS} resulted in increased squared residuals in both R^2 and β, R^2 was also influenced by greater SDOF ductility,which increases the denominator of R^2, making the regression appear more efficient for large values of R_{NS} even though the variability indicated by β does not reduce (Banihashemi et al., 2023).

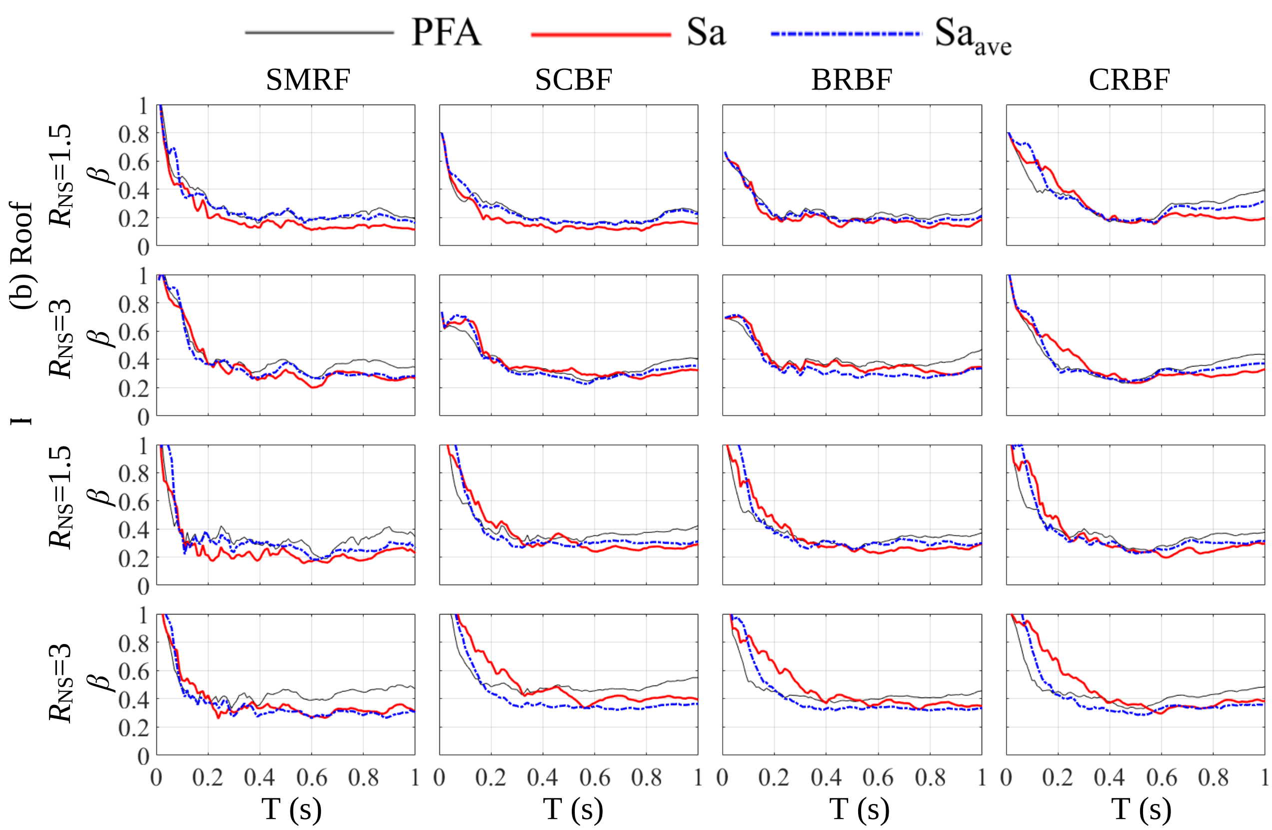

Figure 4-8. Comparing β of the regression models for the SDOF nonstructural components mounted on 12-story buildings.

4.8.2 SUFFICIENCY

In regression analysis, the concept of sufficiency refers to the adequacy of the chosen independent variable, such as the EDP, in explaining the variation observed in the dependent variable, such as μ. In this study, a sufficient EDP should demonstrate a regression that is less influenced by the SFRS of the building or the specific floors on which the SDOF nonstructural components are mounted. For the purpose of assessing this, data pairs of μ-EDP for the SDOF nonstructural components are grouped with respect to the SFRSs or the floors on which the SDOF nonstructural components were mounted.

4.8.3.1 GROUPING OF DATA AND NORMALIZATION

In Figure 4-9, an illustration of grouping μ-EDP pairs with respect to the SFRSs is presented for an SDOF nonstructural component. This specific component, with a period of 1 s and designed with R_{NS} = 3, was installed on the roof of the 12-story buildings. Figure 4-9 (a) displays a notable shift in the data of the μ-Sa(1 s) pairs, highlighting the influence of the type of SFRS on which the SDOF nonstructural component is mounted. This shift occurs because the considered SDOF nonstructural components, which were mounted on different SFRSs, were designed with varying f_y values due to the distinct floor acceleration spectra of the SFRSs. Recognizing that this issue can substantially diminish sufficiency, this shift was mitigated by normalizing the EDPs by yield acceleration (a_y), which is calculated as f_y divided by the mass of the nonstructural component. The effect of this regression model enhancement on various normalized EDPs is shown in Figure 4-9 (b). The regression models for μ-PFA and μ-Sa$_{ave}$ showed slight improvements, and the regression model for μ-Sa(1 s) improves substantially, increasing the R^2 value from 0.46 to 0.72. The same issue is also observed when grouping μ-EDP pairs according to the floors where the SDOF nonstructural components are installed, necessitating the normalization by a_y. Henceforward, since the analyses are conducted on the grouped data, all EDPs are normalized by a_y.

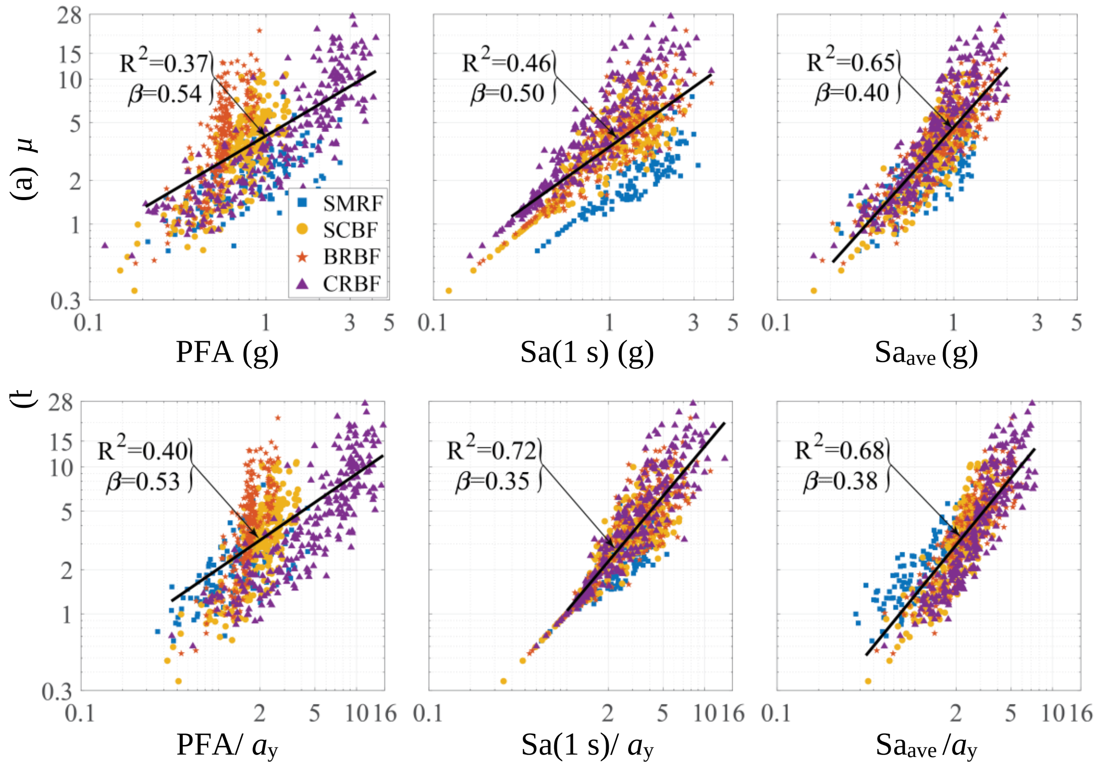

Figure 4-9. Grouping the SDOF nonstructural components, with a nonstructural period of 1 s and an R_{NS} of 3, that are installed on the roof of the building with respect to SFRSs: (a) not normalized, (b) normalized by the yield acceleration (a_y).

4.8.3.2 RELATIVE SUFFICIENCY

A completely sufficient EDP implies that no additional information would be required to predict the value of μ. This condition is quite stringent, and it is unlikely that any EDP would fully satisfy it (Ebrahimian et al., 2015). To address this challenge, Jalayer et al. (2012) introduced a relative sufficiency approach, which is based on the concept of relative entropy (Kullback and Leibler, 1951), to assess the sufficiency of one EDP compared to another. This approach is referred to as $I(\mu|\text{EDP}_2|\text{EDP}_1)$, where in this study EDP$_2$ and EDP$_1$ represent Sa or Sa$_{ave}$ and PFA, respectively. The calculation of $I(\mu|\text{EDP}_2|\text{EDP}_1)$ is as follows:

$$I(\mu|\text{EDP}_2|\text{EDP}_1) \cong \frac{1}{N}\sum_{i=1}^{N} \log_2\left(\frac{\beta_{d|\text{EDP}_1}\phi\left(\frac{\ln(\mu_i) - \ln\left(a_2(edp_2)_i{}^{b_2}\right)}{\beta_{d|EDP_2}}\right)}{\beta_{d|\text{EDP}_2}\phi\left(\frac{\ln(\mu_i) - \ln\left(a_1(edp_1)_i{}^{b_1}\right)}{\beta_{d|EDP_1}}\right)}\right) \tag{4-5}$$

where ϕ is the standardized Gaussian probability distribution function. The relative sufficiency is quantified in units of bits of information. It represents the average amount of information gained or lost about the uncertain response parameter μ when EDP_2 is known instead of EDP_1 (Ebrahimian and Jalayer, 2021). A positive value of $I(\mu|EDP_2|EDP_1)$ indicates that EDP_2 contains more information about μ compared to EDP_1, implying that EDP_2 is more sufficient. Conversely, a negative value of $I(\mu|EDP_2|EDP_1)$, implies a lower level of sufficiency of EDP_2 than EDP_1 in terms of information about μ.

To evaluate the statistical independence of the EDPs with respect to the SFRSs, Figure 4-10 compares the relative sufficiency of regression models for the SDOF nonstructural components designed with R_{NS} of 1.5 and 3 mounted on 12-story buildings. For the SDOF nonstructural components designed with an R_{NS} of 1.5 and installed on the roof, the regression models using Sa were the most sufficient ones as the calculated values of $I(\mu|Sa/\ a_y\ |PFA/\ a_y)$ were positive and greater than values of $I(\mu|Sa_{ave}\ /a_y\ |PFA/\ a_y)$. Conversely, for the SDOF nonstructural components with periods exceeding 0.2 s, designed with an R_{NS} of 3, and installed on the first story, the regression models using Sa_{ave} were the most sufficient. For the SDOF nonstructural components designed with an R_{NS} of 3 and mounted on the roof, as well as those designed with an R_{NS} of 1.5 and mounted on the first floor, the regression models using Sa and Sa_{ave} exhibited similar levels of relative sufficiency, and both were better than PFA for the most of the considered period range. However, for the SDOF nonstructural components designed with R_{NS} of 1.5 and mounted on the first floor, the regression models using Sa were slightly more sufficient than those using Sa_{ave} for the SDOF nonstructural components with a period greater than 0.6 s. The results indicate that the regression models using PFA were more sufficient than those using Sa and Sa_{ave} for the SDOF nonstructural components with a period of less than 0.2 s that were mounted on the first floor since the values of $I(\mu|Sa/\ a_y\ |PFA/\ a_y)$ and $I(\mu|Sa_{ave}\ /a_y\ |PFA/\ a_y)$ were both negative.

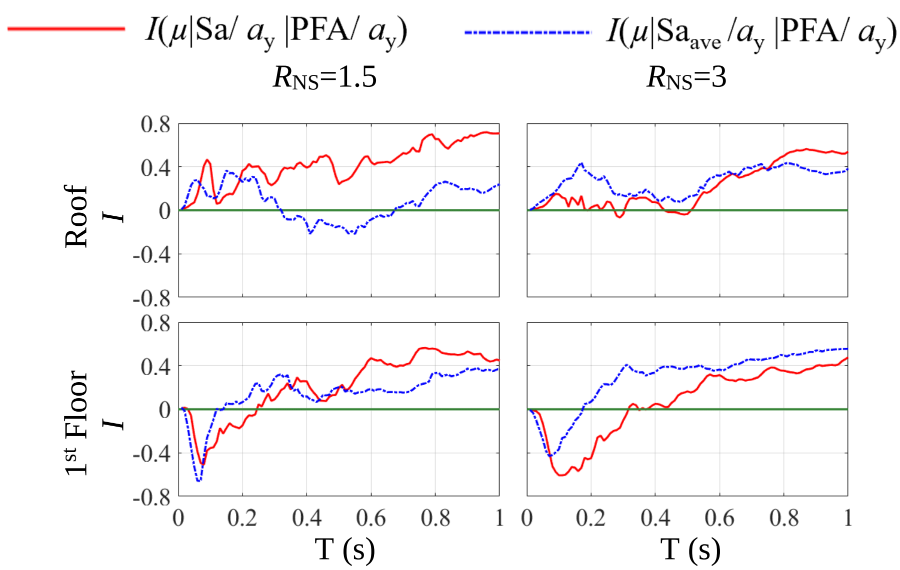

Figure 4-10. Comparing relative sufficiency, I, of the regression models for the SDOF nonstructural components designed with R_{NS} of 1.5 and 3 mounted on the 12-story buildings to assess the level of EDPs' statistical independence with respect to the SFRSs.

Figure 11 compares the relative sufficiency of regression models for the SDOF nonstructural components designed with R_{NS} of 1.5 and 3 installed on 12-story buildings in order to assess the statistical independence of the EDPs with respect to the floor where the SDOF is mounted. For the SDOF nonstructural components designed with R_{NS} of 1.5, using Sa generally resulted in more sufficient regression models regardless of the type of SFRSs. However, when R_{NS} increased to 3, the regression models using Sa and Sa_{ave} exhibited different trends depending on the SFRS. Specifically, for SDOF nonstructural components mounted on the SMRF, there was no significant difference between using Sa or Sa_{ave} in terms of sufficiency. Conversely, for those mounted on the BRBF and the SCBF, the regression models with Sa_{ave} demonstrated greater sufficiency compared to using Sa for the most of the considered nonstructural component period range. In the case of components mounted on a building with CRBFs, while Sa_{ave} exhibited greater sufficiency than Sa when the SDOF nonstructural component's period was less than 0.5 s, using Sa led to greater sufficiency for larger periods. Only for the SDOF nonstructural components with periods of shorter than 0.2 s, regression models using PFA were found to be the most sufficient among the three considered EDPs.

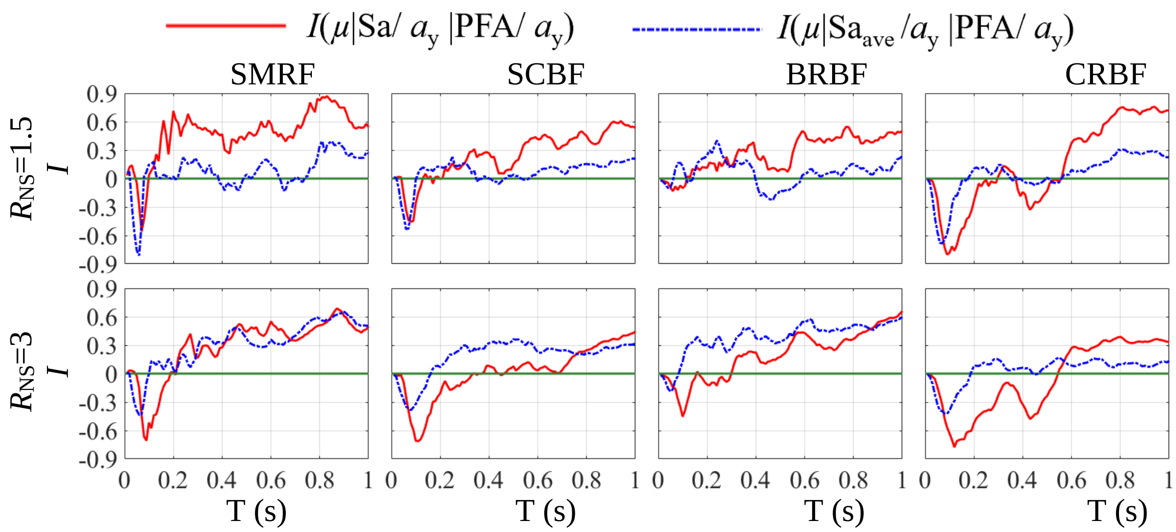

Figure 4-11. Comparing relative sufficiency, *I*, of the regression models for the SDOF nonstructural components designed with R_{NS} of 1.5 and 3 mounted on the 12-story buildings to assess the level of EDPs' statistical independence with respect to the floors.

4.9 Comparing seismic loss assessment of SDOF nonstructural components using candidate EDP-derived damage fragility curves

This section provides direct quantification of the impact of the EDP that is used to define damage fragility curves on the seismic loss estimation associated with a generic acceleration-sensitive nonstructural component, assuming a unit repair cost. To achieve this, the Monte Carlo-based methodology outlined in FEMA P-58-1 (2018) is employed. In this methodology, the response of a building is characterized by sampling EDP data (Yang et al., 2006, 2009) for each intensity level, using the selected candidate EDP. Then, the cumulative probability distribution of repair cost is calculated using damage fragility curves that are defined as a function of the selected EDPs as detailed below. This cumulative distribution of repair cost is computed at each intensity level and combined with the seismic hazard curve, to calculate the aggregate expected annual loss conditioned on the selected EDP (EAL_{EDP}).

Equation (4-1) defined four terms, M_d, $\beta_{d|EDP}$, M_c, and β_c, that describe a damage fragility curve for an SDOF nonstructural component. The values of M_d and $\beta_{d|EDP}$ are determined based on the demands of SDOF nonstructural components and were calculated using regression models conditioned on the selected EDP, as described in the previous sections. In practice, the values of M_c and β_c would be determined based on the capacities of SDOF nonstructural components as determined using laboratory tests specific to each nonstructural component. As a generic representation for this study, the value of M_c for each SDOF nonstructural component was calculated as the median of all ductility demand data at the DE intensity level. These data were obtained from analyses of all components with a given period that were mounted on the buildings with the same height and grouped with respect to both the SFRSs and the floors. This approach represents what would be expected from a single damage fragility curve for each SDOF nonstructural component with a specific period and R_{NS}. The ductility demand of a nonstructural component fully defined its damage state, implying that the capacity logarithmic standard deviation is zero ($\beta_c = 0$).

To compare the EDPs in terms of the seismic loss evaluation, an error between actual expected annual loss and EAL_{EDP} was defined as follows:

$$Error = \frac{|\mathrm{EAL}_{\mathrm{EDP}} - \mathrm{EAL}_{\mu}|}{\mathrm{EAL}_{\mu}} \times 100 \tag{4-6}$$

where EAL_μ represents the calculated actual expected annual loss through direct comparison of the generated ductilities, sampled using the method proposed by Yang et al. (2006, 2009), with the defined capacity.

Figure 4-12 compares the calculated error as defined above using the three candidate EDPs of PFA, Sa, and Sa_{ave}, normalized by a_y for the SDOF nonstructural components mounted on 12-story buildings and designed with R_{NS} of 1.5 and 3. In general, Figure 4-12 shows that using PFA was only a suitable EDP for a few SDOF nonstructural components. Employing PFA as the EDP led to a notable error, surpassing 150% in certain instances. This was particularly evident for the SDOF nonstructural components with a period longer than 0.6 seconds.

For the SDOF nonstructural components mounted on the first floor (Figure 4-12 (b)), using Sa_{ave} generally resulted in similar or even lower errors compared to using Sa, especially for SDOF nonstructural components designed with R_{NS} = 3. This indicates that using Sa_{ave} as the EDP for SDOF nonstructural components mounted on lower floors, especially those with lower strength, is more suitable.

For the SDOF nonstructural components mounted on the roof (Figure 4-12 (a)), the preferred EDP between Sa and Sa_{ave} varies depending on the strength level of the SDOF nonstructural component. When the SDOF nonstructural components were designed with R_{NS} = 1.5, using Sa resulted in lower errors for most cases. For these components, although Sa_{ave} mostly led to lower errors than PFA, there were instances where using Sa_{ave} resulted in large errors exceeding 150%. However, for the SDOF nonstructural components designed with R_{NS} of 3, using Sa_{ave} as the EDP was generally the most suitable. The error in EAL when using Sa as the EDP peaked when the period of the SDOF nonstructural component was tuned with the modal period of a braced frame building. Due to frequency filtering and resonance effects, the floor spectral acceleration tends to peak at modal periods of buildings, particularly for higher floors. When nonlinearity occurs in a SDOF nonstructural component with a period near one of the building's modal periods, the effective period of the component elongates. Consequently, if the peaks in spectral acceleration are used as the EDP, it can lead to an overestimation of the ductility demand on the SDOF nonstructural component, especially when the component is designed with lower strength and therefore exhibits greater nonlinearity.

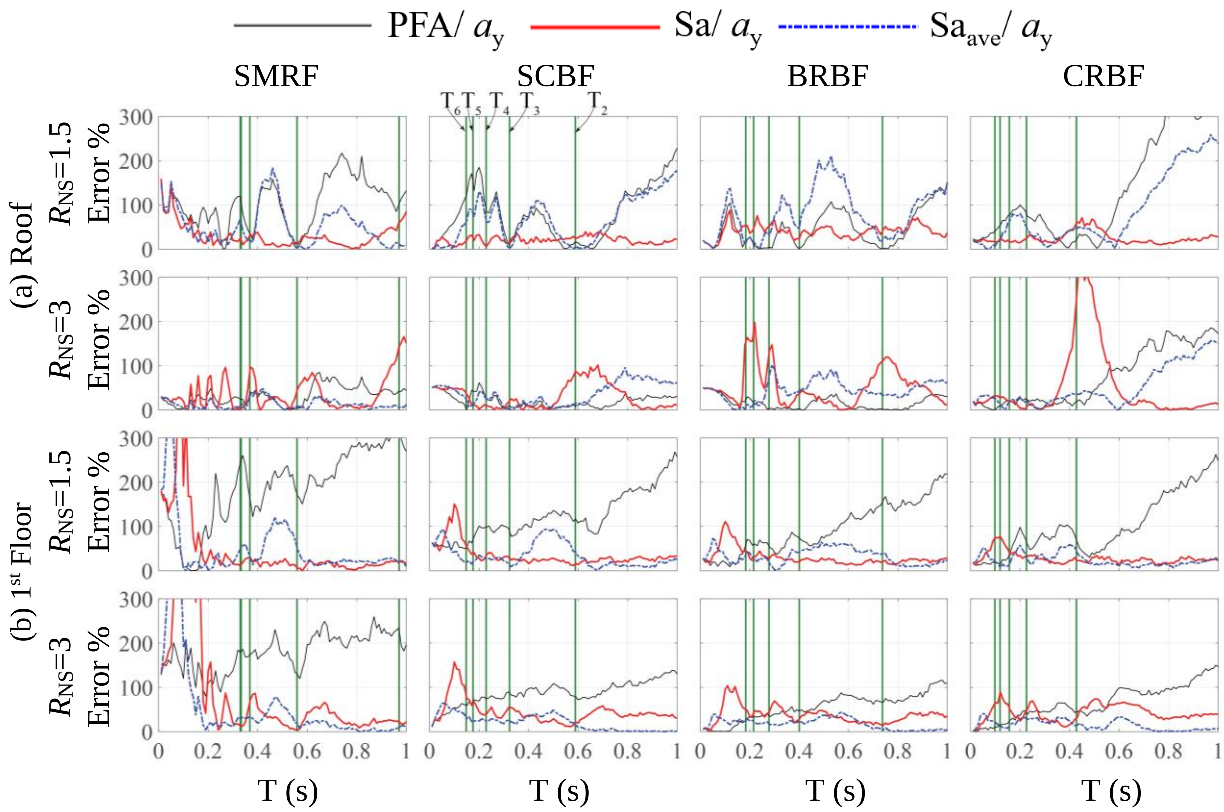

Figure 4-12. Comparing EDPs in terms of seismic loss evaluation using the error between the actual expected annual loss and the expected annual loss calculated using the selected EDP, considering the regression models with grouping based on the SFRSs and the floors.

4.10 CONCLUSIONS

The objective of this study was to identify suitable engineering demand parameters (EDPs) for developing damage fragility curves of acceleration-sensitive nonstructural components, to be used in seismic loss assessments. For this purpose, acceleration-sensitive nonstructural components were modeled as single-degree-of-freedom (SDOF) components with an elastic perfectly plastic material, a period range of 0.01 to 1 second, and varying strength levels. The SDOF nonstructural components were assumed to be installed on the first floor and roof of six-story and 12-story buildings. Each of these buildings was designed with four distinct seismic force-resisting systems (SFRSs): a special moment resisting frame (SMRF), special concentrically braced frame (SCBF), buckling-restrained braced frame (BRBF), and controlled rocking braced frame (CRBF). Nonlinear response history analyses were conducted on each building using ground motions scaled to six intensity levels, ranging from 25% of the design earthquake (DE) to 2.0 times the maximum considered earthquake (MCE). Subsequently, the SDOF nonstructural components were designed based on the median force demand caused by floor motions at the DE level, derived from the nonlinear response history analyses of each building. These components were then subjected to further nonlinear response history analyses to assess their ductility demand (μ).

In total, sixteen EDPs were examined in this chapter, with a focus on the peak floor acceleration (PFA), spectral acceleration at the period of the SDOF nonstructural component (Sa), and the geometric mean of spectral accelerations around the period of the SDOF nonstructural component (Sa_{ave}). To assess the effectiveness of defining damage fragility curves based on these EDPs, a lognormal regression model was fitted for the pairs of μ-EDP, considering ductilities greater than 1. The efficiency of candidate EDPs was assessed based on the logarithmic standard deviation (β) and R-squared (R^2) for each model. Additionally, the relative sufficiency was computed to evaluate the statistical independence of the candidate EDPs with respect to the location of the SDOF nonstructural components within the building and the type of SFRS used in the building. Furthermore, to explicitly quantify the suitability of the damage fragility curves that would be generated using the candidate EDPs, errors between the seismic loss assessments of nonstructural components using the fragility curve produced by each candidate EDP and the assessments computed directly using μ were compared for different EDPs.

Using Sa_{ave} as an EDP was found suitable for the SDOF nonstructural components on lower floors, mitigating spectral-shape bias resulting from less filtered ground motions due to the buildings' modal periods. Also, the findings suggested that when nonstructural components are designed with lower strength, leading to significant nonlinearity during earthquake shaking and subsequent elongation of their effective periods, Sa_{ave} becomes a more suitable EDP because it reflects the influence of period elongation through its calculation over a range of periods.

For SDOF nonstructural components mounted on the roof and designed with higher strength, Sa was a suitable EDP. However, for SDOF nonstructural components designed with lower strength, the use of Sa as the EDP was not appropriate due to frequency filtering, particularly for higher floors. This is because the floor spectral acceleration tends to peak near the building's modal periods, and when nonlinearity occurs in SDOF nonstructural components with periods near these structural periods, the elongation of effective period moves it away from the peak of the floor spectrum. Consequently, an EDP based on these peaks in spectral acceleration can grossly overestimate the component ductility demand, especially for weaker designs experiencing greater nonlinearity.

This study also investigated the implications of these fundamental results for developing unified damage fragility curves for nonstructural components, independent of the distinct types of SFRS and the floors of the building where the component is installed. To evaluate the relative sufficiency of different EDPs for this, the μ-EDP data was grouped based on the types of SFRS and the installation locations of SDOF nonstructural components within the buildings. The analysis revealed notable shifts between the grouped data sets, especially when Sa was used as the EDP, given that SDOF nonstructural components were designed with varying strengths based on the type of SFRS and the building floors they are mounted on. As an alternative approach, this study proposed normalizing the EDP by the yield acceleration (a_y) of SDOF nonstructural components in order to mitigate the observed shifts in data.

While most currently developed damage fragility curves for acceleration-sensitive nonstructural components are constructed based on PFA, the findings of this study underscore the limitations of using PFA as an EDP for accurate damage estimation. The spectral acceleration at the period of the nonstructural component was generally the most suitable considered EDP for nonstructural components with limited ductility demand, while an average spectral acceleration was more suitable when the ductility demand was more extensive. This suggests that a ductility-dependent EDP, reflecting the average spectral acceleration over a range of periods that extends as the ductility increases, would likely be more effective. The intensity measures that have been shown to be effective for characterizing ground motions may not be effective as EDPs to characterize floor motions, because of the significant difference in spectral shape.

Considering the vast library of PFA-based damage fragility curves that have been developed for acceleration-sensitive nonstructural components, replacing these fragility curves with ones that are based on a more suitable EDP would be a significant undertaking. In the meantime, the recommendation arising from this study is to take caution when using existing damage fragility curves for nonstructural components with natural periods exceeding 0.1 s, as the peak floor acceleration is not a reliable indicator of damage to these more flexible acceleration-sensitive nonstructural components.

4.11 ACKNOWLEDGEMENTS

This research was made possible thanks to the financial support provided by the Natural Sciences and Engineering Research Council of Canada (NSERC) and the Ontario Early Researcher Awards program.

4.12 REFERENCES

Adam, C., Kampenhuber, D., and Ibarra, L. F., 2017. Optimal intensity measure based on spectral acceleration for P-delta vulnerable deteriorating frame structures in the collapse limit state. *Bulletin of Earthquake Engineering*, **15**(10), 4349–4373. Springer Netherlands. DOI: https://doi.org/10.1007/s10518-017-0129-3

ANSI/AISC 341-16, 2016. *Seismic provisions for structural steel buildings*. Chicago, IL, United States: American Institute of Steel Construction.

ANSI/AISC 358-16, 2016. *Prequalified connections for special and intermediate steel moment frames for seismic applications*. Chicago, IL, United States: American Institute of Steel Construction. Retrieved from https://www.aisc.org/globalassets/aisc/publications/standards/a358-20w.pdf

ANSI/AISC 360-16, 2016. *Specification for structural steel buildings*. *ANSI/AISC 360-16*. Chicago, IL, United States: American Institute of Steel Construction.

Arias, A., 1970. A measure of earthquake intensity. *Seismic design for nuclear plants*, 438–483.

ASCE/SEI 7-16, 2016. *Minimum design loads and associated criteria for buildings and other structures*. Reston, VA, United States: American Society of Civil Engineers.

Banihashemi, A., Wiebe, L., and Filiatrault, A., 2023. Engineering demand parameters for acceleration-sensitive nonstructural components: comparison between peak floor acceleration and spectral acceleration. *Pacific conference on earthquake engineering*. Vancouver, British Columbia.

Banihashemi, M., 2023. Strategies to reduce seismic losses and improve seismic loss assessment. *Ph.D. Thesis*. Hamilton, Canada: McMaster University.

Bianchini, M., Diotallevi, P., and Baker, J., 2009. Prediction of inelastic structural response using an average of spectral accelerations. *10th international conference on structural safety and reliability (ICOSSAR09)* (pp. 2164–2171).

De Biasio, M., Grange, S., Dufour, F., Allain, F., and Petre-Lazar, I., 2014. A simple and efficient intensity measure to account for nonlinear structural behavior. *Earthquake Spectra*, **30**(4), 1403–1426. Earthquake Engineering Research Institute. DOI: https://doi.org/10.1193/010614EQS006M

Bojórquez, E., and Iervolino, I., 2011. Spectral shape proxies and nonlinear structural response. *Soil Dynamics and Earthquake Engineering*, **31**(7), 996–1008. DOI: https://doi.org/10.1016/j.soildyn.2011.03.006

Bradley, B. A., Dhakal, R. P., MacRae, G. A., and Cubrinovski, M., 2010. Prediction of spatially distributed seismic demands in specific structures: Structural response to loss estimation. *Earthquake Engineering and Structural Dynamics*, **39**(6), 591–613. John Wiley and Sons Ltd. DOI: https://doi.org/10.1002/eqe.955

Cordova, P. P., Deierlein, G. G., Mehanny, S. S., and Cornell, C. A., 2000. *Development of a two-parameter seismic intensity measure and probabilistic assessment procedure*. The second US-Japan workshop on performance-based earthquake engineering methodology for reinforced concrete building structures

Cornell, C. A., Jalayer, F., Hamburger, R. O., and Foutch, D. A., 2002. Probabilistic basis for 2000 SAC federal emergency management agency steel moment frame guidelines. *Journal of Structural Engineering*, **128**(4), 526–533. DOI: https://doi.org/10.1061/(ASCE)0733-9445(2002)128:4(526)

Dávalos, H., and Miranda, E., 2019. Filtered incremental velocity: A novel approach in intensity measures for seismic collapse estimation. *Earthquake Engineering and Structural Dynamics*, **48**(12), 1384–1405. John Wiley and Sons Ltd. DOI: https://doi.org/10.1002/eqe.3205

Dhakal, R. P., 2010. Damage to non-structural components and contents in 2010 Darfield earthquake. *Bulletin of the New Zealand Society for Earthquake Engineering*, **43**(4), 404–411. DOI: https://doi.org/10.5459/bnzsee.43.4.404-411

Eads, L., Miranda, E., and Lignos, D. G., 2015. Average spectral acceleration as an intensity measure for collapse risk assessment. *Earthquake Engineering and Structural Dynamics*, **44**(12), 2057–2073. John Wiley and Sons Ltd. DOI: https://doi.org/10.1002/eqe.2575

Ebrahimian, H., and Jalayer, F., 2021. Selection of seismic intensity measures for prescribed limit states using alternative nonlinear dynamic analysis methods. *Earthquake Engineering and Structural Dynamics*, **50**(5), 1235–1250. Hokkaido, Japan: John Wiley and Sons Ltd. DOI: https://doi.org/10.1002/eqe.3393

Ebrahimian, H., Jalayer, F., Lucchini, A., Mollaioli, F., and Manfredi, G., 2015. Preliminary ranking of alternative scalar and vector intensity measures of ground shaking. *Bulletin of Earthquake Engineering*, **13**(10), 2805–2840. Kluwer Academic Publishers. DOI: https://doi.org/10.1007/s10518-015-9755-9

Fajfar, P., Vidic, T., and Fischinger, M., 1990. A measure of earthquake motion capacity to damage medium-period structures. *Soil Dynamics and Earthquake Engineering*, **9**(5), 236–242. DOI: https://doi.org/10.1016/S0267-7261(05)80002-8

FEMA P-58-1, 2018. *Seismic performance assessment of buildings volume 1-methodology*. Washington, DC, United States: prepared by the Applied Technology Council for the Federal Emergency Management Agency.

FEMA P-58-3, 2018. *Seismic Performance Assessment of Buildings, Volume 3–Supporting Electronic Materials and Background Documentation: 3.1 Performance Assessment Calculation Tool (PACT)*. Version 3.1.2. Washington, DC, United States: prepared by the Applied Technology Council for the Federal Emergency Management Agency.

FEMA P695, 2009. *Quantification of Building Seismic Performance Factors*. Washington, DC, United States: prepared by the Applied Technology Council for the Federal Emergency Management Agency.

Filiatrault, A., and Sullivan, T., 2014. Performance-based seismic design of nonstructural building components: The next frontier of earthquake engineering. Earthquake Engineering and Engineering Vibration, 13(1), 17–46. DOI: https://doi.org/10.1007/s11803-014-0238-9

Housner, G., 1975. Measures of severity of earthquake ground shaking. *Proceedings of US National Conference on Earthquake Engineering*.

Housner, G. W., and Jennings, P. C., 1982. *Earthquake design criteria*. Berkeley, CA: Earthquake Engineering Research Institute. Retrieved from http://ezproxy.cul.columbia.edu/login?url=http://search.proquest.com/docview/23562184?accountid=10226%5Cnhttp://rd8hp6du2b.search.serialssolutions.com/?ctx_ver=Z39.88-2004&ctx_enc=info:ofi/enc:UTF-8&rfr_id=info:sid/Earthquake+Engineering+Abstracts&rft_val

Hwang, S. H., and Lignos, D. G., 2017. Earthquake-induced loss assessment of steel frame buildings with special moment frames designed in highly seismic regions. *Earthquake Engineering and Structural Dynamics*, **46**(13), 2141–2162. John Wiley and Sons Ltd. DOI: https://doi.org/10.1002/eqe.2898

Jalayer, F., Beck, J. L., and Zareian, F., 2012. Analyzing the sufficiency of alternative scalar and vector intensity measures of ground shaking based on information theory. *Journal of Engineering Mechanics*, **138**(3), 307–316. American Society of Civil Engineers (ASCE). DOI: https://doi.org/10.1061/(ASCE)EM.1943-7889.0000327

Jalayer, F., and Cornell, C., 2009. Alternative non-linear demand estimation methods for probability-based seismic assessments. *Earthquake Engineering and Structural Dynamics*, **38**(8), 951–972. DOI: https://doi.org/10.1002/eqe.876

Jalayer, F., De Risi, R., and Manfredi, G., 2015. Bayesian Cloud Analysis: Efficient structural fragility assessment using linear regression. *Bulletin of Earthquake Engineering*, **13**(4), 1183–1203. Kluwer Academic Publishers. DOI: https://doi.org/10.1007/s10518-014-9692-z

Kazantzi, A. K., and Vamvatsikos, D., 2015. Intensity measure selection for vulnerability studies of building classes. *Earthquake Engineering and Structural Dynamics*, **44**(15), 2677–2694. John Wiley and Sons Ltd. DOI: https://doi.org/10.1002/eqe.2603

Kullback, S., and Leibler, R. A., 1951. On information and sufficiency. *The Annals of Mathematical Statistics*, **22**(1), 79–86. DOI: https://doi.org/10.1214/aoms/1177729694

Miranda, E., Mosqueda, G., Retamales, R., and Pekcan, G., 2012. Performance of nonstructural components during the 27 February 2010 Chile earthquake. *Earthquake Spectra*, **28**(S1), S453–S471. DOI: https://doi.org/10.1193/1.4000032

Mollaioli, F., Lucchini, A., Cheng, Y., and Monti, G., 2013. Intensity measures for the seismic response prediction of base-isolated buildings. *Bulletin of Earthquake Engineering*, **11**(5), 1841–1866. DOI: https://doi.org/10.1007/s10518-013-9431-x

Newmark, N. M., and Hall, W. J., 1982. Earthquake spectra and design. *Engineering* *monographs on earthquake criteria*.

Nielson, B. G., and DesRoches, R., 2007. Seismic fragility methodology for highway bridges using a component level approach. *Earthquake Engineering and Structural Dynamics*, **36**(6), 823–839. John Wiley and Sons Ltd. DOI: https://doi.org/10.1002/eqe.655

NIST, 2018. Recommendations for improved seismic performance of nonstructural components. National Institute of Standards and Technology. Gaithersburg, MD. DOI: https://doi.org/10.6028/NIST.GCR.18-917-43

Padgett, J. E., Nielson, B. G., and DesRoches, R., 2008. Selection of optimal intensity measures in probabilistic seismic demand models of highway bridge portfolios. *Earthquake Engineering and Structural Dynamics*, **37**(5), 711–725. John Wiley and Sons Ltd. DOI: https://doi.org/10.1002/eqe.782

Park, Y., Ang, A. H. -S., and Wen, Y. K., 1985. Seismic Damage Analysis of Reinforced Concrete Buildings. *Journal of Structural Engineering*, **111**(4), 740–757. DOI: https://doi.org/10.1061/(ASCE)0733-9445(1985)111:4(740)

Perrone, D., Calvi, P. M., Nascimbene, R., Fischer, E. C., and Magliulo, G., 2019. Seismic performance of non-structural elements during the 2016 Central Italy earthquake. *Bulletin of Earthquake Engineering*, **17**, 5655–5677. Springer Netherlands. DOI: https://doi.org/10.1007/s10518-018-0361-5

Reed, J. W., and Kassawara, R. P., 1990. A criterion for determining exceedance of the operating basis earthquake. *Nuclear Engineering and Design*, **123**(2–3), 387–396. DOI: https://doi.org/10.1016/0029-5493(90)90259-Z

Sarma, S. K., 1971. Energy flux of strong earthquakes. *Tectonophysics*, **11**(3), 159–173. DOI: https://doi.org/10.1016/0040-1951(71)90028-X

Di Sarno, L., and Pugliese, F., 2021. Effects of mainshock-aftershock sequences on fragility analysis of RC buildings with ageing. *Engineering Structures*, **232**. Elsevier Ltd. DOI: https://doi.org/10.1016/j.engstruct.2020.111837

Saxey, B., and Daniels, M., 2014. *Characterization of overstrength factors for buckling restrained braces*. *Proc of the 2014 Australasian Structural Engineering Conference (ASEC), Auckland, New Zealand*. Auckland, New Zealand: Proc of the 2014 Australasian Structural Engineering Conference.

Steele, T., and Wiebe, L., 2016. Dynamic and equivalent static procedures for capacity design of controlled rocking steel braced frames. *Earthquake Engineering and Structural Dynamics*, **45**(14), 2349–2369. DOI: https://doi.org/10.1002/eqe.2765

Sullivan, T. J., Calvi, P. M., and Nascimbene, R., 2013. Towards improved floor spectra estimates for seismic design. *Earthquake and Structures*, **4**(1), 109–132. Techno Press. DOI: https://doi.org/10.12989/eas.2013.4.1.109

Tothong, P., and Luco, N., 2007. Probabilistic seismic demand analysis using advanced ground motion intensity measures. *Earthquake Engineering and Structural Dynamics*, **36**(13), 1837–1860. John Wiley and Sons Ltd. DOI: https://doi.org/10.1002/eqe.696

Trifunac, M., and Novikova, E., 1994. *State of the art review on strong motion duration*. Vienna, Austria: Proceedings of the Tenth European conference on earthquake engineering.

Vargas-Alzate, Y. F., Hurtado, J. E., and Pujades, L. G., 2022. New insights into the relationship between seismic intensity measures and nonlinear structural response. *Bulletin of Earthquake Engineering*, **20**(5), 2329–2365. Springer Science and Business Media B.V. DOI: https://doi.org/10.1007/s10518-021-01283-x

Vargas-Alzate, Y. F., Pujades, L. G., Barbat, A. H., and Hurtado, J. E., 2019. An efficient methodology to estimate probabilistic seismic damage curves. *Journal of Structural Engineering*, **145**(4), 04019010. American Society of Civil Engineers (ASCE). DOI: https://doi.org/10.1061/(ASCE)ST.1943-541X.0002290

Wiebe, L., and Christopoulos, C., 2015. Performance-based seismic design of controlled rocking steel braced frames. I: methodological framework and design of base rocking joint. *Journal of Structural Engineering*, **141**(9), 04014226. DOI: https://doi.org/10.1061/(ASCE)ST.1943-541X.0001202

Yang, T. Y., Moehle, J., Stojadinovic, B., and Kiureghian, D., 2006. An application of PEER performance-based earthquake engineering methodology. *8th U.S. National Conference on Earthquake Engineering*.

Yang, T. Y., Moehle, J., Stojadinovic, B., and Kiureghian, D., 2009. Seismic performance evaluation of facilities: methodology and implementation. *Journal of Structural Engineering*, **135**(10), 1146–1154. DOI: https://doi.org/10.1061/(ASCE)0733-9445(2009)135:10(1146)

Chapter 5

5. Consequences of consequence models: the impact of economies of scale on seismic loss estimates

5.1 Abstract

The detailed evaluation of expected losses and damage experienced by structural and nonstructural components is a fundamental part of performance-based seismic design and assessment. The FEMA P-58 methodology represents the state of the art in this area. Increasing interest in improving structural performance and community resilience has led to widespread adoption of this methodology and the library of component models published with it. This study focuses on the modeling of economies of scale for repair cost calculation and specifically highlights the lack of a definition for aggregate damage, a quantity with considerable influence on the component repair costs. The chapter illustrates the highly variable and often substantial impact of damage aggregation that can alter total repair costs by more than 25%. Four so-called edge cases representing different damage aggregation methods are introduced to investigate which components experience large differences in their repair costs and under what circumstances. A three-step evaluation strategy is proposed that allows engineers to quickly evaluate the potential impact of damage aggregation on a specific performance assessment. This helps users of currently available assessment tools to recognize and communicate this uncertainty even when the tools they use only support one particular damage aggregation method. A case study of a nine-story building illustrates the proposed strategy and the impact of this ambiguity on the performance of a realistic structure. The chapter concludes with concrete

recommendations towards the development of a more sophisticated model for repair consequence calculation.

KEYWORDS: FEMA P-58; Consequence functions; Repair costs and downtime; Seismic loss assessment

5.2 INTRODUCTION

The primary objective of conventional seismic design and retrofit of buildings is to keep collapse risk below a pre-defined threshold by ensuring sufficiently high strength and ductility at the building level (ACI 318-19, 2019; ANSI/AISC 341-16, 2016; EN 1998-1:2008, 2008). Experiences from large earthquakes at the end of the 20th century confirmed that such designs indeed prevent collapse and achieve life safety objectives, but the same experiences also highlighted the substantial economic consequences of structural damage in buildings that did not collapse (McKevitt et al., 1995; Tremblay et al., 1996). These observations pointed out the need to limit the amount of damage and corresponding monetary losses under smaller, more frequent seismic events. Over the last decades, substantial research effort has been dedicated to developing a framework for the simulation of seismic damage and losses in buildings so that engineers and other stakeholders can better communicate these outcomes and make more effective design and retrofit decisions. The Pacific Earthquake Engineering Research (PEER) center developed a performance-based earthquake engineering framework that simulates the seismic performance of structural and non-structural components of a building to arrive at estimates of so-called decision variables such as repair cost, downtime, and casualties (Cornell and Krawinkler, 2000; Miranda and Aslani, 2003; Moehle and Deierlein, 2004). The PEER framework quantifies and propagates various sources of uncertainty in the seismic hazard phenomena and structural behavior. The framework decouples models that describe the intensity of the seismic event (IM – intensity measure), the structural response (EDP – Engineering Demand Parameter), the expected damage (DM – Damage Measure) and the consequences of damages (DV – Decision Variable). These models are combined by applying the theorem of total probability three times, which leads to the following triple integral that has become ubiquitous in structural performance assessment (Attary et al., 2017; Barbato et al., 2013; Ciampoli et al., 2011):

$$G(DV) = \iiint G(DV|DM) \cdot |dG(DM|EDP)| \cdot |dG(EDP|IM)| \cdot |d\lambda(IM)| \tag{5-1}$$

where $G()$ is the complementary cumulative distribution function or exceedance function, and $\lambda()$ is the hazard intensity exceedance function also known as the hazard curve.

Finding a closed-form solution for this triple integral is challenging because the underlying models are typically complex and nonlinear. The PEER framework was used in the ATC-58 project to develop the FEMA P-58 methodology (FEMA P-58-1, 2018) that provides a numerical approach to estimate the triple integral through Monte Carlo simulation. The ATC-58 project also prepared a library of fragility curves and consequence functions that provide parameters of damage and consequence models for over 700 common structural and nonstructural components in typical buildings. This library is used by researchers and practitioners to implement the methodology in practice. Based on the guidelines in FEMA P-58, several software tools have been developed and are currently available to the engineering community to facilitate further research and practical adoption of seismic performance assessment (e.g., FEMA P-58-3, 2018; Haselton Baker Risk Group, 2020; Zsarnóczay and Deierlein, 2020).

FEMA P-58 influenced the performance-based design procedures developed for structural retrofits (ASCE/SEI 41-17, 2017) and tall buildings (LATBSDC, 2020; TBI, 2017) that use simulated structural response, damage, and loss values to arrive at designs that achieve pre-defined damage and loss limitation objectives. Lessons learned from earthquakes of the last decade (Shrestha et al., 2021; Stevenson et al., 2011) pointed out the need to better understand and constrain damage consequences, especially the time it takes for buildings to regain basic functionality before completing all repair interventions. Several research groups and institutions are developing guidelines (EERI, 2019; FEMA P-2090 / NIST SP-1254, 2021) and simulation methods (ATC 138-3, 2021; Molina Hutt et al., 2022; Terzic et al., 2021) to support an extension of existing design procedures with regulations that effectively limit so-called functional recovery times. The influence of the correlation between damage to different components is another important issue that will require further investigation in future studies.

Both performance-based design and functional recovery time calculations rely on the FEMA P-58 methodology to simulate the earthquake consequences (i.e., decision variables) for each building component. The FEMA P-58 methodology is currently being reviewed and updated within the scope of the ATC 138 project. One of the anticipated major updates is the introduction of correlation between component vulnerabilities to simulate more realistic damages in the building. The updated methodology will yield different damage and loss results, but the authors are not aware of any changes that would address the problem presented in this study. Although introducing correlated component vulnerabilities will result in different quantities of damaged components across the building, based on the currently available information, the problem presented below will still affect the consequence calculations.

This chapter focuses on ambiguity in consequence modeling as per FEMA P-58 that can have a significant impact on the simulated repair costs and repair times and affect performance assessment, design, and functional recovery time calculation. The FEMA P-58 methodology involves five main steps for calculating repair consequences for each realization of a Monte Carlo simulation (Figure 5-1): 1) the response of a building is characterized by sampling Engineering Demand Parameters (EDPs) conditioned on intensity measures that represent the local seismic hazard; 2) the building is checked for irreparable damage due to either collapse or excessive residual drift; 3) each building component's Damage State (DS) is calculated using EDP realizations from step 1 and component-specific fragility functions; 4) the unit repair cost of each damaged component is calculated using aggregated damaged quantities and the consequence model associated with each DS; and 5) the product of unit repair costs and damaged quantities is aggregated across all components in the building.

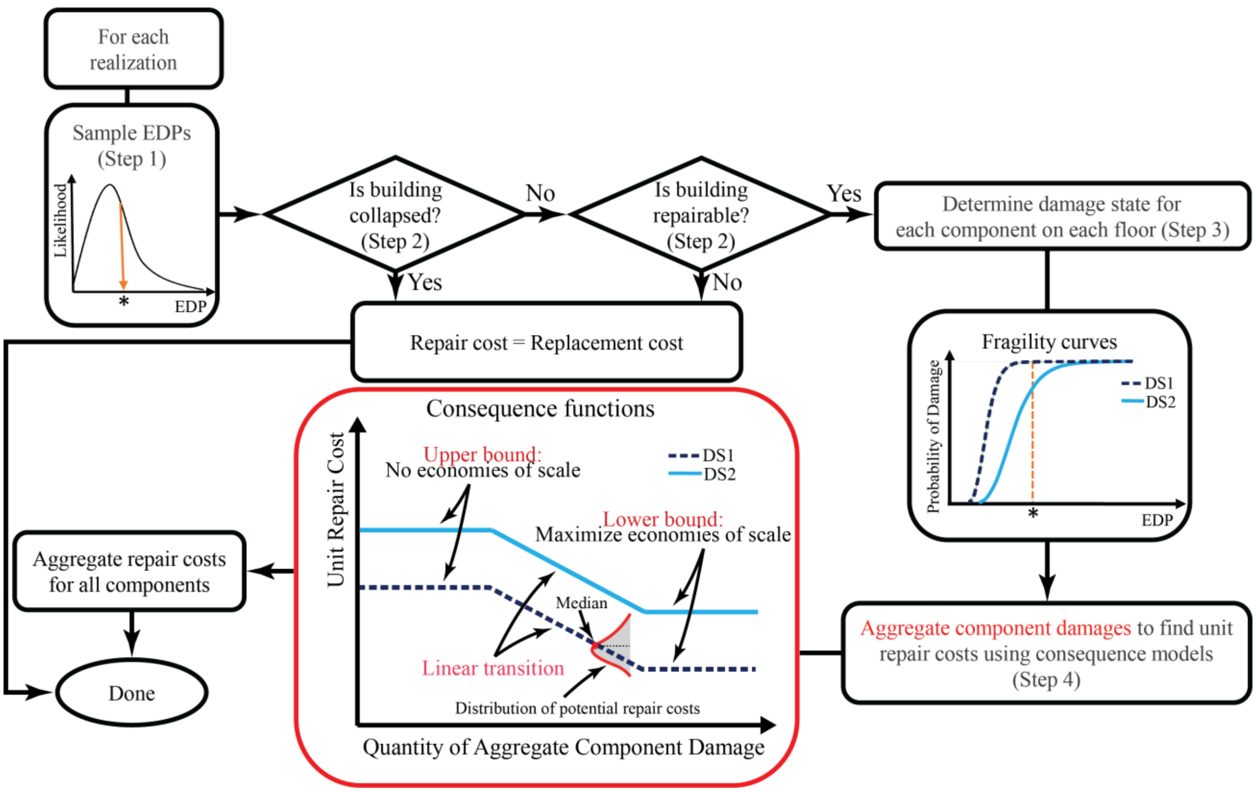

Figure 5-1. Flowchart of the FEMA P-58 methodology for the total repair cost calculation.

This chapter focuses on the consequence models used in step 4 of the procedure. These models describe damage effects (FEMA P-58-1, 2018) using distributions of probable consequences, such as repair cost and time. The shape of a typical median consequence function associated with a specific damage state is illustrated in the red box in Figure 5-1. The aggregate quantity of damaged components is used as an input to consequence functions to determine the median unit repair cost for each damaged component. The applied unit repair cost is then determined by sampling a random distribution of potential repair costs assuming either a normal or a lognormal distribution with a pre-defined variance and using the median unit repair cost determined from the consequence function. Upper and lower bound quantities introduce economies of scale or operational efficiencies in the model to consider the cost savings when similar repairs are performed multiple times, or the same preparations affect multiple repairs in the building. Examples of operations affected by economies of scale include removal or protection of contents close to a damaged area, procurement and delivery of new materials, and clean-up and replacement of contents are. If fewer components are damaged than the lower bound quantity, no economies of scale are considered; if more components are damaged than the upper bound quantity, all reasonable economies of scale and operational efficiencies are considered, resulting in the lowest possible median unit repair cost. Median consequences for intermediate quantities are calculated with linear interpolations.

The FEMA P-58 manual lacks specific instructions on computing the aggregate damage (i.e., the quantity of aggregate component damage used to evaluate the impact of economies of scale when determining the median consequence), resulting in different possible interpretations and corresponding repair cost estimates. The main objective of this study is to review how different approaches for calculating the aggregate damage affect seismic loss estimation through economies of scale and highlight the practical scenarios when the results are substantially affected by the adopted interpretation. Four approaches are reviewed in detail as edge cases to characterize the domain of all possible interpretations of aggregate damage within the scope of FEMA P-58. The following sections explore which component types are more sensitive to the interpretation of the economies of scale and the other parameters of a seismic performance assessment that can have substantial impact on this part of the repair cost calculation. The findings are illustrated through the detailed seismic loss assessment of a nine-story building equipped with various nonstructural and structural components. The last part of the chapter discusses the advantages of developing a more comprehensive approach that could leverage research developments since the publication of FEMA P-58 and encourage future work in this area. Although this chapter focuses on repair costs when describing the impact of possible interpretations on consequences, it is important to emphasize that the same issue arises with repair time simulation as well.

5.3 Aggregate calculation damage in a FEMA P-58 analysis

Two main questions arise when calculating aggregate damage of a particular component type to evaluate the impact of economies of scale in a consequence model: 1) Do repairs across different repair tasks (i.e., different Damage States) include similar operations that could lead to cost reductions when multiple repair tasks need to be performed simultaneously in the same location?; and 2) do we expect cost reductions when identical repair tasks are performed at different locations across the building, or should only damages on the floors that are repaired at the same repair phase be taken into account? The answers to these questions lead to four interpretations of the aggregate damage calculation that we consider edge cases and use to discuss the range of all possible interpretations: approach

1. <u>All damage states, all floors</u>: Aggregate damage across all floors and from every damage state. The assumption behind this interpretation is that economies of scale are applied to all

damaged items regardless of the severity of damage and the location of the item. For instance, this assumption can account for economies of scale in crew mobilization and material costs that can be spread over items on different floors and in different damage states. This approach is used in the current version of the Performance Assessment Calculation Tool (PACT) developed within the scope of FEMA P-58 (FEMA P-58-3, 2018). Although PACT uses this approach, it is not explicitly supported or discussed in the FEMA P-58 documentation. SP3, a widely used commercial tool that implements the FEMA P-58 methodology (Haselton Baker Risk Group, 2020), also uses this approach (Haselton and DeBock, 2023).

2. <u>Individual damage state, all floors</u>: Aggregate damage across all floors but only from one damage state of interest at a time. This approach has been employed in recent publications on consequence functions (e.g. (Vecchio et al., 2020)). According to this interpretation, economies of scale are applied to all damaged items within a particular damage state regardless of their location. This assumption is reasonable when repair costs are not shared by items in different damage states. For example, a damaged component that must be replaced entirely requires different repair operations and corresponding materials and labor than the same type of component with only cosmetic damage. The current version of the Pelicun software (Zsarnóczay and Kourehpaz, 2021) developed by the NHERI Computational Modeling and Simulation Center (Deierlein et al., 2020) employs this approach by default.

3. <u>All damage states, individual floor</u>: Aggregate damage on the floor of interest from every damage state. In this interpretation, economies of scale are applied only to damaged items on the same floor regardless of the severity of their damage. This assumption is reasonable for

repair operations that are shared by components on the same floor, such as removing and reinstalling mechanical systems to gain access to components that need to be repaired.

4. Individual damage state, individual floor: Aggregate damage only on one floor and from one damage state of interest at a time. This edge case combines the two restrictive conditions presented in Cases 2 and 3 above. It is a reasonable model for components with repair actions and operations that are shared only between similarly damaged items that are repaired within the same floor.

5.3.1 ILLUSTRATIVE EXAMPLE OF AGGREGATE DAMAGE CALCULATION FOR PARTITION WALLS

To illustrate how the four interpretations introduced above influence the repair calculation in a FEMA P-58 analysis, ten units of partition walls are considered on each floor of a two-story building. Table 5-1 shows quantities of damaged items for the considered partition wall components on each floor and in each damage state for a single damage realization. The repair consequence functions provided in the FEMA P-58 library for the partition wall component C1011.001b were used and median repair costs were used directly as deterministic consequences for the sake of clarity in the example. The total costs to repair the partition walls in the building, estimated using the four different interpretations for aggregate damage, are also shown in Table 5-1. Figure 5-2 shows the consequence functions for this component and illustrates the evaluation of unit repair costs for each interpretation.

The total repair cost is approximately three times higher for Case 4 (i.e., "Individual damage state, individual floor") than for Case 1 (i.e., "All damage states, all floors"). Case 1 yields the lowest total repair cost since maximum economies of scale are applied, which means the minimum unit repair costs are assigned to all damaged components, regardless of their floor or damage state. In Case 4, on the other hand, a higher unit repair cost is assigned to damaged items (Figure 5-2), because the smaller aggregate damage quantities lead to less cost savings through economies of scale. The total repair costs in Case 2 (i.e., "Individual damage state, all floors") and Case 3 (i.e., "All damage states, individual floor") are nearly the average of those calculated for Cases 1 and 4. The observed variation in total repair costs is solely attributable to the method used to aggregate damages for modeling economies of scale.

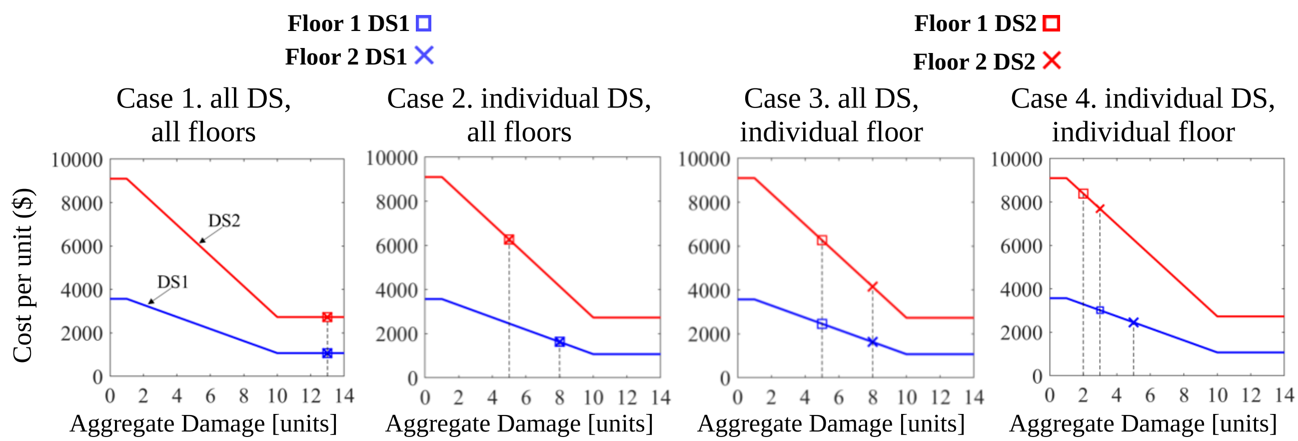

Figure 5-2. Illustrative example of the four interpretations to estimate unit repair cost of a component in two damage states (DS) across two floors in a building.

Table 5-1. Illustrative example of the four interpretations to estimate the total repair cost of a component in two damage states (DS) across two floors in a building.

		Floor 1 DS1	Floor 2 DS1	Floor 1 DS2	Floor 2 DS2	Total component repair cost [$]
Quantity of damaged components [units]		3	5	2	3	
Case 1. All damage states, all floors	Aggregate damage	13	13	13	13	22,218
	Cost per unit [$]	1071	1071	2730	2730	
	Cost [$]	3213	5355	5460	8190	
Case 2. Individual damage state, all floors	Aggregate damage	8	8	5	5	44,355
	Cost per unit [$]	1626	1626	6269	6269	
	Cost [$]	4879	8132	12538	18807	
Case 3. All damage states, individual floor	Aggregate damage	5	8	5	8	40,484
	Cost per unit [$]	2459	1626	6269	4146	
	Cost [$]	7378	8132	12538	12437	
Case 4. Individual damage state, individual floor	Aggregate damage	3	5	2	3	61,178
	Cost per unit [$]	3015	2459	8392	7684	
	Cost [$]	9044	12297	16784	23053	

5.3.2 PRACTICAL EXAMPLE

The previous example illustrates that different interpretations of damage aggregation can yield substantially different repair costs for an individual component. However, the impact on repair costs depends on several factors and the following section shows that for an individual component there are also cases where the impact is negligible. However, the following example uses a practical, realistic performance model to demonstrate that a few components that experience substantial changes in their repair costs can still have a significant impact on the total repair cost of a building. The example performance models bundled with the PACT tool are considered, and the total repair costs are calculated with each of the four edge interpretation cases introduced earlier. The archetype is a three-story office building with a floor area of 22,736 ft^2 and a floor height of 14 ft in the first story and 11.5 ft in upper floors. This reinforced concrete moment-resisting frame structure was designed for a site in Berkeley, California. There are fifteen different nonstructural components and one structural component assigned to each floor in various quantities. A complete specification of component types and assigned quantities is provided in the corresponding PACT example file, and the uncertainty in consequence functions suggested by FEMA P-58-3 is considered. Volumes 2 and 3 of FEMA P-58 provide more information on this performance model (FEMA P-58-2, 2018; FEMA P-58-3, 2018).

Figure 5-3 shows the cumulative distribution function (CDF) of the calculated total repair costs for the four edge cases under a 420-year return period earthquake. Case 1 (i.e., "All damage states, all floors"), which is used in the PACT tool and always leads to the lowest repair costs, is considered a reference and is compared to the other edge cases that yield 10% - 26% ($78,000 – $195,000 in absolute value) higher median repair costs. A variation of this magnitude has the potential to result in an overestimation or underestimation of loss assessments, which could impact stakeholders' decision-making.

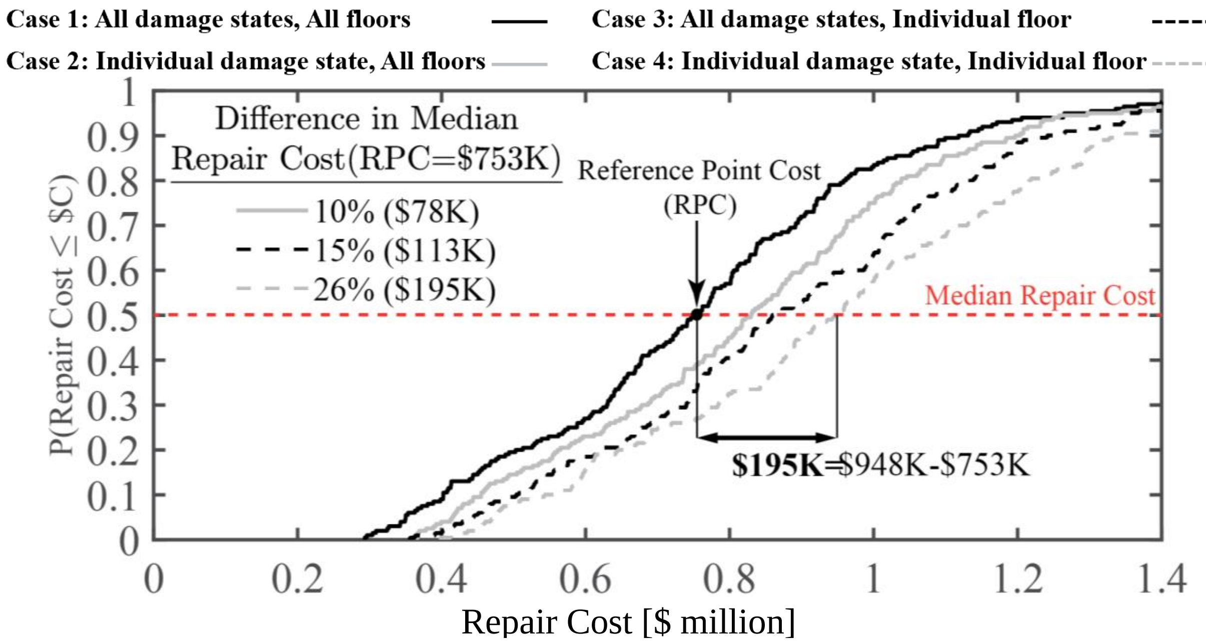

Figure 5-3. Cumulative distribution functions of total repair cost from analyses using different interpretations for damage aggregation in a case study 3-story office building.

5.4 Drivers of economies of scale in FEMA P-58

This section identifies the key drivers that affect the economies of scale calculation in FEMA P-58 and offers guidance on recognizing when the result of a performance assessment is significantly affected by the choice of damage aggregation method. The variance in total repair costs is more pronounced when one damage aggregation method yields a sufficiently large quantity of damaged units to trigger maximum economies of scale (i.e., lower-bound unit repair costs), while other damage aggregation methods lead to upper-bound or intermediate unit repair costs.

A strategy is proposed that uses three steps to review the key drivers and confirm that the results are not sensitive to the choice of damage aggregation method. Starting with a list of every component in the performance model, each of the three steps is used to exclude a set of components where the decision on how the aggregate damage and economies of scale are calculated has negligible impact on the total repair costs. Each step requires more information on the structure and the remaining components; hence, it is desirable to remove as many components as quickly as possible. If any component remains in the list after the three steps, the total repair costs will almost surely be affected by how the damage is aggregated in the calculation of the repair costs of those components.

Figure 5-4 provides an overview of the three steps and corresponding key drivers: First, the *Number of Damage States* and the *Number of Floors with Component* is checked to see if there is an opportunity to aggregate damage across damage states and floors. Components assigned to a single floor with a single possible damage state are indifferent to the damage aggregation method. Second, the *Consequence Functions* are used to evaluate the peak impact for each remaining component – i.e., the maximum possible reduction in repair cost due to economies of scale. Only components with substantial reductions will have a considerable impact on the total repair cost. Third, the *Damaged Component Quantities* are used to check if the four edge cases introduced earlier lead to different unit repair costs given the specific structural response. When the components experiences either very little or very much damage on every floor, the impact of aggregation becomes less pronounced. These three steps and their key drivers are controlled by the following input parameters (black rectangles in Figure 5-4):

- **Component data**: Information on the damage and consequence models for each component are independent of the seismic scenario and design details of the structural system. Each damage model defines the number of damage states and includes a set of fragility functions that define the uncertain component capacity corresponding to each damage state. Each consequence model includes a set of consequence functions (Figure

5-1) that define how economies of scale are applied when repairing damage from each damage state.

- **Component Quantities:** The floor area and number of stories influence component quantities on each floor and along the height of the building. The quantity of non-structural components is often estimated using the normative quantity estimation tool published with FEMA P-58 (FEMA P-58-3, 2018).
- **Structural Response**: Primarily affected by the number of stories, structural system, and earthquake intensity, the structural response characterizes the demands, such as accelerations and displacements, on each story for damage and loss assessment.

The following subsections provide more information on the three steps and highlight which components are typically filtered through each of them. If the list is not empty after the three steps, the remaining components should be examined more carefully. As long as only a few components remain in the list, the impact of damage aggregation on their repair costs can be estimated with a few simple calculations, as shown in the illustrative example in the following section.

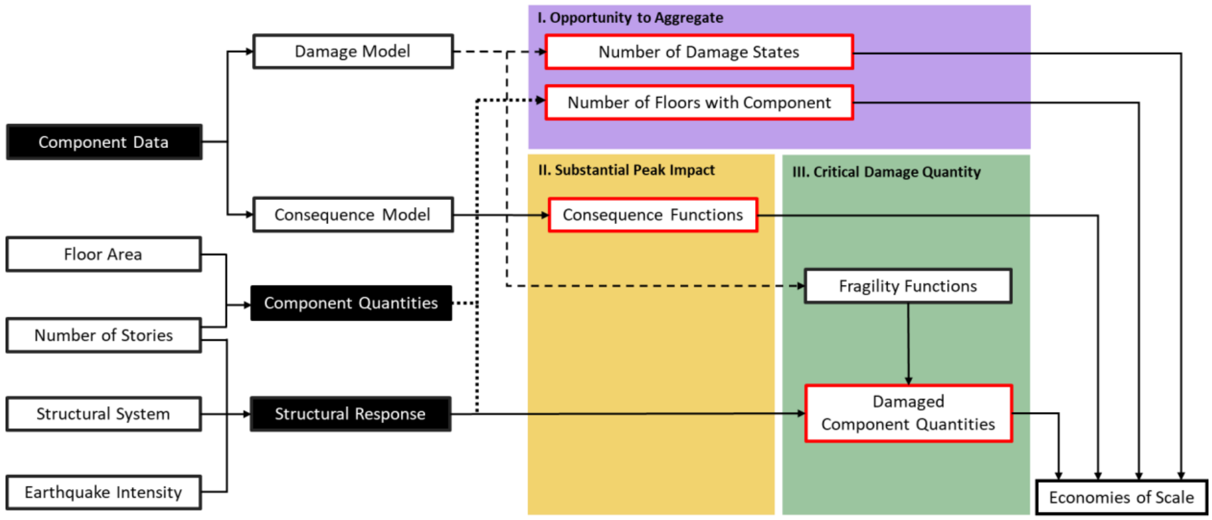

Figure 5-4. Overview of the three steps proposed to evaluate if a FEMA P-58 performance assessment is sensitive to the choice of damage aggregation method (purple, yellow, and green boxes). The key drivers in each step are in red rectangles and the input parameters that influence them are in black boxes. Other important inputs and intermediate data are in white boxes. Line styles differ to distinguish between arrows.

Step 1 – opportunity to aggregate

The first step starts by filtering out components that have a single damage state and are constrained to only one floor in the building. There are 305 (out of 764) components in FEMA P-58 with only one damage state. For components in this large group, such as chevron braces in steel frames and raised access floors, using a method that aggregates across all damage states will yield the same results as one that uses damage only from individual damage states. The other criterion focuses on the location of the component in the building. When a component type is located on a single story, such as HVAC equipment that is typically installed on roofs, there is no difference in component repair costs between approaches that aggregate across all floors and those that use damage only from individual floors.

Components that fulfil both above criteria can be safely excluded from further analysis. If we are only interested in the impact of aggregation across one entity (i.e., either damage states or floors), then it is sufficient to check only for the corresponding criterion. This will allow the filtering of a larger set of components in this step.

Step 2 – substantial peak impact

This second step seeks to identify component types with a potentially large absolute repair cost difference due to changes in the calculation of economies of scale. The evaluation below uses only the consequence functions of the components to provide an upper bound of the potential impact of damage aggregation on repair costs. The peak impact is applicable to any structure and seismic scenario, but the actual impact in a particular scenario might be substantially less depending on the actual amount of damage experienced; this is addressed in Step 3.

The impact (I) of damage aggregation on the repair cost of damaged component units in a specific damage state on a specific floor is defined as the difference shown in Figure 5-5 between the repair cost based on the quantity of damaged units in the specific floor and damage state and the lower-bound cost corresponding to maximum economies of scale. The latter requires sufficient additional damage in other locations and damage states to have the aggregate damage exceed Q_L, the upper limit of economies of scale in the consequence function. Using the notation from Figure 5-5, the impact can be calculated as follows:

$$I(Q) = QC_Q - QC_L \tag{5-2}$$

where Q is the quantity of damaged units in the specific floor and damage state; C_Q is the unit repair cost considering economies of scale for quantity Q, and C_L is the lower bound unit repair cost that requires at least Q_L aggregate damage. The red rectangle represents the impact at a particular Q quantity of damage in Figure 5-5.

The graphical representation in Figure 5-5 clearly shows that the impact (I) is a function of the quantity of damage and that its maximum is in the domain of $Q_U \leq Q < Q_L$. The unit repair cost C_Q for the linear transition section can be expressed as a function of upper and lower-bound quantity constants and corresponding unit repair costs, as shown in Equation (5-3).

$$I(Q) = (\frac{C_U - C_L}{Q_L - Q_U})(QQ_L - Q^2) \tag{5-3}$$

The maximum potential impact is sought by taking the first derivative of Equation (5-3) with respect to Q and finding the critical quantity (Q_{cr}) where the derivative is zero:

$$Q_{cr} = \frac{Q_L}{2} \geq Q_U \tag{5-4}$$

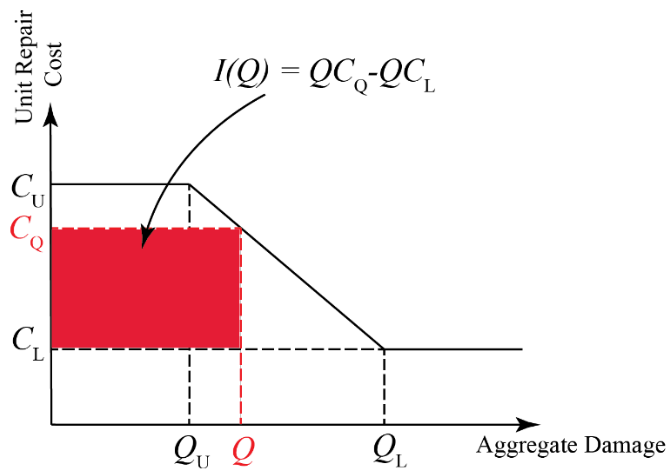

Figure 5-5. Impact of a component.

The area of the red rectangle in Figure 5-5 is maximized when $Q = Q_{cr}$. The critical quantity is typically at half of the upper quantity limit (Q_L) because $Q_L \geq 2\ Q_U$ holds for most components. In practice, this implies that economies of scale will have the maximum impact on the repair costs of components with $Q_L/2$ damaged units when other damages in the building could reach the lower bound unit repair costs. The maximum potential impact ($I_{\max}$) can be calculated by substituting Q_{cr} in Equation (5-3) as follows:

$$I_{\max} = Q_{cr}(C_U - C_L)(\frac{Q_L - Q_{cr}}{Q_L - Q_U}) \tag{5-5}$$

Figure 5-6 shows the computed $I_{\max}$ and Q_{cr} for every damage state of all components with complete consequence model data in the FEMA P-58 library (737 out of 764 components). Each horizontal row in the figure shows groups of similar components based on the first three labels in their ID numbers. For each component group, the position of each marker represents the computed $I_{\max}$ per floor for one of the damage states of a component type. Damage states are identified by the size of the marker. The largest $I_{\max}$ in each damage state in each component group is highlighted with colored markers. Markers with $I_{\max}$ below $1000 are considered negligible and are not shown. The right side of the figure shows rounded Q_{cr} values for each component group. A range of Q_{cr} is specified when a group has different values among its components and damage states.

Figure 5-6 demonstrates that $I_{\max}$ of some components, such as steel braces, chillers, generators, suspended ceilings, and exterior walls, reaches hundreds of thousands of dollars per floor. Others, such as independent pendant lighting and sprinkler water supply, have low $I_{\max}$. For these latter groups of components, damage aggregation and the resulting economies of scale will have negligible impact on repair costs. This second step of the proposed procedure aims to filter component groups that will not exceed a pre-defined minimum $I_{\max}$ threshold. For example, one could argue that the performance assessment of a building with a replacement cost of $4M per floor will not be considerably affected by a difference in repair cost per floor that is guaranteed to be less than $40,000. Using the data in Figure 5-6 and the $40K limit lead to the recognition that piping components (D.20.21 – D.20.61) and air distribution systems (D.30.41) can be neglected when evaluating the impact of damage aggregation. The chosen $I_{\max}$ threshold is a function of the desired absolute accuracy and should be determined on a case-by-case basis considering the total loss ratio (i.e., total repair cost over replacement cost) because an assessment with a smaller total loss ratio is more sensitive to the same absolute difference in the repair cost calculation. For component groups with I_{max} greater than the defined threshold, the following third step can be used to determine how much of the potential maximum impact is realized given the actual structural response and corresponding damage quantities. The results of this calculation for every FEMA P-58 component are provided as supplemental material to this chapter in a tabulated data file. The peak impact threshold can be defined based on the acceptable absolute error in repair costs per floor.

Step 3 – critical damage quantity

This third, and final, step compares Q_{cr} to the damaged component quantities (Q_{d}) given the demands (engineering demand parameters) each component experiences in a particular seismic performance assessment scenario. The impact of damage aggregation is negligible if Q_{d} is either close to zero or greater than $Q_{\mathrm{L}} = 2Q_{\mathrm{cr}}$, the lower-bound quantity limit introduced in Figure 5-5 (Q_{cr} for each component group is shown in Figure 5-6). Similarly, for components with a total quantity across all floors below Q_{U} (the upper-bound quantity limit), there cannot be a sufficiently large number of damaged units to trigger economies of scale regardless of which damage aggregation method is used. Hence, they can be removed from the list of impactful components. For example, $Q_{\mathrm{U}} = 5$ units for elevators allows the filtering of these components in small and mid-size buildings that have only a few elevator units.

For every other remaining component, the decision-making is specific to the structural design and seismic event under investigation and requires significantly more information than previous steps. Component quantities, structural response, and fragility functions are needed to determine Q_d in each seismic scenario for a particular structural design (Figure 5-4).

Figure 5-7 uses an example to illustrate how these inputs affect Q_d and how the calculated damage quantity is used to evaluate components in this third step. Figure 5-7 (a) and (a′) show histograms of story drift distributions for one floor of a multi-story building at two seismic intensity levels: design earthquake (DE) and maximum considered earthquake (MCE). The corresponding median interstory drift ratios are 1.4% and 2.1%, respectively. The first damage state of the glass curtain wall component B2022.002 from FEMA P-58 is used to provide the damage and consequence models for this example. The fragility function in Figure 5-7 (a) and (a′) defines the probability of glass falling from the frame of the curtain wall as a function of interstory drift. The probability of such damage is 0.10 and 0.38 at the median interstory drifts for the DE and MCE intensities, respectively. Considering a floor plan area of 3,300 m^2 and the normative quantities published with FEMA P-58, a total of 357 curtain wall panels are estimated to be installed along the perimeter of each floor. This yields 36 and 136 damaged panels (Q_d) at the DE and MCE levels, respectively. Figure 5-7 (b) and (b′) shows how these damage quantities compare to the critical quantity (Q_{cr}) that is 50 panels for this component.

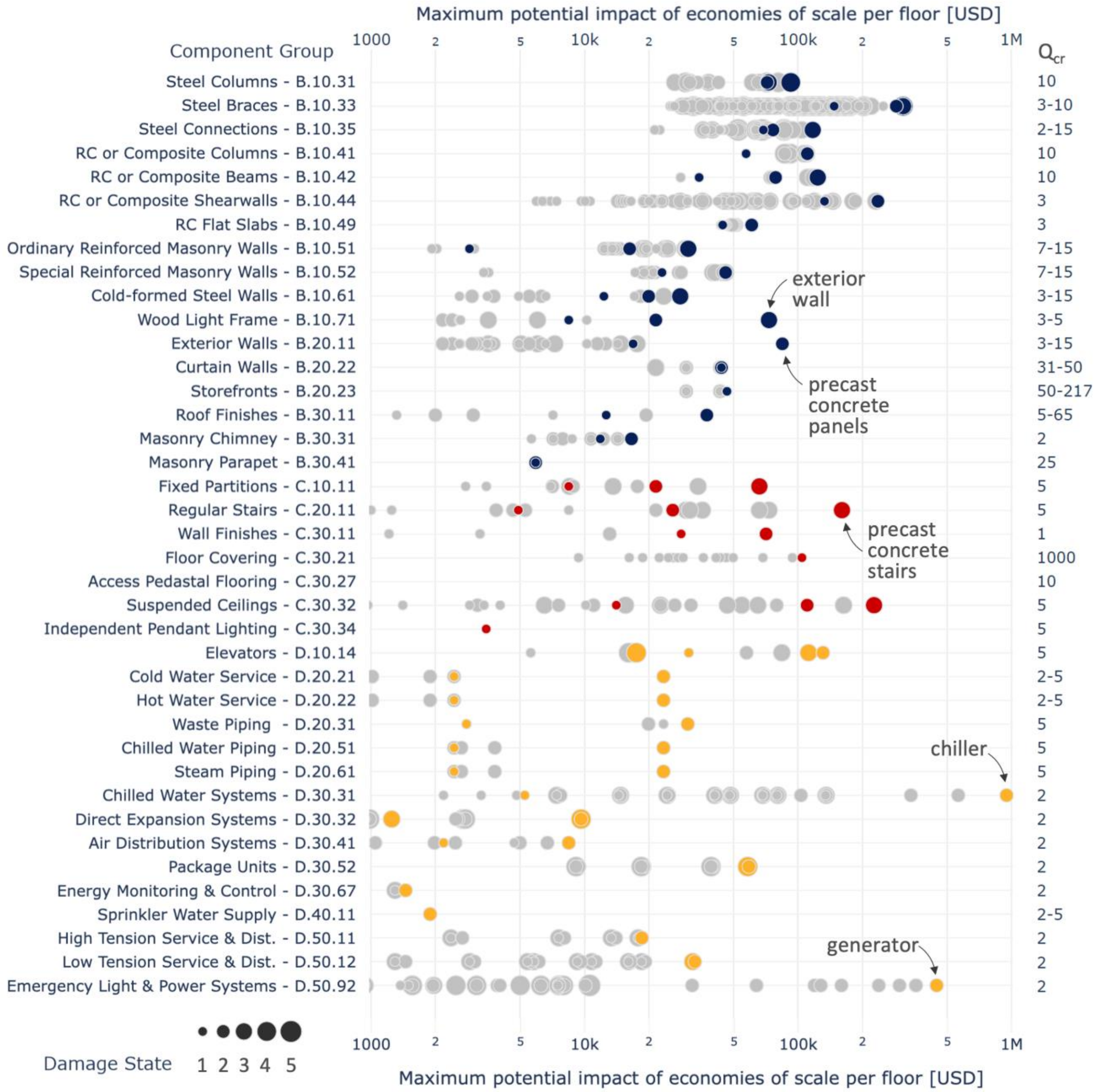

Figure 5-6. Maximum potential impact of economies of scale per floor based on the FEMA P-58 repair cost model for components in various damage states. Marker sizes correspond to damage states; the highest impact in each row for each damage state is highlighted with color. Critical quantities (in FEMA P-58 units) are shown on the right. (The presented data is provided in tabular format for each component and damage state as supplementary material.)

In this example, the number of damaged curtain wall panels at the MCE intensity is sufficiently large to achieve maximum economies of scale. Consequently, their repair cost will not be affected by how damage from other floors or damage states is aggregated in the calculation. On the other hand, the number of damaged panels at the DE intensity is close to Q_{cr} and the choice of damage aggregation has a considerable impact on the repair cost of these components as well as the total repair cost of the building. Specifically, the repair cost of the 36 panels is reduced by \$39,700 if the maximum economies of scale is triggered through damage aggregation. Note that this is slightly below the potential maximum I_{max} = \$43,000 for this component. Since repair costs at the DE intensity are typically only a small fraction of the replacement cost, \$39.7K can be a substantial difference and it suggests that the choice of damage aggregation method would deserve serious consideration for this assessment. Figure 5-7 also illustrates the importance of the floor area by showing results for a case with a smaller 1,100 m^2 floor plan. The smaller area leads to a substantial reduction in the number of installed wall panels (through normative quantity assignment) and, consequently, the number of damaged panels. In this smaller building, the number of damaged curtain wall panels at the DE intensity is significantly below Q_{cr}. The maximum cost saving on these repairs due to economies of scale is considerably reduced (12 x \$1500 = \$18,000) and oftentimes there will not be sufficient damage in other floors and damage states to reach the 100-panel Q_L threshold that triggers maximum economies of scale, regardless of which damage aggregation method is used. As for the MCE intensity, the number of damaged panels is close to Q_{cr}. The impact of damage aggregation in this scenario can be close to the potential maximum of \$45K, which typically warrants further investigation.

When evaluating design variations for a building, different structural designs can lead to different structural responses, and changes in the non-structural configuration of the building can change the total component quantities. These changes, as the above example illustrates, alter the quantity of damaged components and therefore can also affect the impact of the selected damage aggregation method. Thus, the relative performance of design variations can be influenced by how economies of scale are considered, thereby influencing design decisions that depend on performance comparisons.

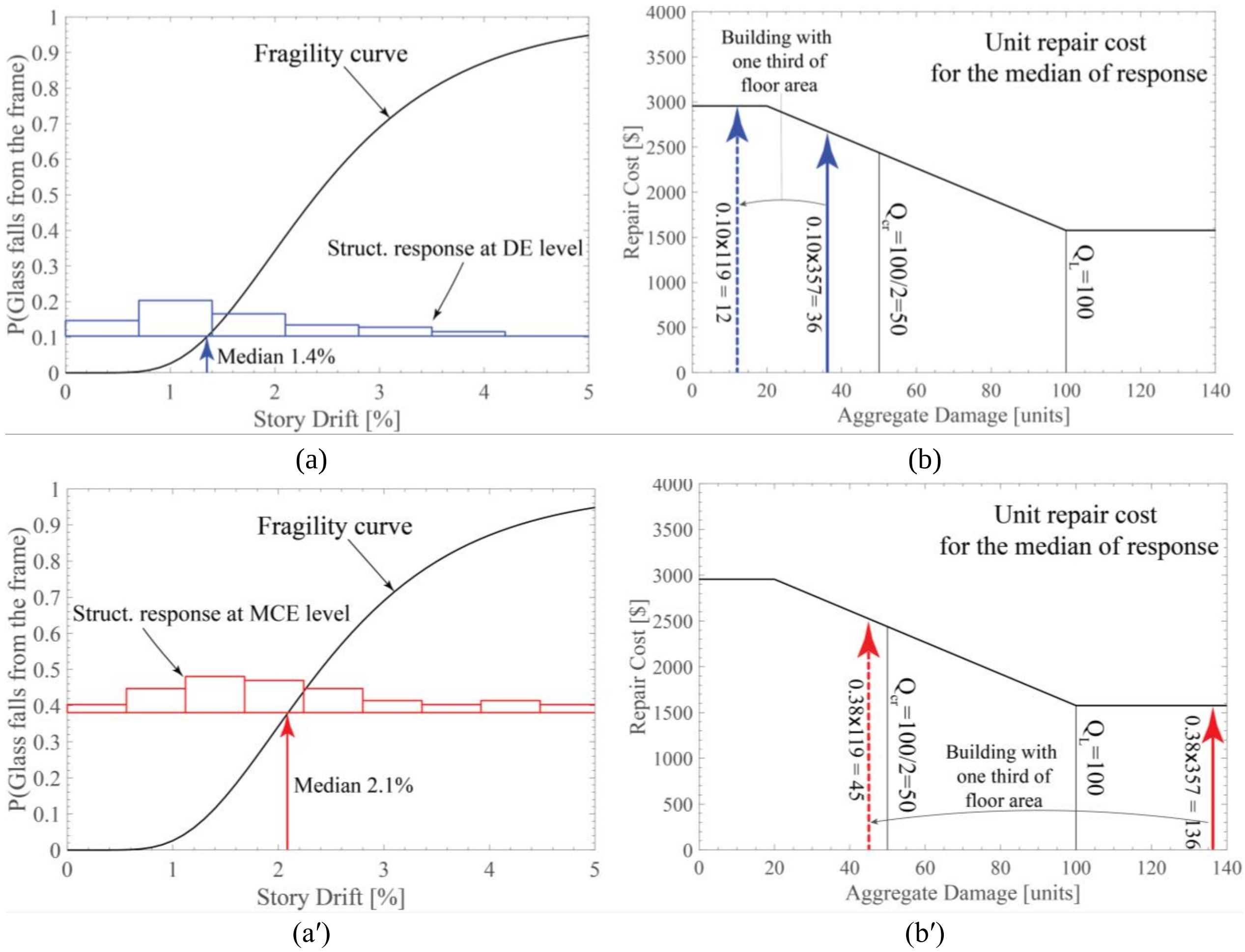

Figure 5-7. Influence of structural response and component quantity at DE and MCE level on unit repair cost estimation in the damage calculation (a) (a′) and repair consequence calculation (b) (b′) steps.

5.5 ILLUSTRATIVE EXAMPLE: REPAIR COST ESTIMATION OF A NINE-STORY BUILDING

This section illustrates how the strategy presented earlier is used to evaluate the impact of damage aggregation on the performance assessment of a case study building. A nine-story office building with a story height of 15 ft was designed with concentrically braced frames (CBFs) for a high seismicity location with stiff soil and mapped short periods and 1-second spectral accelerations of Ss=1.5 g and S1=0.5 g (ASCE/SEI 7-16, 2016), respectively. The building contains two structural and 18 nonstructural components. Nonstructural component quantities were assigned to each floor using the FEMA P-58 normative quantity estimation tool (FEMA P-58-3, 2018). Two performance models were created: a larger building with a footprint area of 21,600 ft^2 and a smaller one with a 10,700 ft^2 footprint. Table 5-2 summarizes the component quantities assigned to each floor and the roof of these buildings. Replacement costs were estimated using \$210 per ft^2 based on RSMeans data from 2020 (RSMeans, 2020). As the reference time of costs in FEMA P-58 consequence functions is 2011, the replacement cost estimates were scaled to a 2011-equivalent value by a factor of 0.8 based on the Historical Cost Index for the construction industry (RSMeans, 2020).

Table 5-2. Performance model summary for the nine-story buildings in the illustrative example.

Component ID	Description	Component Quantities						Unit
		Floors 1-3		Floors 4-9		Roof		
		L*	S*	L	S	L	S	
B1033.021b	Special concentric braced frame with HSS braces, 41 PLF < Column weight < 99 PLF	4	2	-	-	-	-	EA
B1033.021a	Special concentric braced frame with HSS braces, Column weight < 40 PLF	-	-	4	2	-	-	EA
B2022.002	Curtain walls	217	109	217	109	-	-	30 ft^2
C1011.001c	Wall partition (Gypsum with metal studs)	22	11	22	11	-	-	100 ft
C3011.001c	Wall partition with wallpaper	2	1	2	1	-	-	100 ft
C3027.002	Access pedestal flooring	163	82	163	82	-	-	100 ft^2
C3032.004b	Suspended ceiling	33	17	33	17	-	-	250 ft^2
C3034.002	Independent pendant lighting	325	163	325	163	-	-	EA
D2021.014b	Cold or hot potable water piping	1	1	1	1	-	-	1000 ft
D3041.011c	Small HVAC ducting	2	1	2	1	-	-	1000 ft
D3041.012d	Large HVAC ducting	1	1	1	1	-	-	1000 ft
D3041.032d	HVAC drops /diffusers	20	10	20	10	-	-	10 EA
D3041.041b	Variable air volume boxes	5	3	5	3	-	-	10 EA
D4011.023a	Fire sprinkler water piping	5	3	5	3	-	-	1000 ft
D5012.023e	Low voltage switchgear (400 Amp)	1	1	1	1	-	-	EA
D3031.013h	Chiller (500 ton)	-	-	-	-	2	1	EA
D3031.023h	Cooling tower (500 ton)	-	-	-	-	2	1	EA
D3052.013k	Air handling unit (30000 CFM)	-	-	-	-	5	3	EA
D5012.013c	Motor control center	-	-	-	-	8	4	EA
D1014.011	Elevator	6	3	-	-	-	-	EA

Note: Amp= Ampere; CFM=Cubic feet per minute; EA=Each; HVAC=Heating, ventilation, and air conditioning.
* L and S refer to the large building with 21,500 ft^2 area, and the small building with 10,700 ft2 floor area, respectively.

The large and small versions of the building were designed to the same structural specifications and assumed to exhibit similar floor responses and global collapse probability. These assumptions ensure that the differences observed in the results are due only to the differences in the damage and loss assessment methodology. Nonlinear time-history analyses were conducted using the set of far-field ground motion records recommended by FEMA P695 (FEMA P695, 2009). The median drift and acceleration demands are shown in Figure 5-8 for all floors at three seismic intensity levels: 50% DE, DE, and MCE according to ASCE 7-16 (ASCE/SEI 7-16, 2016).

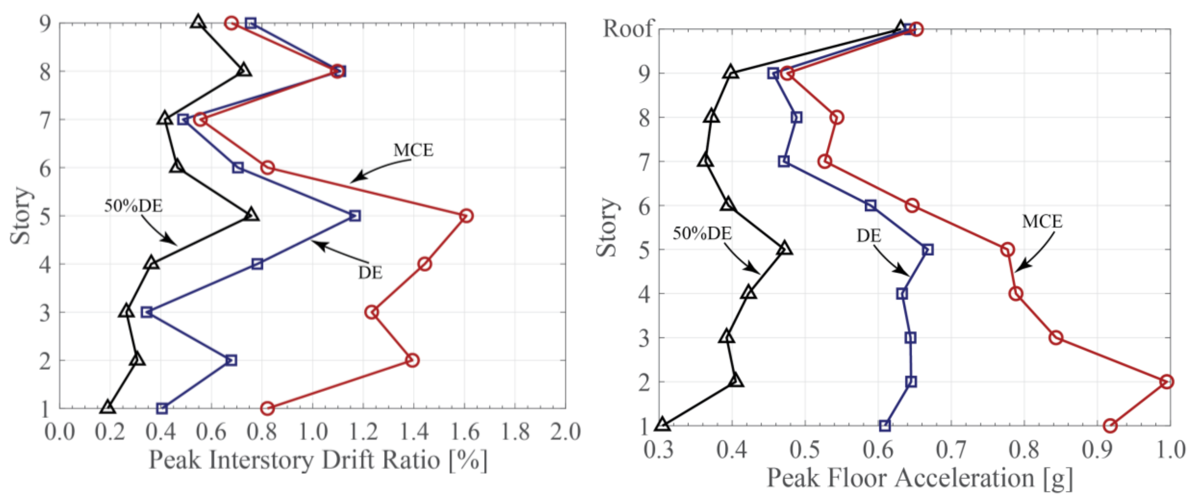

(a) (b)

Figure 5-8. Median (a) peak interstory drift ratio and (b) peak floor acceleration demands for all floors of the nine-story building.

Each building is analyzed in one direction, using the four edge cases for damage aggregation introduced earlier to capture the range of possible total repair cost outcomes. Figure 5-9 shows the cumulative distribution function (CDF) of total repair cost for the two buildings and three intensity levels. Results are in line with expectations: Case 1 (i.e., "All damage states, all floors") yields the lowest total repair cost for all buildings and intensity levels, whereas Case 4 (i.e., "Individual damage state, individual floor") yields the highest.

Comparing the median repair costs from different edge cases for the large and small building illustrates that the differences grow in absolute value with increasing intensity levels. For example, Cases 1 and 2 (i.e., solid lines in Figure 5-9, considering damages from all floors, but either all or only from one damage state) for the large building yield median repair costs that are \$120,000, \$339,000, and \$464,000 apart at the 50% DE, DE, and MCE intensities, respectively. This corresponds to a relative difference of about 12%-17%. The relative differences are in the range of 5% - 30% across all cases and they are generally larger for the building with the larger floor area.

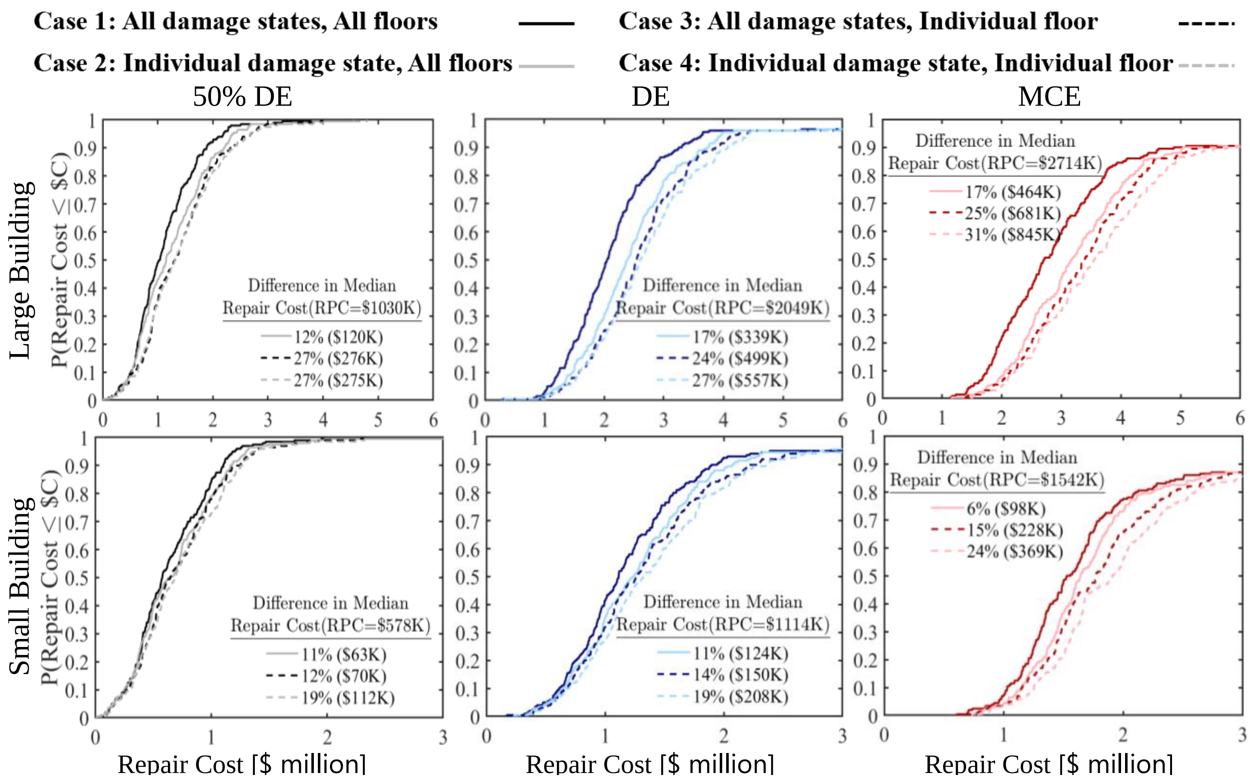

Figure 5-9. Comparison of total repair costs using four edge cases for two buildings' footprints and different intensity levels. The range of repair costs is limited to focus on outcomes of repairable realizations. At the DE and MCE levels, a proportion of realizations correspond to irreparable damage or collapse, leading to a step in the fragility curves beyond the limits of the figure.

5.5.1 Application of the proposed evaluation strategy

For this example, the following paragraphs illustrate how the strategy proposed previously can help recognize if there is a substantial impact of damage aggregation, identify which components are responsible for the majority of differences in repair costs, and estimate the magnitude of the total differences shown in Figure 5-9 without running analysis for the four edge cases. The following description focuses on the large building and the DE intensity for the sake of brevity.

Starting with a comprehensive list of all components from Table 5-2, the first step checks if there is an opportunity to aggregate damage for each component acoss floors or damage states. This leads to the removal of the the Chiller, Cooling tower, and Motor control center components because they have one damage state and are placed only on the roof.

In the second step, the peak impact of each component is compared with a \$10,000 threshold. This limit is chosen by targeting 0.5% of the approximately \$2 million total repair cost at the DE level. Considering that there are nine stories in the building and most of the damage will be concentrated to a few of those, a 0.5% maximum difference per story per component damage state is not expected to add up to more than a few percent difference in total repair costs. Based on Figure 5-6, the Access pedestal flooring, Independent pendant lightning, Air distribution systems, and Sprinkler water supply component groups have lower I_{max} than the threshold and can be removed from the checklist.

At this point, it is worth obtaining I_{max} for each specific remaining component, rather than looking only at the peak I_{max} of their component groups. This information is readily available in the table provided as supplemental information to this chapter, or it can be calculated from consequence function data using Equation (5-2). Components with I_{max} < \$10,000 in all damage states can be identified and removed from the checklist. In this example, Wall partitions with wallpaper and Cold or hot potable water piping fall into this category. These components were not removed earlier because they are part of component groups with at least one other component that has a larger I_{max} as shown in Figure 5-6.

In the last step of the proposed strategy, the quantity of damaged components (Q_d) is compared to the critical damage quantity (Q_{cr}). Assuming that the median Q_d for each component on each floor in each damage state is not directly available, Figure 5-10 shows the results of a proposed simplified calculation. Four demand levels (indicated by markers of different colors and symbols) were identified within the range of story drift and acceleration demands in the building at the DE and MCE intensities (Figure 5-8). The quantity of components is identical on all floors in the performance model of this example, as is often the case when normative quantities are assigned. Given the component quantity and the controlling demand value, Q_d for each damage state can be calculated using the component-specific fragility functions (Figure 5-7). Figure 5-10 shows how the results of this calculation illustrate the changes in the amount and severity of damage with increasing demands and highlight the components that experience damages close to Q_{cr} in the investigated seismic scenarios.

Components with a $Q_d/Q_{cr} \cong 0$ at all four demand levels have high capacity and experience barely any damage. This consideration allows the removal of Suspended ceiling and Low voltage switchgear from the checklist. Components with a $Q_d/Q_{cr} > 2$ at all four demand levels have very low capacity and experience so much damage that it triggers maximum cost savings already on a single floor and damage state and does not benefit from additional damage aggregation. This can occur when a single, high-seismicity scenario is investigated, but it is rare to observe such high damage when lower intensity scenarios, such as the DE level, are included in the performance assessment. Hence, none of the components in this example can be removed for consistently experiencing excessive damage.

Out of the remaining six components, Elevators and Air handling units can be removed by considering a few additional details about them. Although the potential maximum impact of elevators is substantial (I_{max} = \$130,000 in DS2), even if all elevators are damaged, only a small fraction of I_{max} will be realized in this example. There are only six elevators in the building and the costs savings for elevators start at five damaged units with 10 units required to maximize savings. Air handling units are installed on the roof where the median acceleration demand does not exceed 0.7 g in the highest intensity scenario. At that demand level, even less than one unit are expected to be in DS1 or DS2 (see red star markers in Figure 5-10 given Q_{cr} = 2.5). DS1 has negligible impact, and the single unit in DS2 will experience at most \$18,600 cost savings from damage aggregation across damage states. This is considered negligible compared to the \$2 million total reference point cost (RPC).

The four remaining components (two types of HSS braces, Curtain Walls, and Wall partitions) are expected to have substantially different repair costs depending on the chosen damage aggregation method, and these components are expected to be the primary contributors to the differences observed in Figure 5-9. This is confirmed in Figure 5-11, which shows the total repair cost from all but the remaining four components in the large building under the DE and MCE intensities. The maximum difference between the median costs from the four edge cases is less than \$57,000 and \$28,000, which are 2.8% and 1% of the median total repair costs including all components at the DE and MCE levels, respectively. The elevator component is the main contributor to this difference.

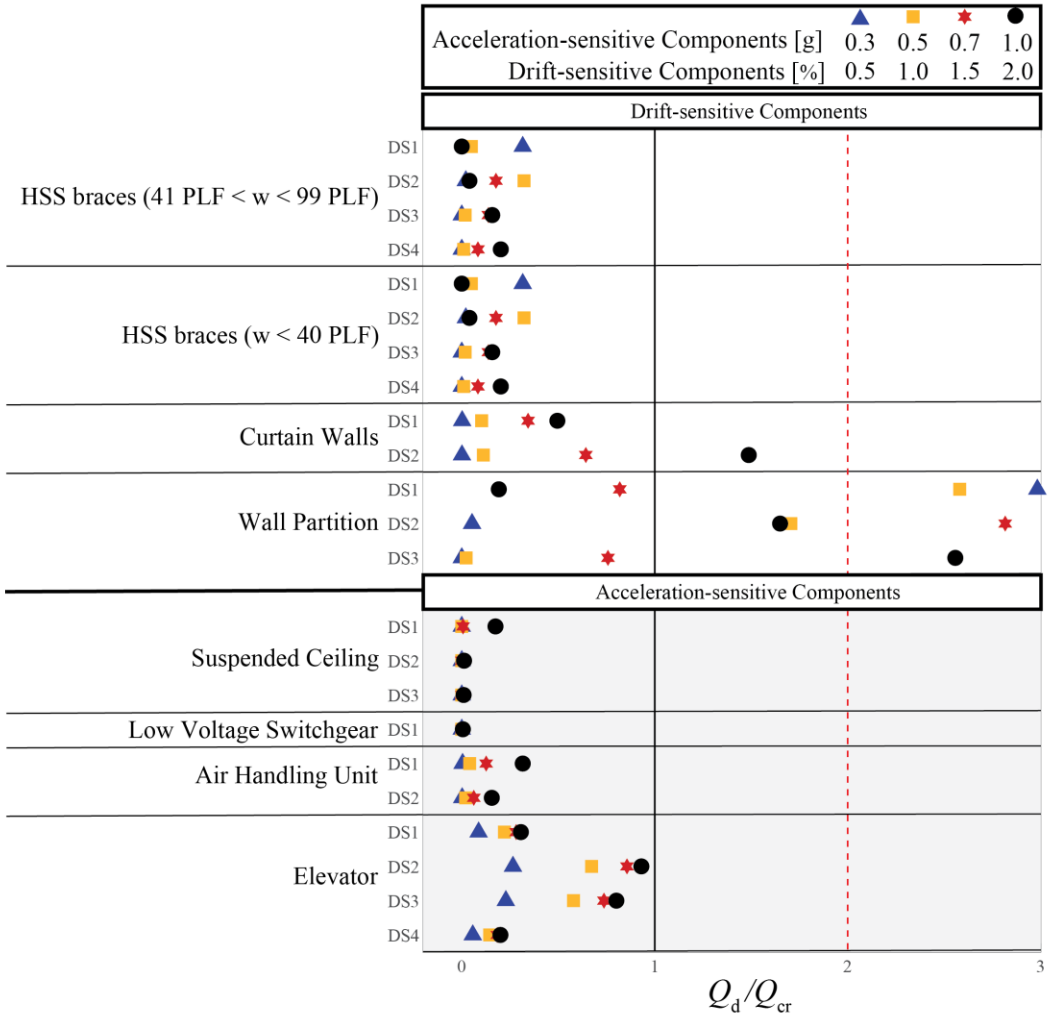

Figure 5-10. Quantity of damaged components at four demand levels compared to the critical damage quantity across the components remaining in the checklist for step 3.

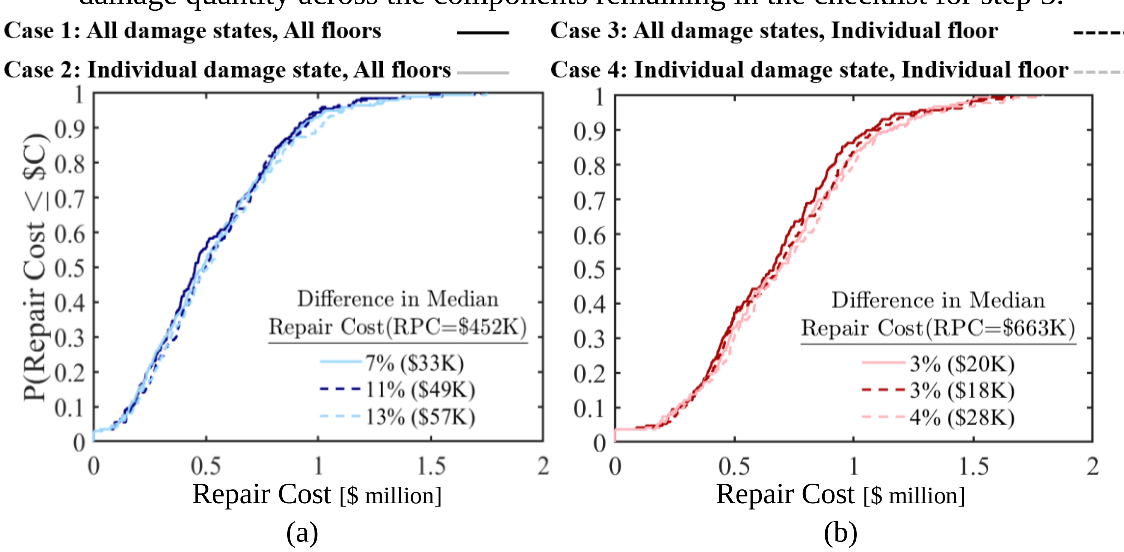

Figure 5-11. Total repair costs of all components that the proposed evaluation identified as having only minimal contribution to the repair cost differences at the (a) DE and (b) MCE levels.

5.5.2 Estimation of the impact of damage aggregation

The impact of various damage aggregation methods on the total repair cost is the sum of the additional cost savings achieved through damage aggregation across floors and damage states for the components that remain after the filtering process described above. These additional cost savings can be estimated through a simple calculation that is summarized in Table 5-3 - Table 5-6 for the remaining four components in this nine-story example building. Additional cost savings for each component are made up from repair costs saved on each floor, which are the product of costs saved per unit and the number of damaged units per floor.

The calculation for the small braces installed on floors 4-9 of the example building under the MCE intensity is presented first in detail (Table 5-3). Using the drift profile shown in Figure 5-8, we can classify the floors into two groups: floors 4-5 experience approximately 1.40% median interstory drift demand, while the drift in the upper floors is around 0.80%. This approximation of drifts leads to substantially simpler calculations and the results below illustrate that it still provides sufficiently accurate estimates. More complex drift profiles might need more than two groups to be captured faithfully and, in general, the more groups are used, the more accurate the calculations will become. Given these median demands, the fragility functions of the component are used to estimate the number of damaged units on each floor following the logic shown in Figure 5-7.

The results for Damage States 2-4 are combined in Table 5-3 only for the sake of brevity. The total number of damaged units on each floor is summed to find the maximum aggregate damage that could be applied for economies of scale calculation. For this component, four damaged units on each of the six floors yields a maximum aggregate damage of 24 units. The consequence functions of this component start considering economies of scale at Q_U = 5 damaged units and the maximum cost savings are reached at Q_L = 20 units of aggregate damage. If every damage state and floor is evaluated independently, these damaged components are always assigned the maximum unit repair cost because fewer than five units are damaged at each floor and damage state. On the other hand, if the damage is aggregated across all floors and damage states, the 24 units are sufficient to maximize the economies of scale, producing the minimum repair cost for every damaged unit.

The entries under Unit Repair Cost in Table 5-3 are the maximum and minimum costs based on the consequence function parameters. Recognizing that the repair cost savings are very similar for DS2 to DS4 for this component and that floors 4-5 only have damage in these higher damage states, the unit repair costs for those floors are based on the DS2 consequence function. The values for floors 6-9 are the mean of DS1 and DS2 consequence function parameters because an equal amount of damaged units are in these damage states there. Such approximations are made to keep this a hand calculation that aims only to provide an estimate of the impact on repair costs. The Additional Cost Savings per unit is the difference between the *max* and *min* Unit Repair Costs. These savings express that the repair cost of each of damaged unit is reduced by \$15,000 to \$16,000 when damages on other floors of the building are considered. These cost savings add up to \$60,000-\$64,000 per floor (considering the four damaged braces per floor) and an estimated \$368,000 considering all six floors with such braces in the building. Hence, these brace components alone can be responsible for shifting the total repair cost of the building by 15% depending on which damage aggregation method is chosen.

Table 5-3. Estimation of the impact of damage aggregation on repair cost savings for small HSS brace components (B1033.021a) in large building at MCE level

Location	Interstory Drift Demand	Damaged Units				Unit Repair Cost		Additional Cost Savings		
		DS1	DS2+	total	aggregate	Max	min	per unit	per floor	total
floors 4-5	1.40%	0	4	4	24	$48K	$32K	$16K	$64K	$128K
floors 6-9	0.80%	2	2	4	24	$45K	$30K	$15K	$60K	$240K
										$368K

The calculations of additional cost savings for the other three components are presented below because they provide a diverse set of cases and demonstrate how to approximate cost savings under various circumstances. The repair of large braces has only 12 aggregate damaged units across three floors, which is not enough to trigger the maximum cost savings for that component (Table 5-4). This needs to be considered when the minimum Unit Repair Cost is calculated based on the consequence function (Figure 5-5) and it significantly reduces the potential impact of these components. The $8K to $10K savings per unit add up to only $122K total savings for these braces.

Table 5-4. Estimation of the impact of damage aggregation on repair cost savings for large HSS brace components (B1033.021b) in large building at MCE level

Location	Interstory Drift Demand	Damaged Units				Unit Repair Cost		Additional Cost Savings		
		DS1	DS2+	total	aggregate	max	min	per unit	per floor	total
floor 1	0.80%	2	2	4	12	$51K	$43K	$8K	$32K	$32K
floors 2-3	1.40%	0	4	4	12	$60K	$50K	$10K	$40K	$80K
										$122K

Curtain walls have identical consequence functions assigned to both of their damage states in FEMA P-58, which simplifies the calculation and allows to enter only one max and min Unit Repair Cost for each row in Table 5-5. The situation is similar to the smaller braces: damaged unit quantities on individual floors and damage states are less than or near Q_U = 20, while the aggregate damage across all floors is above Q_L = 100. Even though the additional cost savings per unit are relatively small, the large number of damaged units in the building yields a substantial impact on the total repair cost.

Table 5-5. Estimation of the impact of damage aggregation on repair cost savings for curtain wall components (B2022.002) in large building at MCE level

Location	Interstory Drift Demand	Damaged Units				Unit Repair Cost		Additional Cost Savings		
		DS1	DS2	total	aggregate	max	min	per unit	per floor	total
5 floors	0.80%	2	2	4	180	$3.0K	$1.6K	$1.4K	$5.6K	$28K
4 floors	1.40%	15	25	40	180	$3.0K	$1.6K	$1.4K	$56K	$224K
										$252K

Wall partitions present a case where large differences between the consequences of various damage states necessitate separate calculations for Unit Repair Costs in each DS. The only simplification made in Table 5-6 is removing DS 1 because the corresponding cost savings are negligible. There are large numbers of units in DS1 and DS2 under 0.80% and 1.40% drift demands, respectively, and these numbers are already more than the Q_L = 10 for the component and trigger the maximum cost savings. In such cases, the component repair unit cost does not benefit from additional aggregate damage from other floors or damage states and there are no Additional Cost Savings. On the other hand, since Q_U = 1 for this component, the max Unit Repair Cost for damage states with more than one damaged unit is interpolated using the linear portion of the consequence function. The introduction of economies of scale at low damage quantities prevents the upper-bound unit cost from being reached with any damage aggregation approach, thus reducing the potential impact on the total repair cost. The potential impact on the total repair cost is small not only because the additional cost savings per unit are relatively small, but also because the number of damaged units for which additional cost savings can be applied is small.

Table 5-6. Estimation of the impact of damage aggregation on repair cost savings for wall partition components (C1011.001c) in large building at MCE level

Location	**Interstory Drift Demand**	**Damaged Units**					**Unit Repair Cost**				**Additional Cost Savings**			
		DS1	**DS2**	**DS3**	**total**	**agg.**	**max DS2**	**min DS2**	**max DS3**	**min DS3**	**per unit in DS2**	**per unit in DS3**	**per floor**	**total**
5 floors	0.80%	17	4	0	21	193	$2.7K	$1.0K			$1.7K		$6.8K	$34K
4 floors	1.40%	5	15	2	22	193	$1.0K	$1.0K	$6.4K	$2.1K	0	$4.3K	$8.6K	$34K
														$68K

Figure 5-12(a) shows the total repair cost CDFs for only the four components discussed above. The results under MCE intensity confirm that the calculated approximate impacts in Table 5-3 to 6 are sufficiently accurate to characterize the magnitude of the impact on total repair costs. The sum of estimated differences for the four components ($810K) is close to the difference in total repair costs when all components are considered in Figure 5-9 ($845K). This observation further supports the approximations suggested in the above calculations. A similar hand calculation can provide estimates of the impact of aggregating only across damage states or only across floors. Figure 5-12(a) illustrates that these impacts might be substantially smaller than the maximum.

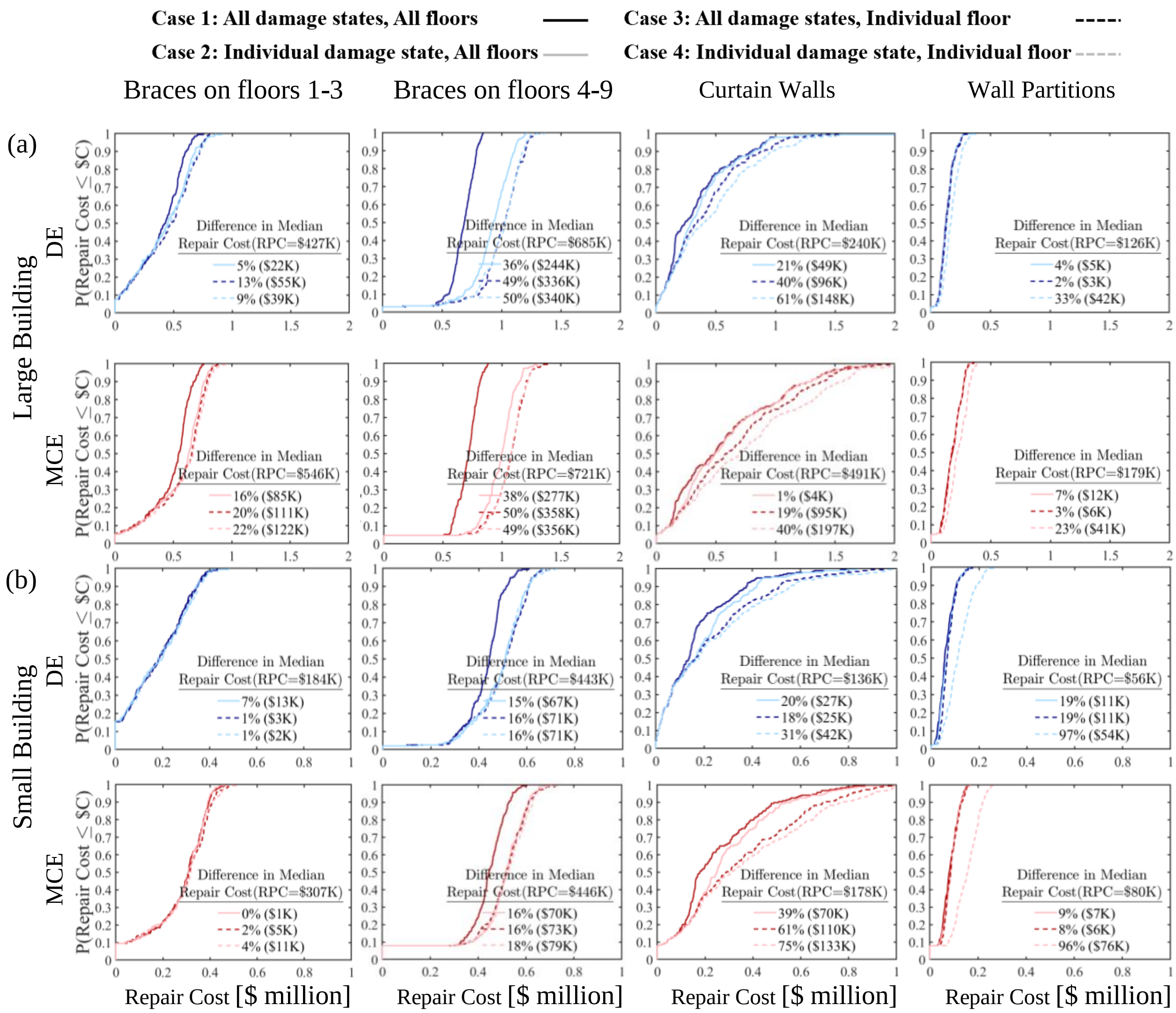

Figure 5-12. Comparison of total repair costs for each of the four components that are the main contributors to the impact of damage aggregation on the total repair cost of the example building. Results are shown at DE and MCE intensity levels for the large (a) and small (b) building footprint.

The results for the smaller building are shown in Figure 5-12 (b) to highlight how the contribution of each of the four components changes when only half the quantity is assigned to each floor. Brace damage in the smaller building, for example, contributes substantially less to the additional cost savings because the total number of damaged braces in the building is not large enough to minimize the unit repair cost. Conversely, the contribution of curtain wall and wall partitions to median repair costs sometimes increases because the number of damaged units is closer to Q_{cr}. This illustrates that it is not trivial to determine the significance of damage aggregation on the total repair cost in a performance assessment. It is recommended to perform the steps of the proposed evaluation strategy to arrive at a reliable estimate.

5.6 RECOMMENDATIONS FOR DAMAGE AGGREGATION

The discrepancy between the estimated losses obtained using the different edge cases in the examples presented above suggests that analysts need to know which damage aggregation method is implemented in popular tools so that they can determine whether to adjust their results. Additionally, the developers of consequence models need to provide information on how the parameters of the models are calibrated based on various potential edge cases. This information is also critical to ensure a fair comparison when benchmarking different tools. Therefore, the authors recommend developers of performance assessment tools to describe their approach to damage aggregation in the documentation and, if possible, provide multiple options for their users. Also, due to the modularity of the FEMA P-58 framework, different components used in a calculation could have been developed by different research groups using different assumptions on damage aggregation. It would be useful to document these assumptions for future studies, as such information is not currently available.

If the damage aggregation method has substantial impact on the repair cost consequences in a seismic performance assessment, the analyst must decide which aggregation method to use in their evaluation. Without knowing how the consequence functions of FEMA P-58 were developed, it is not possible to pick the one that will lead to realistic results. Using any other assumption than the one used when the consequence functions were calibrated will lead to biased results. Hence, the authors cannot recommend any of the approaches for general application. Instead, we recommend analysts to be explicit about this epistemic uncertainty by calculating and communicating the range of possible results using the edge cases presented in this chapter and adjusting the median of the total repair cost CDF accordingly. Alternatively, engineers can use their own judgement and assign an aggregation method to each repair action of each component considering the cost savings modeled by the corresponding consequence functions and how they map to local construction practices at the building's site. This requires a substantial effort and would best be accomplished through collaboration that leads to a consensus in the engineering community around component-specific assignments. Such a consensus would provide a short-term solution if the widely used analysis tools are enhanced to support component-specific damage aggregation when considering economies of scale.

Although the above recommendations would improve how economies of scale are quantified within the existing framework that relies on edge cases, the examples provided earlier in this chapter illustrate that none of the edge cases is a trivial best choice to model the repair of components. Given the importance of repair cost and repair time modeling in performance-based engineering, the authors believe that the repair consequence estimation framework in FEMA P-58 would benefit from fundamental enhancement to model economies of scale more appropriately. In the following subsections, two recommendations are made for improved modeling of consequence functions to better estimate economies of scale. Any enhancement in this part of the methodology should be developed and calibrated in collaboration with contractors to capture their experience.

5.6.1 ECONOMIES OF SCALE ACROSS COMPONENTS

One recommendation that could be implemented relatively easily is to recognize that damage should also be aggregated across different component types when the damaged units of those components require identical repair actions. FEMA P-58 components that only differ in design details that do not affect the repair process are a good example. For instance, the two types of braces used in the analyses earlier in this chapter (B1033.021a and B1033.021b) have identical damage states, corresponding drift capacities and repair actions, and quantity limits in their consequence functions. The same conditions apply to seven additional B1033-type braces, and these nine components could form a so-called Component Group. Numerous other component groups can be defined similarly within the FEMA P-58 component library. The repair consequence calculation of such components would become more realistic by the following simple extension of the methodology: when evaluating economies of scale, every component type within a component group should be considered during damage aggregation.

Figure 5-13 illustrates the impact of such a modification on the calculated total repair costs of the two brace components in the large building configuration evaluated at the MCE intensity in the case study presented earlier. The modification only affects the cases that aggregate damage across floors because only one type of brace was used on each floor – large braces for the first three floors and smaller braces for the remaining six floors. Hence, the results of Cases 3-4 are identical in Figure 5-13. On the one hand, when all damaged units are aggregated following Case 1 (solid lines in the figure), the small braces already have sufficient damaged units to maximize economies of scale without the contribution of damage from large braces. On the other hand, there are only 12 large braces in the first three floors, which is not sufficient to maximize economies of scale. When the additional damage on upper floors is also considered within Case 1, the repair cost of the large braces is reduced by $117K, which is approximately 4% of the total repair cost of the building for this scenario. For Case 2 (dashed lines in the figure), which aggregates damage across floors but not across damage states, both brace types benefit, with a total reduction in median repair costs of $199K due to aggregating across similar components.

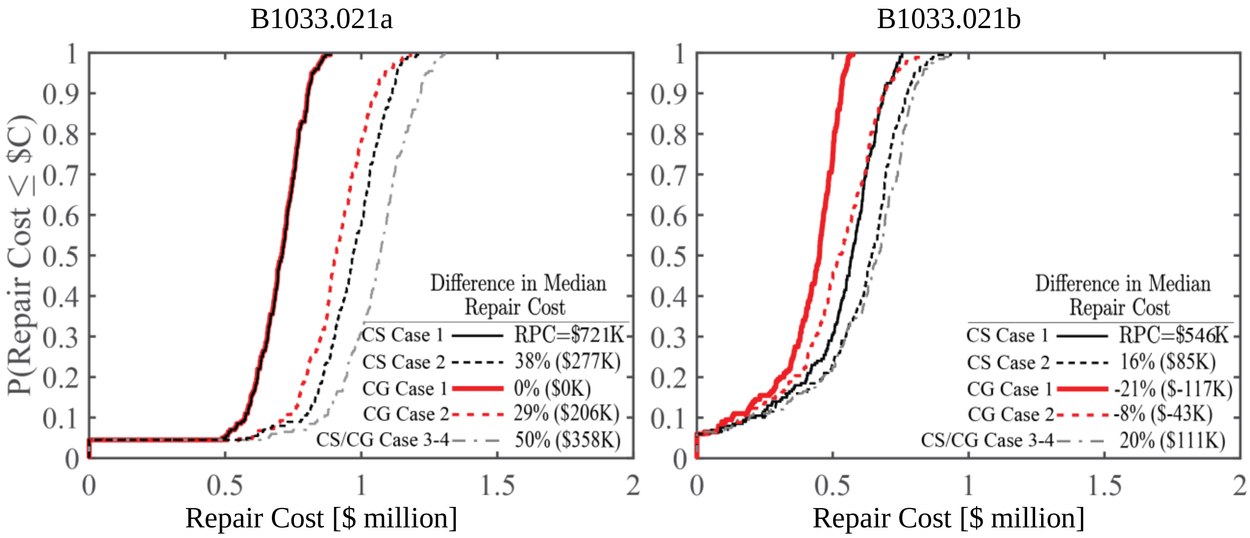

Figure 5-13. Comparing the impact of component-specific (CS) and component-group (CG) damage aggregation methods on the repair costs of small (B1033.021a) and large (B1033.021b) braces that belong to the same component group in the case study building.

5.6.2 Economies of Scale Across Tasks

The similarities between repairs of different components could be modeled more accurately through the following generalization of the component-group approach. The background documentation of FEMA P-58 already breaks down repair actions into a series of tasks. Each task is performed by a particular type of contractor. Economies of scale apply when the same task is performed many times by the same contractor, regardless of which particular component's repair is supported by them. For example, the various pipe components behind suspended ceilings share the repair tasks that involve removing the ceiling panel. Savings and also costs would be easier to measure, model, calibrate, and validate at the specific, explicitly described task level. Some of the tasks might limit damage aggregation to a single floor, while others might use aggregated damage from the entire building to calculate their cost. After determining the cost of each task in the building, the repair costs could be calculated by aggregating the cost of tasks that make up the repair action of each damaged component unit. The types of contractors required to repair each component in the FEMA P-58 library are already assessed and characterized within the scope of the ATC-138 project (ATC 138-3, 2021) for the sake of realistic impeding time calculation and repair sequencing. The outcomes of that project could be incorporated into the FEMA P-58 methodology as part of the more sophisticated model for economies of scale that is proposed here.

5.7 Conclusions

This study focused on the robustness of the high-resolution FEMA P-58 seismic performance assessment methodology for modeling economies of scale in repair consequence simulation. FEMA P-58 is important not only because it is ubiquitous in earthquake engineering research and practice, but also because it serves as a template for high-resolution approaches under other hazards. Neither the published methodology nor its background documentation describes the process of aggregating damaged component units across floors and damage states when evaluating potential repair cost or time reduction due to economies of scale. This chapter highlighted the highly variable and often substantial impact of this ambiguity on total repair costs. The results illustrate that the impact varies across seismic intensities and designs. This is especially concerning when the relative performance of various designs is sought because the outcomes of the evaluation could be dependent on the chosen damage aggregation approach. Similar outcomes for repair times could heavily influence functional recovery time calculations. The authors proposed an approximate calculation to estimate this impact, and suggested future extensions to the FEMA P-58 consequence model and its documentation to address the problem.

Four so-called edge cases were presented to cover the range of possible aggregate damage values within the scope of FEMA P-58. The four edge cases are a combination of two binary decisions: consider one floor or aggregate across all floors, and consider one damage state or aggregate across all damage states. Several examples illustrated that the difference between edge cases ranges from less than 1% to more than 25% of the total repair cost of the building.

To the authors' knowledge, Pelicun (Zsarnóczay and Kourehpaz, 2021) is the only widely available performance assessment tool that supports multiple damage aggregation methods. To support the large number of analysts who use other tools, and the review of past assessments where the model might no longer be available, a three-step strategy was proposed that helps quickly evaluate the impact of this phenomenon on a specific performance assessment. The proposed method was supported by a detailed investigation that demonstrates the complex relationship between performance assessment input data and the observed differences in repair costs. The number of damage states, the quantity of components on each floor, the consequence function parameters, and the quantity of damaged components were identified as key drivers of the outcomes. The proposed strategy provides three steps of increasing complexity to test each component in a performance model and evaluate if its repair costs can be affected by how damage is aggregated. This strategy helps identify the few components responsible for the majority of the differences in repair costs, and a simplified calculation was proposed to approximate their impact.

A case study of a nine-story steel frame structure was presented to illustrate the application of the proposed strategy and to demonstrate the impact of damage aggregation on repair costs at three different seismic intensity levels and with two different floor areas. Braces, curtain walls, and wall partitions were identified as the main contributors, yielding up to 30% difference in total repair costs depending on how damage is aggregated in the analysis. Results of the proposed evaluation strategy were verified by performing detailed simulations with all four edge cases.

This chapter highlights that economies of scale often have significant influence on repair costs in practical cases. Due to the lack of information about the assumptions made by various consequence function developers, it is not possible to select a single damage aggregation method as the correct one. Instead, stakeholders are encouraged to start a discussion and develop a consensus on how to address this problem in the short term. Until then, the authors recommend taking a conservative approach, quantifying the range of possible repair costs, and communicating this uncertainty in the results. In the long term, the authors suggest a more complex repair consequence model that disaggregates repair actions into individual tasks. Economies of scale at the task level would be easier to model, calibrate, and verify and promises a more robust calculation method for this important phenomenon.

5.8 Acknowledgments

The National Science and Engineering Research Council of Canada is gratefully acknowledged for providing funding to the first author of the paper under a Discovery Grant awarded to the fourth author of the paper. The Italian Ministry of Education, University, and Research is also gratefully acknowledged for providing funding to the second author of the paper under the project "Dipartimenti di Eccellenza," at IUSS Pavia. The material presented in the paper is based upon work conducted by the third author of the paper supported by the National Science Foundation under Grants No. 1621843 and No. 2131111. Any opinions, findings, and conclusions or recommendations expressed in this material are those of the authors and do not necessarily reflect the views of the National Science Foundation.

5.9 References

ACI 318-19, 2019. *Building code requirements for structural concrete*. Farmington Hills, MI, United States: American Concrete Institute.

ANSI/AISC 341-16, 2016. *Seismic provisions for structural steel buildings*. Chicago, IL, United

States: American Institute of Steel Construction.

ASCE/SEI 41-17, 2017. *Seismic evaluation and retrofit of existing buildings*. Reston, VA, United States: American Society of Civil Engineers.

ASCE/SEI 7-16, 2016. *Minimum design loads and associated criteria for buildings and other structures*. Reston, VA, United States: American Society of Civil Engineers.

ATC 138-3, 2021. Seismic performance assessment of buildings volume 8 – methodology for assessment of functional recovery time – preliminary report. *Applied Technology Council*. Redwood City, CA, United States.

Attary, N., Unnikrishnan, V. U., van de Lindt, J. W., Cox, D. T., and Barbosa, A. R., 2017. Performance-based tsunami engineering methodology for risk assessment of structures. *Engineering Structures*, **141**, 676–686. Elsevier Ltd. DOI: https://doi.org/10.1016/j.engstruct.2017.03.071

Barbato, M., Petrini, F., Unnikrishnan, V. U., and Ciampoli, M., 2013. Performance-based hurricane engineering (PBHE) framework. *Structural Safety*, **45**, 24–35. DOI: https://doi.org/10.1016/j.strusafe.2013.07.002

Buccella, N., Wiebe, L., Konstantinidis, D., and Steele, T., 2021. Demands on nonstructural components in buildings with controlled rocking braced frames. *Earthquake Engineering and Structural Dynamics*, **50**(4), 1063–1082. John Wiley and Sons Ltd. DOI: https://doi.org/10.1002/eqe.3385

Ciampoli, M., Petrini, F., and Augusti, G., 2011. Performance-based wind engineering: towards a general procedure. *Structural Safety*, **33**(6), 367–378. DOI: https://doi.org/10.1016/j.strusafe.2011.07.001

Cornell, C. A., and Krawinkler, H., 2000. Progress and challenges in seismic performance assessment. *PEER Center News*, **3**(2), 1–3.

Deierlein, G. G., McKenna, F., Zsarnóczay, A., Kijewski-Correa, T., Kareem, A., Elhaddad, W., Lowes, L., et al., 2020. A cloud-enabled application framework for simulating regional-scale impacts of natural hazards on the built environment. *Frontiers in Built Environment*, **6**, 558706. DOI: http://doi.org/10.3389/fbuil.2020.558706

Dyanati, M., Huang, Q., and Roke, D., 2017. Cost-benefit evaluation of self-centring concentrically braced frames considering uncertainties. *Structure and Infrastructure Engineering*, **13**(5), 537–553. DOI: https://doi.org/10.1080/15732479.2016.1173070

EERI, 2019. Functional Recovery: A Conceptual Framework with Policy Options. *Earthquake Engineering Research Institute*. Oakland, CA,United States.

EN 1998-1:2008, 2008. *Eurocode 8: Design of structures for earthquake resistance – Part 1: Genreal rules, seismic actions and rules for buildings*. European Committee for Standardization (CEN).

FEMA P-2090 / NIST SP-1254, 2021. Recommended options for improving the built environment for post-earthquake reoccupancy and functional recovery time. *Federal Emergency Management Agency and National Institute of Standards and Technology*. DOI:

https://doi.org/10.6028/NIST.SP.1254

FEMA P-58-1, 2018. *Seismic performance assessment of buildings volume 1-methodology*. Washington, DC, United States: prepared by the Applied Technology Council for the Federal Emergency Management Agency.

FEMA P-58-2, 2018. *Seismic Performance Assessment of Buildings Volume 2 – Implementation Guide* (2nd Edit.). Washington, D.C.: prepared by the Applied Technology Council for the Federal Emergency Management Agency.

FEMA P-58-3, 2018. *Seismic Performance Assessment of Buildings, Volume 3–Supporting Electronic Materials and Background Documentation: 3.1 Performance Assessment Calculation Tool (PACT)*. Version 3.1.2. Washington, DC, United States: prepared by the Applied Technology Council for the Federal Emergency Management Agency.

FEMA P695, 2009. *Quantification of Building Seismic Performance Factors*. Washington, DC, United States: prepared by the Applied Technology Council for the Federal Emergency Management Agency.

Filiatrault, A., and Sullivan, T., 2014. Performance-based seismic design of nonstructural building components: The next frontier of earthquake engineering. *Earthquake Engineering and Engineering Vibration*, **13**(1), 17–46. DOI: 10.1007/s11803-014-0238-9

Haselton Baker Risk Group, 2020. Seismic Performance Prediction Program (SP3). *Retrieved from www.hbrisk.com*.

Huang, Q., Dyanati, M., Roke, D. A., Chandra, A., and Sett, K., 2018. Economic feasibility study of self-centering concentrically braced frame systems. *Journal of Structural Engineering*, **144**(8), 04018101. DOI: https://doi.org/10.1061/(ASCE)ST.1943-541X.0002093

LATBSDC, 2020. An alternative procedure for seismic analysis and design of tall buildings located in the los angeles region. *Los Angeles Tall Buildings Structural Design Council*. Los Angeles, CA, United States.

Martin, A., Deierlein, G. G., and Ma, X., 2019. Capacity design procedure for rocking braced frames using modified modal superposition method. *Journal of Structural Engineering*, **145**(6), 04019041. DOI: https://doi.org/10.1061/(ASCE)ST.1943-541X.0002329

McKevitt, W. E., Timler, P. A. M., and Lo, K. K., 1995. Nonstructural damage from the Northridge earthquake. *Canadian Journal of Civil Engineering*, **22**(2), 428–437. DOI: https://doi.org/10.1139/l95-051

Miranda, E., and Aslani, H., 2003. *Probabilistic response assessment for building-specific loss estimation*. Pacific Earthquake Engineering Research Center.

Miranda, E., Mosqueda, G., Retamales, R., and Pekcan, G., 2012. Performance of nonstructural components during the 27 February 2010 Chile earthquake. *Earthquake Spectra*, **28**(S1), S453–S471. DOI: https://doi.org/10.1193/1.4000032

Miranda, E., and Taghavi., S., 2003. Estimation of seismic demands on acceleration-sensitive nonstructural components in critical facilities. *Proceedings of the Seminar on Seismic*

Design, Performance, and Retrofit of Nonstructural Components in Critical Facilities., 29–2.

Moehle, J., and Deierlein, G. G., 2004. A framework methodology for performance-based earthquake engineering. *13th world conference on earthquake engineering*, (679).

Molina Hutt, C., Vahanvaty, T., and Kourehpaz, P., 2022. An analytical framework to assess earthquake-induced downtime and model recovery of buildings. *Earthquake Spectra*, **38**(2), 1283–1320. DOI: https://doi.org/10.1177/87552930211060856

Rahgozar, N., Moghadam, A. S., and Aziminejad, A., 2016. Quantification of seismic performance factors for self-centering controlled rocking special concentrically braced frame. *The Structural Design of Tall and Special Buildings*, **25**(14), 700–723. DOI: https://doi.org/10.1002/tal.1279

Reitherman, B., Sabol, T., Bachman, R., Bellet, D., Bogen, R., Cheu, D., Coleman, P., et al., 1995. Nonstructural damage. *Earthquake Spectra*, **11**(2), 453–514.

RSMeans, 2020. *Building construction cost data*. RSMeans Construction Publishers and Consultants.

Shrestha, S. R., Orchiston, C. H. R., Elwood, K. J., Johnston, D. M., and Becker, J. S., 2021. To cordon or not to cordon: The inherent complexities of post-earthquake cordoning learned from Christchurch and Wellington experiences. *Bulletin of the New Zealand Society for Earthquake Engineering*, **54**(1), 40–48. DOI: https://doi.org/10.5459/bnzsee.54.1.40-48

Steele, T., and Wiebe, L., 2016. Dynamic and equivalent static procedures for capacity design of controlled rocking steel braced frames. *Earthquake Engineering and Structural Dynamics*, **45**(14), 2349–2369. DOI: https://doi.org/10.1002/eqe.2765

Steele, T., and Wiebe, L., 2017. Collapse risk of controlled rocking steel braced frames with different post-tensioning and energy dissipation designs. *Earthquake Engineering and Structural Dynamics*, **46**(13), 2063–2082. John Wiley and Sons Ltd. DOI: https://doi.org/10.1002/eqe.2892

Steele, T., and Wiebe, L., 2021. Collapse risk of controlled rocking steel braced frames considering buckling and yielding of capacity-protected frame members. *Engineering Structures*, **237**, 111999. Elsevier BV. DOI: https://doi.org/10.1016/j.engstruct.2021.111999

Stevenson, J. R., Kachali, H., Whitman, Z., Seville, E., Vargo, J., and Wilson, T., 2011. Preliminary observations of the impacts the 22 February Christchurch earthquake had on organisations and the economy: A report from the field (22 February - 22 March 2011). *Bulletin of the New Zealand Society for Earthquake Engineering*, **44**(2), 65–76. DOI: http://doi.org/10.5459/bnzsee.44.2.65-76

TBI, 2017. *Guidelines for Performance-Based Seismic Design of Tall Buildings*. *Tall Buildings Initiative*. PEER Report 2017/06.

Terzic, V., Villanueva, P. K., Saldana, D., and Yoo., D. Y., 2021. F-Rec Framework: Novel framework for probabilistic evaluation of functional recovery of building systems. *Pacific Earthquake Engineering Research Center*, PEER Report 2021/06. Berkeley, CA, United States.

Tremblay, R., Fliatrault, A., Bruneau, M., Nakashima, M., Prion, H. G., and DeVall, R., 1996. Seismic design of steel buildings: lessons from the 1995 Hyogo-ken Nanbu earthquake. *Canadian Journal of Civil Engineering*, **23**(3), 727–756. NRC Research Press Ottawa, Canada. DOI: https://doi.org/10.1139/l96-885

Trifunac, M., and Novikova, E., 1994. *State of the art review on strong motion duration*. Vienna, Austria: Proceedings of the Tenth European conference on earthquake engineering.

Vecchio, C. Del, Ludovico, D. M., and Prota, A., 2020. Repair costs of reinforced concrete building components: From actual data analysis to calibrated consequence functions. *Earthquake Spectra*, **36**(1), 353–377. SAGE Publications Inc. DOI: http://doi.org/10.1177/8755293019878194

Wiebe, L., and Christopoulos, C., 2015. Performance-based seismic design of controlled rocking steel braced frames. I: methodological framework and design of base rocking joint. *Journal of Structural Engineering*, **141**(9), 04014226. DOI: https://doi.org/10.1061/(ASCE)ST.1943-541X.0001202

Zsarnóczay, A., and Deierlein, G. G., 2020. PELICUN - A Computational Framework for Estimating Damage , Loss and Community Resilience. *17th World Conference on Earthquake Engineering*. Japan.

Zsarnóczay, A., and Kourehpaz, P., 2021. NHERI-SimCenter/pelicun: v2.6, Zenodo. DOI: http://doi.org/10.5281/zenodo.5167371

Chapter 6

6. CONCLUSIONS AND RECOMMENDATIONS

Based on the research objectives outlined in the introductory chapter, a research program was executed and presented in a sandwich thesis structure, where each chapter consists of a manuscript addressing specific research objective. This chapter closes the thesis in the following sections. First, Section 6.1 provides summaries of the contributions made in the preceding four chapters. Then, in Section 6.2, the perspective extends beyond the contributions of each individual chapter, offering recommendations for immediate actions and for future research focused on reducing seismic losses and enhancing seismic loss assessments.

6.1 SUMMARY AND CONCLUSIONS

6.1.1 ASSESSING CRBFS AS AN ALTERNATIVE TO CONVENTIONAL DUCTILE SFRSS

Chapter 2 involved a comprehensive assessment and comparison of four distinct steel seismic force-resisting systems (SFRSs) for buildings at various heights. These SFRSs included special moment resisting frames (SMRFs), special concentrically braced frames (SCBFs), and buckling-restrained braced frames (BRBFs) as common ductile systems, as well as controlled rocking braced frames (CRBFs) as a self-centering system. Chapter 2 demonstrated that all considered buildings had acceptable collapse capacities; however, they exhibited distinct characteristics at the design earthquake (DE) level. The CRBF buildings had consistent story drifts over the height due to the rocking mode, while the SCBF and SMRF buildings showed nonuniform drifts, with the SMRF buildings having the largest peak story drifts. Additionally, the CRBF buildings had minimal residual drift and member yielding compared to other systems.

The expected annual loss (EAL) was used as a metric to compare irreparable losses, including structural collapse and demolition due to excessive residual drift, alongside reparable losses, including the repair of both structural and nonstructural elements, for each specific SFRS. Chapter 2 illustrated that, among the considered SFRSs, the SMRF and SCBF buildings experienced the highest total EAL. This increase was mainly attributed to demolition losses and repairable losses. The total EAL was lower for the BRBFs, with the losses primarily attributed to demolition loss, and it was lowest for the CRBFs, with the losses mainly due to acceleration-sensitive nonstructural components. The cost-effectiveness analyses suggested that a reasonable cost premium for CRBFs was justifiable to reduce earthquake-related economic costs over the building's lifetime.

6.1.2. DEFINING CRBF DESIGN PARAMETERS TO CONTROL TOTAL SEISMIC LOSSES

Chapter 3 evaluated how different design parameters impact the performance and seismic loss of controlled rocking braced frame (CRBF) buildings at varying heights (three, six, and 12 stories). Two specific parameters were studied: the response modification factors (R) used for designing base rocking joints and the amplification factor applied to include higher-mode forces in the design. Different R values (ranging from 5 to 12) were considered, along with the amplification of higher-mode forces at two intensity levels: (i) the design earthquake (DE), and (ii) the maximum considered earthquake (MCE).

Chapter 3 showed that most design options resulted in low collapse probabilities, except for the six- and 12-story CRBFs with less resistance to rocking (those designed with R=12), which exhibited collapse probabilities of about 10% at the MCE intensity level. At the DE intensity level, story drifts reduced when the CRBF building was made more resistant to rocking, but, this reduction came at the cost of increased acceleration demands. However, differences in acceleration demands were minor when comparing design options for the CRBFs taller than three stories. Designing the CRBFs using higher-mode forces at the DE intensity level resulted in a more flexible frame with greater story drifts compared to the CRBFs designed with higher-mode forces at the MCE level. However, only slight differences were observed in acceleration demands when comparing the use of these intensity levels for higher-mode forces.

Chapter 3 demonstrated that, with more flexible CRBFs, the increase in seismic losses resulting from drift-sensitive components and irreparable losses is counterbalanced by the decrease in seismic losses caused by acceleration-sensitive nonstructural components. Thus, regardless of the design option used, the total expected annual loss for a particular building height with CRBFs remained very similar, even if there were notable changes in the sources of seismic loss with different design options.

6.1.3 Investigating Suitable EDPs for Developing Damage Fragility Curves of Acceleration-Sensitive Nonstructural Components

Chapter 4 explored suitable engineering demand parameters (EDPs) for constructing damage fragility curves for acceleration-sensitive nonstructural components. To accomplish this, acceleration-sensitive nonstructural components were modeled as single-degree-of-freedom (SDOF) systems with various properties, considering their placement on the first floor and roof of the six-story and 12-story buildings introduced in Chapter 2. The SDOF nonstructural components were subjected to the buildings' nonlinear response history to assess their ductility demand (μ).

Sixteen candidate EDPs were examined, with a specific focus on peak floor acceleration (PFA), spectral acceleration at the SDOF nonstructural component's period (Sa), and the geometric mean of spectral accelerations around that period (Sa_{ave}). The effectiveness of these

EDPs in defining damage fragility curves was evaluated by fitting lognormal regression models for the pairs of μ-EDP, considering ductilities greater than 1. The efficiency of candidate EDPs was assessed using the logarithmic standard deviation (β) and R-squared (R^2). Additionally, relative sufficiency was computed to evaluate the statistical independence of the candidate EDPs with respect to the location of the SDOF nonstructural components within the building and the type of SFRS used in the building.

The study revealed that Sa_{ave} is a suitable EDP for SDOF nonstructural components mounted on lower floors, where the floor motions are less influenced by the model properties of the building. Additionally, it suggested that Sa_{ave} was a suitable EDP when nonstructural components were designed with lower strength, as this leads to significant nonlinearity and elongation of effective periods of nonstructural components.

For SDOF nonstructural components on the roof and designed with higher strength, Sa was a suitable EDP. However, for those designed with lower strength, Sa was not suitable due to frequency filtering, particularly on higher floors. This is because the floor spectral acceleration peaks near the building's modal periods, and when nonlinearity arises in SDOF nonstructural components with periods near these structural periods, the elongation of effective period shifts it away from the peak of the floor spectrum. As a result, an EDP based on these peaks in spectral acceleration can grossly overestimate the component ductility demand, especially for weaker components that exhibit greater nonlinearity.

Chapter 4 also investigated the implications of these findings for developing unified damage fragility curves for nonstructural components, independent of the distinct types of SFRS and the floors of the building where the component is installed. Grouping μ-EDP data based on these factors revealed noticeable shifts in the data sets, especially when Sa was used as the EDP.

To mitigate the observed data shifts, the study proposed normalizing the EDP by the yield acceleration (a_y) of SDOF nonstructural components.

6.1.4 ASSESSING THE IMPACT ON SEISMIC LOSS ESTIMATES OF ECONOMIES OF SCALE IN CONSEQUENCE MODELS

The robustness of the FEMA P-58 seismic performance evaluation methodology for quantifying economies of scale in repair consequence simulation was the main emphasis in Chapter 5. The FEMA P-58 published methodology and its underlying documentation do not specify the approach for aggregating damaged component units across floors and damage states when calculating the reduction in possible repair cost or time caused by economies of scale. To assess all possible approaches for aggregating damaged component units within the scope of FEMA P-58, four "edge cases" were presented. The four edge cases are a combination of two binary choices: consider one floor or aggregate across all floors, and consider one damage state or aggregate across all damage states.

The difference in total repair costs between edge cases spans from less than 1% to more than 25% of the building's total repair cost, as shown by several instances in Chapter 5. The quantity of damaged components, the number of components on each floor, the consequence function parameters, and the number of damage states were all noted as being important drivers of the results. A three-step strategy was presented to help quickly examine the influence of the approach to damage aggregation on a particular performance evaluation in order to accommodate the vast number of analysts who use different tools, and to enable analysts to examine previous assessments where the model might no longer be accessible. The suggested approach offers three steps of escalating complexity to test each performance model component and determine whether the damage aggregation approach can have an impact on its repair costs. Also, a simplified calculation was suggested to enable analysts to roughly estimate the impact of the few components that account for the majority of the differences in repair prices.

6.2 Recommendations

As this thesis described advances toward its stated objectives to reduce seismic losses and improve seismic loss assessments, it also identified several aspects that require further study. The following recommendations are provided in two sections: those that can be changed to current practice on considered immediately and those that require further investigation.

6.2.1 Immediate recommendations

- As the design of controlled rocking braced frames advances towards codification, it is recommended to define their design parameters primarily based on considerations of collapse fragility. Excessive concern about the influence of these decisions on total expected seismic losses may not be necessary.
- It would be a major task to replace the extensive library of PFA-based damage fragility curves that have been created for acceleration-sensitive nonstructural components with ones that are based on a more suitable EDP. In the meantime, Chapter 4 suggests that existing damage fragility curves for nonstructural components with natural periods longer than 0.1 s should be used with caution, as PFA is not a suitable EDP for more flexible acceleration-sensitive nonstructural components.
- The variations observed in estimated losses using different edge cases in the examples detailed in Chapter 5 emphasize the need for analysts to be aware of the specific damage aggregation method employed in commonly used tools. This knowledge is crucial for making informed decisions about whether adjustments to results are necessary. Furthermore, developers of consequence models should furnish details on the calibration

of model parameters, accounting for various potential edge cases, to facilitate clear comparisons when evaluating different tools. It is therefore advised that developers of performance assessment tools document their approach to damage aggregation and, where feasible, offer multiple options to users. Additionally, given the modular nature of the FEMA P-58 framework, components used in calculations may have been developed by various groups with differing assumptions regarding damage aggregation. Documenting these assumptions for future studies would be valuable, as this information is currently unavailable.

6.2.2 RECOMMENDATIONS FOR FUTURE RESEARCH

- In Chapter 2 and Chapter 3, the research employed one regular archetype building as the basis for designing the investigated SFRSs. Furthermore, the numerical model of CRBFs was developed for structures designed with particular post-tensioning systems and energy-dissipating devices. These models also assumed a specific inherent damping model and that the connections would effectively transfer inertial forces from the floors to the CRBFs without impacting the uplift response. Expanding the database to include a wider range of designs would be helpful to validate the findings in these chapters for a broader spectrum of practical applications.
- In Chapters 2 and 3 of this thesis, the main criterion for evaluating different SFRSs and design options for CRBFs was the EAL, with a specific focus on repair costs. However, the results demonstrated that the trade-off between irreparable and repairable losses led to small differences in EAL, which may not be as small when comparing expected repair time. The expected recovery time is crucial because community resilience, which is a key objective in disaster recovery, relies on reducing repair time to expedite the return to

normalcy and minimize long-term social and economic consequences. Given this significance, it is recommended that the results of Chapters 2 and 3 be extended with consideration of repair time as a central metric.

- While many of the currently developed fragility curves for acceleration-sensitive nonstructural components rely on peak floor acceleration (PFA) as their basis, the conclusions drawn in Chapter 4 shed light on the limitations of PFA as an EDP for precise damage estimation. Generally, the spectral acceleration at the nonstructural component's period emerged as the more suitable EDP when components experience lower ductility demands. In contrast, an average spectral acceleration became more suitable when dealing with components with higher ductility demand. This implies that there is a need for further exploration into damage fragility curves based on a ductility-dependent EDP, which would consider the average spectral acceleration across a range of periods that extends as the ductility demand increases.
- The examples presented in Chapter 5 demonstrated that none of the edge cases provides an ideal choice for modeling component repairs. Considering the significance of modeling repair cost and repair time in performance-based engineering, it is suggested that the repair consequence estimation framework in FEMA P-58 could benefit from substantial enhancements to more accurately model economies of scale. Two recommendations for refining the modeling of consequence functions to achieve a better estimation of economies of scale are:

  (i) Economies of scale across components: Damage aggregation should consider multiple types of components when the damaged units of those components require identical repair actions. For instance, FEMA P-58 components that differ only in design details that do not affect the repair process can be grouped together.

(ii) Economies of scale across tasks: The similarities in repairing different components could be more precisely modeled by extending the component-group approach. FEMA P-58's background documentation already breaks down repair actions into a series of tasks, each carried out by a specific type of contractor. Economies of scale come into play when the same task is performed multiple times by the same contractor, regardless of the specific component's repair that is considered.

- The conclusions and insights drawn in Chapter 2 and Chapter 3 rely on the using PFAs as EDPs for acceleration-sensitive nonstructural components and the consideration of one of the edge cases for consequence modeling. Nevertheless, as Chapter 4 and Chapter 5 underscore the need for enhancing damage and consequence models, there is a recommendation to confirm the findings of Chapter 2 and Chapter 3 using these updated models.
- All results and trends were derived from the analysis conducted in Chapters 2 to 4 under the chosen design seismic hazard level, classified as 'high seismic.' It remains uncertain whether the observed results and trends would persist under different seismic design hazard levels, particularly those higher than the one selected. This raises a potential avenue for future research to explore the impact of varying seismic hazard levels on the outcomes, providing valuable insights for a more comprehensive understanding of the subject matter.
- The CRBFs investigated in this thesis are limited to those decoupled from the gravity system. It is suggested to also investigate CRBFs coupled with the gravity system to

better understand the effect of vertical acceleration on nonstructural components and damage in the floor system due to uplifting.

Appendix A.

Results for SDOF nonstructural components mounted on 6-story buildings

This appendix presents similar results shown in Chapter 4 but for nonstructural components mounted on the 6-story buildings.

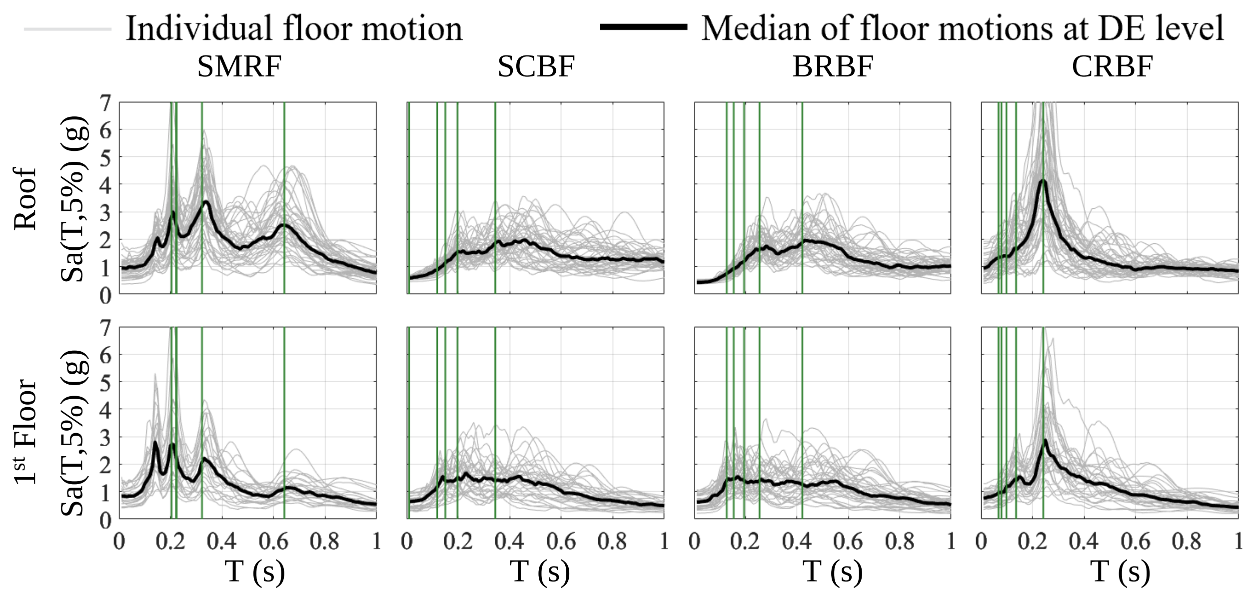

Figure A-1. Median acceleration floor response spectra for six-story buildings at the design earthquake (DE) level.

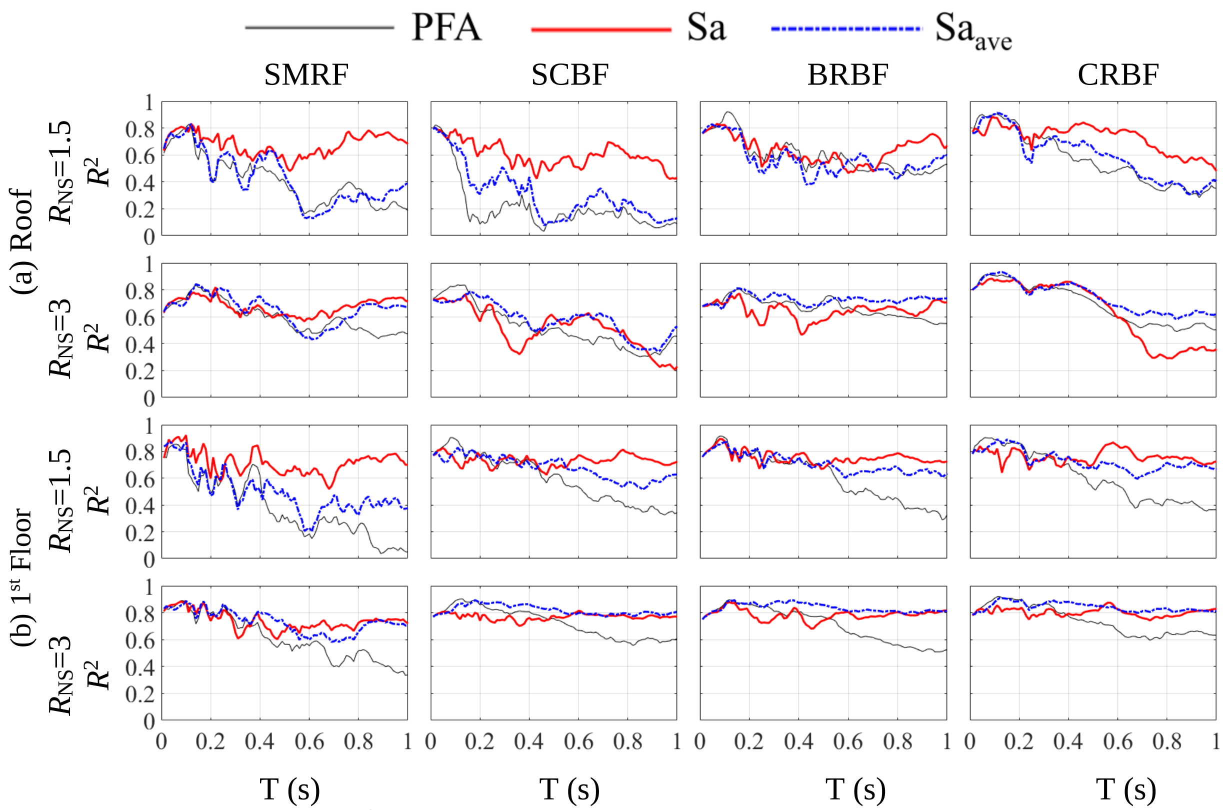

Figure A-2. Comparing R^2 of the regression models for the SDOF nonstructural components mounted on six-story buildings.

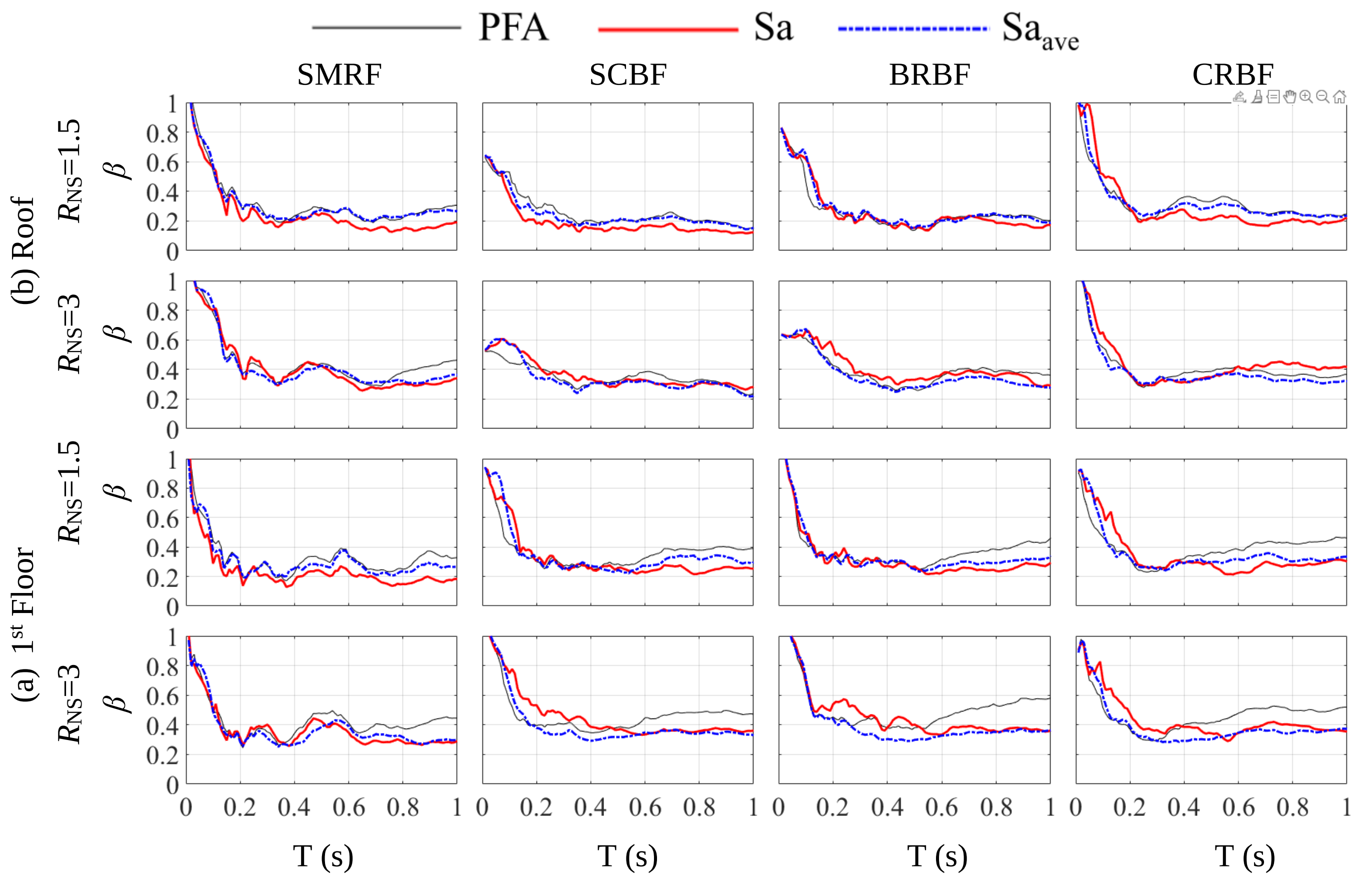

Figure A-3. Comparing β of the regression models for the SDOF nonstructural components mounted on six-story buildings.

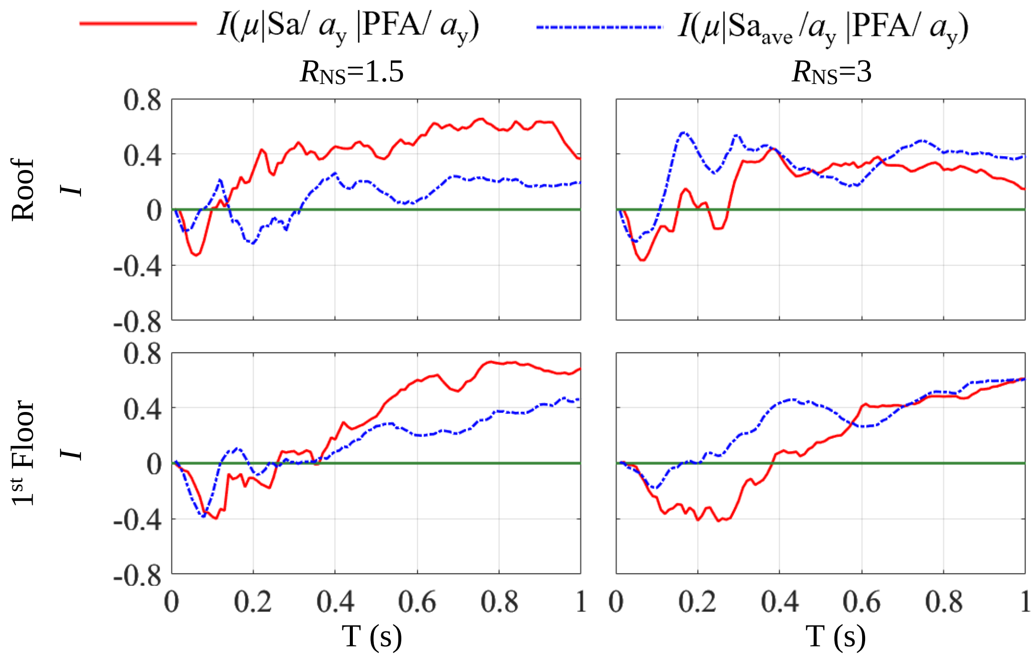

Figure A-4. Comparing relative sufficiency, I, of the regression models for the SDOF nonstructural components designed with R_{NS} of 1.5 and 3 mounted on the six-story buildings to assess the level of EDPs' statistical independence with respect to the SFRSs.

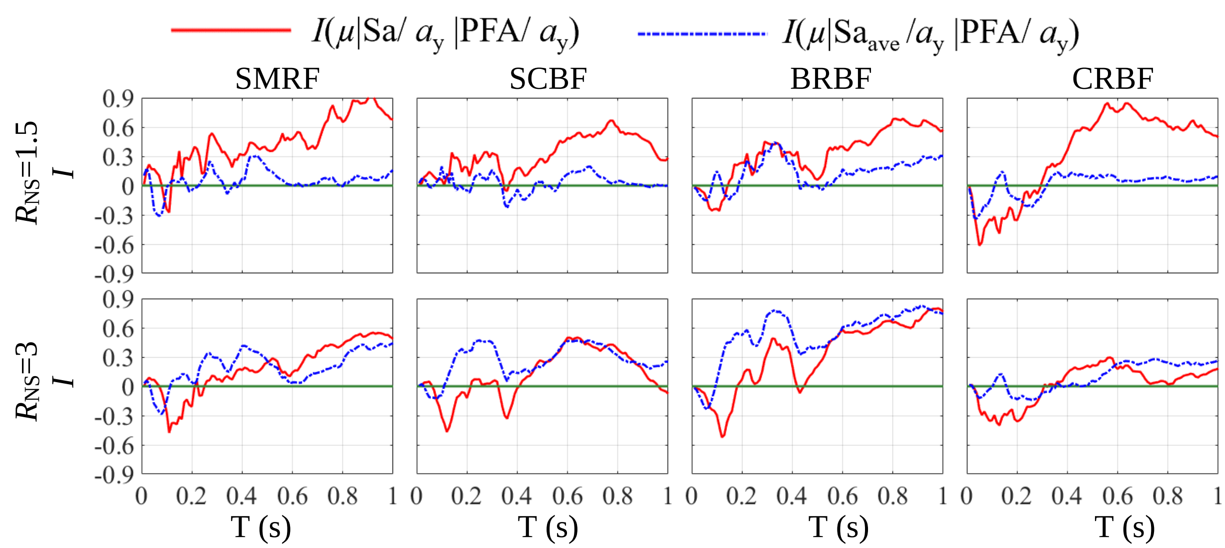

Figure A-5. Comparing relative sufficiency, I, of the regression models for the SDOF nonstructural components designed with R_{NS} of 1.5 and 3 mounted on the six-story buildings to assess the level of EDPs' statistical independence with respect to the floors.

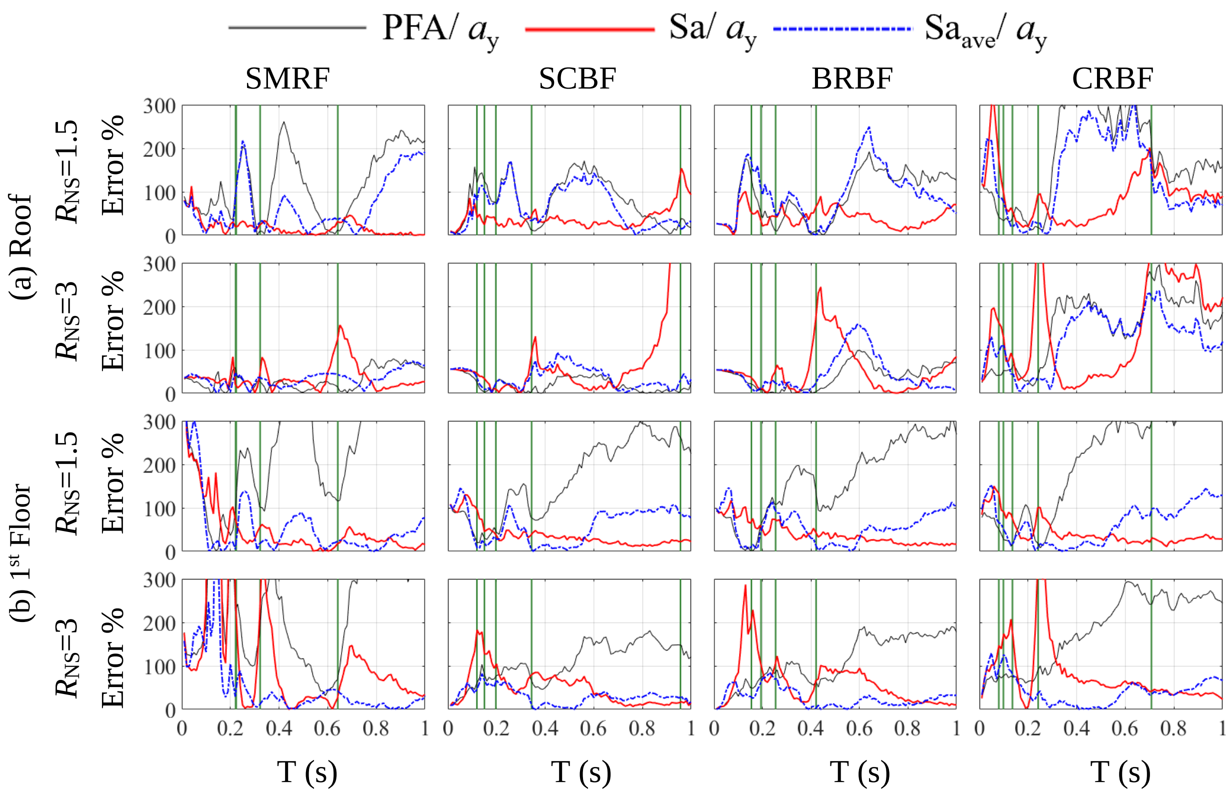

Figure A-6. Comparing EDPs in terms of seismic loss evaluation using the error between the actual expected annual loss and the expected annual loss calculated using the selected EDP, considering the regression models with grouping based on the SFRSs and the floors (six-story buildings).